

SIGNAL PROCESSING FOR MONITORING CEREBRAL HEMODYNAMICS IN NEONATES

Alexander Caicedo Dorado

Dissertation presented in partial
fulfillment of the requirements for the
degree of Doctor in Engineering

June 2013

SIGNAL PROCESSING FOR MONITORING CEREBRAL HEMODYNAMICS IN NEONATES

Alexander CAICEDO DORADO

Supervisory Committee:

Prof. dr. ir. D. Vandermeulen, chair

Prof. dr. ir. S. Van Huffel, promotor

Prof. dr. G. Naulaers, promotor

Prof. dr. ir. B. Puers

Prof. dr. ir. M. Moonen

Prof. dr. F. van Bel

(University Medical Center/Wilhelmina
Children's Hospital)

Prof. dr. Sc.Tech. M. Wolf

(University Hospital Zurich)

Dr. ir. I. Tachtsidis

(University College London)

Dissertation presented in partial
fulfillment of the requirements for
the degree of Doctor
in Engineering

June 2013

© KU Leuven – Faculty of Engineering
Kasteelpark Arenberg 10 box 2446, B-3001 Leuven (Belgium)

Alle rechten voorbehouden. Niets uit deze uitgave mag worden vermenigvuldigd en/of openbaar gemaakt worden door middel van druk, fotocopie, microfilm, elektronisch of op welke andere wijze ook zonder voorafgaande schriftelijke toestemming van de uitgever.

All rights reserved. No part of the publication may be reproduced in any form by print, photoprint, microfilm or any other means without written permission from the publisher.

D/2013/7515/59
ISBN 978-94-6018-673-8

Acknowledgments

Are there people inside the speakers making music?, that is the first question that I remember troubled me when I was a child. I have always been driven by curiosity and a need to know the "why" of the things surrounding me. Things were not much different when I grew up and started the high school or even the university, old questions were replaced by new ones and new "enigmas" were added to the list. Specially, when they are related to the functioning of the human body. It was such a need the one that motivated me to pursue a PhD. This book, somehow, represents the sum of all those efforts, and it makes me realize that I have made it, I have accomplished one of my dreams, I will become a Doctor :D. However, this quest has not been easy, there have been highs and downs, but without the help of the people that, directly or indirectly, contributed to this achievement, this book will not be in your hands today. It is for that reason that I would like to dedicate this work to all the people that shared in one moment or another my path.

Since there are a lot of people to whom I am grateful, since they helped me through my journey, I would like to start in chronological order. First of all, I would like to thank my family. Gracias Mamá, Papá, hermanas y sobrinas por su apoyo, ayuda y motivación a lo largo de este viaje. Especialmente quiero agradecer a mis Padres por su dedicación. Sin su apoyo incondicional yo no podría haber alcanzado esta meta. Siempre recordare lo que mi madre decía: "Aprovechen el estudio que es lo único que quedará de todo lo que les damos", esas palabras siempre estuvieron en mi mente y fueron el pilar que me ha permitido llegar a donde estoy hoy. Yo se que uno de los grandes sueños de mi Mamá fue que nosotros, sus hijos, obtuviéramos un título universitario, es por esta razón que alcanzar este grado no es solamente cumplir mi sueño sino también cumplir con creces el tuyo Mamá, gracias por todo. A mi papá, hermanas y sobrinas, les agradezco por haber estado siempre cuando les necesite, papá, Lida, Martica, Jenny, Marcela, y Jainy, muchas gracias por todo, saben que a todos los llevo en el corazón y siempre los recuerdo.

I would also like to thank to my Colombian friends for the support and the nice moments that we spent together, Sady, Edna, Gato, Mario, Alfonso, and of course Carolina. Carola thank you for being there when I needed, there are so many things for which I am grateful to you. For this reason I will dedicate a special paragraph to you later on ;). How to forget my professors at the university, Zosimo and Luisa, among all of them you were the ones which whom I worked the closest. Thanks to you Luisa I was introduced in the world of Biomedical Signal Processing, I will always be grateful for that. Zosimo, you always trusted in me and my capabilities thank you for your confidence. I would also like to thank my professors during the master, Luis Alfonso, Aldemar, Ricardo, Oscar, thanks to you I got to be in contact with universities in Belgium, you all are responsible in a great part for this achievement.

How to forget my time in Gent, there are so many people that I would like to thank. First of all, Marian and Janice, thank you for making my stay in Gent brighter, there will always be a place in my heart for you both. Niño and Douglas thank you for the beers next to the channel and the nice talks. Clara, thank you for helping me to polish my abilities.

I sincerely want to thank to my Belgian friends, Elisabeth, Nele, Dennis, Hans, Ruben, Sam and Simon. Thanks to you and your recommendation letter I was able to come to Belgium to pursue my dream. I will always be thankful to you all. Especially, I want to thank to Dennis, Hans and Simon. From the moment that I arrived in Belgium you were always there. In Colombia, people always told me that Belgians were cold, you showed me something different, I always felt welcome by you. Thank you!. Hans, I would like to specially thank you for your friendship, you have been there from the beginning of this part of my journey, sorry for complaining so much and for taking so much of your time during the coffee breaks. I know that you will always be there when needed.

Now, I would like to thank to my promotor prof. Sabine van Huffel. Sabine, without your trust and your help through these years this dream would have not become true. Thank you for your guidance and support during my PhD. Especially, thank you for your vote of confidence. I can imagine it was not an easy choice to decide whether to give or no the opportunity to a Colombian, from an unknown University - that is not even listed in the top 100 in Colombia - and who only has as support a recommendation letter from some Belgian students. Thank you Sabine, I hope that you have no regrets with your decision :D. I also would like to thank to my co-promotor Prof. Gunnar Naulaers. Gunnar, thank you for all the input that you have given me, I can imagine is not easy to work with such a stubborn engineer as I am :D. You have always be patient and have always trust in my work, thank you!.

Now, to my colleges in BioMed, I know you were expecting this part ;). My first

memory in BioMed is from when I arrived at ESAT and Maria Isabel pick me up at the reception. Maria, thank you very much for all your help, you were and always will be one of my favorite persons in the group. To my first office mates, Steven and Bogdan. What a contrast!, just by looking at the desks, Steven's was always organized, while Bogdan's was, how to say it, a little bit more chaotic :D. I could have not imagine a better environment to start my PhD, thanks to you I laugh a lot and enjoyed my time at work. To the girls office, Anca, Diana, Maryia Ishteva, Maria Isabel, thank you very much for the candies and cakes :D. Anca, I will never forget our hunt for penguins, together with Bogdan, in Argentina :D. Diana, thank you for your nuts cake :D, and I am really sorry for all my silly questions about linear algebra, you have always had the time and patient to answer them, thank you very much. Maryia Ishteva, you are such a nice person, BioMed without you was not the same. Bori, thank you for everything, specially in the last months. I have been quite a burden distracting you from work, just because I was felling tired and needed a break, thank you for never kicking me out of your office :D. Katrien, you have always welcome me with a smile, thank you for visiting in London. We spend such a pleasant time walking in London streets, you are also one of the person that I miss the most in BioMed. Joachim, we worked together during the last year, thank you for your help with the measurements for the Duchenne study, it was always nice to work with you. To my new office mates, Carolina, Devy and Milica, thank you for the nice discussions and laugh, Milica, I am sorry for bothering you so much, I hope you have notice that 90% of the things I say are just joking, the other 10% are not true :D. Carola, from the work point of view, thank you very much for all the discussions and ideas, as I have already mentioned to some people, you are one of the best researches that I know, thanks to you I have had several ideas for my work, thank you!. Kris, Yipeng and Vladimir, thank you for the nice time during the conference in San Diego. We had a really nice time. Kris, I am still waiting for the invitation to travel in your yacht with your friend Lionel :D. Ivan, how to forget the Latin Serbian :D, thank you for the nice talks and your jokes, even though some of them were to difficult for me to understand :D. Ninah and Rob, the two Hollanders :D, thank you for the nice time, specially in the *whiteboard* ;). Ninah I am sorry for my awkward sense of humor, I hope you have found it funny :D. Rob, thanks for the Frisbee and for suggesting me to watch Game of Thrones, what a series man!!. Tim, I will always remember the conversation about UFO and Aliens in the way back from one meeting in Brussels, that was really funny and somehow scientific :D. Vanya, first of all I would like to thank you for attending the MEDSIP conference, it was such a nice surprise to see you there. I would also like to thank you for the discussions about the work related to kernel PCR, your ideas and insight have been of much help. Kirsten and Laure, thank you for your help with statistics and the discussions during the BioMed social events :D. I also would like to thank Jan,

Ben, Wouter, Maarten, Rosy, Franco, Yang, Amir, Nicolas, and Teresa for the nice moments during the different activities organized at Sabien's place. To all my BioMed colleagues, thank you very much!!!

I also would like to thank to the people outside BioMed with whom I collaborated. Prof. Frank van Bel, Dr. Petra Lemmers, Prof Martin Wolf., Dr. Ursula Wolf, Dr Ilias Tachtsidis, Dr. Maria Papademetriou. It has been a pleasure to have the opportunity to work with you all. Thank you for your confidence. Especially, I would like to thank Ilias for receiving me in his lab at UCL. It was such a nice experience, not only in the academy life, but also personally. I have to say that after that experience, London has become my favorite place in the world. I also would like to thanks to Joke, Liesbeth and Eva. Thank you for all your insight, the time we spend during the conferences, and the nice talks. You all made of this experience a pleasant journey.

I also would like to thank to Jeroen Lecoutre for helping me with the translation of the abstract :D, and also for the nonsense talks during the coffee breaks, thanks for bearing with my silliness :D. I also want to thank to all the members of the IEE branch that welcomed me as if I were one of them, even though I was, at the time, the only non Belgian member. Thank you very much for making my first years in Leuven such a pleasant experience. also to the Colombian community in ESAT, Mauricio, Fabian and Carlos, thank you for the jokes and conversations.

Now, as I promise, I want to specially thank to Carolina and Steven. You both are my family in Belgium. You are some of the people that I know will always be there when I needed, and I hope that you know that you can count with me too. There are no words to describe how important you have become for me. I will always be grateful for your help, your jokes, your company, the dinners, the Christmas and new year celebrations, but more importantly for taking care of me when I was felling sick. Thank you for all!!!

Alexander Caicedo
Leuven, June 2013

Abstract

Disturbances in cerebral hemodynamics are one of the principal causes of cerebral damage in premature infants. Specifically, changes in cerebral blood flow might cause ischemia or hemorrhage that can lead to motor and developmental disabilities. Under normal circumstances, there are several mechanisms that act jointly to preserve cerebral hemodynamics homeostasis. However, in case that one of these mechanisms is disrupted the brain is exposed to damage. Premature infants are susceptible to variations in cerebral circulation due to their fragility. Therefore, monitoring cerebral hemodynamics is of vital importance in order to prevent brain damage in this population and avoid subsequent sequelae. This thesis is oriented to the development of signal processing techniques that can be of help in monitoring cerebral hemodynamics in neonates.

There are several problems that hinder the use in clinical practice of monitoring cerebral hemodynamics. On one hand, continuous measurements of cerebral blood flow, or hemodynamical variables, are difficult to obtain in premature infants. In this context, Near Infrared Spectroscopy (NIRS) is one of the few technologies that is available for the measurement of hemodynamical variables in this population. NIRS is a noninvasive and safe technology that is based on light radiation. NIRS allows the continuous measurement of cerebral oxygenation that under certain considerations reflects changes in cerebral blood flow. On the other hand, cerebral hemodynamics assessment is performed by evaluating the strength of the relationship between some systemic variables, e.g. mean arterial blood pressure and concentration of CO_2 , and the cerebral hemodynamics variables. Under normal conditions cerebral hemodynamics variables should be independent of systemic variations. Coupled dynamic between systemic and cerebral hemodynamics variables represents a high risk situation for the patient. Among the techniques available for the monitoring of cerebral hemodynamics, most of them assume that the mechanisms responsible for its control are linear and univariate. In reality, these mechanisms are nonlinear, multivariate, nonstationary and highly coupled.

This thesis, on one hand, introduces the use of more sophisticated signal processing techniques for monitoring cerebral hemodynamics, which can address the multivariate and/or the nonlinear nature of the mechanisms involved in its control. Linear techniques such as canonical correlation analysis, subspace projections and wavelet based transfer function; and nonlinear techniques such as least squares support vector machines and kernel principal component regression, have been introduced for the NIRS-based monitoring of cerebral hemodynamics. On the other hand, kernel principal component regression is a nonlinear methodology that produces as result a black box model, which lacks clinical interpretability. Therefore, in this thesis attention has been given to the development of methodologies that allow to interpret the results produced by this nonlinear model in a clinical framework. For this purpose a method based on subspace projections is proposed. In addition, in this thesis, results from several clinical studies related to monitoring cerebral hemodynamics are presented.

Samenvatting

Verstoringen in de cerebrale hemodynamiek is een van de voornaamste oorzaken van cerebrale schade bij prematuren. Concreet zouden veranderingen in cerebrale doorbloeding ischemie of bloeding kunnen veroorzaken, wat kan leiden tot stoornissen in de motoriek en de ontwikkeling. Onder normale omstandigheden zijn er verschillende mechanismen die gezamenlijk optreden om cerebrale hemodynamiek in homeostase houden. In het geval dat een van deze mechanismen wordt verstoord, worden de hersenen blootgesteld aan schade. Premature zuigelingen zijn gevoelig voor variaties in cerebrale circulatie vanwege hun kwetsbaarheid. Daarom is het opvolgen van de cerebrale hemodynamiek van vitaal belang in deze populatie om schade aan de hersenen en de daarbij horende gevolgen te voorkomen. Deze thesis is gericht op het ontwikkelen van signaalverwerkingstechnieken die van hulp kunnen zijn bij het opvolgen van de cerebrale hemodynamiek in neonaten.

Er zijn verschillende problemen die het opvolgen van de cerebrale hemodynamiek verhinderen. Enerzijds zijn continue metingen van de cerebrale doorbloeding, of hemodynamische variabelen, moeilijk te meten bij prematuren. In deze context is Nabij InfraRood Spectroscopie (NIRS) een van de weinige beschikbare technieken voor het meten van hemodynamische variabelen in deze populatie. NIRS is een niet-invasieve en veilige technologie die gebaseerd is op lichtstraling. NIRS maakt de continue meting van hersenoxygenatie mogelijk. Onder bepaalde overwegingen weerspiegelt deze hersenoxygenatie veranderingen in de cerebrale doorbloeding. Anderzijds wordt cerebrale hemodynamiek gelueerd door de afhankelijkheid tussen enkele systemische variabelen zoals gemiddelde arteriële bloeddruk en CO₂-concentratie en de cerebrale hemodynamiekvariabelen te onderzoeken. Onder normale omstandigheden zouden cerebrale hemodynamiekvariabelen onafhankelijk van systemische variaties moeten zijn. Een gekoppelde dynamiek tussen systemische en cerebrale hemodynamische variabelen vertegenwoordigt een hoge risicosituatie voor de pati. Onder de technieken die beschikbaar zijn voor de opvolging van de cerebrale hemodynamiek gaan de meeste ervan uit dat de mechanismen

die verantwoordelijk zijn voor de controle lineair en univariate zijn. In werkelijkheid zijn deze mechanismen niet-lineair, multivariaat, niet-stationair en sterk gekoppeld.

Eenzijds introduceert dit proefschrift voor het opvolgen van de cerebrale hemodynamiek het gebruik van meer geavanceerde signaalverwerkingstechnieken die de multivariate en/of niet-lineaire aard van de controlemechanismen in rekening brengen. Lineaire technieken zoals canonische correlatie analyse, deelruimteprojecties en waveletgebaseerde overdrachtfunctie, en niet-lineaire technieken zoals kleinste kwadraten support vector machines en kernel hoofdcomponent regressie, zijn ingevoerd voor de op NIRS gebaseerde opvolging van cerebrale hemodynamiek. Anderzijds is kernel hoofdcomponent regressie een niet-lineaire methode die leidt tot een black box-model dat klinisch niet interpreteerbaar is. Daarom is in dit proefschrift aandacht besteed aan de ontwikkeling van methoden waarmee de meetresultaten van dit niet-lineaire model in een klinisch kader kunnen worden geïnterpreteerd. Hiertoe wordt een werkwijze op basis van deelruimteprojecties voorgesteld. Ten slotte zijn in dit proefschrift de resultaten van verschillende klinische studies met betrekking tot de opvolging van cerebrale hemodynamiek gepresenteerd.

Nomenclature

Symbols

x, s, \dots	vectors
A, B, \dots	matrices
$ a $	absolute value of a
A^T	transpose of the matrix A
A^\dagger	pseudoinverse of the matrix A
$\kappa(x_i, x_k)$	kernel function evaluated with the vectors $\{x_i, x_k\}$
$\mathbf{K}(x, x_k)$	Column from the kernel matrix corresponding to x_k
$C(A)$	column space of the matrix A
\oplus	addition of subspaces

Abbreviations

ΔHbD	Changes in Hemoglobin concentration differences
ΔHbO_2	Changes in oxy-hemoglobin concentration
ΔHbT	Changes in Total hemoglobin concentration
ΔHHb	Changes in deoxy-hemoglobin concentration
6MWT	6 minute walk test
a.u.	Arbitrary units
CA	Cerebral Autoregulation
CBF	Cerebral blood flow
CBFv	Cerebral blood flow velocity
CBV	Cerebral blood volume
CCA	Canonical Correlation Analysis
CO_2	Carbon dioxide
COH	Coherence
COR	Correlation
CVP	Central venous pressure
CWS	Continuous wave spectrometry

CytOx	Cytochrome Oxidase
DFT	Discrete Fourier transform
DMD	Duchenne muscular dystrophy
DPF	Differential path length
DWT	Discrete wavelet Transform
ECMO	Extra Corporeal Membrane Oxygenation
EE	Elementary Effects
EtCO ₂	End tidal CO ₂
FRS	Frequency resolved spectrometry
FTOE	Fractional tissue oxygen extraction
FOE	fractional oxygen extraction
HbD	Hemoglobin concentration differences
HbO ₂	oxy-hemoglobin concentration
HbT	Total hemoglobin concentration
HHb	deoxy-hemoglobin concentration
HR	Heart rate
IVH	Intraventricular haemorrhage
KPCA	Kernel principal component analysis
KPCR	Kernel principal component regression
L	Liter
LS-SVM	Least Squares Support Vector Machines
MABP	Mean arterial blood pressure
MDI	Mental Development Index
μmol	Micro-molar
ml	Milliliter
mmHg	Millimeter of mercury
min	Minutes
MoCOH	Modified Coherence
MVIC	Maximal voluntary contraction
NICU	Neonatal Intensive Care unit
NIRS	Near infrared spectroscopy
OSP	Oblique subspace projections
OrSP	Orthogonal subspace projections
PCA	Principal component analysis
PDI	Physicomotor Development Index
pCO ₂	Partial pressure of CO ₂
PCR	Principal component regression
pO ₂	Partial pressure of oxygen
PVL	Periventricular leukomalacia
RKHS	Reproducing Kernel Hilbert Space
rScO ₂	regional cerebral oxygen saturation
SaO ₂	arterial oxygen saturation
sEMG	surface electromyogram

SRS	Spatially resolved spectrometry
SVD	Singular value decomposition
SVM	Support Vector Machines
TCD	Transcranial Doppler
TOI	tissue oxygenation index
TRS	Time resolved spectrometry
WBTF	Wavelet Based Transfer Function

Contents

Acknowledgments	i
Abstract	v
Samenvatting	vii
Nomenclature	ix
Contents	xiii
1 Introduction	1
1.1 Clinical Framework	1
1.1.1 Brain pathologies in neonates	3
1.1.2 Causes of brain damage in neonates	5
1.2 Cerebral Autoregulation	6
1.3 Near Infrared Spectroscopy (NIRS)	9
1.3.1 Continuous wave spectroscopy	13
1.3.2 Spatially resolved spectroscopy	13
1.3.3 Time resolved spectroscopy	16
1.3.4 Frequency domain TRS	16
1.4 Clinical applications of NIRS	17

1.5	Goals of the Thesis	20
1.6	Thesis Overview	21
1.6.1	Part I: Advanced Signal Processing Methodologies	22
1.6.2	Part II: Clinical Case Studies	23
1.7	Personal Contributions	24
2	Linear Methods	29
2.1	Traditional Methods	29
2.1.1	Correlation	30
2.1.2	Coherence	31
2.1.3	Partial Coherence	33
2.1.4	Transfer Function	34
2.1.5	Cerebral autoregulation assessment	38
2.2	Wavelet Based Transfer Function Analysis	38
2.2.1	Wavelet Transform	39
2.2.2	Wavelet Power Spectrum	40
2.2.3	Wavelet Cross-power Spectrum	42
2.2.4	Wavelet Coherence and transfer Function	43
2.2.5	Discrete Wavelet Transform	48
2.3	Canonical Correlation Analysis	54
2.3.1	Introduction to CCA	54
2.3.2	Interpreting CCA	55
2.3.3	Visualizing the results from CCA	57
2.3.4	Example	58
2.4	Subspace Projections	60
2.4.1	Orthogonal subspace projections	60
2.4.2	Oblique subspace projections	61

2.4.3	DWT and projectors	62
2.4.4	Consecutive Projectors	64
2.4.5	Example	66
3	Nonlinear Regression	71
3.1	Least Squares support Vector Machines in Nonlinear Regression	72
3.1.1	LS-SVM for function estimation	72
3.1.2	Robust LS-SVM	73
3.1.3	Weighted LS-SVM for signal preprocessing	75
3.2	Principal Component Regression	76
3.3	Kernel Principal Component Regression	77
3.4	Projection Matrices in a RKHS	79
3.4.1	Projections onto the regressor subspaces	80
3.5	Sparsity in the KPCR Model	82
3.5.1	RBF Kernel and the trace of P_{Φ}	83
3.6	Toy Examples	85
3.6.1	Noisy sinc function	85
3.6.2	Artificial dataset	87
3.7	Conclusion	90
4	Data and Preprocessing	95
4.1	University Hospital Leuven	95
4.1.1	Propofol dataset	97
4.1.2	Leuven dataset	97
4.2	University Medical Centre Utrecht	98
4.2.1	Utrecht dataset	99
4.2.2	Labetalol dataset	100
4.3	University Hospital Zurich	100

4.4	ECMO Dataset	101
4.5	Duchenne Dataset	101
4.6	Lamb Dataset	105
4.7	Preprocessing	105
4.7.1	Artifacts	105
4.7.2	Filtering	107
5	The Use of TOI and rScO₂ in Cerebral Autoregulation Assessment	109
5.1	Introduction	109
5.2	Methods	110
5.3	Results	111
5.3.1	Analysis on the patient level	111
5.3.2	Analysis on the epoch level	112
5.3.3	Analysis for epochs with high variations in MABP	112
5.3.4	Patient data sampled at 3 sec	114
5.4	Discussion	115
5.5	Conclusion	117
6	Standardization of Traditional Methodologies for Cerebral Autoregulation Assessment	119
6.1	Introduction	119
6.2	Data	120
6.3	Methods	122
6.3.1	Methodology for correlation	122
6.3.2	Methodology for coherence	123
6.3.3	Methodology for Transfer Function	124
6.4	Sensitivity Analysis	124
6.4.1	Elementary effects	125

6.4.2	Variance based approach	126
6.4.3	Test for stationarity	127
6.5	Results	127
6.5.1	Test for Stationarity	127
6.5.2	Elementary Effects Analysis	128
6.5.3	Variance Based Analysis	129
6.6	Discussion	131
6.7	Conclusion	134
7	Clinical Case Studies	137
7.1	Cerebral autoregulation assessment I	138
7.1.1	Introduction	138
7.1.2	Data	138
7.1.3	Results	139
7.1.4	Discussion	140
7.1.5	Conclusions	142
7.2	Cerebral autoregulation assessment II	142
7.2.1	Introduction	142
7.2.2	Methodology	143
7.2.3	Results	144
7.2.4	Discussion	144
7.3	ECMO study I	148
7.3.1	Introduction	148
7.3.2	Methods	150
7.3.3	Results	150
7.3.4	Discussion	152
7.4	ECMO study II	153

7.4.1	Introduction	153
7.4.2	Methods	153
7.4.3	Results	154
7.4.4	Discussion	155
7.5	Lamb Study	156
7.5.1	Introduction	156
7.5.2	Data and Methods	157
7.5.3	Results	158
7.5.4	Discussion	164
7.6	Labetalol study	166
7.6.1	Introduction	166
7.6.2	Methods	166
7.6.3	Results	167
7.6.4	Discussion	169
7.6.5	Conclusion	170
7.7	Duchenne Muscular Distrophy Study	170
7.7.1	Introduction	170
7.7.2	Methods	171
7.7.3	Results	175
7.7.4	Discussion	176
7.8	Sleep Apnea Study	181
7.8.1	Introduction	181
7.8.2	Data and Methods	181
7.8.3	Results	182
7.8.4	Discussion	183

8 Summary and Future Work

185

8.1 Summary	185
8.2 Discussion	188
8.3 Future Work	190
Bibliography	193
List of publications	221

Chapter 1

Introduction

In this chapter the principal concepts treated in this thesis will be introduced. The chapter will define the clinical and methodological framework for the development of this thesis. In Section 1.1 the basis about cerebral hemodynamics and its clinical importance will be discussed. In section 1.2 the concept of cerebral autoregulation (CA) and its importance in cerebral hemodynamics monitoring will be introduced. Section 1.3 will briefly present the basis about Near Infrared Spectroscopy (NIRS) technology. The clinical applications of NIRS will be discussed in section 1.4. The chapter will end with a discussion of the main goals of this thesis in section 1.5, an overview of the thesis in section 1.6, and a summary of the personal contributions presented in this dissertation in section 1.7.

1.1 Clinical Framework

One of the most important causes of brain injury are disturbances in cerebral hemodynamics [156, 233]. In premature newborns, brain injury might lead to mental and motor disabilities. Therefore, monitoring cerebral hemodynamics is of importance in this population. Cerebral hemodynamics covers the terms related to the dynamics of cerebral blood flow (CBF), cerebral blood volume (CBV) and cerebral blood flow velocity (CBFv), among other variables. Under normal circumstances the brain is protected from pathological disturbances, and variations of some physiological variables, by a series of homeostatic mechanisms; which keep the CBF relatively constant. When one or more of these mechanisms are disrupted, the brain is exposed to damage. Studies

of cerebral hemodynamics, reported in the literature, quantify the status of these mechanisms by investigating the physiology of CBF and its relation with variations in systemic variables.

Cerebral blood flow plays a central role in cerebral metabolism since it is responsible for the delivery of nutrients and oxygen to the brain [149]. An adequate CBF will keep a balance between nutrients delivery and consumption in order to maintain the brain homeostasis, by preserving the brain energy levels through the oxidative metabolism of glucose. Deficit in these levels will result in disturbance or loss in brain function, and, if sustained, can lead to brain damage [122]. Therefore, changes in CBF might be caused by pathological conditions related to a reduction in brain energy levels. However, changes in CBF without knowing the status of oxygen delivery and consumption is of no clinical use, since they cannot be linked to pathological conditions.

There are several systemic variables that affect cerebral circulation. First of all, under extreme or pathological conditions, changes in mean arterial blood pressure (MABP) produce changes in CBF. However, under normal circumstances the brain is protected from variations in MABP by the cerebral autoregulation (CA) mechanism. CA has been extensively studied in the literature. CA acts over a wide range of blood pressure values where changes in MABP do not reflect changes in CBF [85]. But, when MABP values are outside this range the CBF starts to follow the dynamics of MABP, under this condition the CBF is said to become *pressure passive*. The lower and upper bounds where CA is active are known in adults, but unknown in the neonatal population. Some studies indicate that the lower bound in MABP values might be located around 30mmHg, but no information has been reported for the upper limit [76]. Since low MABP values may cause hypoxia due to a low brain perfusion, while a high MABP might cause hemorrhage due to the rupture of small capillaries, monitoring MABP and its relation with CBF is of vital importance in order to avoid brain damage. Second, concentration of gases such as CO_2 and O_2 and their partial pressures, pCO_2 and pO_2 respectively, have a high impact on CBF [157, 144, 2, 51]. On one hand, increasing values of pO_2 produce a mild vasoconstriction which causes a decrease in CBF. On the other hand, in contrast with pO_2 , an increase in pCO_2 values produces vasodilation which increases CBF. The effect of pCO_2 is more pronounced than the effect of pO_2 on the CBF [85]. The mechanisms underlying these phenomena are related with the sensitivity of the vascular bed to changes in pH [114, 240]. High concentration of CO_2 produces hypercapnia, which leads to tissue acidosis. Tissue acidosis produces a reduction of the pH level in the smooth muscles surrounding the capillary bed, causing vasodilation. Third, changes in temperature and blood viscosity also affect CBF, an increase in viscosity produces a decrease in CBF, while a decrease in temperature produces a decrease in CBF [85]. Furthermore, an

increment in metabolic rate will also produce an increase in CBF [23], which can be explained by a joint increment in the delivery of nutrients to meet the brain metabolic demand, and an increase in $p\text{CO}_2$ levels, which, as explained before, causes vasodilation. By monitoring the relation between systemic changes and cerebral hemodynamics variables pathological conditions can be identified and adequate treatment can be provided in order to avoid brain damage.

In clinical practice monitoring of cerebral hemodynamics present several challenges. On one hand, brain homeostasis is maintained by several mechanisms that react to changes in several systemic variables and are highly interrelated. This implies that variations in one of the systemic variables produces a cascade of reactions that will affect the other variables as well [23]. Therefore, the multivariate nature of cerebral hemodynamics should be taken into account in order to identify, accurately, pathological conditions. On the other hand, measurements of variables related to cerebral hemodynamics are difficult to obtain, particularly in the neonates. Due to the fragile situation of the neonates, noninvasive techniques are needed for the assessment of brain hemodynamics variables. However, these techniques can only obtain surrogate measurements that under certain conditions might reflect changes in the hemodynamical variables of interest.

An ideal monitoring system for cerebral hemodynamics should be able to accurately identify pathological conditions that might expose the neonates to brain damage. Among these pathological conditions, Intraventricular hemorrhage (IVH) and Periventricular leukomalacia (PVL) are the most common causes of brain damage in the neonatal population at the neonatal intensive care units (NICU).

1.1.1 Brain pathologies in neonates

Among the most important brain pathologies, intraventricular hemorrhage (IVH) and periventricular leukomalacia (PVL) are of particular interest in this thesis; since their origin is related to fluctuations in the cerebral circulation. The outcome of these lesions ranges from mental and motor developmental retardation up to death.

Intraventricular Hemorrhage

IVH is one of the major complications found in premature neonates. IVH is defined as a bleeding in the cerebral ventricles. It typically initiates in the capillary bed of the germinal matrix. IVH is originated by multiple factors,

being the fragility of the germinal bed and disturbances in the CBF the most important ones. Some of the risk factors for the development of IVH include a low Apgar score, severe respiratory distress syndrome, hypoxia, hypercapnia, among others [7, 103, 52, 222].

Fluctuating CBF is associated with the development of IVH [215, 167, 166]. Other causes for CBF fluctuations, like hypercarbia and hypotension, have also been correlated with the development of IVH [17, 143, 40]. Lee and colleagues found a significant association between metabolic acidosis and the development of IVH, using a multivariate logistic regression [115]. Other influencing factors related to changes in CBF are the use of inotropes, transfusion of blood products and sodium bicarbonate bolus infusions [167]. Furthermore, the withdrawal and infusion of blood via umbilical catheters can cause a significantly rapid change in cerebral blood flow of preterm infants [27], which may disturb cerebral hemodynamics. Analysis of CBF using NIRS has also shown that impaired cerebral autoregulation was highly correlated with development of IVH [216]. Perlman and colleagues demonstrated that the transitions from autoregulation to a pressure passive circulatory pattern appears to be an important step in the development of periventricular or intraventricular hemorrhage (PV-IVH) [167]. In these cases when there is a sudden change in CBF and MABP, hemorrhage can occur in the immature germinal matrix [167, 27, 166]. In summary, Lee et al. [115] showed that the risk factors for the pathogenesis of PV-IVH are related to hemodynamics changes. A more comprehensive review of the causes for IVH can be found in [11].

Periventricular Leukomalacia

Like IVH, periventricular leukomalacia (PVL) is the result of an inadequate brain perfusion. PVL is caused by ischemic damage in the periventricular white matter adjacent to the external angles of the lateral ventricles [12, 49, 9, 190, 116] in the brain. PVL is a common outcome of neonatal hypoxic-ischemic encephalopathy [223], and it is strongly related to a poor neurological developmental outcome. Chow and colleagues showed that the evolution of PVL correlates with changes in computer tomography scans and electroencephalography (EEG) [38]. In this study, normal scans and EEG were reported at birth, while a suppression in EEG amplitude was observed with the presence of a PVL lesion at 2-3 weeks after birth.

The main cause for PVL is a propensity for the occurrence of cerebral ischemia, which may be related to decreases in CBF. Altman and colleagues showed that PVL was developed in premature infants with extremely low blood flow to cerebral white matter, measured by means of positron emission tomography [5].

This suggests that monitoring of CBF is important to prevent PVL damage, especially in premature sick infants that are exposed to a passive pressure CBF [197]. In this population falls in MABP are common; which, under an impaired CA, might result in a fluctuating CBF exposing their brain to severe ischemia. Stable premature infants are less likely to present impaired CA [74, 78, 172, 174, 241], therefore they are also less likely to suffer PVL injury. However, some studies have shown that impaired regulation can be found also in healthy patients [24]. In addition, some studies have indicated that the autoregulation range is narrower in preterm lambs [162, 204] than in term lambs. If this is the case for premature infants, mild variations in MABP may cause a major variation in CBF, resulting in a higher risk for the development of PVL. Volpe and colleagues described a list of factors related to development of PVL [223]. Among the factors they mentioned: severe hypotension, marked hypocarbia, hypoplastic left heart syndrome, patent ductus arteriosus with retrograde cerebral diastolic flow, and severe illness requiring extracorporeal membrane oxygenation, among others. However, impaired CA was not listed in this review. The main problem to relate impaired CA with the genesis of PVL is the difficulty to indicate which infants exhibit abnormal hemodynamics. A more comprehensive review of the neurobiology for PVL in preterm infants can be found in [221].

In summary, IVH and PVL are mainly caused by instabilities in the cerebral circulation. Monitoring cerebral hemodynamics and its relation with the systemic variables, in particular MABP and $p\text{CO}_2$, may be useful to prevent brain damage due to these pathologies.

1.1.2 Causes of brain damage in neonates

There are several causes for brain damage in sick premature neonates. Among them, the more important ones are due to hypoxia. Hypoxia is a condition where the tissue is deprived of an adequate supply of oxygen. Three different classes of hypoxia are reported in literature: hypoxic hypoxia, anemic hypoxia and ischemic hypoxia.

Hypoxic Hypoxia

Hypoxic hypoxia is caused by a reduction in arterial oxygen saturation SaO_2 . When there is a reduction in SaO_2 the brain compensates for this deficit by increasing CBF [107, 99, 68]. However, when CBF reaches an upper limit, and if the balance between the supply and demand of oxygen is no longer met, the brain is exposed to damage [68]. In clinical practice, hypoxic hypoxia is avoided

by monitoring SaO_2 . However, due to the fact that it is accompanied by an increase in CBF, the brain might be exposed to damage due to hemorrhage.

Anemic Hypoxia

Anemic hypoxia is caused by a deficit in the concentration of hemoglobin in the blood. Hemoglobin is the molecule responsible for the transport of oxygen to the tissue. Under mild anemia the oxygen delivery is kept constant by an increase in CBF. However, when an upper limit in CBF is met and if the balance between the supply and demand of oxygen is not met, the brain will be exposed to damage [99, 229, 89].

Ischemic Hypoxia

Ischemic hypoxia is caused by a low CBF. Low values of CBF will cause an insufficient supply of oxygen and other nutrients needed for a correct brain functionality. CBF is normally controlled via the cerebral autoregulation mechanism. However, this mechanisms might be impaired and/or affected by other physiological variations, such as the concentration of CO_2 [104]. Therefore, a correct monitoring of CBF is needed in order to avoid brain damage due to ischemic hypoxia. Continuous measurements of CBF in clinical practice are difficult. Traditional methods involved the use of transcranial Doppler (TCD), but its use for continuous monitoring of cerebral blood flow is limited. However, one may wonder whether maintaining an adequate CBF is what is needed or, more importantly, the supply of oxygen for a correct brain functionality. In this context, near-infrared spectroscopy (NIRS) represents a noninvasive technology that allows to monitor cerebral oxygenation.

1.2 Cerebral Autoregulation

As has been mentioned before, CA assessment is a field of high interest due to its high clinical impact. Detection of disruptive CA can help to prevent brain damage due to ischemia or hemorrhage. However, due to the multivariate and nonlinear nature of the underlying mechanisms involved in the regulation of CBF, the physiological pathways responsible for CA are not yet fully understood [133].

Cerebral Autoregulation is defined as the property of the brain to regulate the changes in CBF in the presence of changes in MABP. The first approaches to

assess the status of CA evaluated the relation between CBF and MABP, by provoking changes in MABP and measuring the response in CBF. Figure 1.1 shows how this relation looks like. In this figure it can be seen that for low or high values of MABP, small changes in MABP produce large variations in CBF. While, for a certain range of values, changes in MABP will produce a mild variation in CBF. It is important to note that in this autoregulative region, the slope of the relation between MABP and CBF is not zero, revealing a weak linear relation between those variables. However, figure 1.1 represents the static relation between MABP and CBF. When autoregulation was observed for the first time the static, due to technological limitations, the measurements of CBF were taken several seconds, or even minutes, after the changes in MABP were produced [145]. Therefore, the transient response in CBF was not observed. The main limitation in this approach was the difficulties in measuring CBF continuously.

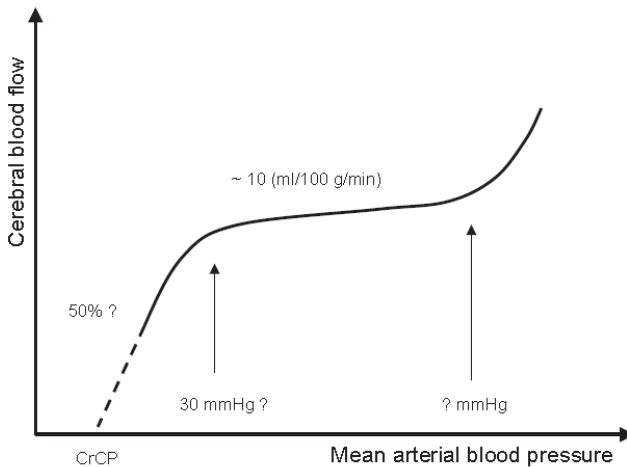


Figure 1.1: Cerebral autoregulation plateau. The lower limit for CA in neonates is around 30mmHg, the CrCP represents the critical closing pressure. It is important to notice that the slope in the autoregulative region is not zero, therefore there is a small increase in CBF with increasing MABP. Taken from [76].

By the inclusion of new technologies such as transcranial Doppler (TCD), the time resolution of CBF measurements was improved, allowing the study of the transient relations between changes in MABP and CBF. This permits the use of dynamical models to assess the status of CA. In this context correlation, transfer function analysis, coherence, and other methods were introduced to quantify the status of CA [1, 243]. These models have provided exciting results

that have helped in the understanding of the underlying physiology of CA. However, on the one hand, these models do not take into account the effect of other physiological variables on CA. It has been shown that variations in $p\text{CO}_2$ modulate the response of CBF to changes in MABP, indicating that $p\text{CO}_2$ modulates CA [1]. Moreover, ganglion blockade has been shown to also affect the status of CA [244]. Recently, it has been suggested that CA is a multivariate process where several mechanisms are involved in its control [158]. Among those the myogenic, metabolic and neurogenic mechanisms have been indicated as the most relevant ones for the regulation of CBF. Recent studies in CA have investigated the influence of $p\text{CO}_2$ on CA [157, 2, 144]. However, these influences have been studied as an additive effect using linear models [1, 158]. In addition, the relation between the different mechanisms regulating CA is not expected to be linear. Recent studies have investigated the use of Volterra Kernel models to include the nonlinearities in CA. However, these models are difficult to relate with the underlying physiological processes, which limits their applicability. A more recent study proposed to modify these models in order to obtain better interpretability [133]. However, even though these models are easier to analyze, they are still far from being applicable in a clinical environment.

Even though TCD has provided a suitable framework for assessment of CA, its measurements are highly affected by movement artefacts. This indicates that TCD is not suited for online monitoring. Near infrared Spectroscopy (NIRS) is a recent technology that has been used to measure hemodynamical variables. Since this technology is based on light radiation it represents a safe methodology for continuous monitoring of tissue oxygenation [234, 34, 219]. NIRS allows the continuous monitoring of changes in oxy- and deoxy-hemoglobin concentration, from which the tissue oxygenation index (TOI) can be computed. However, NIRS does not measure CBF but tissue oxygenation. Several studies have shown that NIRS measurements are related to changes in CBF under constant cerebral oxygen consumption and constant arterial oxygen saturation (SaO_2) [234]. Therefore, NIRS represents a good framework for CA monitoring provided that the aforementioned assumptions are held. As consequence, several studies that use NIRS for CA assessment can be found in the literature nowadays. But, strong evidence of the link between impaired CA assessed by NIRS with clinical outcomes, in premature infants, is still scarce [81, 36].

In contrast with methods using TCD, most of the CA studies using NIRS take only into account univariate-linear approaches. Nonlinear multivariate approaches for CA assessment using NIRS are still scarce. TCD studies have shown that the use of a nonlinear multivariate framework improves the assessment of CA. In this context, the main challenges lie in the design of a methodology that accounts for nonlinear multivariate interrelations, that can

be easily related to the physiology of the underlying mechanisms that control CBF regulation.

CA assessment is still far from being used in clinical practice as an online monitoring parameter. The main problems for its clinical implementation are: the lack of a robust preprocessing algorithm, the lack of a gold standard and standardization of the algorithms used in CA assessment, and the lack of a robust nonlinear multivariate methodology that allows to identify the influence of each physiological variable on the regulation of CBF. First, the preprocessing algorithms used in CA assessment should mitigate the effect of outliers, and reduce the influence of other signals. In the case of NIRS, first the development of algorithms that can decouple the influence of variations in SaO_2 from the NIRS measurements is of particular interest. Second, since NIRS provide only a surrogate measurement for CBF there is no gold standard to validate results obtained for CA assessment using NIRS. Third, several studies of CA use classical mathematical tools like correlation, transfer function analysis and coherence. However, these studies select arbitrarily the parameters used in each one of these methods, e.g. the overlapping percentages and the length of the epoch under analysis when estimating the power spectrum. This complicates the comparison of results provided by other research groups. Recently, it has been noticed that these parameters have a great impact in the outcome of the aforementioned methods. Standard values for those parameters need to be proposed in order to standardize these methods, and facilitate the comparisons with the results reported in the literature. Finally, a suitable nonlinear multivariate framework for CA assessment should be able to predict the changes in CBF, given the measurements from some physiological variables. In addition, they should also be able to indicate the effect of those variables, individually and jointly, on the cerebral circulation. Unfortunately, sophisticated methods are more likely to be computationally expensive. However, since the dynamics of CA is slow, no important time constraints exist for its assessment. Evaluation of CA scores, once every couple of minutes, is tolerable in clinical practice. Therefore, the computing power, e.g. needed in complex nonlinear regression methods, and the computing time is not a big limitation for online CA monitoring [164, 158, 133].

1.3 Near Infrared Spectroscopy (NIRS)

Near Infrared Spectroscopy (NIRS) is a technology that allows to monitor the tissue oxygenation. NIRS takes advantage that the biological tissue is relative transparent to infrared light between 650nm and 900nm, which allows the light to penetrate several centimeters into the tissue and illuminate the brain [156, 225, 233, 97]. Furthermore, in human tissue, there are three main oxygen

dependent chromophores that present an important absorption spectrum in the near infrared range, which causes attenuation in the emitted light. These chromophores are oxy-hemoglobin (HbO_2), deoxy-hemoglobin (HHb) and the Cytochrome c oxidase (CytOx). HbO_2 represents the hemoglobin molecules that are linked to an oxygen molecule (O_2), while HHb represents a hemoglobin molecule that has already given its O_2 to the tissue. CytOx is the terminal member of the mitochondrial respiratory chain, therefore changes in CytOx indicate changes in cellular oxygenation [28]. Figure 1.2 shows the absorption spectrum for CytOx, HbO_2 and HHb in the infrared range. In the tissue, the concentration of CytOx is around 10% of the concentration of HHb. Therefore, in vivo measurements of CytOx are difficult to obtain.

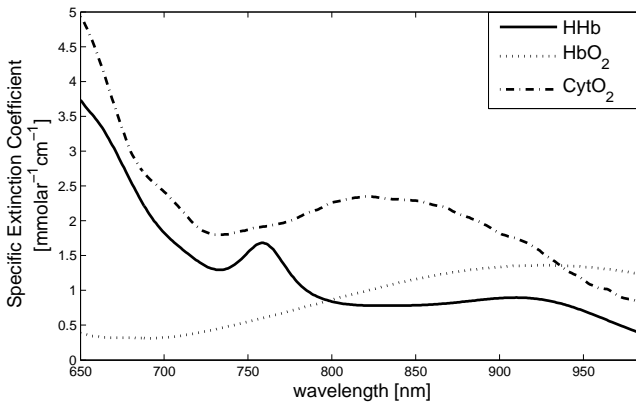


Figure 1.2: Absorption spectrum for CytOx, and oxy- and deoxy-hemoglobin, taken from <http://www.ucl.ac.uk/medphys/research/borl/intro/spectra>

The principles behind NIRS technology are quite simple, attenuation in light in the near infrared range is due to the changes in concentration in HHb, HbO_2 and CytOx [225, 156]. NIRS technology is similar to pulse oximetry, however, pulse oximetry looks at the pulsatile component of the tissue absorption signal coming from the arteries. From this signal the arterial oxygen saturation is estimated by means of calibration tables. NIRS technology as Pulse oximetry irradiates light through the tissue of interest and measures the reflecting light. Contrary to pulse oximetry, NIRS looks for the non-pulsatile component of the tissue absorption signal. In addition, due to the fact that NIRS uses more wavelengths than pulse oximetry, it can identify more chromophores [156, 136]. Changes in concentration of the chromophores can be obtained by measuring the attenuation in light at different wavelengths. This attenuation in a non-scattering medium can be modeled using the Beer-Lambert Law. This law

indicates that changes in attenuation of an absorbing component dissolved in a non-absorbing medium are proportional to the product of the compound concentration and the distance traveled by the light (pathlength) [112, 15], as follows:

$$A = \log \frac{I_0}{I} = \alpha \cdot C \cdot d \quad (1.1)$$

where A represents the attenuation, I_0 is the incident light intensity, I is the emergent light intensity, α is the specific extinction coefficient of the absorbing compound, C is the concentration of the absorbing compound, and d is the pathlength, which is a measure of the path followed by the photons.

However, the Beer-Lambert law assumes a homogeneous, non-scattering medium. This condition is not met when it is used in clinical practice, since the tissue of interest is normally surrounded by other tissue. Therefore, the Beer-Lambert law needs to be modified in order to account for these differences [48, 57, 39]. First, considering the monitoring of cerebral oxygenation in neonates, the head of the neonates is too big to allow the emitted light to be measured on the other side. Therefore, the optodes should not be connected facing each other. In clinical practice it is common to put the electrodes separated by a distance higher than 3 cm [149, 57, 63]. Second, due to scattering factors, the emitted light does not travel along a linear path. Simulation studies and experimental measurements have shown that due to scattering properties of the tissue the photons that reach the receiver optode, are likely to have traveled along a path inside the brain that resembles a banana shape [22, 106, 152, 153]. An extra term to account for this increment in distance is normally taken into account. This term is known as the differential path length factor (DPF) [10, 110, 237]. Figure 1.3 shows a schematic representation of the path traveled by the photons. DPF is usually set to a fixed value depending on the tissue under study. For neonatal brain studies DPF is set to a constant value of 4.39 [205, 54, 149]. Third, also due to scattering, the path followed by the photons will be disorder, which causes some photons to travel deeper or more superficially in the tissue. In the former case, the photons can either exit the tissue at a location further away from the photodetector, or they can be absorbed by the chromophores. In the latter case, when the photons travel more superficially, they are more likely to exit the tissue before reaching the photodetector. Therefore, only a small amount of photons will be able to reach the photodetector. Since, this attenuation in the received light is not related to changes in concentration [152], an extra term should be included in the Beer-Lambert law to account for these losses. By taking into account all the considerations mentioned before, the following modified Beer-Lambert law is proposed:

$$A = \log \frac{I_0}{I} = \alpha \cdot C \cdot d \cdot B + G \quad (1.2)$$

where B represents the differential pathlength factor (DPF), and G represents an additive geometry-dependent term reflecting scattering loss. The DPF represents a scalar that corrects for the effects of scattering on the real traveled distance.

Today, several technologies for NIRS exist, namely continuous wave spectroscopy (CWS), spatial resolved spectroscopy (SRS), time resolved spectroscopy (TRS) in the time and frequency domain.

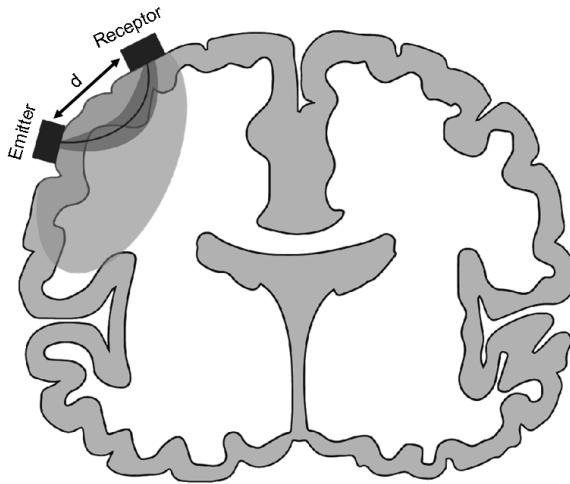


Figure 1.3: Schematic representation for the propagation of near-infrared light in the brain. The distance between the optodes is indicated as d . The light shadow region indicates the region that is illuminated by the source light. The dark shade with the banana shape indicates the most likely path that detected photons have traveled. Photons that travel superficially are more likely to exit before they reach the photo-detector, due to scattering. On the other hand, photons that have traveled too deep into the tissue are more likely to be absorbed before they reach the photo-detector.

1.3.1 Continuous wave spectroscopy

CWS uses a constant light source. CWS cannot compute directly the DPF and the scattering loss G . However, some estimates of DPF exist, and together with the scattering, they are considered constant. In addition, it is assumed that the only variable that can change relatively fast inside the tissue is the hemoglobin concentration. By evaluating only the changes in equation (1.2) the scattering factor can be eliminated. This implies that absolute values of concentrations will not be measured by CWS technology, but only relative changes [245, 61, 94, 91, 86, 208]. The equation for absorption becomes:

$$\Delta A = \Delta \left(\log \frac{I_0}{I} \right) = \alpha \cdot \Delta C \cdot d \cdot B \quad (1.3)$$

By measuring the absorption of light in at least two wavelengths, the changes in concentration for the oxy- and deoxy- hemoglobin can be found. By including more wavelengths a better estimation of the concentrations is obtained. Consider we are interested in knowing the concentration changes for the oxy- and deoxy-hemoglobin, C_1 and C_2 respectively. Considering the extinction coefficients for the oxy- and deoxy-hemoglobin α and β , respectively, and assuming that attenuation measurements were obtained simultaneously at 2 different wavelengths, λ_1 and λ_2 , by using (1.3) the following equations are obtained:

$$\begin{aligned} \Delta A_1 &= \alpha_{\lambda_1} \cdot \Delta C_1 \cdot d \cdot B + \beta_{\lambda_1} \cdot \Delta C_2 \cdot d \cdot B \\ \Delta A_2 &= \alpha_{\lambda_2} \cdot \Delta C_1 \cdot d \cdot B + \beta_{\lambda_2} \cdot \Delta C_2 \cdot d \cdot B \end{aligned} \quad (1.4)$$

which represent a set of 2 equations with 2 unknowns. If measurements of other chromosomes are required, measurements from more wavelengths are needed. In addition, by including more wavelengths more robust estimations for the changes in concentration are obtained. However, most commercial devices use only 2 wavelengths.

1.3.2 Spatially resolved spectroscopy

SRS as CWS uses a continuous light source, but it uses more receiver optodes. In addition, SRS considers that for large distances between the light source and the receiver optodes the scattering loss is constant [163]. Therefore, measured differences in the intensity can be interpreted as differences in absorption loss [135, 134, 203, 3].

SRS uses a solution of the approximate photon diffusion equation in order to estimate the chromophore concentrations. This method describes the propagation of photons in a highly scattering medium such as living tissue [96], and indicates the relation between the changes in absorption and the distance. This relation is given by:

$$\frac{\partial A}{\partial \rho} = \frac{1}{\ln(10)} \left(\sqrt{3\mu_a\mu'_s} + \frac{2}{\rho} \right) \quad (1.5)$$

where ρ represents the mean distance in cm, μ_a is the absorption coefficient, and μ'_s is the transport scattering coefficient. By measuring $\partial A/\partial \rho$ at several wavelengths, the product $\mu_a(\lambda)\mu'_s(\lambda)$ can be estimated. The scattering coefficient $\mu'_s(\lambda) = k(1 - h\lambda)$, where λ is the wavelength, k is a factor of proportionality, and h is the normalized slope of the scattering versus the wavelength. From equation (1.5) the absorption coefficient can be computed as:

$$k\mu_a(\lambda) = \frac{1}{3(1 - h\lambda)} \left[\ln(10) \frac{\partial A}{\partial \rho} - \frac{2}{\rho} \right]^2 \quad (1.6)$$

Consider equation (1.6), using 2 different wavelengths, the relative concentrations $k\text{HbO}_2$ and $k\text{HHb}$ can be found as follows:

$$\begin{bmatrix} k\text{HbO}_2 \\ k\text{HHb} \end{bmatrix} = \begin{bmatrix} \varepsilon_{\text{HbO}_2}(\lambda_1) & \varepsilon_{\text{HbO}_2}(\lambda_2) \\ \varepsilon_{\text{HHb}}(\lambda_1) & \varepsilon_{\text{HHb}}(\lambda_2) \end{bmatrix} \begin{bmatrix} k\mu_a(\lambda_1) \\ k\mu_a(\lambda_2) \end{bmatrix} \quad (1.7)$$

where $\varepsilon_{\text{HbO}_2}(\lambda)$ and $\varepsilon_{\text{HHb}}(\lambda)$ correspond to the measured extinction coefficient for the, HbO_2 and HHb , respectively, at a given wavelength λ .

Patterson and colleagues proposed that the effective attenuation coefficient of the tissue can be measured by analyzing the spatial variation of the intensity of retro-reflected light, as a function of the distance d between the light source and detector [163]. They showed that the scatter loss becomes homogenous if d is large enough ($d > 3\text{cm}$). In Figure 1.4 the schematic representation of the NIRS probe is shown. The value $\frac{\partial A}{\partial \rho}$ is estimated from the measurements using 3 photodiodes located at different distances.

From the relative quantities, the tissue oxygenation index (TOI) can be computed as follows:

$$\text{TOI} = \frac{k\text{HbO}_2}{k\text{HbO}_2 + k\text{HHb}} \quad (1.8)$$

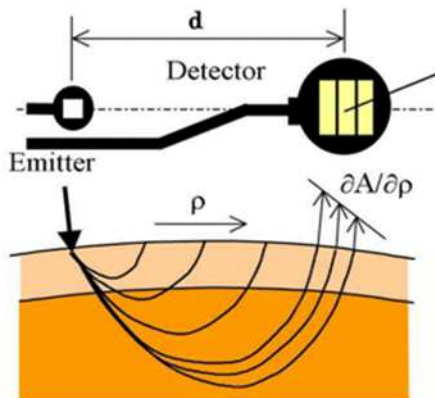


Figure 1.4: Schematic representation for spatially resolved spectroscopy, taken from [203].

TOI is an important quantity since it represents an absolute measure of tissue oxygenation [149, 57, 205]. SRS assumes that the measurements in the three different receptors are affected similarly by superficial tissue layers, therefore, their influence on the measurements is canceled out [233]. The SRS method described before is used in the NIR spectrometer series (NIRO), commercialized by Hamamatsu.

The regional cerebral oxygenation ($rScO_2$) is another parameter that, like TOI, has been used as a measure of cerebral oxygenation. $rScO_2$ is provided by the NIR spectrometer series (INVOS), commercialized by Somanetics, and it is based on SRS. However, little is known about the algorithm used for its computation. INVOS uses 2 photodetectors located at 3cm and 4cm from the light source. The photodetector located at 3cm is assumed to measure the scatter light, while the sensor at 4cm measures primarily changes in oxy- deoxy-hemoglobin in deeper tissue. A subtraction algorithm is used in order to correct for scattering. From these measurements the relative concentrations $kHbO_2$ and $kHHb$ are found, and the ($rScO_2 = kHbO_2 / (kHbO_2 + kHHb)$) is computed [146]. A good correlation between TOI and $rScO_2$ have been found in the literature [146], indicating that both variables measure the same underlying process.

1.3.3 Time resolved spectroscopy

Unlike CWS and SRS, time resolved spectroscopy (TRS) uses a modulated light source. In the literature two different techniques based on TRS can be found: time domain and Frequency domain TRS.

Time domain TRS

In time domain TRS the tissue is irradiated using a short pulse of light with a duration in the range of the pico seconds [48, 121, 42, 214]. Using a fast photodetector as a receiver, a profile in time of the incident photons can be obtained. The morphology of this time profile changes accordingly to the optical and geometrical properties of the medium. The scattering will wider the time profile, while short distances between emitter and detector will shift the profile towards smaller times. In addition, the absorption can be estimated by measuring the changes in intensity between the emitted and the received light. TRS also provides information about the depth of the measurement, photons that are received early are more likely to have traveled inside the superficial layers of the tissue, while late photons are more likely to have traveled deeper. By computing a mean time of travel of all the received photons, \hat{t} , the differential path length, DPF, can be computed as follows:

$$\text{DPF} = \frac{c\hat{t}}{d \cdot \eta} \quad (1.9)$$

where c represents the velocity of light in the vacuum, η is the refractive index of the tissue and d is the distance between the electrodes.

1.3.4 Frequency domain TRS

Frequency domain TRS is a technology that, like time domain TRS, allows the computation of the DPF. Frequency domain TRS uses a modulated light source with frequencies between 50MHz to 1GHz [233]. By measuring the difference in phase between the emitted and the received light, the distance traveled by the photons can be estimated [60, 65, 73, 21, 171, 170, 61]. With frequency domain TRS the distance traveled for the photons is given by:

$$\text{DP} = \frac{\phi c}{2\pi f \eta} \quad (1.10)$$

where ϕ represents the changes in phase between the input and the measured light, and f is the modulation frequency.

As in time domain TRS, the absorption can be estimated by measuring the changes in intensity. In addition, by exploring the changes in phase in the complete frequency range (50MHz - 1GHz), information similar to the one provided by time domain TRS can be obtained.

Figure 1.5 shows a schematic representation for time and frequency domain TRS.

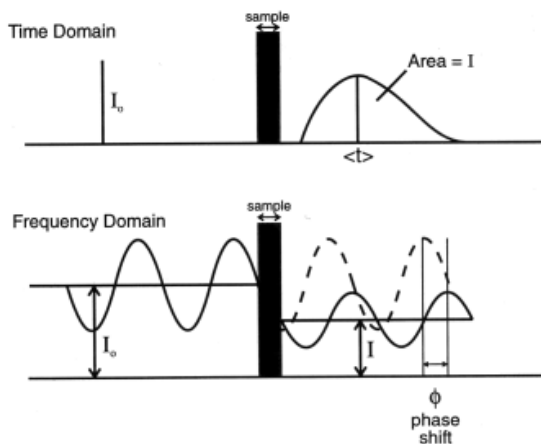


Figure 1.5: Schematic representation for time and frequency domain TRS, taken from http://www.medphys.ucl.ac.uk/research/borg/research/NIR_topics/nirs.htm.

1.4 Clinical applications of NIRS

Near Infrared spectroscopy was first used for medical purposes by Jöbsis [97]. In the neonatal brain monitoring field the first applications of NIRS were presented by Brazy et al. [28], and Delpy et al [48]. Recently, thanks to the introduction of SRS, the use of NIRS has become more popular and more studies can be found in the literature. This is due to the fact that SRS is more robust against movement artifacts, and it is able to produce absolute oxygenation values [135, 203].

By using the Fick principle, proposed by Kety et al [105], measurements of CBF were possible using NIRS. The Fick principle establishes that the rate

of accumulation of a substance is proportional to the inflow of the substance minus the outflow. In the literature 2 methods based on this principle for the measurement of CBF can be found. The first one uses the SaO_2 as a dye [55, 31, 191, 69]. In summary the method works as follows: a disturbance in SaO_2 at time 0 is produced, at the same time ΔHbO_2 is measured using NIRS. Assuming that the measuring time t is shorter than the transition time for the oxygen in the brain, it can be concluded that the outflow of oxygen from the brain arterial compartment to the venous compartment is zero. Therefore, according to the Fick's law, any measured increase in ΔHbO_2 , up to time t , will be produced by the product between the induced change in SaO_2 and the CBF. The relation between these quantities is given by the following formula:

$$CBF(t) = \frac{\Delta\text{HbO}_2}{\int_0^t \text{SaO}_2 dt} \quad (1.11)$$

However, changes in SaO_2 are difficult to perform in the neonatal population in the intensive care unit; which hinders the applicability of this methodology in clinical monitoring. The second method uses indocyanine green as a tracer. This tracer absorbs NIRS light and its measurement principle is similar to the one described before [29, 108, 178].

NIRS has also been used to obtain measurements of cerebral blood volume (CBV) [236, 57, 13]. However, the methods proposed in the literature have not been fully validated, and their use is restricted to research purposes. In summary these methods compute a surrogate measurement for the changes in CBV by summing the changes in oxy- and deoxy-hemoglobin concentration as follows: $\Delta\text{HbT} = \Delta\text{HbO}_2 + \Delta\text{HHb}$, where ΔHbT represents the changes in total hemoglobin concentration. When comparing measurements of CBF and CBV using NIRS, some studies have reported a good relation between them [122, 177, 80].

In the literature there are several studies that validate the use of changes in cerebral oxygenation, measured using NIRS, with the jugular venous saturation [231, 147, 139, 189, 150]. This indicates that NIRS is a suitable technology for the monitoring of jugular venous saturation. However, there are discrepancies in the percentages of arterial vs venous oxygenation measured by NIRS; Brun et al. reported a relation of 1:2 [30], while Benni and colleges reported a relation of 30:70, [20]. Other studies claim that these percentages are patient dependent [230].

Another key parameter for monitoring the homeostatic state of the brain is the Fractional oxygen extraction (FOE). This parameter is computed as the ratio between the oxygen delivery and the oxygen consumption. Wardle et

al, have developed a way to compute a surrogate measure for FOE using NIRS [227, 228, 229]. They called this variable the fractional tissue oxygen extraction (FTOE). Naulaers et al. [150] found a good match between FOE and FTOE computed from NIRS measurements as follows: $FTOE = (SaO_2 - TOI) / SaO_2$. FTOE is an important variable to monitor since normal brain functioning depends on a proper balance between oxygen supply and cerebral metabolic demand. Based on this, some authors have proposed that monitoring CBF is less important than monitoring oxygen consumption in order to detect hypoxia or ischemia [242]. As discussed before, there are three different types of ischemia, each one related to a deficit in one of the variables influencing the hemodynamical variables. Alterations in SaO_2 produce hypoxic hypoxia, low CBF produces ischemic hypoxia and a reduction in hemoglobin produces anemic hypoxia. Hypoxia has been described using NIRS in [169, 168].

NIRS has also been used in order to detect patent ductus arteriosus. Patent ductus arteriosus is a disorder where the ductus arteriosus does not close after birth. The ductus arteriosus is a fetal blood vessel that connects the aorta with the pulmonary artery. In presence of a patent ductus, oxygenated blood from the aorta returns to the pulmonary aorta. Therefore, neonates with a patent ductus are likely to suffer hypoxia. In the presence of an important hemodynamics ductus, a reduction in CBF that produces a reduction in cerebral oxygenation is observed [117, 218]. In addition NIRS has also been used in order to assess liver hemodynamics [149]. Naulaers et al. [149] found that changes in TOI in the liver reflect changes in the intestinal blood flow.

Even though NIRS possesses a high potential for clinical use, it has been limited to research purposes. This is due to some limitations that hinders its introduction in clinical practice. First of all, NIRS measurements are affected by movement artifacts [191], even if their effect is smaller than in TCD. Several studies have observed a bias in the values provided by NIRS when the location of the optodes is changed [195, 196, 53, 219]. Second, the reproducibility of the results provided by NIRS is still poor [122]. Finally, even though some studies have reported normal values ranging from 60% up to 75% [219, 151, 118, 169], standard values of oxygenation are yet to be defined and validated. In this context some studies have reported brain damage due to hypoxia, measured using NIRS. Hou et al. reported mitochondrial damage of CA1 neurons when a cerebral oxygenation was sustained below 40% during more than 30 minutes. Morphological damage in CA1 neurons and suppression of EEG amplitude was observed for oxygenation values below 30%. Kurth et al. have proposed a threshold between 33% and 44% for $rScO_2$ to indicate impairment due to ischemic hypoxia. On the other hand, some studies have indicated that elevated oxygenation values are dangerous for the neonates. Saugstad et al. have reported damage due to oxidative stress [185]. They found that values of $rScO_2$

were higher in premature infants than in term infants.

Finally, some studies have reported the use of NIRS for autoregulation studies. These studies quantify the relation between changes in ΔHbD or ΔHbT and MABP by means of correlation, coherence or transfer function analysis [197]. However, measurements of ΔHbD and ΔHbT are highly sensitive to movement artifacts, requiring more sophisticated preprocessing techniques and limiting their use in clinical monitoring. However, van Bel et al [219] have shown that TOI and $r\text{ScO}_2$, also derived from NIRS, are less prone to movement artifacts than ΔHbD and ΔHbT . However, their use in CA is yet to be validated. In addition, some studies using NIRS have studied the influence of hypercapnia and hypoxemia on CA [122]. These studies have found loss of CO_2 reactivity in severe asphyxia, while in moderate asphyxia CO_2 reactivity was intact but CA was impaired [173]. Other studies have shown a reduction in CBF, which is reflected in NIRS measurements, caused by hypocapnia [229, 51, 59, 75, 120, 141, 192, 238]. These studies indicate that CA is a far more complicated phenomenon which involves several mechanisms that are highly interrelated in order to preserve the cerebral homeostasis. Appropriate signal processing techniques for the monitoring of these mechanisms are scarce.

1.5 Goals of the Thesis

The main goal of this thesis is to investigate the use of signal processing techniques in monitoring cerebral hemodynamics in neonates by means of NIRS. However, on one hand, NIRS technology presents several drawbacks that hinder its use in clinical practice; therefore, appropriate techniques should be used in order to reduce the impact of these drawbacks. On the other hand, cerebral hemodynamics regulation is a complex process that requires sophisticated signal processing tools for its analysis; adequate methodologies are needed in order to obtain a reliable monitoring system.

Concerning the limitations of NIRS for clinical use, this thesis will aim to introduce sophisticated preprocessing techniques that facilitate the applicability of NIRS technology in clinical monitoring. In this context two main objectives will be pursued. First of all, the removal of movement artifacts is addressed. The removal of movement artifacts is a key factor for an online monitoring system using NIRS, since displacement of the NIRS optodes due to movements is common. Secondly, the influence from physiological variables, such as SaO_2 , should be removed from the dynamics of NIRS derived signals. This is of high importance in monitoring cerebral hemodynamics applications, since NIRS only

provides surrogate measurements for CBF assuming a constant arterial oxygen saturation. This condition is likely to be violated in sick premature infants.

Concerning the use of sophisticated methods for cerebral hemodynamics monitoring, this thesis will aim at introducing the use of several linear and nonlinear techniques for its monitoring. First of all, cerebral hemodynamics homeostasis is preserved by a series of complex processes that involve the interaction of several physiological signals. Therefore, the use of multivariate techniques is needed for its correct assessment. Specifically, studies in CA have hypothesized that its underlying mechanism is the result of a multifactorial process that involves the influence of three main components, namely the myogenic, the metabolic and the neurogenic one. In the literature more attention has been given to the study of the myogenic component. However, by ignoring the influence of the other components, monitoring of CA may produce misleading results. Secondly, the interaction of the processes involved in cerebral hemodynamics is likely to be nonlinear. This can be seen from the autoregulation curve presented in figure 1.1. The use of nonlinear techniques in cerebral hemodynamics monitoring have been poorly studied. In addition, existing nonlinear models have not been included yet in clinical practice due to their difficult interpretation. In this thesis we aim at the development of a framework that facilitates the interpretation of a nonlinear regression model.

In summary, the objectives of this thesis can be summarized as follows:

- Development of a framework for the preprocessing of NIRS signals, with special attention to the removal of artifacts and undesired variations introduced by other physiological variables.
- Introduction of linear multivariate techniques for cerebral hemodynamics monitoring.
- Development of multivariate nonlinear and clinically interpretable hemodynamical models for monitoring of cerebral hemodynamics.
- Validation of the above mentioned methods in a variety of clinical case studies.

1.6 Thesis Overview

This thesis is divided in two main parts. In the first part the mathematical methodologies that will be used as a foundation for the clinical studies are introduced, chapters 2, 3, 5, and 6 are included in this part. The second part

addresses the clinical case studies mostly related to the monitoring of cerebral hemodynamics. It consists of chapters 4 and 7. A flowchart of the thesis chapters is shown in Figure 1.6. The abbreviations used in the figure are explained below, together with the description of each chapter.

1.6.1 Part I: Advanced Signal Processing Methodologies

Chapter 2 provides a methodological foundation for the linear methodologies that will be used in this thesis. Traditional methodologies like correlation (CORR), coherence (COH) and transfer function (TF) are briefly presented. More advanced mathematical tools like partial coherence (PaCOH), wavelet transform, wavelet based transfer function, canonical correlation analysis (CCA), and orthogonal and oblique subspace projections (O(r)SP) are presented. When considered necessary, an illustrative example has been used in order to describe the principles of these methodologies, and to highlight their importance in the framework of this research.

Chapter 3 provides a methodological foundation for the nonlinear methods used in this thesis. The chapter introduces the use of least squares support vector machine (LS-SVM) for function estimation. This methodology will be used in the preprocessing of NIRS signals. Furthermore, the chapter introduces the concept of principal component regression (PCR), and kernel principal component regression (KPCR), which represents a nonlinear version of PCR. Computation of projection matrices in a reproducing kernel Hilbert space (RKHS) are introduced as well as their use in the formulation of a sparse KPCR. Finally, the chapter presents some toy examples that illustrate the main advantages of these methods.

Chapter 5 presents a study, where the use of TOI and $rScO_2$ for the assessment of CA is validated against the most commonly used variables ΔHbD and ΔHbT . This chapter provides a base for the clinical applications that will be described in the chapter 7.

Chapter 6 studies the influence of the selection of some user defined parameters on the output provided by traditional methods used in cerebral autoregulation assessment, e.g. correlation, coherence and transfer function analysis. As a result, this chapter proposes a set of parameters that aim to standardize the use of these methodologies, facilitating the comparison of results provided by different research groups.

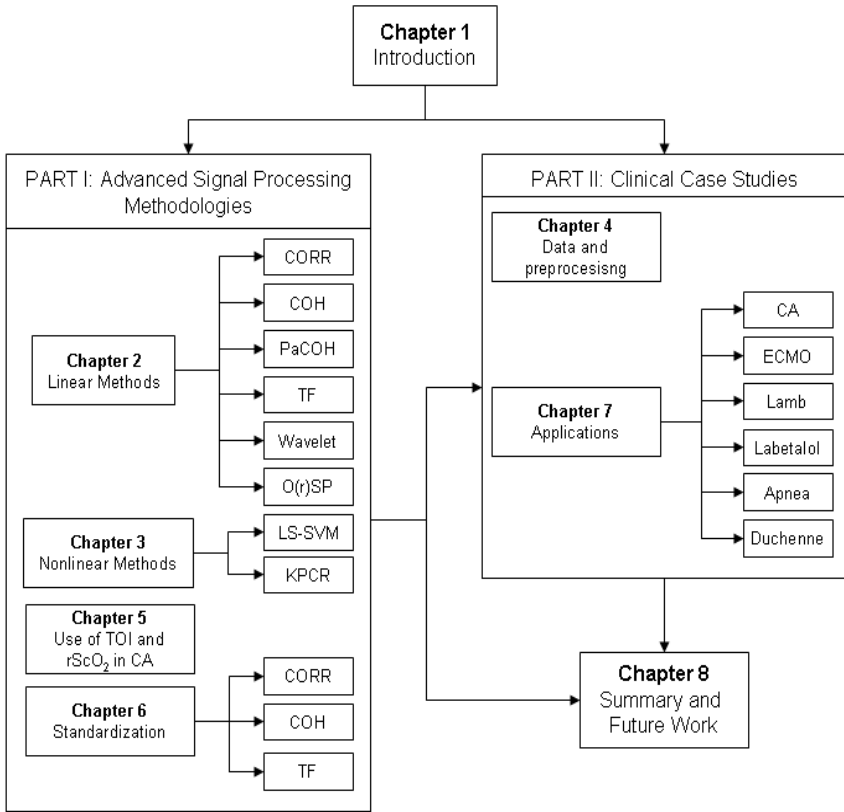


Figure 1.6: Flowchart of the thesis chapters.

1.6.2 Part II: Clinical Case Studies

Chapter 4 provides a description of the datasets that will be used in Chapter 7. In addition, the preprocessing procedure applied to the data is summarized.

Chapter 7 presents some clinical studies that were performed during the course of this doctoral research. The first clinical study is related to the evaluation of the assessment of CA by means of NIRS. In this study only univariate methods are used. The second study investigates the influence of MABP and pCO₂

on the cerebral oxygenation. The third and fourth study are performed on data obtained from patients undergoing extra corporeal membrane oxygenation (ECMO) procedure. For this study concomitant measurements of several physiological variables are available. Multivariate linear methods like CCA and subspace projections were used, these methods will be described in chapter 2. In the fifth case study the wavelet based transfer function (WBTF), as well as nonlinear methodology based on kernel principal component regression (KPCR), will be tested in the framework of cerebral hemodynamics monitoring. In the sixth study, the effect of the maternal use of labetalol on the CA of the neonates was investigated. In the seventh study, the use of NIRS in the monitoring of children with Duchenne muscular dystrophy is investigated. Finally, the last clinical case study, presents results on the application of subspace projection techniques in the classification of sleep apnea events. Even though this last study is not related to the main topic of this thesis, it presents an interesting example where subspace projection techniques are applicable. This application highlights the potential use of this technique in other areas related to biomedical signal processing.

Finally, in **Chapter 8** the main findings of these thesis are summarized and future research directions are indicated.

1.7 Personal Contributions

My contributions in this thesis are oriented to the development of methodologies for biomedical signal preprocessing and processing, and the application of these methodologies, among others, in clinical studies related, mainly, to cerebral hemodynamics monitoring. Since this work was done in close collaboration with partners from the University Hospitals Leuven (UHL), the Wilhelmina Children Hospital in Utrecht (WCH), the University Hospital in Zurich (UZ), the University College London (UCL) and the Katholieke Universiteit Leuven (KU Leuven), I will first list the people involved in each study, afterwards I will highlight my contributions. The contribution of the partners was mainly focused to the acquisition of the signals for the studies, and the interpretation of the results obtained in a clinical framework. The clinical studies about cerebral autoregulation were done in close collaboration with Prof. Dr. Gunnar Nauelaers and Dr. Joke Vanderhaegen from UHL, Prof. Dr. Frank van Bel and M.D. Dr. Petra Lemmers from WCH, and Prof. Dr. Martin Wolf from UZ. The labetalol study was performed in collaboration with Prof. Dr. Frank van Bel, M.D. Dr. Petra Lemmers, Prof. Dr. Gunnar Nauelaers and M.D. Liesbeth Thewissen from UHL. The ECMO studies were performed in collaboration with Dr. Ilias Tachtsidis and Dr. Maria Papademetriou from UCL. For the lamb study I

collaborated with Dr. Flora Wong who provided the data for the analysis. The Duchenne study was performed in collaboration with Prof. Dr. Gunnar Buyse, M.D. Eva Van Ginderdeuren, Dr. Nathalie Goemans and Marleen van den Hauwe from UHL, and Dr. Joachim Taelman from KU Leuven. The sleep apnea study was performed in close collaboration with MSc. Engr. Carolina Varon from KU Leuven.

Since my personal contributions are scattered through the complete document, I will address them on a chapter-by-chapter basis.

In chapter 2 I present an algorithm based on subspace projection. This algorithm aims at decomposing a target signal in the components related to other measured variables. In a regression framework, these measured variables represent the regressor matrix. In this context, I propose an extension of the regressor matrix using a discrete wavelet transform. This new regressor matrix is further extended by a block hankelization procedure. This approach increases the dimension of the subspace defined by the regressor variables, provides a structure for the relation between the regressors and the target signal in the frequency domain, and reduces the effect of noise in the regressors. Furthermore, since the relation between the regressors is not orthogonal, I propose the use of oblique projectors in order to retrieve the relation between each regressor variable and the target signal. In addition, in this chapter, this methodology is proposed to be used in the preprocessing of NIRS signals.

In chapter 3 I proposed a modification in the cost function of the robust LS-SVM regression, by introducing an extra weight vector that prioritizes the regression fit at the borders. This approach will allow to correct segments affected by artifacts, by estimating the corrupted segment with a LS-SVM model. Furthermore, by the inclusion of the extra weight factor, discontinuities between consecutive segments are reduced. This new approach does not require the use of extra parameters or training and its computational cost is similar to the one of the robust LS-SVM regression. On the other hand, in this chapter the concept of subspace projections is extended to kernel principal component regression (KPCR). In a nonlinear regression framework, these projections allow to identify the nonlinear contribution of each regressor variable on the target function. Clinically, this methodology has a high impact, since it allows to obtain a nonlinear model of a physiological process where the influence of each measured variable can be retrieved. This information may help the clinicians in the evaluation of the effects for a particular treatment. Furthermore, in this chapter, I propose to use the trace of the projection matrix to produce a sparse KPCR model. In this new sparse model, the number of observations equals the dimension of this trace. In addition, I also study the influence of the bandwidth of the RBF kernel on the sparsity of the KPCR model.

In chapter 5 I investigate the influence of the use of the tissue oxygenation index (TOI), cerebral oxygen saturation (rScO₂), differences in hemoglobin concentration (HbD) or total hemoglobin (HbT) as a surrogate variable for cerebral blood flow (CBF), which will be used on autoregulation studies. Classically ΔHbD and ΔHbT have been used in CA studies. However, these signals are highly affected by movement artifacts. Since TOI and rScO₂ are less prone to movement artifacts, they are more suited for clinical use. In this study I performed the preprocessing and processing of the data. In addition I was actively involved in the analysis of the results.

In chapter 6 I propose a standard set of parameters that should be used in cerebral autoregulation assessment when correlation, coherence or transfer function analysis is employed. The selection of those parameters is based on a sensitivity analysis of each method. The results provided in this chapter have a high impact, since standardization of these methodologies is a problem that is currently being addressed in this field.

Finally, in chapter 7 I present several clinical case studies that have been performed during my PhD. In the cerebral autoregulation studies, I used classical tools in order to investigate the use of cerebral autoregulation assessment in the prediction of clinical outcome in neonates. In the ECMO studies, I propose the use of new parameters for cerebral hemodynamics monitoring. These parameters are computed from the results provided by CCA and subspace projections. In this context, I propose to use the relation between the systemic changes and the peripheral hemodynamical variables as a reference to monitor cerebral hemodynamics. In the lamb study I proposed the use of wavelet based transfer function analysis for the monitoring of cerebral autoregulation. In addition, in this study, I present results using the KPCR methodology proposed in chapter 3. In the labetalol study, I use transfer function analysis in order to evaluate the influence of the maternal use of labetalol on the cerebral autoregulation of neonates. This study reveals that labetalol might impair cerebral autoregulation. In addition, in this study I point out the importance of including the analysis of pulse pressure values in the context of cerebral autoregulation. In this chapter, another important clinical study is performed to investigate the use of NIRS in the monitoring of children with Duchenne muscular dystrophy (DMD). One of the main problems for the monitoring of DMD progression is the lack of quantitative measurements. Qualitative tests exist but they rely on the patient mobility. The study presented in this thesis reveals a different behavior in the muscular hemodynamics for the DMD patients when compared to control subjects, during and after a voluntary induced contraction. In this study I define and compute a set of parameters related to these differences. These parameters correlate linearly with the qualitative tests for DMD monitoring. Therefore, they provide a quantitative way to measure the progression of DMD.

Moreover, since these parameters rely only on the voluntary contraction of the arm, they can still be measured in patients who cannot walk. Finally, in the sleep apnea study, I proposed a feature that can be used for the detection of apnoeic episodes. This feature is computed from the results provided by the subspace projection algorithm. This last study highlights the potential use of subspace projections in other biomedical applications.

Chapter 2

Linear Methods

This chapter will introduce the linear methods that will be used in the rest of the thesis. The chapter will start by introducing concepts for univariate analysis and will progress towards a multivariate approach. Time based, frequency based and time-frequency based methodologies will be discussed. In section 2.1 the traditional methods used in cerebral hemodynamics monitoring will be presented. In section 2.2 the wavelet transform will be introduced, as well as its use for the time-frequency analysis of signals. In this section the concept of coherence, cross-power spectrum and transfer function will be extended from the classical Fourier analysis to their counterpart using wavelet transform. Sections 2.1 and 2.2 represent the univariate methods used in this thesis. In section 2.3 Canonical correlation analysis (CCA) is introduced. The interpretation of results of CCA will be covered in detail. Finally, in section 2.4 the concepts of orthogonal and oblique subspace projections are presented. The content of this section is based on papers 15 and 16 in my publication list.

2.1 Traditional Methods

In clinical practice several methods are used in order to assess the status of cerebral hemodynamics. In this field, particular attention has been given to the assessment of cerebral autoregulation and CO₂ reactivity [159, 67, 197, 234, 51]. Among these methods correlation, coherence, and transfer function are the most commonly used ones. Partial coherence has also been proposed as an improved version of coherence, where the influence of a third signal is removed from the

calculation of the coherence values [193]. These methods represent a univariate framework for the analysis of the common dynamics between two signals.

Generally, cerebral autoregulation and CO₂ reactivity are assessed, in clinical practice, by applying the aforementioned methods. In these methods the mean arterial blood pressure (MABP) and the partial pressure of CO₂ (pCO₂) are used as the “input” while the cerebral blood flow (CBF) is used as output.

2.1.1 Correlation

Correlation is one of the most commonly used statistical measures in order to determine the degree of linear relation between two variables. Its value varies between -1 and 1, where -1 represents a perfect negative dependence, 1 represents a perfect positive dependence and 0 represents a lack of dependence between the variables. The correlation coefficient r_{xy} between the signals $x \in \mathbf{R}^N$ and $y \in \mathbf{R}^N$ is calculated using the following equation:

$$r_{xy} = \frac{\sum_{i=1}^N (x_i - \bar{x})(y_i - \bar{y})}{\sqrt{\sum_{i=1}^N (x_i - \bar{x})^2 \sum_{i=1}^N (y_i - \bar{y})^2}} \quad (2.1)$$

where \bar{x} and \bar{y} represent the mean values of x and y respectively.

Although the calculation of the correlation coefficient is simple, it is a powerful tool to quantify the strength of a linear relationship between two signals. However, there are several drawbacks that should be taken into account. First of all, it can only be used to identify linear dependence between two variables. Nonlinear relationships can lead to correlation coefficients equal to zero. Secondly, correlation is not a measure of causality, which means that the correlation coefficients only give information about the linked dynamics, but no information about the direction of the relationship, i.e. whether changes in CBF are caused by changes in MABP. However, in cerebral autoregulation assessment it is supposed that changes in MABP induce changes in CBF. Thirdly, correlation measures the linear dependency between two variables but not the magnitude of this relationship. Therefore, weakly linked dynamics can produce high correlation coefficients. In this case it is important to note that the slope in the autoregulative region curve is not zero. This is an important factor to take into account when using correlation for autoregulation assessment. Finally, the correlation coefficient in (2.1) does not take into account phase shifts between the variables, which can produce misleading results, e.g. the correlation coefficient between a sine and a cosine is 0, while the variables are strongly related. This can be corrected by the use of the correlation function

which computes the correlation coefficients in function of the phase shift between the signals.

The correlation function is defined as follows:

$$C(\tau) = \text{corr}(x(t), y(t - \tau)) \quad (2.2)$$

where *corr* is the correlation coefficient computed in (2.1), τ is a scalar representing the delay between both signals, and $y(t - \tau)$ is a delayed version of y . Even though the correlation function is used in signal processing it has not been used for CA studies. In CA studies only the correlation coefficient without delay or with a delay of 10s is used. This value represents the delay between MABP and NIRS measurements due to cerebrovascular transit time [81].

Since a positive correlation, as well as a negative correlation, indicates a pressure passive cerebral blood flow, the absolute value of the correlation coefficients is usually used in the literature as a score for cerebral autoregulation. High correlation values indicate a strong coupling between the dynamics of MABP and CBF, which suggest that the subject is outside the autoregulative plateau or that the subject does not possess an autoregulative plate as indicated in figure 1.1. Low correlation values, on the other hand, suggest that the subject autoregulates properly. However, correlation values should be interpreted carefully, as indicated in the figure 1.1 the slope between MABP and CBF in the autoregulative region is not zero; which, in presence of high signal to noise ratio might produce high correlation values. In addition, some studies have indicated that a negative correlation is a sign of a proper autoregulation mechanism, however there is no strong evidence to support this claim in the literature [200].

2.1.2 Coherence

Coherence can be interpreted as the equivalent form of correlation in the frequency domain. Coherence values vary between 0 and 1 and are frequency dependent. Each value of the coherence function represents the strength of the relation between the signals for a particular frequency component. The coherence function is then estimated by the following equation:

$$C_{xy}(f) = \frac{|G_{xy}|^2}{G_{xx}G_{yy}} \quad (2.3)$$

where $C_{xy}(f)$ represents the coherence coefficient between x and y at the frequency f . G_{xy} represents the cross power spectral density between the signals x and y , G_{xx} and G_{yy} represent the power spectral density for x and y , respectively. The cross power and power spectra represent the power distribution of the signals in the frequency domain.

Normally, the Welch method is used to estimate the cross power spectral and power spectral densities[232]. This method assumes that the signals are stationary, which means that the statistical properties of the signals do not change in time. Because of this assumption the bias and variance, implicit in spectral density estimation, are reduced. The Welch method works as follows:

- Consider the signal $x \in \mathbf{R}^N$. The signal is divided in p overlapping segments x_a for $a = 1, \dots, p$
- For each segment x_a the power spectrum is computed using the following formula:

$$P_{x_a}(\omega) = X_a(\omega)^* X_a(\omega) \quad (2.4)$$

where $P_{x_a}(\omega)$ represents the power spectrum for the segment a , $\omega = 2\pi f$ represents the angular frequency measured in *rad/sec*, $*$ represents the complex conjugate, and $X(\omega)$ is the continuous Fourier transform of the signal x . The Fourier transform of the signal x is defined as follows:

$$X(\omega) = \int_{-\infty}^{\infty} x(t)e^{-j\omega t} dt \quad (2.5)$$

- Calculate the power spectral density of the signal $x(t)$ as the mean value of the power spectral densities computed previously, as follows:

$$P_x(\omega) = \frac{1}{p} \sum_{i=1}^p P_{x_a}(\omega) \quad (2.6)$$

In the Welch method as the number of segments increases the spectral density average converges to its real value. However, in practice, the number of windows must be limited due to the finite sampling frequency and data length. Under conditions of stationarity, the use of consecutive segments with an overlapping higher than 50% does not improve the estimation of the power spectrum. Therefore, in practice an overlapping of 50% is used [232].

Coherence is also restricted to linear analysis and only provides information about the strength of the linear relationship between the signals. Nonlinear

relationships can produce misleading results. On the other hand, the condition of stationarity is not always satisfied. Normally, biological processes are highly non-stationary hence a bias in the spectral density estimation should be expected. In contrast with correlation, coherence takes into account the phase shift or delay between the signals.

2.1.3 Partial Coherence

Partial coherence has been recently introduced for cerebral autoregulation assessment. The main advantage of this method over the classical coherence analysis, is that it is able to subtract the influence of a third signal in the calculation of the coherence values [193]. When using NIRS signals as a surrogate measurement for CBF only segments with relatively constant arterial oxygen saturation (SaO₂) can be used. Variations in SaO₂ are reflected in NIRS signal, therefore, coherence values between MABP and CBF might be affected by such variations. Altered coherence values does not reflect the real common dynamic between MABP and CBF but a parasite effect introduced by the SaO₂.

Consider the signals x_1 , x_2 and x_3 , the partial coherence between x_1 and x_2 is computed after eliminating the linear influence of x_3 in both signals in a least squares sense [119]. Let's take as reference the signals x_1 and x_2 and remove the influence of x_3 from them:

$$\begin{aligned} X_1^\dagger &= X_1 - \frac{P_{13}}{P_{33}} X_3 \\ X_2^\dagger &= X_2 - \frac{P_{23}}{P_{33}} X_3 \end{aligned} \quad (2.7)$$

where X_i represents the Fourier transform of x_i , X_i^\dagger is the clean spectrum of x_i , P_{ij} is the cross-power spectrum of the signals x_i and x_j , and P_{ii} represents the power spectrum of the signal x_i .

From the new "clean" spectrum presented in (2.7), the power spectrum can be calculated, this leads to the following equations:

$$\begin{aligned} P_{11}^\dagger &= P_{11} - \frac{|P_{13}|^2}{P_{33}} = P_{11}(1 - C_{13}) \\ P_{22}^\dagger &= P_{22} - \frac{|P_{23}|^2}{P_{33}} = P_{22}(1 - C_{23}) \end{aligned} \quad (2.8)$$

where C_{ij} represent the coherence between the signals x_i and x_j . If the signals x_i and x_j are linearly related, this influence is subtracted from their spectrum. With the clean signals the partial coherence between x_1 and x_2 is computed as follows:

$$C_{12-3}^\dagger = \frac{|(X_1^\dagger)^* X_2^\dagger|^2}{P_{11}^\dagger P_{22}^\dagger} \quad (2.9)$$

where $*$ represents the complex conjugate.

2.1.4 Transfer Function

Transfer function analysis is derived from system theory where the transfer function describes the relationship between the input-output of a system. Let's consider the system represented by the transfer function $H(\omega)$, the input $x(t)$ and the output $y(t)$. In the frequency domain, the relation between input and output can be represented as:

$$Y(\omega) = H(\omega)X(\omega) + E(\omega) \quad (2.10)$$

where $X(\omega)$ and $Y(\omega)$ represent the Fourier transform of the input and the output time series, respectively; and $E(\omega)$ represents the residual spectrum that is uncorrelated to the input $X(\omega)$.

Figure 2.1 shows how the transfer function works. In this Figure the input signal is decomposed as a sum of sinusoids of different frequencies, amplitudes and phases. The transfer function acts on each sinusoid to compute the output of the system. For each sinusoid the system retrieves a sinusoid of the same frequency with a modified amplitude and phase. The output of the system is obtained by adding up all the modified sinusoids. From the transfer function, the gain and phase can be computed. The gain of the transfer function, for a given frequency, is equal to the ratio between the amplitude of the output and the amplitude of the input sinusoid, a_2/a_1 . The phase is computed as the difference between the phase for the output and the input sinusoid, $\theta_2 - \theta_1$.

Based on (2.10), if the transfer function $H(\omega)$ is known, the output of the system to any input can be estimated. Therefore, the transfer function contains all the information needed to represent the system. In the system identification framework, the transfer function is calculated by means of black-box models [126]. These models are called black-box since the physical model that explains the system is unknown, and only measurements of the input-output are used to

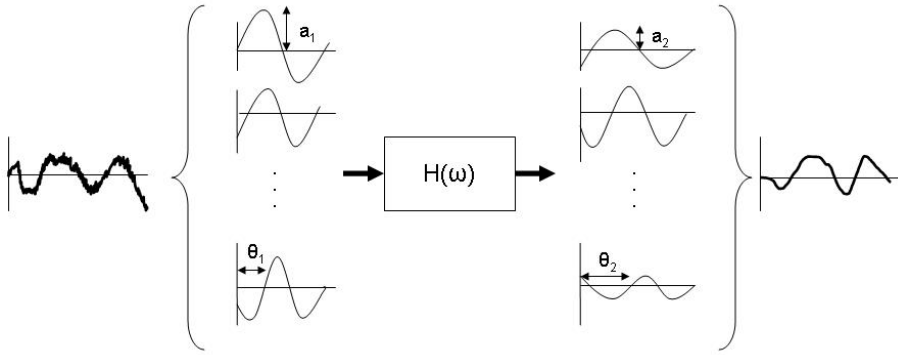


Figure 2.1: Basic representation of the relation between input-output of a system. The input of the system can be seen as a sum of sinusoids with different frequencies, amplitudes a , and phase θ . The system with transfer function $H(\omega)$, retrieves for each sinusoid of frequency ω a sinusoid of the same frequency but with a different amplitude and phase. The output of the system can be seen as the sum of the modified sinusoids.

find it. Traditionally, two different approaches exist to address this problem: the parametric and the non-parametric one.

In the parametric approach, the data is fitted to a mathematical model [126]. Normally, this model is of the form of a linear differential equation with constant coefficients, where the coefficients are the unknown parameters that are to be found, in a least squares sense, in order to fit the observed data. There are several restrictions to this approach. First of all, a mathematical model should be assumed; results depend strongly from this selection. Secondly, due to the fact that the model selected is not based on the physical modeling of the mechanism involved in the real system, the model is difficult to interpret. Hence, no physiological information can be extracted from the parameters defining the obtained transfer function. Although a physiological model can be used as starting point for the identification framework, the tuning of the model can be computationally expensive, which is not appealing in a clinical environment. Finally, the model is assumed to be linear. Nonlinearities will not be explained by the model and can produce misleading results.

From equation (2.10), the transfer function can be obtained as:

$$H(\omega) = \frac{Y(\omega)}{X(\omega)} \quad (2.11)$$

however, a more robust estimation is obtained by means of the power spectrum. In this approach no mathematical model is imposed and the system is represented by a vector in the frequency or time domain. The frequency vector is computed as follows:

$$H(\omega) = \frac{G_{io}(\omega)}{G_{ii}(\omega)} \quad (2.12)$$

where $H(\omega)$ represents the system transfer function, $G_{io}(\omega)$ and $G_{ii}(\omega)$ are the input-output cross power spectral density and the input power spectral density, respectively. If the inverse Fourier transform is applied to the transfer function $H(\omega)$, the time series $h(t)$ is obtained. $h(t)$ is known as the impulse response of the system. The input-output relationship of the system can also be represented in the time domain by using $h(t)$ as follows:

$$y(t) = \int_{-\infty}^t x(\tau)h(t - \tau)d\tau + e(t) \quad (2.13)$$

Equation (2.13) is called convolution equation and is the time domain equivalent of equation (2.10).

The non-parametric approach is more flexible than the parametric one, since no model is imposed to the system. In order to estimate the cross power and power spectral densities, the Welch method is used as in the calculation of the coherence [232, 126]. Therefore, the same restrictions of stationarity should be taken into account. Transfer function produces complex values from which the gain and the phase of the transfer function can be calculated.

The gain of the transfer function represents the strength of the relationship between the system input and output and is computed as follows:

$$\text{Gain}(\omega) = \sqrt{\Re(H(\omega))^2 + \Im(H(\omega))^2} \quad (2.14)$$

where $\Re(H(\omega))$ and $\Im(H(\omega))$ represent the real and imaginary part of $H(\omega)$.

In contrast with the correlation and the coherence coefficients that only measure the presence of a linear relationship, transfer function, particularly the gain, provides information about the strength of this relation. Hence, a high gain value implies a high variation in the output driven by a small variation in the input, while a small gain implies a low variation in the output driven by a big variation in the input. This property of the gain is of great interest for the analysis of cerebral autoregulation as the cerebral autoregulation plateau is not

completely flat but presents a small inclination as shown in figure 1.1. This inclination in the autoregulation curve can lead to high values of correlation and coherence but will produce small gain values.

On the other hand, the phase represents the delay between the input and the output for each frequency component and is calculated as follows:

$$\text{Phase}(\omega) = \angle H(\omega) = \tan^{-1} \left(\frac{\Im(H(\omega))}{\Re(H(\omega))} \right) \quad (2.15)$$

The transfer function represents one of the most important tools for system analysis. The power of transfer function analysis resides in the fact that all continuous signals can be represented as an infinite sum of sine and cosine functions of different frequencies, amplitudes and phases. From (2.10) it can be seen that the output of a system at a particular frequency ω_i can be estimated as the product of the transfer function at that frequency, $H(\omega_i)$, and the Fourier transform of the input at that frequency, $X(\omega_i)$. In terms of gain and phase values it means that the output at a frequency ω_i is equal to the product of the input at that frequency with the respective gain value, with a delay given by the phase at that frequency $Y(\omega_i) = X(\omega_i + \text{Phase}(\omega_i))\text{Gain}(\omega_i)$. Figure 2.1 illustrates this property.

Discrete signals

Coherence and transfer function analysis have also been formulated in the context of discrete time signal processing. In this framework, the Fourier transform needs to be defined in discrete time. The discrete Fourier transform (DFT) is computed as follows:

$$X[k] = \sum_{n=1}^N x[n] e^{-j2\pi kn/N} \quad (2.16)$$

where, $x[n]$ represents a discrete signal, n indicates the sample number, $X[k]$ represents the DFT of $x[n]$, and k is an integer that is related to the frequency. The relation between k and the normalized angular frequency ω is given by: $\omega_k = 2k\pi/N$, where ω_k , for $\{k = 1, \dots, N\}$ is the frequency related to the k^{th} component in $X[k]$. Coherence, and transfer function values can be computed from discrete signals using the DFT.

2.1.5 Cerebral autoregulation assessment

In clinical research, analysis of the common dynamics between MABP and CBF has been used in order to determine the status of cerebral autoregulation. High correlation, coherence and gain values are interpreted as impaired cerebral autoregulation, since they indicate a strong linear coupling between both signals.

Classically, the autoregulation mechanism has been thought as an on-off process. However, recent evidence indicates that autoregulation is a more complex process, and the question is not anymore whether the patient autoregulates but how much the patient does it [77], i.e. the level or degree of autoregulation. Correlation and coherence values are useful in order to detect the presence of a linear dependency between MABP and CBF, however they cannot provide information about the strength of this relation. Transfer function gain provides such information, which makes it a promising score for cerebral autoregulation. However, transfer function scores are only meaningful when the coherence values are high. Some authors have proposed the combined use of coherence and transfer function values in order to determine if the patient autoregulates and how much (s)he autoregulates [81]. Even though the results provided by these methodologies are promising they lack of precision and are not suitable for online monitoring [81].

Phase values, are analyzed differently. Perfect cerebral autoregulation is represented by a large phase difference between MABP and CBF. While impaired cerebral autoregulation produces smaller phase differences, this is an indication of a more pressure passive CBF. When analyzing phase values, literature studies have focused on phases differences at 0.1Hz since they have shown the best results differentiating between impaired and normal autoregulation [50]. There is no physiological explanation for the selection of this particular frequency. However, these results may be related to the Mayer waves. Mayer waves are oscillations of arterial pressure occurring that occur spontaneously at a frequency around 0.1 Hz. They might be generated by oscillations in baroreceptor and chemoreceptor reflex control systems; however, their physiological origin is still unclear [100]. Since spontaneous variations in MABP are not strong enough [82], the influence of the Mayer waves around this frequency might result in an increased signal-to-noise ratio (SNR) for the calculation of the transfer function.

2.2 Wavelet Based Transfer Function Analysis

Wavelet transform is a mathematical tool that provides an optimal representation of a signal in the time-scale domain. In contrast with Fourier analysis, wavelet

provides a framework to study non-stationary signals. An introduction to wavelet analysis can be found in any of the following texts [226, 44, 33].

2.2.1 Wavelet Transform

Consider a continuous function $f(t)$, its wavelet transform, $F(a, b)$, is given by:

$$F(a, b) = \frac{1}{\sqrt{|a|}} \int_{-\infty}^{\infty} f(t)\Psi^*\left(\frac{t-b}{a}\right)dt \tag{2.17}$$

where Ψ represent the mother wavelet, $*$ is the complex conjugate, b represents the translation coefficient in time and a is a scaling factor. The properties of the wavelet transform are given by the selection of the mother wavelet Ψ . Wavelet analysis can be performed using complex and real valued wavelet functions. When using complex valued wavelets the magnitude and phase of the wavelet transform can be used in a similar way as in Fourier analysis. In Figure 2.2, different wavelet functions are shown.

Wavelet functions are located in time and frequency. Their location in frequency is changed by the scaling factor a which is responsible of shrinking or expanding the mother wavelet function. Shrinking the wavelet function moves its frequency content to a higher frequency band and also increases its bandwidth. Expanding the wavelet function will move its frequency content to a lower frequency band and will reduce its bandwidth. The location in time of the wavelet function is changed by the translation coefficient b . The time and frequency localization of the wavelets is what make them suitable for the analysis of nonstationary signals.

Even though a wavelet transform does not provide directly a time-frequency representation, an approximation can be obtained due to the relation between scale and frequency. As mentioned before, wavelet functions are localized in frequency, the power spectrum of a wavelet function is located around a central frequency f_0 . This central frequency can be used to describe the frequency of the wavelet for a scaling factor $a = 1$. For $a > 1$ the frequency content of the wavelet function is moved to lower frequencies, an intuitive way of calculating the new central frequency of the expanded wavelet function is $f = \frac{f_0}{a}$, where f is normally called a pseudo-frequency. It is important to note that f only represents the central frequency of the wavelet function at a scale a . In Figure 2.3 the time and frequency content of the Morlet wavelet for different scales is shown.

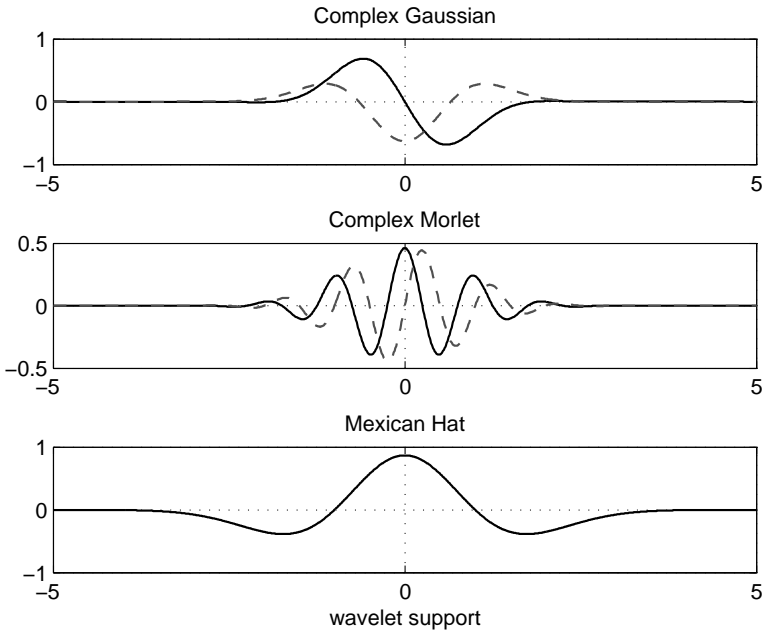


Figure 2.2: Example of complex and real valued wavelet functions. For the complex-valued wavelet functions the solid line represents the real part while the dashed line represents the imaginary part. The x-axis represents the support of the wavelet functions. The support is defined as the set of points where the function is not zero-valued.

2.2.2 Wavelet Power Spectrum

The power spectrum of a function $f(t)$ can be calculated as $|F(\omega)|^2$, where $F(\omega)$ represents the Fourier transform of the signal. This power spectrum is a representation of the contribution in power of each frequency contained in the original signal to the total power of the signal. In the presence of nonstationarities this contribution changes in time. Therefore, a more appropriate representation of the power spectrum should be given using a time-frequency approach [213].

In order to overcome the problems of nonstationarities the concept of power spectrum can be extended to the wavelet domain. The wavelet power spectrum of a signal can be computed as:

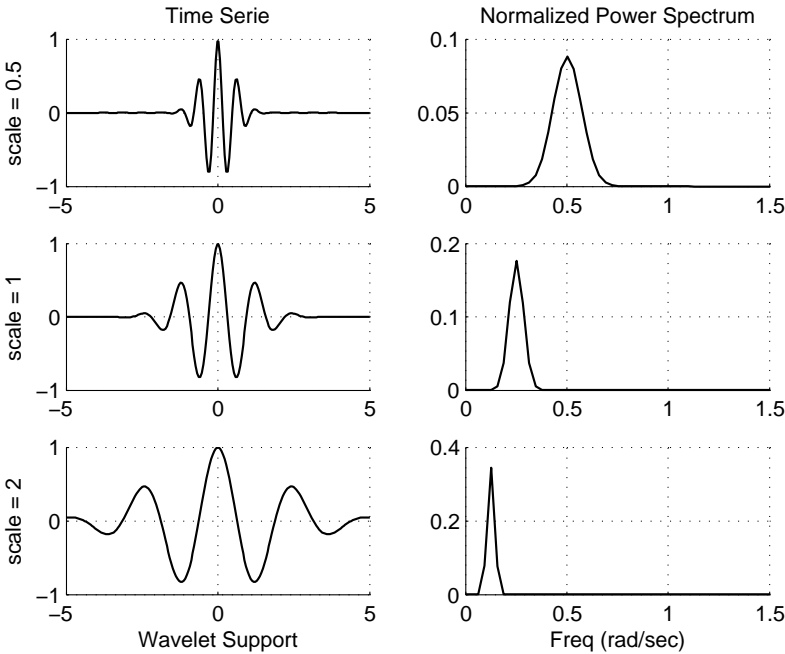


Figure 2.3: Time and frequency content for the Morlet wavelet using different scale values. From top to bottom $a = 0.5, 1$ and 2 . As the scale factor increases, the wavelet expands in time, which moves its spectral content to lower frequencies and decreases its bandwidth. This increases the frequency resolution but decreases the time resolution. For a better visual inspection the x-axis for the time series and the power spectral density was fixed.

$$P(a, b) = |F(a, b)|^2 \tag{2.18}$$

where $F(a, b)$ represents the wavelet transform of the signal, computed using equation (2.17).

When using a complex-valued mother wavelet, the power spectrum in (2.18) can be calculated using the equivalent formulation $P(a, b) = F(a, b) * F(a, b)$, where $*$ represents the complex conjugate. The wavelet spectrum can be used to compute the *scalogram* of the signal. The scalogram is the wavelet equivalent of the spectrogram. The spectrogram is a visual representation of the changes in time-frequency in a signal, which is constructed using the Fourier transform in consecutive segments of a nonstationary signal [154].

2.2.3 Wavelet Cross-power Spectrum

The cross-power spectrum in the wavelet domain can be found by an extension of the concept of power spectrum from Fourier analysis to wavelet analysis [213]. In Fourier analysis, the cross-power spectrum provides a representation of the power shared by two functions in the frequency domain.

Consider the functions $f(t)$ and $g(t)$, with Fourier transforms $F(\omega)$ and $G(\omega)$ respectively. The cross-power spectrum of the two series is defined as:

$$P(\omega) = F(\omega)^*G(\omega) \quad (2.19)$$

By extension of (2.19), the wavelet cross-power spectrum of those two functions is calculated as:

$$P(a, b) = F(a, b)^*G(a, b) \quad (2.20)$$

where $F(a, b)$ and $G(a, b)$ represent the wavelet transform of $f(t)$ and $g(t)$ respectively.

The wavelet cross-power spectrum provides a representation of the common power between the two signals in time and frequency. This representation allows to detect changes in the common dynamics between the two signals, providing a base for the analysis of nonstationary systems.

In addition to wavelet cross-power spectrum, wavelet cross correlation (WCC) represents the cross-spectral power in two time series (shifted relative to each other by τ) as a fraction of the total power in the two time series [182]. Consider two time series x and y with wavelet transform F_x and F_y , respectively. The normalized WCC between the signals x and y is computed using the following equation:

$$WCC(a, \tau) = \frac{|R_{X,Y}(F_x, F_y, a, \tau)|}{\sqrt{|R_{X,X}(F_x, a, 0) \cdot R_{Y,Y}(F_y, a, 0)|}} \quad (2.21)$$

where $R_{X,Y}(F_x, F_y, a, \tau)$ represents the cross-correlation of the wavelet coefficients between the time series x and y at the scale a and a time shift τ ; and $R_{X,X}(F_x, a, \tau)$ and $R_{Y,Y}(F_y, a, \tau)$ represent the autocorrelation of the time series x and y at a scale a and time shift τ .

In this context, Rowley et al evaluated the use of wavelet cross-correlation (WCC) for the analysis of the relation between MABP and ΔHbO_2 in patients

suffering from autonomic failure and age-matched controls [182]. They found Statistically significant differences in the WCC values induced by posture change in patients, but no in controls. In addition, they suggested that for a short-duration clinical test previous transfer-function-based approaches may suffer due to the inherent nonstationarity of low-frequency oscillations that are observed in the resting brain. This findings suggest that wavelet based techniques are more suited to be used in the monitoring of cerebral hemodynamics.

2.2.4 Wavelet Coherence and transfer Function

The wavelet coherence is an extension of the concept of coherence in Fourier analysis [79, 213, 102]. Wavelet coherence values change between 0-1, where 1 indicates perfect linear coupling between two signals, while 0 represents the absence of linear coupling. Wavelet coherence can be computed as follows:

$$C^2(a, b) = \frac{|F(a, b)*G(a, b)|^2}{(F(a, b)*F(a, b))(G(a, b)*G(a, b))} \tag{2.22}$$

where $F(a, b)$ and $G(a, b)$ represent the wavelet transform of $f(t)$ and $g(t)$, respectively.

However, the wavelet coherence values given in (2.22) produce values equal to 1. This is due to the fact that there is no spectral smoothing involved in the computation of the wavelet power spectrum [79, 213]. Coherence values computed using the Fourier transform, calculate the cross-power and power spectrum of the signals using the Welch method. This method smooths the spectrum by computing an average of different realizations of the process under study. When using the wavelet transform, the signal under analysis is considered non-stationary, therefore using the Welch method can produce misleading results. However, by introducing a smoothing operator $S(\cdot)$, in scale and time, the wavelet spectrum can be smoothed. This operation will reduce the coherence values in segments with no spectral coupling, but will spread the influence of coupled segments in the time-frequency domain. The wavelet coherence using the smoothing operator can be computed as follows:

$$C^2(a, b) = \frac{|S(F(a, b)*G(a, b))|^2}{S(F(a, b)*F(a, b))S(G(a, b)*G(a, b))} \tag{2.23}$$

In order to select an appropriate smoothing operator the characteristics of the mother wavelet should be taken into account. A suitable smoothing operator for the *Morlet* wavelet is given by:

$$\begin{aligned}
S(P) &= S_{scale}(S_{time}(P(a, b))) \\
S_{time}(P)|_a &= \left(P(a, b) c_1^{\frac{-t^2}{2a^2}} \right) \\
S_{scale}|_b &= (P(a, b) * c_2 \prod(0.6a))
\end{aligned}$$

where c_1 and c_2 are normalization constants and \prod represents a rectangular function.

Using the smoothing functions $S(\cdot)$ the concept of transfer function in the Fourier domain can also be extended to the wavelet domain. By using the definition of transfer function presented in (2.12), the wavelet based transfer function (WBTF) can be computed as:

$$H(a, b) = \frac{|S(F(a, b) * G(a, b))|^2}{S(F(a, b) * F(a, b))} \quad (2.24)$$

In case a complex wavelet is used to compute the power spectrum the derived transfer function will be a complex function, where its absolute value is the gain of the transfer function and the angle represents the phase.

$$\text{Gain} = \sqrt{\Re(H(a, b))^2 + \Im(H(a, b))^2} \quad (2.25)$$

$$\text{Phase} = \angle(H(a, b)) = \tan^{-1} \frac{\Im(H(a, b))}{\Re(H(a, b))}$$

Example

Let's consider a system described by the following difference equation:

$$a_1 y[n] = b_1 x[n] + b_2 x[n-1] - a_2 y[n-1] \quad (2.26)$$

where n represents the sample number, and a_1 , a_2 , b_1 , b_2 represent the coefficients of the filter. By assigning different values to the filter coefficients, the characteristics of the system can be changed. Assume that this system

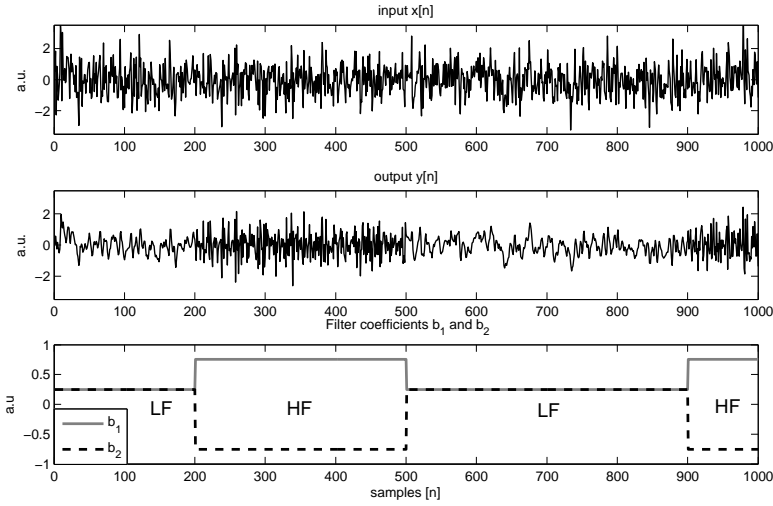


Figure 2.4: Input and output signal of the systems described in equation (2.26). The bottom Figure presents the profile of the changes in the system coefficients b_1 and b_2 , the coefficients a_1 and a_2 were kept constant as indicated in Table 2.1. The low pass and high pass filter regions were indicated in the figure by LF and HF respectively.

varies in time, its behavior changes between a low-pass and a high-pass filter. Consider the cut-off frequency $f_c = 0.1f_s$, for both the low and the high pass filter, where f_s represents the sampling frequency. The corresponding filter coefficients for this f_c are shown in Table 2.1. The output of the system is computed using as input a random signal of 1000 samples and initial conditions set to zero. The system coefficients are changed in time in order to fluctuate from a low-pass to a high-pass filter characteristic. The profile of these changes is depicted in Figure 2.4.

	a_1	a_2	b_1	b_2
Low-pass Filter	1	-0.5095	0.2452	0.2452
High-pass Filter	1	-0.5095	0.7548	-0.7548

Table 2.1: Filter coefficients for the Low-pass and High-pass Butterworth filter

As indicated in Figure 2.4 the system behaves as a low-pass filter between the samples (0-200) and (500-900), and it behaves as a high pass filter between the samples (200-500) and (900-1000). In Figure 2.5 the gain and phase of

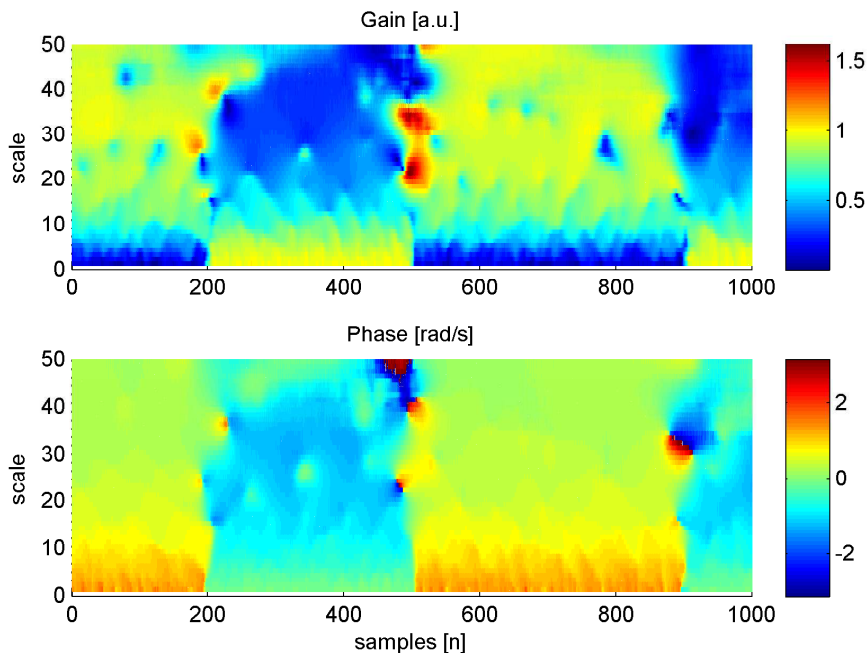


Figure 2.5: Wavelet based transfer function gain and phase for the system described in equation (2.26). The Figure shows the changes from low-pass to high-pass filter profile in the system. It is important to note the inverse relationship between frequency and scale. The cut-off frequency $0.1f_s$ corresponds approximately to the 10^{th} scale.

the WBTF are shown. It is important to notice the inverse relation between scale and frequency. In addition, wavelet coefficients at a specific scale does not represent a single frequency component but a frequency band. In order to be able to interpret the results provided by the wavelet transform in terms of frequencies instead of scales, a *pseudo-frequency* has to be assigned to each wavelet scale. This pseudo-frequency can be computed as follows: $f_p = f_0 f_s / \text{scale}$, where f_p is the pseudo-frequency corresponding to the specified scale, f_0 is the central frequency of the mother wavelet, and f_s is the sampling frequency. The WBTF, for this example, was computed using a complex Morlet as mother wavelet, with central frequency $f_0 = 1.5\text{Hz}$ and a bandwidth of 1Hz . With these settings, the cut-off frequency of the filters is located around the 10^{th} scale. This example shows clearly the advantages of the use of the wavelet based transfer function in the study of nonstationary signals.

Feature extraction

One of the main problems of wavelet analysis is that it provides an abundant amount of information. Due to this problem its application in clinical monitoring is not appealing. However, it is possible to condense the information contained in the WBTF by means of appropriate processing. In this thesis, two approaches will be used: the temporal and frequency profiles, and the mean gain and phase.

Temporal and spectral profiles: WBTF can be used in order to compute the frequency and time profile of the changes in the system. On one hand, by calculating the mean along the time axis, a profile of the system frequency response, similar to the one obtained by Fourier analysis, can be found. However, if many changes in the spectral characteristics of the system are present in the segment under analysis, this mean average won't provide useful information. On another hand, if the mean is computed along the scales axis a mean profile of the changes in the system in time is given. Similarly to the case mentioned before, if several changes are presented in the scales under analysis this won't provide useful information. In Figure 2.6 the frequency and time profile for the changes in the system used in the previous subsection are shown. As it can be seen the frequency profile does not provide useful information about the nature of the system, while the time profile is able to identify the changes in the system. Four different regions can be identified in the time profile shown in Figure 2.6. If an average along time in each one of this segments is used, a better estimation of the system behavior during these segments can be obtained. Figure 2.7 shows the spectral characteristics of the system in the 4 different regions indicated by the time template. It is clear from the Figure that by including the information given by the temporal profile, the low-pass and high pass characteristics of the system were retrieved. Even though this analysis reduces the amount of information obtained from WBTF analysis, it is still far from clinical practice. However, from the temporal profiles is possible to extract more information, such as the standard deviation, the power, among others.

Mean gain and phase: Wavelet cross-power spectrum and coherence have been widely used in the analysis of geophysical data. In [213] the wavelet cross-power spectrum and coherence were analyzed by finding the regions in the time-scale representation of the signal where the cross-spectral power was significant. This was done by comparing the wavelet cross-power spectrum of the time series against the wavelet cross-power spectrum of the background noise. The mean average of the phases in those regions was calculated as indication of the coupling between both signals. This methodology can be extended to the analysis of the WBTF, where the average is computed in the gain and phase coefficients with significant cross-power spectrum. Notice that the phase of the cross-power spectrum is identical to the phase obtained from the WBTF.

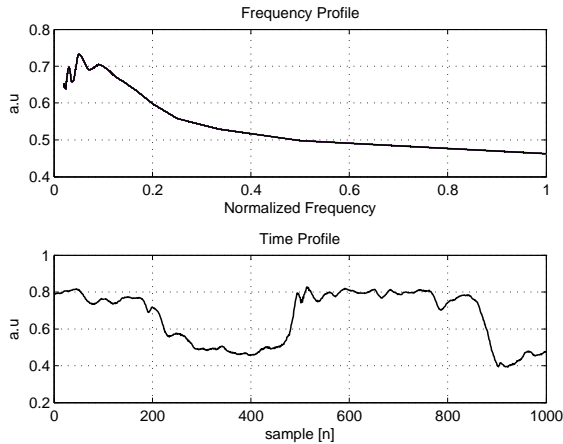


Figure 2.6: Frequency and temporal template for WBTF of the system described in (2.26). As can be seen the frequency template does not provide relevant information about the system, while the temporal template is more informative about the changes in the system.

2.2.5 Discrete Wavelet Transform

The continuous wavelet transform provides an abundant amount of redundant information. By computing the wavelet coefficients using a *dyadic* scale a more efficient computation of the wavelet transform can be obtained. A *dyadic* scale is formed by using the scales equal to powers of 2, $a(i) = 2^i$ for $i = 1, \dots, L$, where L denotes the level of decomposition. This new formulation represents the discrete wavelet transform (DWT). The DWT is closely related to multi-resolution analysis where the signal is decomposed in a series of signals obtained by applying an appropriate low-pass and high-pass filter. In the frequency domain this decomposition divides the frequency content of the signal in two different frequency bands. In the DWT the characteristics of these filters are given by the selection of the mother wavelet.

In the DWT one level of decomposition is achieved by low and high pass filtering the input signals and decimating the output of the filters by a factor of 2, generally the low pass filters are represented by $h[n]$ and the high pass filter by $g[n]$. This decimation of the filtered signals reduces the amount of redundant information produced by the decomposition. The coefficients obtained from the low pass filter are called the *approximation* coefficients, while the ones obtained from the high pass filter are called the *detail* coefficients.

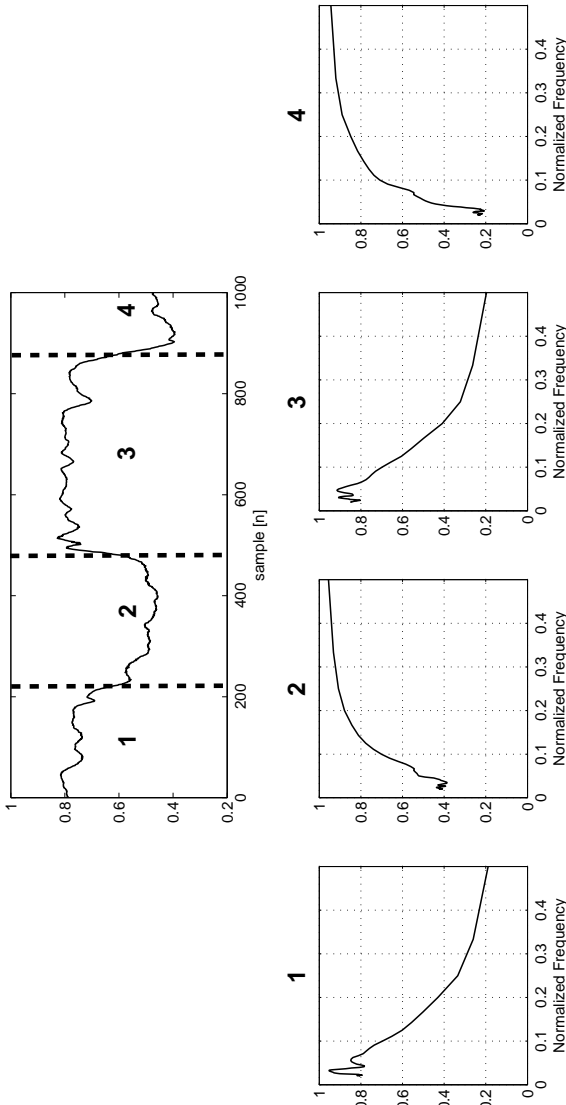


Figure 2.7: Frequency profiles for the 4 different segments identified by the time profile of the system described in (2.26). The low-pass and high-pass filter characteristics in the segments (1,3) and (2,4), respectively, were adequately identified.

Further levels of decomposition are achieved by repeating this procedure to the filtered signals. When this decomposition is done consecutively in the approximation coefficients the *wavelet decomposition tree* is obtained. In Figure 2.8 a schematic representation of the wavelet decomposition tree is shown. The input sequence $x[n]$ is filtered by the low-pass and high-pass filters, $g[n]$ and $h[n]$, the output of the filters is decimated, one of each 2 samples is kept. The decimated output of the high-pass filter is filtered again using the same procedure. If the output of the filters is not decimated, the signal can be reconstructed just by adding the outputs of the high-pass filter and the output of the last low-pass filter. Each one of these signals is orthogonal, since they represent different frequency bands. Figure 2.9 displays the frequency band for the filters at each stage in the three level decomposition tree shown in Figure 2.8.

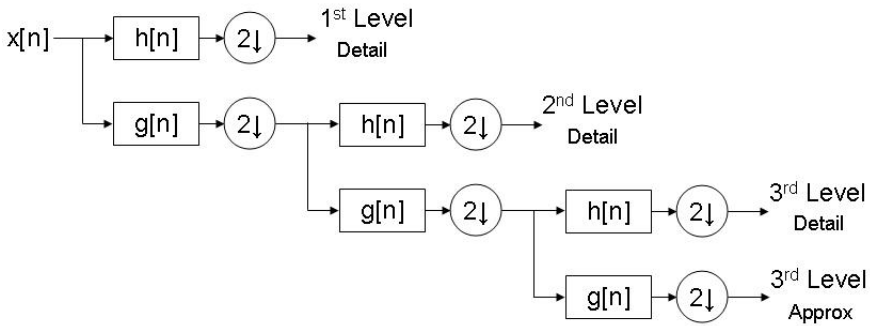


Figure 2.8: Schematic representation of a three-level DWT decomposition. $h[n]$ and $g[n]$ represent the high-pass and low-pass filters used in the DWT.

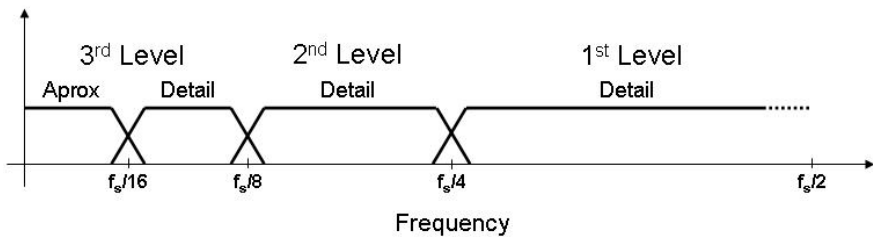


Figure 2.9: Frequency band representation for the filters in the three level decomposition shown in Figure 2.8.

In order to obtain the original signal from the approximation and detail coefficients, an inverse procedure should be performed, this is called *reconstruction*. Signal processing techniques such as filtering and compression, manipulate the detail coefficients of the signals in order to eliminate undesired information or to obtain a more compact representation of the signal.

Filtering using wavelets is achieved by reconstructing the original signal after thresholding or elimination of some of the approximation and detail coefficients. In Figure 2.10 the 4th level decomposition of a signal using the DWT is shown. In order to have a better interpretation of the DWT, the approximation and detail coefficients were not decimated, therefore, the detail and approximation coefficients represent the outputs of the filters for each level of decomposition. In this example one measurement of the changes in tissue oxygenation index (TOI) in one neonate was used. The TOI is decomposed in different signals each one representing a different frequency band. It can be clearly seen that the approximation coefficients represent the lowest dynamics, while the detail coefficients represent faster dynamics. The dynamics of the first detail coefficients are faster than the dynamics of details in deeper levels. In order to filter the input signal, the first detail coefficients were set to zero, since they represent mostly noise measurement. In addition, a thresholding operation was performed to the detail coefficients from the levels 2 to 4. The threshold should be set in order to detect outliers in the distribution of the details coefficients. Assuming that the detail coefficients are normally distributed, the threshold is set to ± 3 times the standard deviation of the corresponding detail. Values of the detail coefficients higher or lower than the threshold were set equal to the threshold. The selection of the thresholding operation done in this example is just illustrative. More refined criteria can be used in their selection. The filtered TOI signal, computed as the sum of the approximation and modified detail coefficients, is presented in Figure 2.11. From the filtered signal it can be seen that slow and fast oscillations were preserved, while discontinuities were smoothed.

As shown in Figure 2.10, a signals can be decomposed using the DWT without decimating. This corresponds to a reconstruction procedure where all the coefficients are set to zero, except the ones of interest. By doing this over the complete set of coefficients, the original signals is decomposed in a set of sub-signals of the same length, where each sub-signal represents a different frequency band. This approach will be used in the section 2.4 to increase the dimensionality of the subspaces defined by the signal. In addition, all the concepts discussed in this section, such as the wavelet coherence, cross-power spectrum and transfer function can also be applied using the DWT.

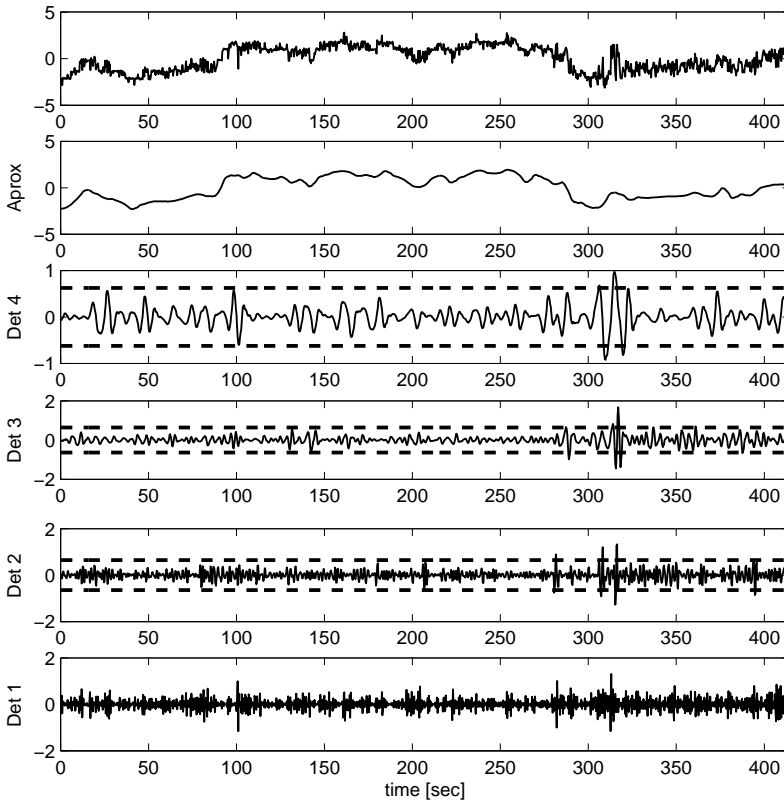


Figure 2.10: Decomposition of the changes in TOI using DWT. From top to bottom, Original signal, approximation coefficients, Detail coefficients for levels 4, 3, 2 and 1. The dashed line represent the threshold used for the detail coefficients 2-4.

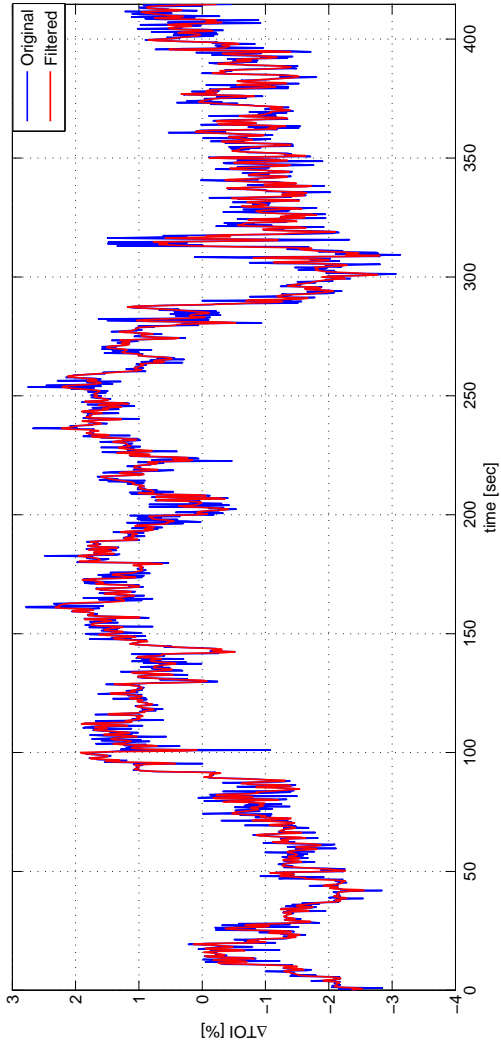


Figure 2.11: Original (blue) and filtered (red) TOI signals. Slow and Fast oscillations were preserved while the discontinuities were smoothed.

2.3 Canonical Correlation Analysis

2.3.1 Introduction to CCA

Canonical Correlation Analysis (CCA) is a statistical methodology that allows to analyze multidimensional datasets. CCA was first described in [92]. CCA can be seen as an extension to normal correlation analysis, in which the closeness between two multidimensional datasets, instead of vectors, is analyzed by means of canonical angles. Consider the set of vectors $x_i \in \mathbf{R}^{n_x}$ and $y_i \in \mathbf{R}^{n_y}$ with $i = 1, 2, \dots, N$ and $N \gg n_x + n_y$, stored row-wise in the matrices $X \in \mathbf{R}^{N \times n_x}$ and $Y \in \mathbf{R}^{N \times n_y}$. CCA decomposes these matrices in different projected variables $z_x = X\omega$ and $z_y = Yv$, where $\omega \in \mathbf{R}^{n_x}$ and $v \in \mathbf{R}^{n_y}$, such that the correlation between them is maximized. In this context the CCA problem consists in finding the vectors ω and v that maximize the correlation between the projected variables. This problem is stated as follows:

$$\max_{\omega, v} \rho = \frac{\omega^T C_{xy} v}{\sqrt{\omega^T C_{xx} \omega} \sqrt{v^T C_{yy} v}} \quad (2.27)$$

where $C_{xx} = X^T X$, $C_{yy} = Y^T Y$ represent the autocorrelation matrix of X and Y and $C_{xy} = X^T Y$ represents the cross-correlation matrix between X and Y . If the columns of X represent a set of independent variables and the columns of Y represent a set of dependent variables, CCA can be used to investigate the interrelation between each set of variables. This is achieved by analyzing the relationship between z_x and z_y . CCA determines how strongly the variables in the independent/dependent dataset are related. In addition CCA provides information about which independent variables explain most of the variation in the dependent dataset, as well as information about the amount of variance in the dependent dataset explained by the independent variables.

The CCA problem in (2.27) can be reformulated as the following optimization problem:

$$\begin{aligned} \max_{\omega, v} \quad & \omega^T X^T Y v \\ \text{subject to} \quad & \omega^T X^T X \omega = 1 \\ & v^T Y^T Y v = 1 \end{aligned} \quad (2.28)$$

The solution of this problem produces the first pair of canonical variates ω_1 and v_1 . The rest of the variates can be found by solving again (2.28) and imposing

that the new variates are orthogonal to the ones previously found. An equivalent solution is given by solving the following eigenvalue problem:

$$\begin{aligned} X^T Y v_j &= \lambda_j X^T X \omega_j \\ Y^T X \omega_j &= \alpha_j Y^T Y v_j \end{aligned} \tag{2.29}$$

for $\{j = 1, 2, \dots, r\}$ with $r = \min(\text{rank}(X), \text{rank}(Y))$.

2.3.2 Interpreting CCA

CCA can be seen as a multilinear regression where the independent and the dependent datasets are multidimensional [6, 4]. In this framework CCA is related to Partial Least Squares (PLS). The general idea of CCA is to decompose both datasets in functions called canonical variates. These canonical variates are orthogonal and each pair has maximum correlation.

CCA produces the following outputs:

1. *Canonical correlation coefficients (ρ):* These are the correlation coefficients between corresponding canonical variates in the independent and dependent dataset, they are computed as the correlation between z_x and z_y . These coefficients are maximal for the first pair of canonical variates and decrease as more canonical variates are generated. This is due to the fact that the first linear transformation of the data maximizes the correlation between the first canonical variates, this information is then extracted from the original dataset leading to more uncorrelated residuals. The canonical correlations are equivalent to the eigenvalues
2. *Left and right Canonical vectors:* These are the vectors used to transform the original dataset in order to generate the canonical variates. In equation (2.29) they are represented by the vectors ω_j and v_j for $j = 1, 2, \dots, r$ with $r = \min(\text{rank}(X), \text{rank}(Y))$.
3. *Canonical variates:* They are functions generated by a linear transformation of the independent and dependent dataset. They are represented by the variables z_x and z_y .

In order to analyze the results that CCA produces, some considerations should be taken into account. CCA looks for a linear transformation of the variables

in the independent and dependent dataset in such a way that the correlation between the generated canonical variates is maximized. This does not imply that the right and left canonical vectors (ω, v) represent a measure of the influence on the dependent dataset of the corresponding variable in the independent dataset. In addition, the canonical correlations only measure the explained variability between canonical variates. Therefore, conclusions cannot be drawn just based on these two parameters.

By using the canonical variates and the canonical correlations, the concept of loading, cross-loadings and redundancy coefficients can be introduced. Loading coefficients are the correlation between the variables of one dataset and the generated canonical variates corresponding to the same dataset. They are computed as follows:

$$l_{j,x_i} = \frac{x_i^T (z_x)_j}{|x_i|_2 |(z_x)_j|_2} \quad (2.30)$$

where $(z_x)_j$ represents the j^{th} canonical variate of X and x_i represents the i^{th} column of X . Loading coefficients for Y are computed in the same way. The loading coefficients indicate how well the variations in the canonical variates are related to the variations of a particular variable. Highly correlated variables and canonical variates will produce high loading coefficients.

On the other hand, cross loading coefficients are defined as the correlation coefficient between the variables of the independent/dependent dataset and the canonical variates in the dependent/independent dataset. They are computed as follows:

$$Cl_{j,x_i} = \frac{x_i^T (z_y)_j}{|x_i|_2 |(z_y)_j|_2} \quad (2.31)$$

where $(z_y)_j$ represents the j^{th} canonical variate of Y . Cross loadings for the dependent variables in Y can be found in the same way. Cross-loadings can be used to find which independent variables are more linearly related with the variations in the dependent dataset.

However, since several canonical variates are produced, it is difficult to select the most representative ones. Several approaches can be taken. The most straightforward approach is to select the canonical variates with the highest canonical correlations. However, this can produce misleading results since the canonical variates are computed by maximizing the correlation among them. Therefore, the first pair of canonical variates may not be enough to explain the variance in the dependent variables, and other canonical variates may contain

relevant information. In order to address this problem, the so-called index of redundancy is used. The index of redundancy is the product of the mean value of the squared loading values and the square of the canonical correlation coefficient for the corresponding canonical variate. In simple words, it tells how the variables in the independent/dependent dataset are related to the corresponding canonical variates in the dependent/independent dataset. Redundancy indices are computed as follows:

$$re_j^2 = \rho_j \left[\frac{1}{n_x} \sum_{i=1}^{n_x} \frac{(x_i(z_y)_j)^2}{|x_i|_2^2 |(z_y)_j|_2^2} \right] = \frac{\rho_j}{n_x} \sum_{i=1}^{n_x} (Cl_{j,x_i})^2 \quad (2.32)$$

where ρ_j represent the canonical correlation between the j^{th} pair of canonical variates $(z_x)_j$ and $(z_y)_j$. The redundancy indices computed as in (2.32) indicate the amount of variance in the dependent dataset explained by variations in the independent dataset. The total explained variance can be found using the following equation:

$$\sigma^2 = \frac{1}{r} \sum_{i=1}^r re_i^2 \quad (2.33)$$

using the information given by the redundancy indices the canonical variates that explain most of σ^2 can be selected for further processing.

In summary, CCA results should be analyzed as follows:

1. Select the canonical variates with the highest redundancy indices re^2 .
2. From those canonical variates use the loading and cross-loading coefficients in order to draw conclusion about the relation between variables in the dependent and independent datasets.
3. Do not use the right and left canonical vectors since they can produce misleading results.

2.3.3 Visualizing the results from CCA

CCA provides an abundant amount of information which makes it difficult to interpret. Two approaches can be followed in order to facilitate its analysis. CCA results can be presented either in a way where the overall interactions can be observed or by summarizing all the information provided in one single score. For the first alternative, the results in this thesis will be presented using

biplots or the total explained variance [209]. With the use of biplots the overall interaction between the variables is observed, while the explained variance gives an idea of the overall relation between the datasets in only one score.

Biplots: a biplot is a exploratory graph used in statistics. The biplots can be used to look for relation between several variables in different datasets by plotting the data using a common axes. In CCA a biplot can be created using the canonical variates as axes. In order to represent the variables from each dataset, the loading and cross-loading coefficients can be used. In CCA, for example, the canonical variates for the dependent dataset can be used as reference for the axes in the biplot. The variables in the independent dataset can then be represented as a vector composed of the cross-loadings between that variable and the respective axis (canonical variate), while the variables in the dependent dataset are represented as a vector composed of the loading coefficients. Since each variable in a biplot is represented as a set of correlation values, all the vectors should be contained inside the unitary circle. Therefore, a unitary circle can be drawn in order to facilitate visual interpretation. From the biplots the relation between the variables is assessed just by looking how close are the vectors that represent each variable. In addition, the dot product between two vectors in a biplot represents the correlation between the two variables that are represented by the vectors.

Explained variance: by computing the explained variance as indicated in equation (2.33) a global assessment of the relation between both datasets can be obtained. This value indicates the percentage of explained variance in the dependent dataset driven by the variations in the independent variables. The main drawback of this approach is that the information about the relation between each independent variable and the variables in the dependent dataset is lost. But by using this variable the results provided by CCA are simplified in a single score, which is more suitable for clinical monitoring than using several scores.

2.3.4 Example

Let's consider the following independent/dependent datasets $X = [x_1, x_2, x_3]$ and $Y = [y_1, y_2, y_3]$, constructed as follows:

$$\begin{aligned}
 x_1 &= \sin(2\pi t) + 0.2\eta_1 & y_1 &= 0.5x_1 + 0.2x_2 + 0.1\eta_4 \\
 x_2 &= \sin(\pi t) + 0.2\eta_2 & y_2 &= \eta_5 \\
 x_3 &= \eta_3 & y_3 &= 0.3x_2 + 0.1\eta_6
 \end{aligned} \tag{2.34}$$

where η_i for $\{i = 1, \dots, 6\}$ represents normalized Gaussian noise. From this set of variables the following conclusions can be drawn:

- The variables in the independent datasets are orthogonal.
- y_1 is correlated with the variables x_1 and x_2 and it is orthogonal to the variable x_3 .
- y_2 is orthogonal to all the variables in the independent and dependent dataset.
- y_3 is correlated with the variable x_2 and is orthogonal to the other variables.

In Figure 2.12 the results of the CCA analysis using biplots are shown. In the Figure the independent variables are plot in blue, while the dependent variables are plot in red. The biplots were constructed using the three canonical variates in order to produce a 3-dimensional representation of the relation between the variables. In this Figure it can be seen that all variables in the X dataset are orthogonal. In addition, variable y_1 is close to the variables x_1 and x_2 indicating a high correlation among them, while variable y_3 is close to variable x_2 . Also it can be seen that variable y_2 is orthogonal to all the variables included in the analysis. This is indicated by the small length of the vector representing that variable.

The canonical correlations (ρ) and the redundancy indices (re) are displayed in Table 2.2. Biplots are good to illustrate the structure of the relationship between the variables. However, even though the information is summarized in one Figure, it is still complex to interpret. By summarizing all the information provided by CCA in the total explained variance σ^2 , it is known that about 50% of the variance in the dependent dataset is explained by the variations in the dependent dataset. This value also represents the amount of variance or power transferred from the independent dataset to the dependent variables. This can be seen as follows: the variance of the signals x_1 and x_2 is 0.7, therefore the total contribution of those variables in the power of the dataset X is 1.4; according to (2.34), the power in y_1 and y_3 transferred from x_1 and x_2 is equal to 0.49 and 0.21, respectively. Therefore, the total power transferred from the dataset X to the dataset Y is 0.7, which is half of the total power in X and is equal to σ^2 .

	1 st Canon. Var.	2 nd Canon. Var.	3 rd Canon. Var.
canon. Corr. ρ	0.933	0.760	0.002
re^2	0.330	0.166	0.000

Table 2.2: Canonical correlations ρ and redundancy indices re obtained from the CCA of (2.34). The columns represent the different canonical variates.

2.4 Subspace Projections

2.4.1 Orthogonal subspace projections

An orthogonal projection matrix is a linear transformation that maps any vector in \mathbf{R}^N to a subspace defined by a given basis. Consider the matrix $A \in \mathbf{R}^{N \times m}$

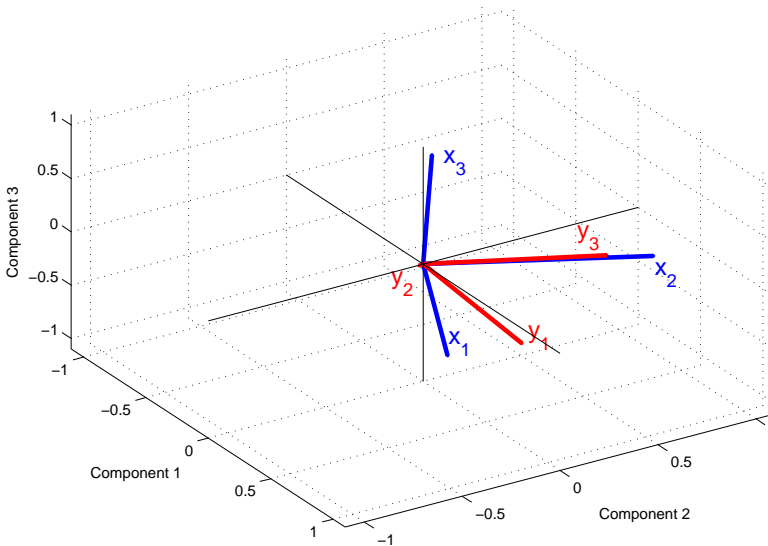


Figure 2.12: Results provided by CCA. The blue vectors represent the independent dataset, while the dependent variables are represented by the red vectors. The small length of the vector representing the variable y_2 indicates that this signal is orthogonal to the other variables in the analysis.

composed of the vectors $\{s_1, s_2, \dots, s_m\}$, with $s_k \in \mathbf{R}^N$ for $\{k = 1, 2, \dots, m\}$, in its columns. Assuming that A is full rank ($\text{rank}(A) = m$, with $N > m$) the vectors $\{s_1, s_2, \dots, s_m\}$ form a basis for the column space of A , $C(A)$. Given A , the orthogonal projection matrix can be found as follows:

$$P = A (A^T A)^\dagger A^T \quad (2.35)$$

where P represents the projection matrix, and \dagger is the pseudoinverse.

In a linear regression problem of the form $y = Ax + \varepsilon$, with A the regressor matrix, the projection matrix P maps the vector $y \in \mathbf{R}^N$ into $C(A)$. The projection of y onto $C(A)$ is calculated as $\hat{y} = Py$. Its projection onto the orthogonal subspace of $C(A)$ is $y^\perp = (I - P)y$. The matrix $Q = (I - P)$ is also a projection matrix. Q maps any vector $y \in \mathbf{R}^N$ onto the null space of S^T , $\mathbf{N}(A^T)$. In this way y is decomposed in two orthogonal components \hat{y} and y^\perp with $y = \hat{y} + y^\perp$.

In case that the basis vectors s_k are orthogonal, \hat{y} can be decomposed in m orthogonal components, each one related to a regressor vector s_k . However, in case that the regressor vectors are not orthogonal, an oblique projection is needed. A more detailed explanation about projectors, orthogonal and oblique can be found in [239]. Applications in signal processing can be found in [16].

2.4.2 Oblique subspace projections

An oblique projection, is a projection that is carried out along a reference subspace onto a target subspace, where the reference and target subspaces are not orthogonal. In case that the reference and target subspace are orthogonal an oblique projector becomes orthogonal. Therefore, an orthogonal projection is just a special case of oblique projections. In addition, in order to compute an orthogonal projector only a basis for the column space of the target subspace is needed, since the reference subspace can be found using the same basis. However, oblique projectors need a separate basis for the reference and the target subspace.

Let $V \subset \mathbf{R}^N$ represent the subspace spanned by A , and $V_k \subset V$ the subspace spanned by a partition of A , A_k . If $V = V_1 \oplus V_2 \oplus \dots \oplus V_m$, then the oblique projector onto V_k along $V_{(k)} = V_1 \oplus \dots \oplus V_{k-1} \oplus V_{k+1} \oplus \dots \oplus V_m$, denoted by $P_{k.(k)}$, is given by:

$$\begin{aligned}
 P_{k.(k)} &= A_k(A_k^T Q_{(k)} A_k)^{\dagger} A_k^T Q_{(k)} \\
 &+ Z[I_n - (Q_{(k)} A_k)(A_k^T Q_{(k)} A_k)^{\dagger} A_k^T] Q_{(k)}
 \end{aligned}
 \tag{2.36}$$

where, $Q_{(k)} = I_N - P_{(k)}$, is the orthogonal projector onto $N(V_{(k)}^T)$ and Z is any arbitrary $N \times N$ matrix.

By using oblique subspace projections the vector \hat{y} can be decomposed in m components, each one related to a regressor vector s_k .

2.4.3 DWT and projectors

Projection matrices are related to signal subspace filtering methods. The main goal of these methods is to decompose a target signal in 2 components, one that is related to the signal subspace and another one perpendicular to it. These methods assume that the signal subspace is low-rank while the noise is distributed along a larger subspace. Therefore, by defining a proper basis for the signal subspace the level of noise in the target signal is reduced.

Signal subspace filtering is based on the Hankelization of the regressor matrix. This procedure allows the computation of the covariance matrices for the noise and the signal, and a low-rank approximation of the signal subspace. This approach has been used in order to filter noise from speech signals [88]. A Hankelization procedure consist of the following: consider a vector $s \in R^N$. A ‘‘Hankelization’’ of s consist in forming a square matrix B , with the following relation in the matrix entries $B_{(i,j)} = B_{(i-1,j+1)}$. To illustrate better this concept, assume that $s = [a_1, \dots, a_9]$, then the Hankel matrix will be equal to:

$$B = \begin{pmatrix} a_1 & a_2 & \cdots & a_5 \\ a_2 & a_3 & \cdots & a_6 \\ \vdots & \vdots & \ddots & \vdots \\ a_5 & a_6 & \cdots & a_9 \end{pmatrix}
 \tag{2.37}$$

However, in the system identification framework the Hankelization procedure can produce rectangular matrices, generating a block Hankel matrix as follows [155]:

$$B = \begin{pmatrix} a_1 & a_2 & \cdots & a_4 \\ a_2 & a_3 & \cdots & a_5 \\ \vdots & \vdots & \ddots & \vdots \\ a_6 & a_7 & \cdots & a_9 \end{pmatrix} \quad (2.38)$$

the size of the matrix is controlled by the user. in this context, generally the number of rows is larger than the number of columns.

Another representation of the signal subspace can be obtained by decomposing each regressor using the DWT, as illustrated in section 2.2.5. This decomposition allows to divide the signal in different frequency bands using a dyadic scale. A block Hankel matrix can be obtained from this new regressor matrix, as shown in equation (2.38), where each entry a_i is now replaced by a row vector containing the DWT coefficients of each regressor. Consider the regressor matrix $A = \{s_1, s_2, \dots, s_m\}$, lets compute the d^{th} level DWT of each regressor variable s_i , for $i = \{1 \dots, m\}$. Now each regressor variable is decomposed in $d + 1$ components. By replacing each regressor s_i in A by its decomposed vector, the new regressor matrix $A_d \in R^{N \times (d+1)*m}$ is obtained. The regressor matrix A_d can be further extended by a block hankelization procedure. The block Hankel matrix, obtained from A_d , will have the following dimension $A_H \in R^{(N-p+1) \times p*(d+1)*m}$. The new regressor matrix A_H will reduce the influence of noise in the estimation, since the components related to noise will be less representative in this matrix.

The subspace spanned by A_H is larger than the one spanned by the original regressor matrix A . This will increase the dimensions of the signal subspace. The column space of A_H can be subdivided in orthogonal subspaces representing each frequency band obtained with the DWT of the regressors. By segmenting the regressor subspaces in subspaces representing different frequency bands, the original problem is relaxed, which allows to identify different relations in different frequency bands between the regressors. On the other hand, by appropriately defining the subspace spanned by each regressor variable, i.e. by taking a partition of A_H where only coefficients related to one regressor are selected, a decoupling algorithm can be formulated. Therefore, in order to decouple the influence of one of this regressors, that may be considered as noise, its subspace can be used as a reference for an oblique projector. An algorithm to decompose the influence of a signal in a number of components related to a set of regressor variables is proposed in algorithm 1. In this algorithm $P_{k.(k)}$ denotes the projector onto the k^{th} regressor variable along the subspace spanned by the rest of the variables as shown in (2.36).

Algorithm 1 Decoupling algorithm

input: Regressor variables: $A = [s_1, \dots, s_m]$ with $A \in R^{N \times m}$, target vector $y \in R^N$, and number of delays p .

output: decomposed target $Y_A \in R^{(N-p) \times m}$.

begin

$A_c \leftarrow$ subtract the mean value from A

$\text{aux} \leftarrow DWT(A_c)$

$A_H \leftarrow$ block Hankel matrix of aux , using a delay of p samples. As shown in (2.38)

for $k=1:m$

$A_k \leftarrow$ a partition of A_H as indicated in section 2.4.2.

Compute $P_{k.(k)}$ as shown in (2.36).

$Y_{A_k} \leftarrow P_{k.(k)}y$

end for

end

2.4.4 Consecutive Projectors

The calculation of a projection matrix is an $O(N^3)$ operation. Therefore, for large N a faster approach will be to segment the data into smaller windows and perform the calculations in each individual window. However, due to the fact that projection matrices are frame dependent, the projections on consecutive frames might present high discontinuities in the borders. Therefore, in monitoring applications this approach is not feasible.

There are several sources for the discontinuities between consecutive frames, among them we can find:

- In the calculation of projection matrices the data should be centered, differences in the centering between consecutive frames produce differences when the data is projected. This bias effect is mild and can be corrected by overlapping consecutive frames and computing the bias between the projections in the previous and the actual frame.
- Border distortions also introduce an error in the projections. This effect can be reduced by including a future horizon in the basis. Consider the observation matrix A as defined before, and a future horizon A_f of size $p \times n$, the projection matrix can be calculated using the extended matrix $A_E = [A; A_f]$. By projecting the data onto this new subspace and removing the last p data points, the border problem is reduced.

- Consecutive projectors in time might represent the same subspace but the projections can present a 180° change in phase. This problem can be addressed by overlapping consecutive segments and checking the sign of the correlation between the projections in both segments. This correlation should be positive; in case of negative correlation the projection in the new frame should be inverted. It is important to note that the longer the overlap the more reliable the correlation estimator.
- Changes in the dynamics of the system, due to non-stationarities, affect the column space defined by the basis. By the inclusion of a future horizon and an overlapping between consecutive frames these changes are smoothed. However a more elegant way to reduce this effect is by the introduction of a forgetting factor in the calculation of the projection matrices. This forgetting factor penalizes “old” data points and gives priority to the subspace defined by new data.

All the problems mentioned before have been addressed by adaptive signal processing, where a forgetting factor and a sliding approach is used, [47, 125]. To formulate the problem including a forgetting factor between consecutive frames, let's consider the following regression problem:

$$y = Ax + e \quad (2.39)$$

where A represents the regressor matrix and e represent the error. The least squares solution to this problem is obtained by the following optimization problem:

$$\begin{aligned} \min_x \quad & e^T e \\ \text{subject to} \quad & e = y - Ax \end{aligned} \quad (2.40)$$

The solution to (2.40) leads to:

$$\hat{x} = (A^T A)^\dagger A^T y \quad (2.41)$$

where \dagger represents the pseudoinverse and the projection of y onto $C(A)$ is given by $\hat{y} = Py$ with $P = A(A^T A)^\dagger A^T$. This problem can be modified by including a forgetting factor in the errors. This forgetting vector penalizes some errors while rewarding others. In this way the column space defined by the solution of the original regression problem will favor the errors that were rewarded. This new problem is defined as follows:

$$\begin{aligned} \min_x \quad & e^T e \\ \text{subject to} \quad & e = \Gamma(y - Ax) \end{aligned} \tag{2.42}$$

where Γ is a positive-definite diagonal matrix with the weight vector in its diagonal. The solution of this problem is given by:

$$\hat{x} = (A^T \Gamma A)^\dagger A^T \Gamma y \tag{2.43}$$

which leads to $P_\Gamma = A(A^T \Gamma A)^\dagger A^T \Gamma$.

2.4.5 Example

Introduction

In this section subspace projections will be used to decouple the influence of variations in SaO_2 on the TOI. The results provided by subspace projection will be compared with the ones provided by partial coherence.

Assessment of CA is based on the quantification of the strength in the relationship between MABP and CBF. However, measurements of CBF are difficult to obtain continuously in a clinical environment. For this reason surrogate measures are used in practice. Near-infrared Spectroscopy (NIRS) allows to measure the variations in oxy- and deoxy-hemoglobin, ΔHbO_2 and ΔHhb respectively. In addition NIRS also allows to compute the tissue oxygenation index ($\text{TOI} = \text{HbO}_2 / (\text{HbO}_2 + \text{HHb})$), defined as the percentage of oxygen available in the tissue, and the difference in hemoglobin concentration ($\Delta\text{HbD} = \Delta\text{HbO}_2 - \Delta\text{HHb}$).

Measurements of TOI are more appropriate for cerebral autoregulation assessment [219], since they are less affected by movement artefacts. In [235] was shown that, under a constant brain metabolic demand and constant arterial oxygen saturation (SaO_2), changes in TOI and ΔHbD represent changes in CBF. Several studies have been presented in the literature that evaluates the use of NIRS as a promising tool for cerebral hemodynamics monitoring [219, 25, 81]. In premature neonates it can be assumed that the cerebral metabolic demand is more or less constant during the length of the measurements. However, changes in SaO_2 influence directly changes in TOI or ΔHbD . For this reason, only segments with stable SaO_2 are used for CA assessment. This limits the possibilities of NIRS to be used for online CA monitoring. This limitation can

be mitigated by an appropriate preprocessing algorithm, which eliminates the influence of SaO_2 on $\text{TOI}/\Delta\text{HbD}$.

Methods

For this example recordings from 20 infants from the University Hospital Leuven (Belgium) will be used. In all infants the peripheral oxygen saturation (SaO_2) was measured continuously by pulse oximetry, and MABP by an indwelling arterial catheter. With NIRS, TOI was continuously and non-invasively recorded using the NIRO 300 (Hamamatsu). MABP, SaO_2 and NIRS signals were simultaneously measured during the first three days of life and downsampled at 0.333Hz. The total length of the recordings was 6-9 hours. The recordings were segmented in epochs without movement artifacts, where the artifacts were defined as fast and large changes in the signals that are more likely to be produced by movements than by a physiological phenomena.

Using the algorithm 1, the TOI is projected onto the subspace defined by the MABP along the subspace defined by SaO_2 . In this way the influence of SaO_2 is decoupled from the TOI. When needed consecutive projectors were used. To define the basis for the subspace spanned by the regressors, a 5th level DWT using a Daubechies 4 as mother wavelet, together with a delay of 10 samples were employed.

In addition, using partial coherence the influence of SaO_2 was subtracted from the TOI and the MABP, as indicated in section 2.1.3. In addition, the decoupled signals were transformed back in the time domain. Correlations and average coherence values in the frequency range 0-0.1Hz between SaO_2 , TOI and MABP were computed in order to compare both methods.

Results

Figure 2.13 shows a representative segment where variations in SaO_2 are reflected on the TOI and ΔHbD . As can be seen from the figure, the MABP is not influenced by the changes in SaO_2 . Figure 2.14 shows the decoupling of the TOI using the algorithm 1.

Table 2.3 presents the results for the correlation and coherence values between the original and the preprocessed signals. The values are presented as median, 25th and 75th percentile. In general, both preprocessing methods reduce the correlation and coherence values between SaO_2/TOI , while increasing the scores between MABP/TOI. In addition it seems that the reduction in coherence between SaO_2/TOI is better achieved by the partial coherence method. Figure

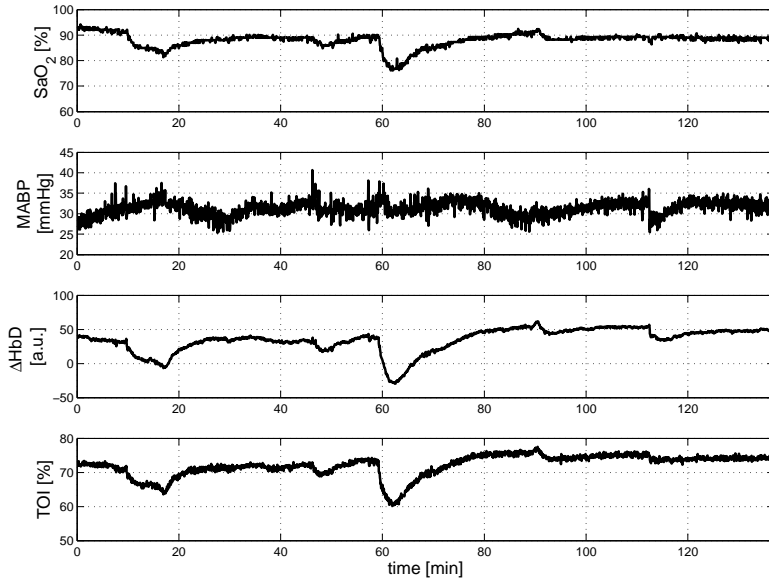


Figure 2.13: Raw measurements. From top to bottom, SaO₂, MABP, Δ HbD in arbitrary units, and TOI. A strong relation between SaO₂ variations and TOI/ Δ HbD is shown.

2.15 shows the residuals obtained from the subspace projections and the partial coherence method. First of all, it can be seen that the residuals from the subspace projections are cleaner than the ones produced by the partial coherence method. Secondly, the residuals from the subspace projections resembles more the variations in MABP than the residuals from partial coherence. These results are expected from the subspace projections, since the TOI is projected onto the subspace spanned by MABP, and by using a DWT the effect of the noise is reduced.

Discussion

Partial coherence and subspace projections were able to decouple the influence of SaO₂ from the TOI. Even though partial coherence achieves larger reduction in the coherence values between TOI and SaO₂ the output obtained from subspace projection is cleaner. This is due to the fact that subspace projection takes into account only the subspace spanned by the regressors, in this case SaO₂

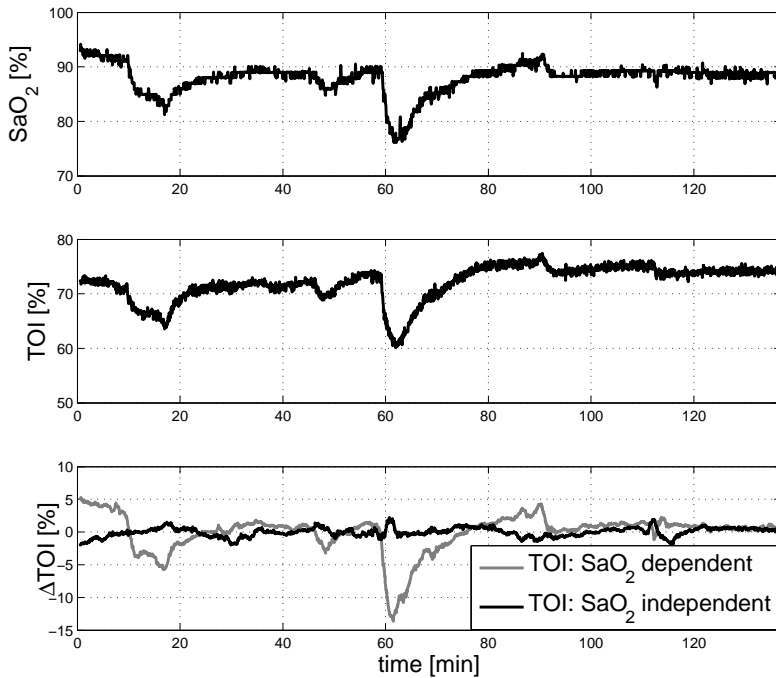


Figure 2.14: TOI projection onto the subspace defined by SaO_2 and the subspace defined by MABP. From top to bottom: SaO_2 variations, TOI variations, and finally the decomposition of the TOI.

		Before Preprocessing	Subspace Projections	Partial Coherence
Correlations	MABP/TOI	0.18 (0.08-0.35)	0.27 (0.15-0.40)	0.23 (0.12-0.42)
	SaO_2 /TOI	0.38 (0.16-0.60)	0.20 (0.06-0.38)	0.20 (0.06-0.42)
Coherence	MABP/TOI	0.16 (0.14-0.18)	0.18 (0.16-0.20)	0.17 (0.15-0.18)
	SaO_2 /TOI	0.18 (0.15-0.23)	0.14 (0.13-0.16)	0.12 (0.10-0.13)

Table 2.3: Correlation and Coherence values between MABP/TOI and SaO_2 /TOI, before and after eliminating the influence of SaO_2 from TOI. Decoupling was performed using subspace projections and partial coherence.

and MABP. This acts as a filtering stage increasing the signal-to-noise ratio of the projections. In addition, by projecting onto the MABP subspace the

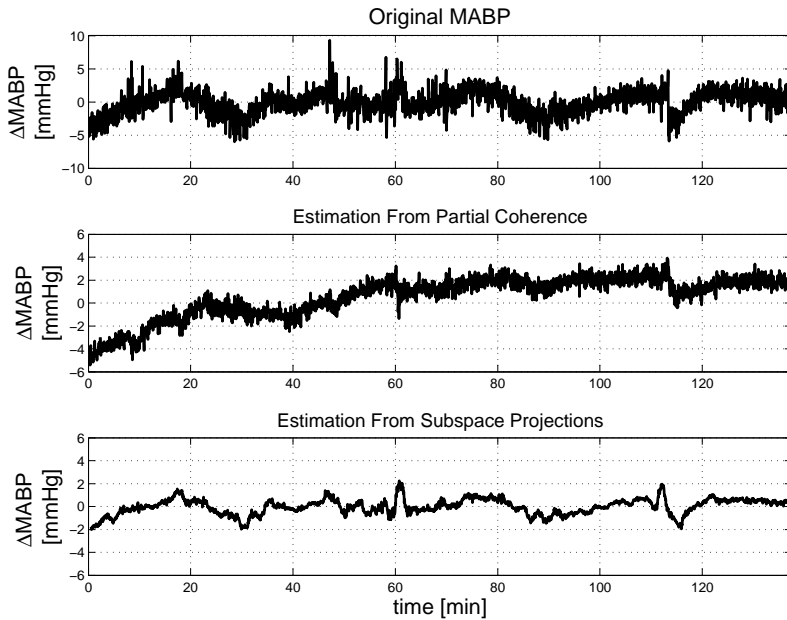


Figure 2.15: Residuals obtained from the partial coherence and the MABP method. From top to bottom, original MABP signal, residuals obtained from the partial coherence method, and residuals obtained from the subspace projections.

relation between MABP/TOI is strengthened. In addition, a larger reduction is observed in the correlation coefficients than in the coherence coefficients, between SaO_2/TOI , after preprocessing using subspace projections, this is due to the fact that the projector matrices tend to reduce the correlation coefficients, and not the coherence. Since an oblique projector is being used, the correlation values are not zero.

In this example we have shown that subspace projection algorithms are appropriate for preprocessing NIRS signals. Subspace projection not only decouples the influence of undesired physiological variations from the NIRS measurements, but it also increases the signal-to-noise ratio of the filtered signals.

Chapter 3

Nonlinear Regression

In this chapter least squares support vector machines (LS-SVM) and kernel principal component regression (KPCR) will be presented as methods to solve a nonlinear regression problem. Since the mechanisms involved in the regulation of cerebral hemodynamics are likely to be nonlinear, a linear regression approach might not be appropriate to address its study. KPCR, as well as other nonlinear regression analysis procedures, produces a mathematical model that explains the relation between the input/output data. However, from the obtained model, the individual contribution of each variable to the model output is unknown. This is of vital importance in cerebral hemodynamics monitoring, since clinicians are interested on the impact of the treatment of some systemic variables on this mechanism. In order to overcome this problem, a methodology in this chapter is proposed. This chapter starts by introducing LS-SVM in section 3.1. In this section, the use of LS-SVM for the preprocessing of NIRS signals is presented. In section 3.2 a brief introduction to principal component regression is given. KPCR is introduced in section 3.3. Section 3.4 presents the computation of projection matrices in a RKHS, as well as the algorithm to decompose the target vector in nonlinear contributions of each regressor variable. In section 3.5 a sparse version of the KPCR model is obtained. Finally, in section 3.6 the proposed algorithms are tested using some toy examples. This section is based on papers 8 and 14 from my publication list.

3.1 Least Squares support Vector Machines in Nonlinear Regression

A Support Vector Machine (SVM) formulation is performed within the context of complex optimization theory, which involves a high computational cost [41]. Least squares SVM (LS-SVM) is a reformulation of the SVM problem where inequality constraints are replaced by equality constraints and a quadratic loss function is taken for the error variables [202]. As a result, the problem simplifies to find the solution of a set of linear equations instead of solving a quadratic programming problem. In order to improve the robustness of the method a weighted version of the original LS-SVM algorithm is used [201]. But, large scale problems that involve a large number of samples can become memory and time consuming. By selecting a training subset from the original data or by the use of several LS-SVMs that later on are combined by means of a committee network of LS-SVMs or a neural network, this problem can be addressed [202]. However, the model complexity is increased. Hence, joint LS-SVM models will be a better approach; but, big discontinuities are presented in the joint borders. By including an extra weight in the cost function the problems with border distortion can be reduced. In this section this new problem will be formulated, starting step by step from the formulation of LS-SVM for function estimation.

3.1.1 LS-SVM for function estimation

Consider a dataset composed of the training data $\{x_i, y_i\}_{i=1}^N$ with $x \in \mathbf{R}^{N \times p}$ a p -dimensional input vector and $y \in \mathbf{R}^{N \times 1}$ the measured variable. Now consider the following regression model:

$$y = \omega^T \varphi(x) + b \quad (3.1)$$

where ω is an unknown vector parameter, $\varphi(x) : \mathbf{R}^{N \times p} \rightarrow \mathbf{R}^{N \times d}$ represents a linear or nonlinear mapping of the variable x in a feature space of dimension d . In the context of LS-SVM the regression problem in (3.1) can be solved by the following optimization problem:

$$\begin{aligned} \min_{\omega, b, e} \quad & J_p(\omega, e) = \frac{1}{2} \omega^T \omega + \gamma \frac{1}{2} \sum_{i=1}^N e_i^2 \\ \text{subject to } & y_i = \omega^T \varphi(x_i) + b + e_i \end{aligned} \quad (3.2)$$

where e is the error estimation and γ is the regularization constant. By constructing the Lagrangian from equation (3.1):

$$\mathfrak{L}(\omega, b, e, \alpha) = J_p(\omega, e) - \sum_{i=1}^N \alpha_i (\omega^T \varphi(x_i) + b + e_i - y_i) \quad (3.3)$$

where α are the Lagrange multipliers. By setting the following conditions for optimality:

$$\begin{aligned} \frac{\partial \mathfrak{L}}{\partial \omega} = 0 &\rightarrow \omega = \sum_{i=1}^N \alpha_i \varphi(x_i) \\ \frac{\partial \mathfrak{L}}{\partial b} = 0 &\rightarrow \sum_{i=1}^N \alpha_i = 0 \\ \frac{\partial \mathfrak{L}}{\partial e} = 0 &\rightarrow \alpha_i = \gamma e_i \\ \frac{\partial \mathfrak{L}}{\partial \alpha} = 0 &\rightarrow \omega^T \varphi(x_i) + b + e_i - y_i = 0 \end{aligned} \quad (3.4)$$

and eliminating e and ω from the equation (3.3) the following set of equations is obtained:

$$\left[\begin{array}{c|c} 0 & 1_v^T \\ \hline 1_v & \Omega + I/\gamma \end{array} \right] \left[\begin{array}{c} b \\ \alpha \end{array} \right] = \left[\begin{array}{c} 0 \\ y \end{array} \right] \quad (3.5)$$

where $1_v = [1, \dots, 1]$, $\Omega_{ij} = \varphi^T(x_i) \varphi(x_j) = K(x_i, x_j)$ is the kernel matrix. By replacing (3.4) in (3.1) the following relation is obtained:

$$y(x) = \sum_{i=1}^N \alpha_i K(x, x_i) + b \quad (3.6)$$

3.1.2 Robust LS-SVM

Equation (3.6) represents the solution to the nonlinear regression problem presented in (3.1). Since outliers and noise with non-Gaussian distribution affect the performance of this solution, a weighted version of (3.6) has been proposed. The weighted LS-SVM algorithm first computes an unweighted LS-SVM as in (3.6) and then calculates the errors e . The distribution of e is estimated in order to detect outliers. Once the outliers have been detected, a weight vector v is defined as follows [181]:

$$v_i = \begin{cases} 1 & \text{if } |e_i/\hat{s}| \leq c_1 \\ \frac{c_2 - |e_i/\hat{s}|}{c_2 - c_1} & \text{if } c_1 < |e_i/\hat{s}| \leq c_2 \\ 10^{-4} & \text{otherwise} \end{cases} \quad (3.7)$$

with c_1 and c_2 equal to 2.5 and 3, respectively, and \hat{s} equal to the standard deviation of the errors e . The vector v is used to weight the error vector in a new LS-SVM regression problem. The new LS-SVM regression is given by:

$$\begin{aligned} \min_{\omega, b, e} J_p(\omega, e) &= \frac{1}{2}\omega^T\omega + \gamma\frac{1}{2}\sum_{i=1}^N v_i e_i^2 \\ \text{subject to } y_i &= \omega^T\varphi(x_i) + b + e_i \end{aligned} \quad (3.8)$$

which leads to the following solution:

$$\left[\begin{array}{c|c} 0 & 1_v^T \\ \hline 1_v & \mathbf{\Omega} + V_\gamma \end{array} \right] \left[\begin{array}{c} b \\ \alpha \end{array} \right] = \left[\begin{array}{c} 0 \\ y \end{array} \right] \quad (3.9)$$

with $V_\gamma = [\frac{1}{\gamma v_1}, \dots, \frac{1}{\gamma v_N}]$.

Equation (3.9) represents a system of $N \times N$ equations. Hence, there exists computational restriction for the number of data points used. Long signal recordings cannot be processed directly and should be processed by dividing the data in consecutive segments. Each segment can be used to train a LS-SVM and by combining all the resulting models, by means of a committee or a neural network, the regression model for the complete signal can be found. But this increases the computational cost to find the regression model. A faster approach is to join all estimated functions from consecutive segments. However, the lack of share information between consecutive LS-SVM models will produce high discontinuities in the borders when joining the models output. In order to address this problem, an extra weight vector is used. This leads to the following optimization problem:

$$\begin{aligned} \min_{\omega, b, e} J_p(\omega, e) &= \frac{1}{2}\omega^T\omega + \gamma\frac{1}{2}\sum_{i=1}^N \frac{v_i}{\mu_i} e_i^2 \\ \text{subject to } y_i &= \omega^T\varphi(x_i) + b + e_i \end{aligned} \quad (3.10)$$

which leads to the following solution:

$$\left[\begin{array}{c|c} 0 & 1_v^T \\ \hline 1_v & \mathbf{\Omega} + M_\gamma \end{array} \right] \left[\begin{array}{c} b \\ \alpha \end{array} \right] = \left[\begin{array}{c} 0 \\ y \end{array} \right] \quad (3.11)$$

with $M_\gamma = [\frac{\mu_1}{\gamma v_1}, \dots, \frac{\mu_N}{\gamma v_N}]$.

The new weight vector M should be designed in order to give priority to the borders, in such a way that consecutive segments will produce similar output at the borders. The vector M can also be designed to give priority to other segments free of noise in order to reduce the influence of noisy samples in the regression model.

3.1.3 Weighted LS-SVM for signal preprocessing

A weighted LS-SVM can be used to preprocess segments of a signal contaminated by artifacts. By identifying the location of an artifact, a LS-SVM can be trained with data points around it. Once the model has been obtained, it can be used to estimate the value of the data points during the artifact. However, in order to guarantee that the LS-SVM model converge to a proper solution, the duration of the artifact should small enough, compared with the data points used for training. In addition, since the biomedical signals are non-stationary and the LS-SVM model is localized around the artifact, when concatenating the process segments with the clean data points, border distortion is likely to occur. This is avoid by a proper selection of the weight vector v as presented before.

In this section a weighted LS-SVM model will be used in order to preprocess continuous measurements of MABP. For this example, the weight vector v has been selected as a Blackman window with its lowest value set to 10^{-4} . This value was selected in order to avoid numerical problems in (3.11). A segment of the signal contaminated with artifacts was used, from which 2200 data points without artifact contamination were used for the training of the model. The model was trained using 10-fold cross-validation. Results from the preprocessing the signal around an artifact are shown in figure 3.1. In this figure the results from the proposed weighted LS-SVM regression are compared with the results from a normal robust LS-SVM model presented in (3.9). The segment of the signal displayed in the figure corresponds to the first 500 samples of the regression model output. It can be seen that both models perform similarly; however, in this segment the proposed model performs slightly better than the normal joint LS-SVM model. This behavior is expected, since the weight vector v prioritize the regression at the borders. In addition, figure 3.2 shows the performance of both regression models when concatenating the output of 2 continuous LS-SVM models. In this figure it can be seen that the proposed model reduces the border distortion, while the robust LS-SVM model produces high discontinuities in the joint point of the outputs for the 2 consecutive models.

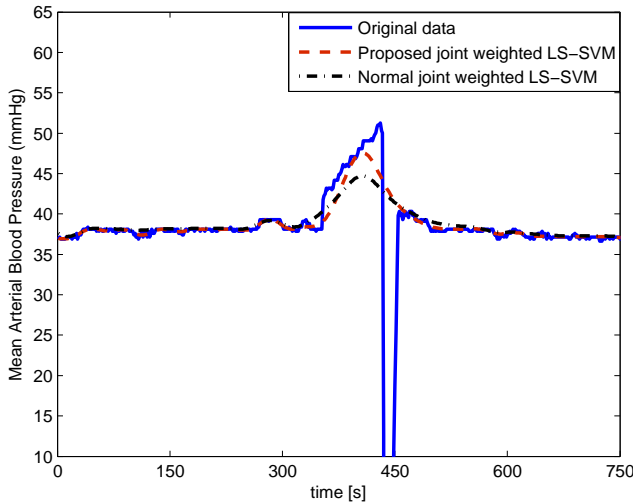


Figure 3.1: Comparison of the outputs for the LS-SVM regression models. In blue the original signal, in black the output of a normal robust LS-SVM model. In red the output of the LS-SVM model with the new weight vector. For both models $\gamma = 100.5$ and $\sigma^2 = 438$

3.2 Principal Component Regression

In a linear regression problem of the form $y = A\omega + b$, where $A \in R^{N \times d}$ and $\omega \in R^d$, the regression coefficients can be found using least squares as follows: $\omega = (A^T A)^{-1} A^T y$. However, in case that A is nearly ill-conditioned the regression coefficients might inflate, thereby strongly, affecting the accuracy of the regression. One way to solve this problem is to use a linear transformation that mitigates the effect of multicollinearity in the regressor matrix, i.e by replacing A with an orthogonal basis that describes the same column space.

Principal component analysis (PCA) is a methodology that allows to perform an orthogonal transformation on a matrix A . PCA changes the coordinate system of the data in matrix A to a new coordinate system with orthogonal basis, in which the basis vectors are organized according to the direction of the maximum variance. PCA is obtained by the eigenvectors of the covariance matrix $A^T A$ [98]. Consider the singular value decomposition (SVD) of A , $A = U\Lambda V^T$, where U and V are orthogonal matrices and Λ is a diagonal matrix. The eigenvalues of $A^T A$ are defined by V . By defining a transformed matrix $T = AV = U\Lambda$, T being orthogonal, an equivalent regression problem can be formulated:

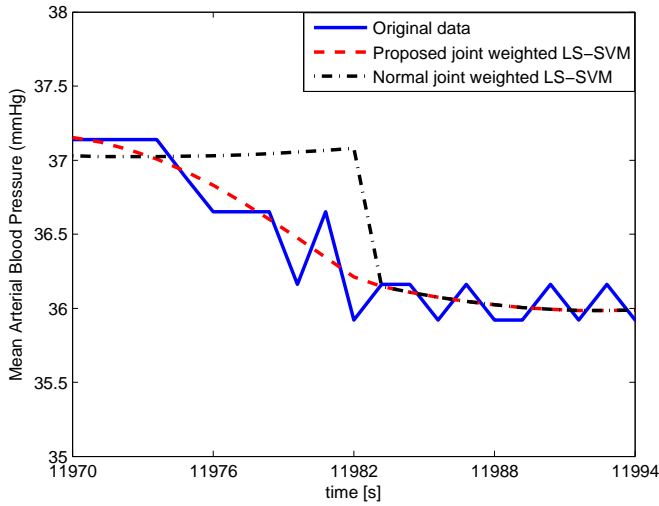


Figure 3.2: Discontinuity in the border due to the concatenation of consecutive LS-SVM regression models. In blue the original signal, in black the output of a normal robust LS-SVM model and in red the output of a robust LS-SVM model with an extra weight.

$$y = T\alpha + b \tag{3.12}$$

where α represents a new set of regression coefficients, which are related to the original regression coefficients as follows: $\omega = V^T\alpha$. The new regression problem in (3.12) can be solved using least squares as follows: $\alpha = (T^T T)^{-1} T^T y = \Lambda^{-1} U^T y$. This is known as principal component regression (PCR). A more exhaustive introduction to PCR can be found in [127].

3.3 Kernel Principal Component Regression

Kernel PCR is a nonlinear version of PCR where the nonlinearity is introduced by the use of kernel functions [179]. Consider now a nonlinear regression model in the feature space:

$$y = \Phi\omega + \varepsilon \tag{3.13}$$

where y is a vector of N observations of size $(N \times 1)$, $\Phi = [\varphi(\mathbf{x}_1) \dots \varphi(\mathbf{x}_N)]^T$ is a $(N \times d)$ regressor matrix with $\varphi(\mathbf{x}_i)$ being the nonlinear transformation of $\mathbf{x}_i = [s_{i,1}, s_{i,2}, \dots, s_{i,d}]$, $\omega \in \mathbf{R}^d$ is the unknown regressor coefficient vector, and ε is the error of the estimation. Consider the projection matrix P_Φ as the projection matrix onto $C(\Phi)$, and ε is the error. The least squares solution of (3.13) is given by:

$$\hat{\omega} = (\Phi^T \Phi)^\dagger \Phi^T y \quad (3.14)$$

However, since the nonlinear transformation is unknown this solution cannot be obtained.

As in PCR, KPCR solves (3.13) by introducing a change of variable. The model is then transformed to:

$$y = B\xi + \varepsilon \quad (3.15)$$

where $B = \Phi V$ is a matrix of transformed regressors, with V equal to the eigenvectors matrix of $\Phi^T \Phi$. Therefore, B can be interpreted as the projection of the regressors Φ onto its principal components. However, since the matrix Φ is unknown, its principal components cannot be estimated. But, this projection can be approximated by means of kernel PCA [138, 188], where the SVD of the kernel matrix, $\Omega = \Phi \Phi^T = U \Lambda \Lambda^T U^T$, is used to approximate V .

The solution of (3.15) is given by:

$$\hat{\xi} = \Lambda^{-1} B^T y \quad (3.16)$$

The solution given in (3.16) is equivalent to the solution of (3.13). If all the projections in the regression are used, $\hat{\xi}$ corresponds to the least squares solution of the system in the reproducing kernel Hilbert space (RKHS). However, since small eigenvalues increase the variance of the estimation they are removed from the final solution; this introduces a bias in the model but reduces its variance. By taking only p components the KPCR regression model is reduced to:

$$\hat{y} = \sum_{i=1}^N c_i \Omega(x_i, x) + b \quad (3.17)$$

with $\{c_i = \sum_{k=1}^p \hat{\xi}_k u_i^k\}_{i=1}^N$, where u_i^k represents the k^{th} element of the i^{th} eigenvector from the kernel matrix Ω . This solution can be written as:

$$\hat{y}(x_i) = \Omega(x_i, x)U\hat{\xi} + b \tag{3.18}$$

3.4 Projection Matrices in a RKHS

A Reproducing Kernel Hilbert Space (RKHS) is a Hilbert space that is defined by reproducing kernels [46]. Which means that the dot products of 2 vectors in the RKHS can be obtained by means of evaluations of a kernel function. Since a RKHS is a dot product space that preserves the metrics used in a Euclidean space, the concept of projection matrices can be extended to this space. However, in order to define a projection in a subspace of the RKHS a basis for this subspace is needed. In the regression problem presented in (3.13) this basis is given by the columns of the regressor matrix Φ . Consider the singular value decomposition of Φ :

$$\Phi = U\Lambda V^T \tag{3.19}$$

using (3.19) and replacing it in the computation of an orthogonal projection, then the following relation is obtained:

$$P_\Phi = UU^T \tag{3.20}$$

Consider now the kernel matrix and its singular value decomposition:

$$\Omega = \Phi\Phi^T = U\Lambda\Lambda^T U^T \tag{3.21}$$

The eigenvectors of the kernel matrix span $C(\Phi)$, and the projection matrix can be calculated using the kernel matrix as follows:

$$P_\Phi = \Omega(\Omega^T\Omega)^\dagger\Omega^T = UU^T \tag{3.22}$$

However, since the dimension of the nonlinear transformation might be bigger than the number of observations ($d > N$), P_Φ represents an approximate N -dimensional subspace of $C(\Phi)$. In case that the kernel matrix is rank deficient with rank p , only the first p left singular vectors are needed to reproduce the projection matrix. The use of the pseudoinverse can be avoided by calculating $P_\Phi = U_p U_p^T$ where U_p are the first p eigenvectors with largest eigenvalues of the kernel matrix, with $p = \text{rank}(\Omega)$. Other equivalent derivations for the projection matrices in a RKHS can be found in [124].

3.4.1 Projections onto the regressor subspaces

In the last section it was shown that a projection matrix onto $C(\Phi)$ can be computed using the kernel matrix Ω . In this section the focus will be given to the calculation of a projection matrix onto the column space spanned by each regressor. This projection will represent the nonlinear transformation of the respective regressor variable. In order to decompose $C(\Phi)$ into d subspaces, each one corresponding to the subspace spanned by the nonlinear transformation of the regressor \mathbf{s}_k for $\{k = 1, \dots, d\}$, a basis for that nonlinear transformation is needed.

Consider $\mathbf{x}_i = [s_{i,1}, s_{i,2}, \dots, s_{i,d}]$ with $s_{i,j} \in R$, and let y be decomposed as follows:

$$y = \sum_{k=1}^d \omega_k f(\mathbf{s}_k) + \varepsilon \quad (3.23)$$

where $f(\mathbf{s}_k)$ represents the nonlinear contribution of the regressor $\mathbf{s}_k \in \mathbf{R}^N$ in the observed signal y , and ε the error. From this definition $C(\Phi) = S_1 \oplus S_2 \oplus \dots \oplus S_M$, where S_k represents the subspace spanned by the nonlinear transformation of the regressor \mathbf{s}_k .

In order to find a suitable representation for the column space of $f(\mathbf{s}_k)$ the influence of the other variables should be eliminated. This can be obtained by evaluating the kernel function in a new set of regressors, where the “unwanted” regressors are set to 0 as follows:

$$K_k = K(\mathbf{x}_i, \hat{\mathbf{x}}_{jk}) \quad (3.24)$$

where $\mathbf{x}_i = [s_{i,1}, \dots, s_{i,d}]$, and $\hat{\mathbf{x}}_{jk} = [0, \dots, s_{jk}, \dots, 0]$. By using (3.24) to represent the column space of $f(\mathbf{s}_k)$, the oblique projection matrix onto this subspace can be calculated as:

$$\begin{aligned}
 P_{k.(k)} &= \mathbf{\Omega}_k(\mathbf{\Omega}_k^T Q_{(k)} \mathbf{\Omega}_K)^\dagger \mathbf{\Omega}_k^T Q_{(k)} \\
 &+ Z[I_n - (Q_{(k)} \mathbf{\Omega}_k)(\mathbf{\Omega}_k^T Q_{(k)} \mathbf{\Omega}_k)^\dagger \mathbf{\Omega}_k^T] Q_{(k)}
 \end{aligned}
 \tag{3.25}$$

where $\mathbf{\Omega}_k$ represents the kernel matrix evaluated in the set of variables \mathbf{x}_{j_k} for $\{j = 1, \dots, N\}$, and $Q_{(k)} = (I_N - P_{(k)})$; where I_N is a $N \times N$ identity matrix and $P_{(k)}$ is the orthogonal projector onto the subspace spanned by the regressor variables with $\mathbf{s}_k = 0$. To calculate $P_{(k)}$ the kernel function is evaluated as follows:

$$K_{(k)} = K(\mathbf{x}_i, \hat{\mathbf{x}}_{j(k)})
 \tag{3.26}$$

where $\hat{\mathbf{x}}_{j(k)} = [s_{j,1}, \dots, s_{j,k-1}, 0, s_{j,k+1}, \dots, s_{j,d}]$, from which:

$$P_{(k)} = \mathbf{\Omega}_{(k)}(\mathbf{\Omega}_{(k)}^T \mathbf{\Omega}_{(K)})^\dagger \mathbf{\Omega}_{(k)}^T
 \tag{3.27}$$

This decomposition can be performed for every regressor. The algorithm is summarized below.

The algorithm 2 can be extended in order to find the influence of interactions between the regressor variables on y . In this context, the target subspace will be defined by the set of regressor variables of interest. The kernel function is evaluated in a new set of variables, where only the regressors of interest are used, the rest are set to 0. The projection onto this subspace is computed as shown in algorithm 2. However, when projecting the signal y onto this subspace the influence of each regressor, independently, should be subtracted; indeed, we are interested in the intersection of the subspaces and not the complete subspace spanned by those regressions. In the case that there is no interactions between the selected regressor variables in the target signal the intersection of the subspaces will be 0.

Algorithm 2 Decomposition of y as a linear combination of $f(\mathbf{s}_k)$

input: $\mathbf{X} = [\mathbf{s}_1, \dots, \mathbf{s}_d]$ with $\mathbf{X} \in R^{N \times d}$, $y \in R^N$
output: $\mathbf{Y} = [\hat{y}(\mathbf{s}_1), \dots, \hat{y}(\mathbf{s}_d)]$ with $Y \in R^{N \times d}$
begin
var $k := 1, d$
for all k

compute the kernel matrices $\mathbf{\Omega}_k$ and $\mathbf{\Omega}_{(k)}$
 $P_{(k)} \leftarrow \mathbf{\Omega}_{(k)} (\mathbf{\Omega}_{(k)}^T \mathbf{\Omega}_{(k)})^\dagger \mathbf{\Omega}_{(k)}^T$
 $Q_{(k)} \leftarrow I_N - P_{(k)}$

compute $P_{k.(k)}$ as shown in (3.25)

 $\mathbf{Y}_k \leftarrow P_{k.(k)} y$
end for
end

3.5 Sparsity in the KPCR Model

In KPCR the number of components used in the decomposition is normally selected based on a cross-validation procedure [179, 180, 186]. Moreover, the model should use the complete set of training samples in order to produce the model output [90]. A sparse model for KPCR can be obtained by exploiting the properties of the projection matrix P_Φ . The trace of P_Φ indicates the dimensions of $C(\Phi)$; therefore, if $tr(P_\Phi = p)$ only the first p columns in U are needed. From now on $U_p \in R^{N \times p}$ represents a matrix with the first p columns of U . This indicates that only p data points are needed to describe this subspace. However, the p selected data points should be independent in the RKHS. This means that the nonlinear transformation, $\phi(x_k)$ for $\{k = 1, \dots, p\}$, should produce independent vectors in the RKHS.

The proposed algorithm presented in this section selects the data points that are closer to $C(\Phi)$, which is defined by the hyperplane represented by the projection matrix P_Φ . The algorithm is based on the following least squares problem, $\mathbf{\Omega} = U_p A$, where $\mathbf{\Omega} \in R^{N \times N}$ represents the kernel matrix, and $A \in R^{p \times N}$. After solving the least squares problem the solution \hat{A} can be used to compute the error matrix $E = \mathbf{\Omega} - U_p \hat{A}$, from which the mean of the absolute values of the error per column is computed as $e = \frac{1}{N} \sum_{i=1}^N |E(:, i)|$, where $E(:, i)$ represent the i^{th} column in the matrix E . The first p data points that correspond to the lowest e values are selected as the reduced set to be used in the KPCR model. The algorithm is detailed in the algorithm 3.

Once the reduced set of vectors X_r is found, the regression model in (3.13) can

Algorithm 3 Selection of the reduced set of data points for a sparse KPCR regression.

input: $X = [x_1, \dots, x_N]^T$ with $X \in R^{N \times d}$, Kernel matrix Ω
output: $X_r \in R^{p \times d}$

begin

compute the orthogonal projection matrix using Ω

$p \leftarrow \text{rank}(P_\Phi)$

compute the SVD from Ω

solve $\Omega = U_p A$

$E \leftarrow \Omega - U_p \hat{A}$

$e(j) = \sum_{i=1}^N |E(j, i)|$

$r \leftarrow$ indices for the first p lowest e

$X_r \leftarrow X(r, :)$

end

be solved by using only the X_r data points, this leads to the solution vector $\hat{\xi}_p \in R^{(p)}$ and to the following reduced KPCR model:

$$\hat{y}(x_i) = K(x_i, X_r) U_{p_r} \hat{\xi}_p \quad (3.28)$$

where X_r represents the reduced set of vectors used in the model. U_{p_r} are the eigenvectors of the Kernel matrix formed with the reduced set X_r , and $\hat{\xi}_p$ is the solution vector found using only the reduced set during the training. This new model can also be used in order to find the nonlinear contribution of each regressor variable.

3.5.1 RBF Kernel and the trace of P_Φ

In machine learning the main goal is to learn the structure of a model for regression, clustering or classification using the provided data. When using kernel methods, the model output is normally expressed in terms of evaluation of the kernel function. However, there exist different types of kernels, and some of them depend on other parameters that need to be found in order to obtain a complete description for the model. The process of finding these parameters will be called *tuning* from here on. One of the most popular kernel functions in machine learning is the radial basis function (RBF) kernel given by the following equation:

$$K(x, y) = \exp\left(-\frac{|x - y|_2^2}{\sigma^2}\right) \quad (3.29)$$

where x and y represent 2 vectors, and σ is the kernel bandwidth. In this particular case, using the RBF kernel, the hyperparameter σ needs to be tuned.

The tuning, in supervised learning, is normally performed using k -fold cross-validation. During the tuning a set of values for the kernel hyperparameters is provided and the performance of the model is evaluated for different combinations of hyperparameters. The set of hyperparameters that performed the best is selected and is used in the final model. In k -fold cross-validation the available data is divided in two different sets: training, and test set. During the training phase, the training set is used to find the model parameters, while the test set is used to evaluate the generalization properties of the model. When using k -fold cross-validation the training set is divided in k different subsets. From these k subsets one is used for validation while the other $k - 1$ subsets are used for training. This procedure is repeated k times, each time using a different subset for validation. At each step the error between the target output and the estimated output in the validation subset is computed, at the end of the k rounds the root mean squared average of the error is computed and assigned to the particular combination of hyperparameters.

The validation set during the training phase is used to avoid overfitting. Overfitting occurs when the model is able to closely reproduce the output in the training set but is not able to produce an accurate response to new data. When using a RBF kernel, overfitting occurs when the σ is too small. This leads to kernel matrices that are close to diagonal matrices. However, if the σ is too large the kernel matrix will be close to a matrix with entries close to 1 and the model will behave poorly, leading to underfitting. Therefore, a proper selection of the kernel hyperparameters is crucial for the model performance.

Interestingly enough, the effect of overfitting and underfitting can be seen in the trace of the projection matrix P_Φ . Small σ values produce kernel matrices with a high rank, leading to a large trace in P_Φ , while large σ values lead to lower trace values. When using the RBF kernel, the nonlinear transformation involved maps the input data into a highly, possibly infinite, dimensional RKHS. However, due to the finite size of training data the projection matrix P_Φ can only represent a N dimensional approximation of this space, with N equal to the number of observations, i.e data points. Assume that for a given σ_u value the trace $tr(P_\Phi) = N$, this suggests that the model using σ_u needs at least N dimensions in order to map the input data in the RKHS. This may represent overfitting. Conversely, if using σ_l results into $tr(P_\Phi) = 1$ this suggests that the data is mapped onto a line, or a point, in the RKHS, and may indicate

underfitting. Therefore, optimal values for σ are likely to be in the interval $\sigma_l < \sigma_o < \sigma_u$. This criterion may be used in combination with other measures such as mutual information and entropy, in order to avoid the search grid in the cross-validation procedure and reduce the computing time during training. In addition this concept is related to sparsity in the KPCR presented in the previous section, where only p data points are needed in order to describe P_{Φ} in the RKHS.

3.6 Toy Examples

In this section we will present the results obtained with the KPCR model for two different toy examples. In the first toy example the KPCR model will be used in order to approximate a sinc function from noisy entries. This model will be used in order to illustrate the concepts about sparsity and the relation between the $tr(P_{\Phi})$ and overfitting. In the second toy example, an artificial nonlinear mixture of three sources will be used. This model will be approximated using KPCR. From the resulting model the contribution of each source and their interactions will be estimated. The impact on the estimation by using a sparse model will be evaluated. It is important to take into account that in the figures shown in this section, the data have been centered since the KPCR model and the computation of the projection matrices in the RKHS require centered matrices.

3.6.1 Noisy sinc function

A sinc signal was generated using $N = 300$ data points equally sampled in the interval $\{-5, 5\}$. The target function was calculated using the sinc function of Matlab. Gaussian noise, $N(0, 0.1)$, was added to the signal. The results of the output for the KPCR model are shown in figure 3.3. It can be seen that the output of the model using the complete set of training data points resembles quite closely the dynamics of the original sinc function. Moreover, using the procedure presented in algorithm 3, 16 datapoints were selected to create a sparse model. The data points and the output for this sparse model are also shown in figure 3.3. The dynamics for the sparse model is close to the dynamics of the complete KPCR. However, figure 3.3 presents the results for the training dataset, which are shown just to illustrate the performance for the sparse model using the training data. In order to test the real performance for the KPCR model, 200 new entries were generated from a Gaussian distribution with a standard deviation of 1. These new entries were used as the regressor variables and their output using the KPCR model previously tuned was computed. Figure

3.4 presents the results for the complete and the sparse KPCR models. It can be seen that both models are able to retrieve a fair approximation to the sinc signal, and the sparse model using only 16 data points is able to perform similarly to the complete KPCR.

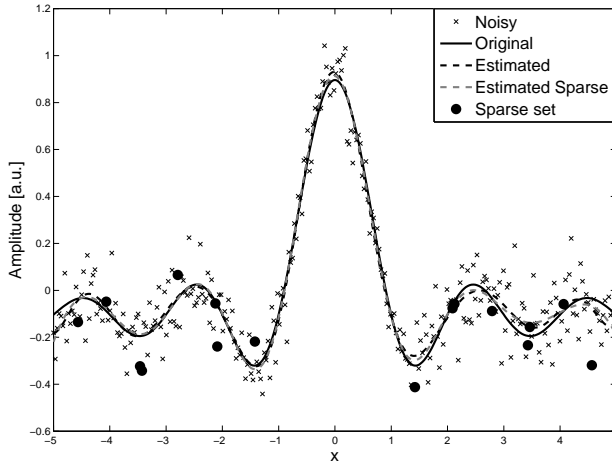


Figure 3.3: Output of the KPCR model for the estimation of a sinc signal. The crosses represent the noisy data points used to train the model. The solid black line represents the original sinc signal without noise. The dashed black line represents the output of the KPCR model. The dashed gray line represents the output obtained with an sparse model of 12 data points. The reduced dataset used in the sparse model is represented by the black circles. When training, the tuning parameter for the RBF kernel $\sigma^2 = 1.7310$ was obtained.

In addition, in figure 3.5 the relation between the trace of the projection matrix P_{Φ} and the bandwidth σ^2 is shown. It can be seen that for small σ^2 values the trace of P_{Φ} is large, indicating that the data is mapped on a larger subspace in the RKHS. However, as σ^2 increases the trace of P_{Φ} is reduced and smoothly converges towards 1, this indicates that the data is now mapped in a smaller subspace in the RKHS.

Finally, the performance of KPCR was also tested by including Gaussian noise, $N(0, 0.1)$, in the regressor variables. Figure 3.6 shows the results from the KPCR regression using the complete and the sparse set. Comparing the results from figures 3.3 and 3.6, it can be seen that the performance of the regression is highly affected by the quality of the regressor variables. It is also observed

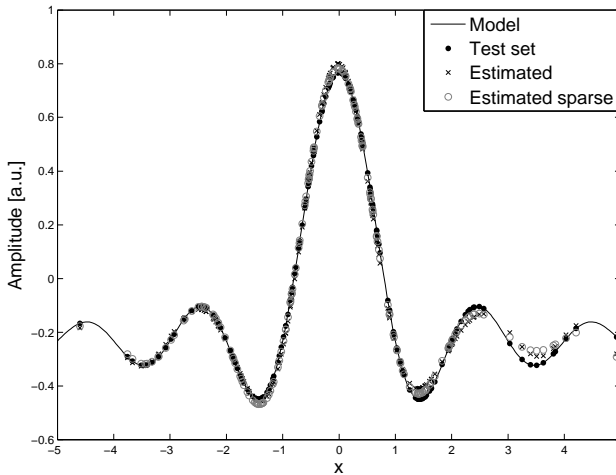


Figure 3.4: Output for a test set composed of 200 data points drawn from a $N(0, 1)$. The original sinc function is shown in the solid line. The data points used are shown as dots. It is important to take into account that the data used as input for the KPCR model are only the x value of the data points shown in the figure. The crosses represent the output of the complete KPCR model, while the circles represent the output of the sparse KPCR model using only 16 datapoints.

that the performance of the sparse model is worse by the inclusion of noise in the regressor variables. Further research in this direction is needed.

3.6.2 Artificial dataset

In this example a signal y of 400 points was generated. The signal y is calculated from two independent variables $\{s_1, s_2\}$. The variables s_1 and s_2 were defined in the interval $\{-3, 3\}$. A linear grid of 20×20 values, in the interval $\{-3, 3\}$, was created in order to excite the model in the complete range of $\{s_1, s_2\}$. Therefore, s_1 and s_2 have in total 400 points and 20 different values in the interval $\{-3, 3\}$. In addition, by creating this grid it is guaranteed that for a fixed s_1 , the output y is computed for all 20 different values in s_2 . The nonlinear model imposed in the output is the following:

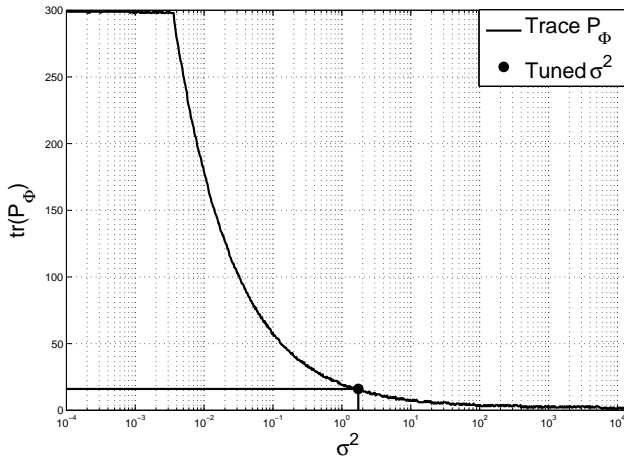


Figure 3.5: Relation between the trace of the projection matrix P_Φ and the bandwidth of the kernel function σ^2 . The black dot represents the tuned value for the example shown in this subsection.

$$y = \sqrt{s_1 + 3} + \frac{1}{1 + e^{-2s_1s_2}} + \eta \quad (3.30)$$

where η represents a Gaussian noise $N(0, 0.1)$. Results from the original KPCR model and the sparse KPCR model are compared.

In figure 3.7 the results from the KPCR complete and sparse model are shown. As in the previous example the results from the complete and the sparse model are closely related.

In addition, the output of the model has been decomposed using the procedure presented in algorithm 2. The algorithm allows to decompose the output in the direct influence of each regressor and the higher order interactions. In the figures 3.8 and 3.9 this decomposition is shown. First, the left plot in figure 3.8 shows the projection of the target vector in the subspace defined by the nonlinear transformation $\sqrt{s_1 + 3}$. The crosses represent the target function and the circles represent the projection of the input data. It can be seen that the model is able to retrieve the nonlinear contribution of the regressor variable s_1 on the model output. The right plot in figure 3.8 shows the projection of the target vector on the subspace defined by the second order interaction between s_1 and s_2 . In this plot, as in the left one, the crosses represent the target function while the circles represent the projected data. It can be seen that the projections

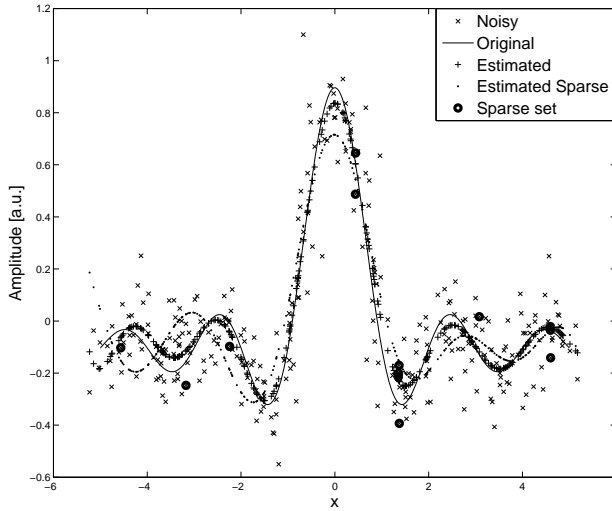


Figure 3.6: Output for KPRC model using regressors with a Gaussian noise $N(0, 0.1)$, the original data is presented with the 'x' symbols, the target sinc function is shown in the solid line. The '+' symbols represent the output of the complete KPCR model, while the dots represent the output of the sparse KPCR model. The data points for the Sparse set are shown as black circles.

are able to represent the nonlinear contribution due to the interaction between these 2 variables. However, in the borders the projections start to diverge, this can be due to the fact that even though the input variables, s_1 and s_2 , are equally spaced in the interval of interest, there are not enough data points at the extreme values for $s_1 s_2$. Increasing the resolution in these intervals will produce a more accurate representation for the projection matrices at these points.

Figure 3.9 shows the projection of the output on the subspace defined by the nonlinear transformation of the variable s_2 . Since there is no direct individual influence of the variable s_2 on the output, this projection is expected to be zero. In the figure it is shown that these projections are not zero, but they are small compared with the contributions from the other variables. The residuals are likely to be related to the input noise, since it is normally spread over the complete RKHS space defined by the nonlinear transformation.

Finally, the relation between the trace of the projection matrix and the kernel parameter σ^2 is depicted in figure 3.10. As in the example discussed previously

the trace of P_{Φ} slowly converges towards 1 with increasing values of σ^2 .

3.7 Conclusion

In this chapter a methodology for a nonlinear regression using kernel principal component regression (KPCR) has been presented. This methodology has been further extended using projection matrices in order to identify the nonlinear contribution of each individual regressor and/or their higher order interactions in the model output. Furthermore, a sparse KPCR model has been proposed. The methodology has been validated by examples from artificially generated data. In both cases the nonlinear relations between the regressors and the output was retrieved satisfactorily.

The methodology proposed in this chapter has a high clinical impact in the context of biomedical signal processing. This methodology allows to identify the nonlinear influence of some physiological variables on the variations of another physiological parameter, which provides a tool for the evaluation of the effects of treatment. In the context of cerebral hemodynamics monitoring, this methodology can be used to assess the individual, or joint, influence of systemic variables on the brain hemodynamics. By assessing this influence potentially pathological changes can be detected.

However, the model presented in this chapter only takes into account static nonlinear relationships between the target signal and the regressors. In order to be able to include dynamic information a model structure should be imposed. In linear system identification, specifically in subspace system identification, the system is described by the interactions between the input-output subspaces defined by the past and "future" data points. These subspaces are described by a matrix formed by a hankelization of the input-output observations. In this chapter we have shown how the subspaces in a RKHS can be defined using kernel evaluations. Therefore, this concept can be used to extend the linear subspace system identification to a nonlinear framework, where a nonlinear transformation is applied to the input-output data and a linear subspace system identification is applied in the RKHS. Further research on how this methodology can be adapted to nonlinear subspace system identification in the RKHS is needed.

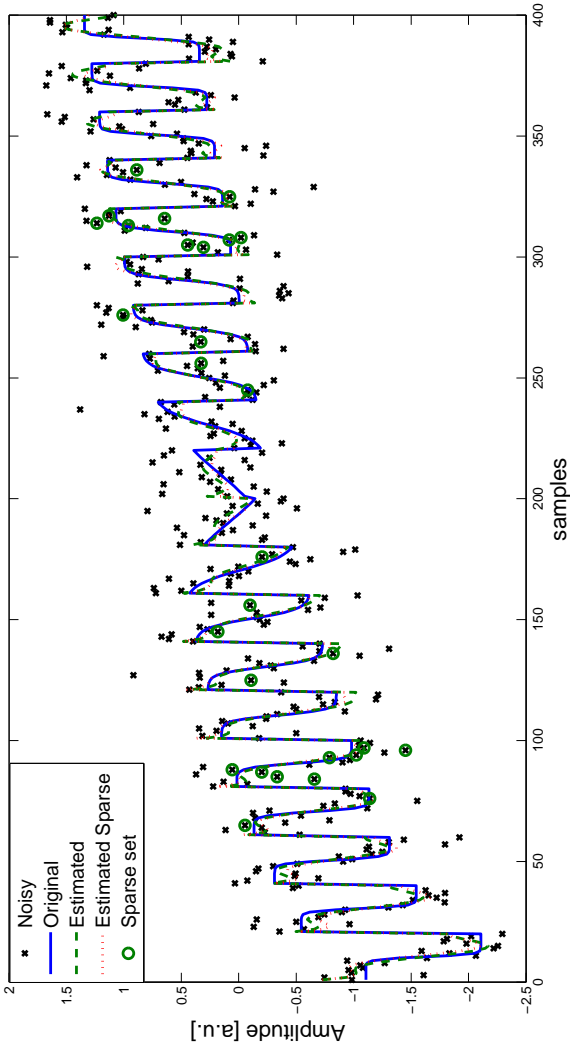


Figure 3.7: Results from the complete and sparse KPCR model, the crosses represent the noisy input data used for the training, the solid blue line represents the model. The dash green line represents the output of the complete KPCR model, while the dotted red line represents the output of the sparse KPCR model. Finally, the green circles represent the data points used in the sparse model. In total 29 datapoints were selected for the sparse model, and the tuning parameter for the kernel was $\sigma^2 = 13.36$.

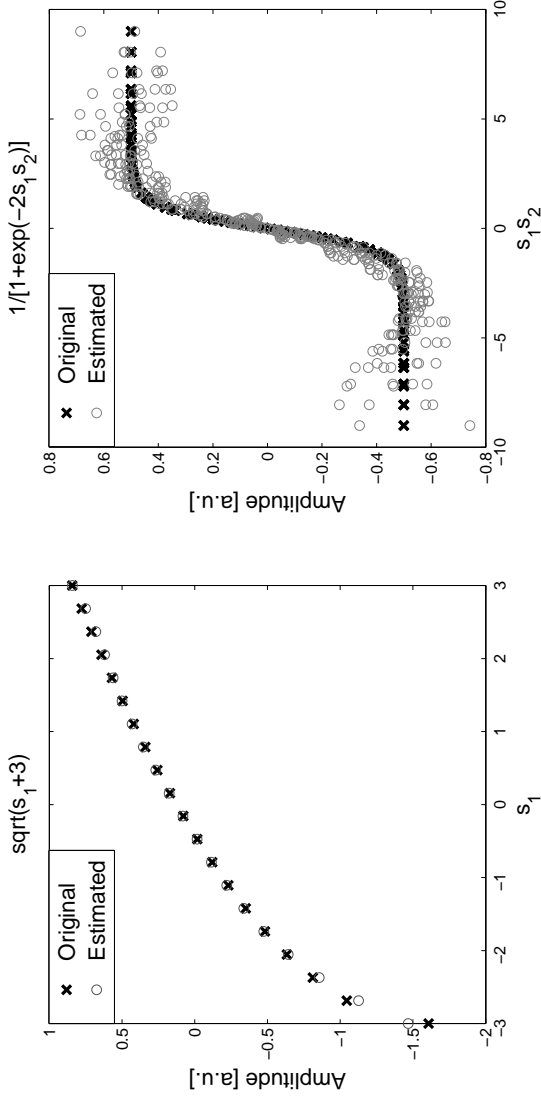


Figure 3.8: Decomposition of the model in the components related to the signal s_1 and the second order interaction of s_1 and s_2 . The black crosses represent the original model while the circles represent the estimated output.

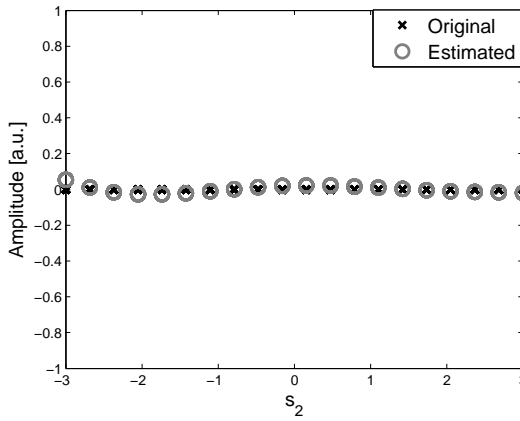


Figure 3.9: Output of the model for the individual contribution of the signal s_2 in the model output. Since there is no direct influence of the signal on the model output the target, represented by the black crosses, is zero. The circles represent the output of the model. It can be seen that even though the estimated output is not zero, it is small compared to the other variables.

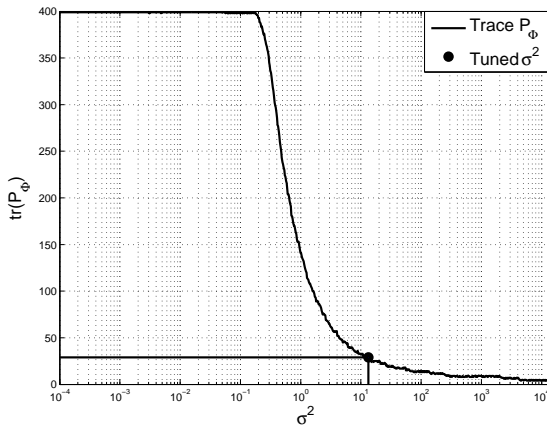


Figure 3.10: Relation between the trace of the projection matrix and the tuning parameter σ^2 . As shown in figure 3.5 the trace of the projection matrix slowly converges towards 1. The dotted point represents the selected tuning parameter for this example.

Chapter 4

Data and Preprocessing

This chapter introduces the data that will be used in the clinical studies discussed in chapter 7. In addition, the general preprocessing algorithm used on the data will be presented. Sections 4.1 - 4.6 presents a description of the different dataset used in the clinical studies. The description of the data has been divided in different sections due to the lack of homogeneity of the dataset. The dataset used in this thesis contains measurements from different centers, NIRS instruments, and different measured variables. Finally, In section 4.7 a description of the preprocessing procedure used is presented.

4.1 University Hospital Leuven

Two different datasets were collected from measurements of neonates at the neonatal intensive care unit (NICU) at the University Hospital Leuven, in Belgium. Regular cranial ultrasounds were performed at day 1,3, and 7 after birth. The medical ethical committee of the hospitals approved the use of these data in the clinical studies presented in this chapter. Informed parental consent was obtained in all cases.

In both datasets systemic measurements of SaO_2 and MABP were taken. SaO_2 was continuously recorded by pulse oxymetry on a limb and MABP by an indwelling arterial catheter (umbilical, tibial or radial artery). The NIRO300 (Hamamatsu®, Japan) was used for noninvasive monitoring of cerebral hemodynamics and oxygenation parameters TOI, ΔHbO_2 , and ΔHHb . The differential pathlength factor (taking into account the scattering of the infrared

light into the brain) was set at 4.39 [18, 237] and encoded into the PC as a constant value. For calculation of TOI, the absorption of near-infrared light was measured at two points and the diffusion equation was used, this can be found in equation (1.5). ΔHbD was calculated afterwards as the difference between ΔHbO_2 and ΔHHb .

MABP and SaO_2 data in Leuven were generated at 2 Hz and recorded at a sampling frequency of 100Hz by a data acquisition system CODAS (Dataq Instruments, USA) and stored on a PC. The NIRO 300 signals were digital and recorded with a sampling frequency of 6Hz. They were converted to analog signals with a sample-and-hold function before being introduced in the CODAS system. A detailed explanation of the population in the datasets is given below. A representative recording for the data measured in the University hospital Leuven is shown in figure 4.1.

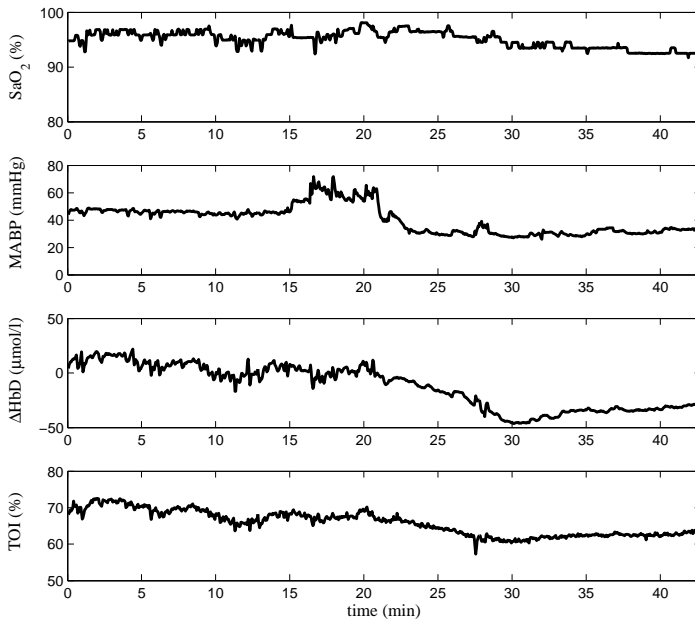


Figure 4.1: Typical recordings of SaO_2 , MABP, ΔHbD and TOI measured on a preterm infant in Leuven.

4.1.1 Propofol dataset

This dataset consists of measurements for a total of 14 infants from the NICU of the University Hospital Leuven. Neonates were included following approval of the study protocol by the ethical board of the University Hospital Leuven, Belgium, and after informed written consent was obtained from the parents. These infants with a mean post menstrual age (PMA) of 37 6/7 weeks (27 - 47) and a mean body weight of 2931g (855 - 4380) were treated with propofol to attain a short lasting sedation during elective chest tube removal to facilitate chest tube removal and avoid external aspiration of air. Recordings were taken 5 min before up to 60 min after intravenous bolus propofol 3mg/kg⁻¹ administration. This dataset will be called the *propofol dataset* from here on. A detailed demographic and clinical data description of the dataset is depicted in table 4.1.

Parameter	Value
Weight (gr)	2931 (855 - 4380)
GA (weeks)	35 3/7 (26 - 40)
PMA, (weeks)	37 6/7 (27 - 47)
PNA, (days)	18 (3 - 71)
Apgar 1	7 (4 - 9)
Apgar 5	8 (4 - 10)

Table 4.1: Mean (range) for the clinical data of the propofol dataset. Weight, gestational age (GA), Post-menstrual age (PMA), post-natal age (PNA) and the Apgar scores 1, 5 are indicated. The Apgar score is a medical score computed from 5 characteristics of the newborns at 1 and 5 minutes after birth. These characteristics are graded between 0-2, and their sum produce the Apgar score. The characteristics that are measured are heart rate, respiratory effort, muscle tone, reflex irritability, and color. Scores higher than 7 indicate a good status in the newborn. This test was proposed in 1952 by Virginia Apgar [8].

4.1.2 Leuven dataset

This dataset contains the recordings of 20 prematurely born infants with need for intensive care that were monitored during the first 3 days of life at the NICU of the University Hospital Leuven. Mean PMA of the Leuven infants was 28 5/7 weeks (SD \pm 3 2/7), mean body weight 1125g (SD \pm 503.76) and mean PNA at the time of measurements was 1.4 days (SD \pm 1.06). Demographic and clinical data of the infants are summarized in table 4.2. This dataset will be called the *Leuven dataset* from here on.

Parameter	Value
Weight (gr)	1007 (570-2935)
GA (weeks)	29 2/7 (24-39)
Male/Female	10/10
Apgar 1	7 (0-9)
Apgar 5	9 (1-10)
IVH [no (%)]	7 (35%)
PVL [no (%)]	7 (35%)
Neonatal Mortality [no (%)]	1 (5%)

Table 4.2: Characteristics for the Leuven dataset. Median (range) unless otherwise stated.

4.2 University Medical Centre Utrecht

Two different datasets were collected from measurements of neonates at the neonatal intensive care unit (NICU) at the University Medical Centre Utrecht, specifically from the Wilhelmina Children’s Hospital, in The Netherlands. A detailed explanation of the datasets is given below. Regular cranial ultrasounds were performed at day 1,2,3 and then weekly. The medical ethical committee of the hospitals approved the present study. Informed parental consent was obtained in all cases.

In both datasets systemic measurements of SaO_2 and MABP were taken. SaO_2 was continuously recorded by pulse oximetry on a limb and MABP by an indwelling arterial umbilical catheter. The INVOS4100 (Somanetics Corp®, MI) was used to measure the rScO_2 . The optical densities at a distance 4cm (deep signal) and 3cm (shallow signal) from the detector, were recorded simultaneously. For the calculation of rScO_2 the scattering of near-infrared light at 2 wavelengths, namely 730 and 810 nm, is measured at 3cm and subtracted from the measurement at the second optode at 4 cm. ΔHbT was computed afterwards as the inverse of the difference between both optical densities.

MABP, SaO_2 and rScO_2 were collected simultaneously by the Poly5(Inspektor Research Systems, the Netherlands) system with a sampling frequency of 10Hz, and they were stored on a personal computer for offline analysis. Since the optical densities were sampled at 0.0167Hz (i.e. one value per minute) on a separate disk drive, all signals were filtered with a mean average filter and then downsampled to this lower frequency in order to avoid loss of information in the new downsampled signal. By adopting this new sample frequency, we stay in accordance with the findings of von Siebenthal et al.(17) concerning the periodicity of the studied signals. A similar study of the influence of the

sampling frequency on the scores, as with the NIRO300 data, was not possible with the INVOS4100 data due to the low sample frequency of ΔHbT . A detailed explanation of the population in the dataset is given below. A representative recording from the data measured at the University Medical Centre Utrecht is shown in figure 4.2, this recording belongs to a subject from the Labetalol dataset.

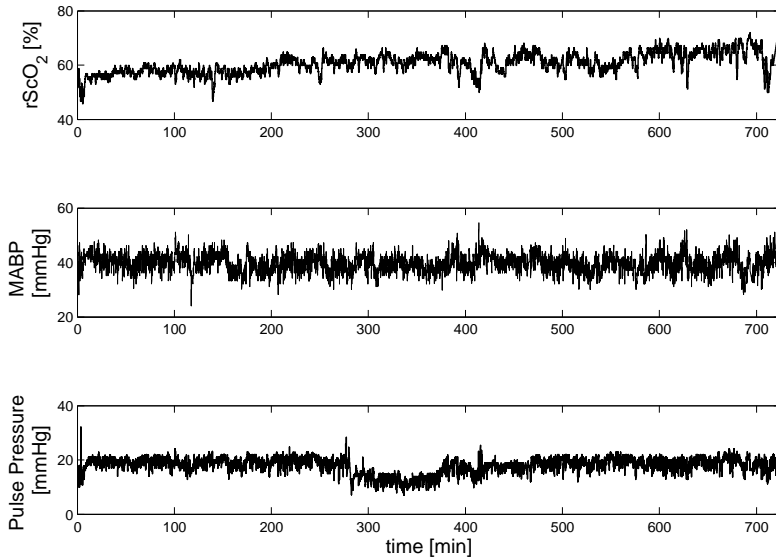


Figure 4.2: . Measurements of rScO₂, MABP and Pulse pressure for one of the subjects during the first day of life.

4.2.1 Utrecht dataset

This dataset includes the recordings of 20 prematurely born infants monitored at the NICU of the University Medical Centre Utrecht, The Netherlands. Infants from this dataset have a mean PMA of 29 2/7 weeks (SD ± 1 2/7) and a mean body weight of 1114g (SD ± 316.94). This dataset will be referred to as the Utrecht dataset from here on. Demographic and clinical data of the infants are summarized in table 4.3.

Parameter	Value
Weight (gr)	1025 (640-1690)
GA (weeks)	29 3/7 (26-31)
Male/Female	10/10
Apgar 1	6 (1-9)
Apgar 5	8.5(4-10)
IVH [no (%)]	4 (20%)
PVL [no (%)]	1 (5%)
Neonatal Mortality [no (%)]	1 (5%)

Table 4.3: Characteristics for the Utrecht dataset. Median (range) unless otherwise stated

4.2.2 Labetalol dataset

This dataset consists of measurements from 56 infants with a gestational age of 29 (24.7- 31.9) weeks and a birth weight of 960 (540-1585) grams. With NIRS, regional oxygen saturation (rScO₂) was continuously and noninvasively recorded using the INVOS4100. Blood pressure, SaO₂ and NIRS signals were simultaneously measured during the first three days of life. From the blood pressure signal, the MABP and the pulse pressure were computed. The pulse pressure was calculated as the difference between the systolic and diastolic blood pressure measurements. Figure 1 shows a representative set of measurements for a control subject. From the 56 infants 16 correspond to control subjects, and 40 correspond to the group of mothers who were treated for hypertensive disorders of pregnancy (HDP). All the groups were matched for gestational age, weight and sex. From the HDP group 21 neonates correspond to mothers treated with labetalol, this sub-group will be called the (HPD+Lab) group, and 19 correspond to mothers with other treatment, this group will be called the (HPD-Lab) group. The subjects from the three groups were matched for gestational age, birth weight and gender in order to exclude the influence of these parameters on the results provided by the analysis. From here on this dataset will be called the *labetalol dataset*.

4.3 University Hospital Zurich

This dataset consists of measurements from 42 infants with a gestational age of 28.1 ± 2.27 weeks and a birth weight of 1155 ± 467 gram. In all infants the pCO₂ was measured by a transcutaneous monitor, arterial oxygen saturation (SaO₂)

was measured continuously by pulse oximetry, and MABP by an indwelling arterial catheter. With NIRS, the cerebral intravascular oxygenation (ΔHbD) was continuously and noninvasively recorded using the Critikon Cerebral RedOx Monitor from Johnson & Johnson Medical. MABP, SaO_2 and NIRS signals were simultaneously measured during the first three days of life and downsampled at 0.333Hz for further processing.

4.4 ECMO Dataset

The ECMO dataset consists of measurements from 5 subjects (ranging from 1-1825 days) on a veno-arterial (VA) extra corporeal membrane oxygenation (ECMO) procedure. A dual channel near infrared system NIRO200 (Hamamatsu®, Japan) was used to measure the changes in HbO_2 , HHb and TOI using spatially resolved spectroscopy. From these signals ΔHbD and total hemoglobin changes ($\Delta\text{HbT} = \Delta\text{HbO}_2 + \Delta\text{HHb}$) were calculated and used, together, with TOI for further analysis. NIRS data were collected at frequency of 6Hz. Channel 1 was placed on the forehead in order to assess cerebral NIRS changes, while channel 2 was placed on the calf to assess peripheral NIRS changes. A full set of systemic data including, MABP, central venous pressure (CVP), end-tidal carbon dioxide pressure (EtCO_2), heart rate (HR), respiration rate (RR), core and skin temperatures and SaO_2 , were continuously measured in real time at the bedside using the IntelliVue MP70 (Philips, USA). All signals were down-sampled to 1Hz and artifacts were removed manually by means of interpolation. Figure 4.3 shows an example of the systemic and NIRS measurements from one neonate.

Measurements in this dataset were collected during stepwise changes in the ECMO flow. The flow was reduced from baseline (100% ECMO flow) in steps of 10%, approximately every 10 minutes, until 70% of the baseline ECMO flow was reached. Afterward the flow was increased back to baseline following the same profile. In cases where the patients could not accommodate a 30% reduction in ECMO flow, it was only reduced by a total of 20%.

4.5 Duchenne Dataset

This dataset contains measurement from 8 subjects with Duchenne muscular dystrophy (DMD). These patients were enrolled between November 2010 and April 2011 and followed up at the pediatric neuromuscular reference center of the University Hospitals Leuven. Furthermore, measurements from 11 age-matched

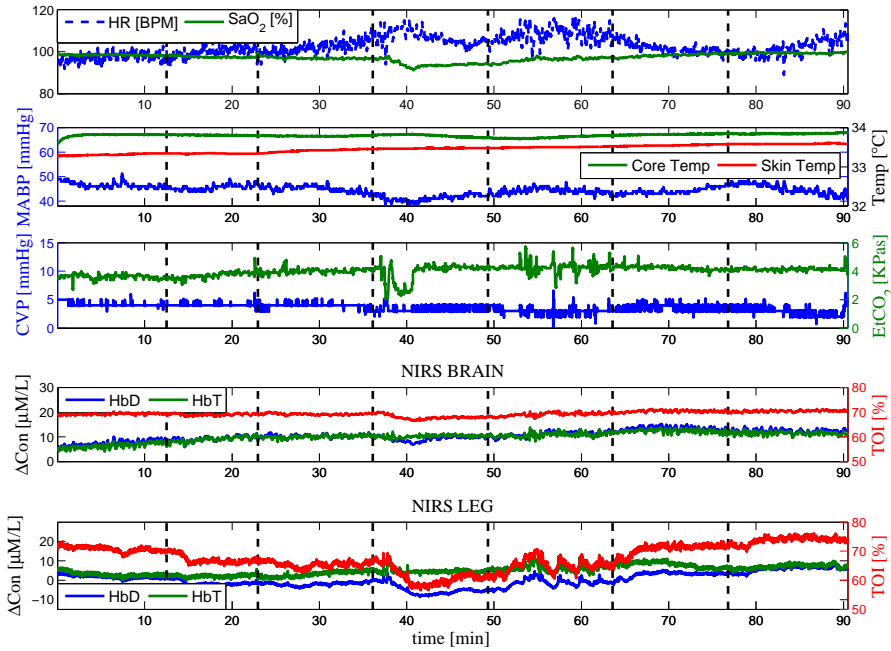


Figure 4.3: Systemic and hemodynamical variables of a patient undergoing ECMO procedure. Systemic variations of HR, SaO_2 , MABP, core Temperature, skin temperature, CVP and EtCO_2 were simultaneously acquired with NIRS measurements from the leg and the brain. The vertical dotted lines represent the time when changes in the ECMO flow were performed.

healthy male controls aged 9-12 years were included. The study protocol was approved by the institutional review board and informed consent was obtained from all parents of the children.

Muscle NIRS and sEMG signals were continuously measured in the biceps muscle during a protocol consisting of 6 phases. Cutaneous sEMG electrodes were placed on the medial side of the right biceps brachii, according to the recommendations of SENIAM (Surface ElectroMyoGraphy for the Non-Invasive Assessment of Muscles) [87]. A NIRS device NIRO300 was utilized to measure the hemodynamical variables in the muscle using a NIRS probe (source-detector distance: 4 cm) that was placed on the lateral side of the right biceps brachii symmetrically in the direction of the muscle fibers at 1 cm of the midline. A myometer microFET2 (Biometrics BV, The Netherlands) was located on the right wrist and used to register the generated force. The protocol consisted of

the following steps:

- The subject was located in a supine position with the arms relaxed. A baseline measurement of approximately 2 minutes was recorded.
- After the baseline measurements the subject was asked to perform two consecutive maximal voluntary isometric contractions (MVIC). The force generated during these contractions was recorded using a myometer. The average force was used as a reference measurement for MVIC.
- A rest period of 2 minutes followed the MVC phase. During this time it is expected that the hemodynamic variables will stabilize.
- After recovery, the patients were then asked to flex their right arm. The arm was held in the flexed position by an assistant present during the measurements. No force should be exerted at this moment. The patients sustained this flexion for one minute in order to allow for recovery of the muscle for any change caused.
- The patients were asked to exert a prolonged submaximal at 60% of their respective MVIC during one minute.
- After the sustained contraction a 10 minutes recovery period was measured.

In figure 4.4 a schematic representation of the protocol used is shown. Figure 4.5 shows a typical recording during the execution of the protocol.

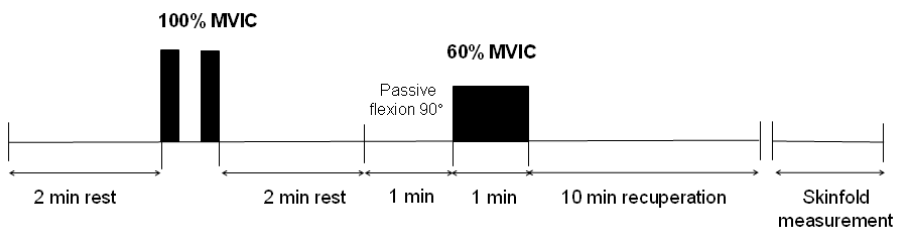


Figure 4.4: Protocol used for the measurements in the Duchenne study.

All signals were digitized via an analog-digital conversion of 24bits cDAQ(National instruments, USA) on a PC for further analysis. After the measurement, the skin fat layer was measured twice on the central part of the biceps with a Harpenden skinfold Caliper (British Indicator Ltd., UK). The mean value of the 2 measurements obtained from the harpenden skinfold caliper was used as the skin fat layer value for the patient. Since NIRS measurements are attenuated

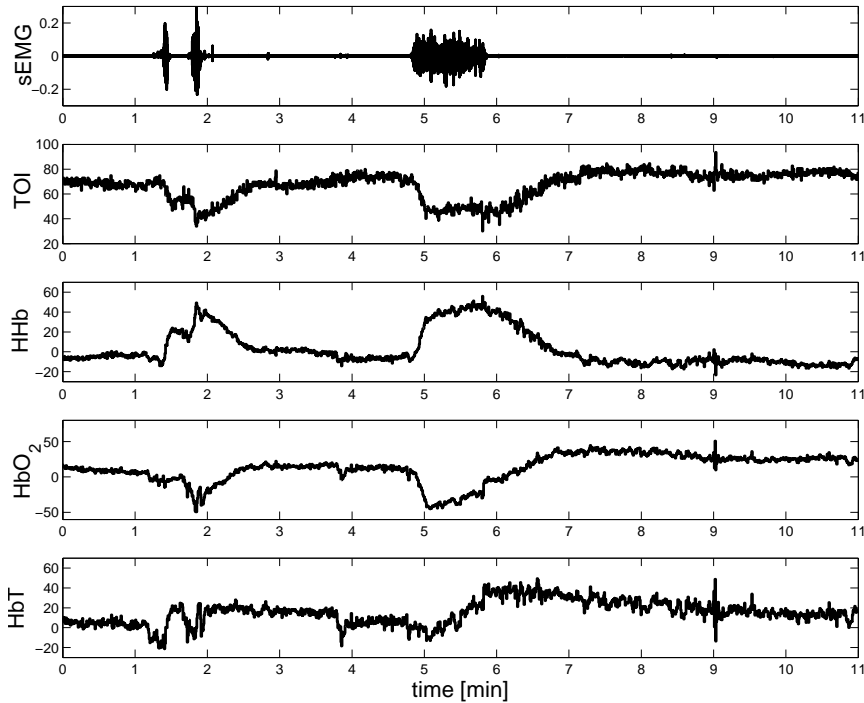


Figure 4.5: Typical recording for a control subject during the execution of the protocol in the Duchenne study. From top to bottom sEMG, TOI, HHb, HbO₂ and HbT.

by the fat layer, the skin fat layer value obtained for each patient was used to correct for the attenuation in the NIRS signals as explained in [14].

For the DMD patients, a functional assessment was done at the time of measurement by one experienced evaluator using the 6 minute walking test (6MWT), a measure utilized as an important clinical tool for progression of the disease [137]. In addition, timed functional tests (time to rise from floor, 10-m walk and 4-stair climb) were performed. The level of ambulation was recorded. All patients had an evaluation of the cardiac function by echocardiography using a echocardiograph iE33 (Philips Medical Systems, USA) and pulmonary-function tests were performed (forced vital capacity (FVC), forced expiratory volume in 1s (FEV1)) by spirometry (Pneumotrac Vitalograph, UK).

4.6 Lamb Dataset

This dataset has been provided by Dr. Flora Wong. The dataset is composed of measurements performed in lambs between 3-6 days after birth. A complete description of the dataset can be found in [235]. Briefly, the dataset contains concomitant measurements of several systemic and cerebral hemodynamic variables during changes in cerebral perfusion pressure. These changes were produced by controlled reductions of distal arterial pressure by means of an inflatable occluder cuff that was located around the common brachiocephalic artery. The changes in MABP were performed during a time interval of 20 min approximately. The duration of the inflation and deflation range between 3 - 100 s. Measurements of SaO₂ using a pulse oximeter placed on the lamb's tongue Nellcor 200 (Nellcor Incorporated, USA), EtCO₂, CBFv using a transit time ultrasonic flow probe with 2 mm diameter #2S632 (Transonic System, USA), MABP using a calibrated strain-gauge pressure transducer Cobe CDX III (Cobe Laboratories, USA) and tissue oxygenation TOI using a NIRO200 were performed during the protocol. The data were acquired at a sampling frequency of 400Hz. For the analysis performed in this dissertation the data were downsampled to 1Hz, by first applying a moving average filter with length 400 samples and then decimating the signals by a factor of 400. A sample of the data used is shown in figure 4.6. From here on this dataset will be called the *Lamb Dataset*.

4.7 Preprocessing

4.7.1 Artifacts

Biomedical signals are normally corrupted by different artifacts and noise sources. These sources are related to physiological phenomena, i.e. contamination due to other physiological signals, electronic instrumentation, i.e. power line interference or movement of electrodes and probes, or environmental conditions such as ambient light. The removal of the undesired disturbances in the signals is of utmost importance considering their impact in the processing algorithm used in later stages [176]. Due to the big variety of artifacts and their different impact in the signals, there exist different types of algorithms designed to reduce their influence under some specific condition. Noise, in contrast with artifacts, is generally considered as a random additive component in the signal. The noise is normally reduced by the use of filters of which the characteristics depend on the problem specifications.

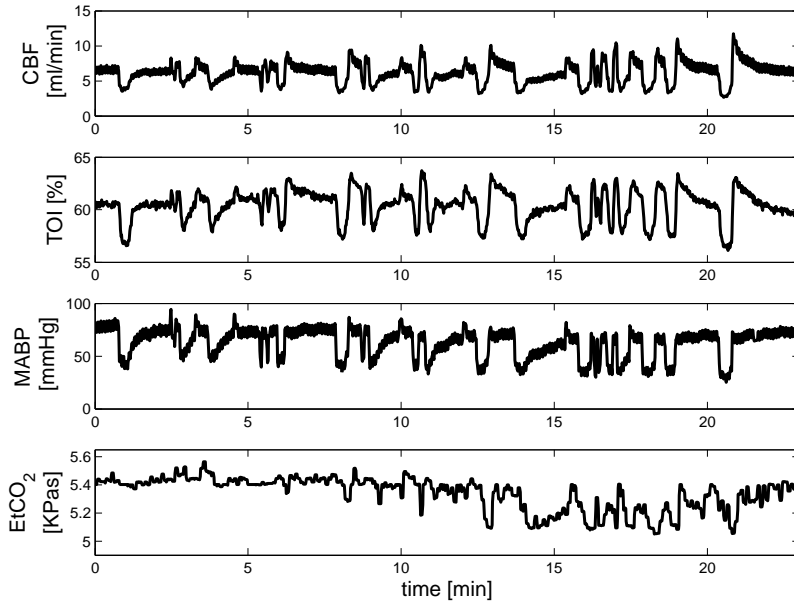


Figure 4.6: Typical recording for the Lamb dataset. From top to bottom, CBF, TOI, MABP, and EtCO₂.

Function estimation from noisy samples is closely related to signal denoising. In this framework the general problem is reduced to find a function, f , that minimizes the error, e , between the predicted values $f(x)$ and measured values y . Statistics (linear and nonlinear regression), neural networks and support vector machines among other methodologies have been used to address this problem.

The signals used in this thesis were preprocessed using a least squares support vector machines (LS-SVM) in order to remove and correct segments contaminated by artifacts. Only segments with artifacts shorter than 30 seconds were preprocessed using the algorithm presented in section 3.1. When the artifacts were longer than 30 seconds the data was truncated. This preprocessing divides a continuous recording in several segments free of artifacts. These segments were used for further processing. An illustrative example of this preprocessing stage can be seen in figure 4.7, where a set of measurements of SaO₂, MABP and TOI is decomposed in a set of segments free of artifacts.

4.7.2 Filtering

After the removal of artifacts and the segmentation of the signals in segments free of artifacts, a basic filtering was applied to the signals. a low-pass filter with a cut off frequency of 0.14Hz or 0.5Hz, depending on the application, was used. In addition the linear trend presented in the signals was subtracted in order to avoid high values at low frequencies in the computation of the power spectrum. The preprocessing algorithm is further explained in the algorithm 4.

Algorithm 4 Preprocessing algorithm.

input: signals to preprocess: s , with $s \in R^N$.

output: S_r is a set of all the r segments free of artifacts from the signal s .

begin

$r \leftarrow 1$

while duration of s

if detect artifacts in s

If duration artifact < 30 s

aux \leftarrow segment from s

aux \leftarrow output from robust LS-SVM model in (3.11)

aux \leftarrow Filtered and detrended version of aux

$S_r \leftarrow$ aux

$r \leftarrow r + 1$

else segment is rejected, continue to next segment

endif

endif

endwhile

end

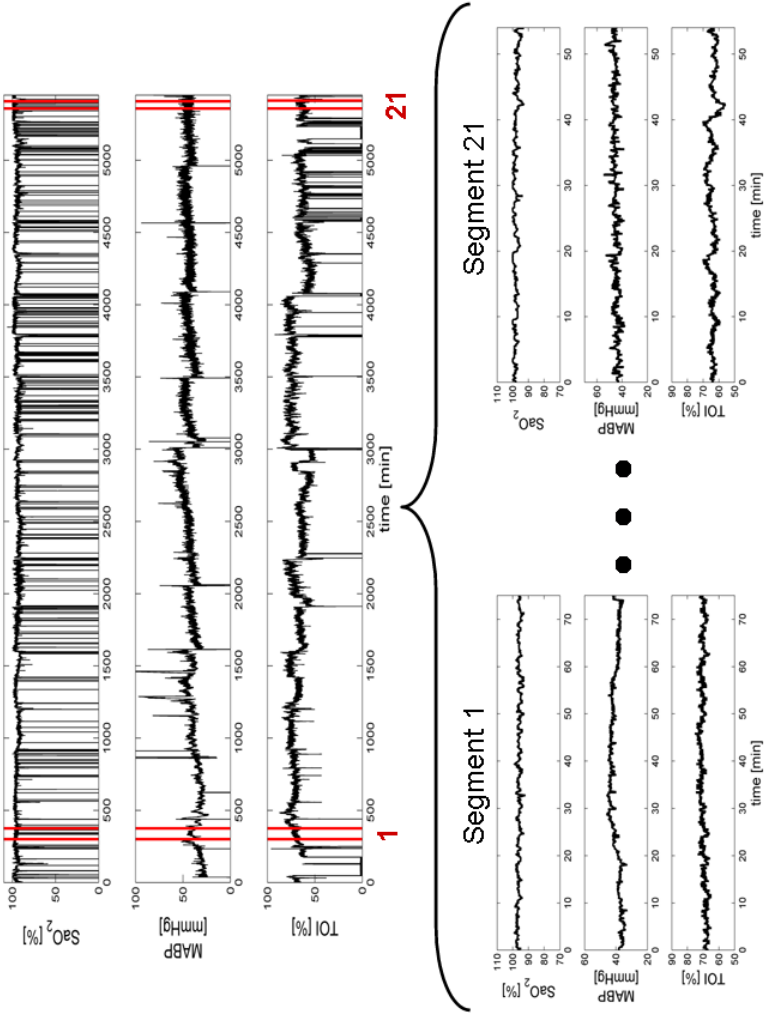


Figure 4.7: Preprocessing stage. In the upper panel, continuous measurements of SaO₂, MABP and TOI. In the lower panel, segments free of artifacts extracted after preprocessing.

Chapter 5

The Use of TOI and rScO₂ in Cerebral Autoregulation Assessment

In this chapter the use of TOI and rScO₂ in cerebral autoregulation (CA) studies is investigated. In the framework of cerebral autoregulation assessment, several studies have used measurements of ΔHbD and ΔHbT as a surrogate measure for cerebral blood flow (CBF). However, these measurements are prone to movement artefacts. TOI and rScO₂ are more stable measurements that are also obtained with NIRS technology. In this chapter, an analysis of the differences between CA assessment using TOI and rScO₂ instead of ΔHbD and ΔHbT is presented. This chapter is based on paper 2 in my publication list.

5.1 Introduction

The main goal of this study was to investigate whether TOI and rScO₂ could replace ΔHbD and ΔHbT , respectively, in the assessment of cerebral autoregulation. Tsuji et al [216] were the first to report the use of NIRS as a tool for the continuous measurement of autoregulation and to validate the cerebral intravascular oxygenation (ΔHbD) as a measure of CBF [215]. ΔHbD can be continuously measured by means of any NIRS device. Tsuji et al [216] found a good correlation between ΔHbD and MABP changes, indicating loss in cerebral autoregulation. Furthermore, a good correlation

was found between autoregulation and outcome, i.e. the frequency of severe intraventricular bleeding. However, ΔHbD is a relative parameter and difficult to measure because of movement artifacts. If the goal is to have a continuous robust measurement, other parameters of oxygenation, that are more stable and easy to interpret, should be used. TOI and rScO₂ are 2 promising NIRS parameters, based upon spatially resolved spectroscopy, that provide absolute values of regional hemoglobin oxygen saturation in absolute terms, they have been validated against the jugular venous saturation and each other, see e.g. [148, 45]. In addition TOI and rScO₂ are less prone to movement artifacts [219].

5.2 Methods

Data from the Leuven, propofol and Utrecht dataset were used in this study. The data were preprocessed using the algorithm 4. Only segments free of artefacts and that were longer than 40 minutes were used in this study. Mean recording time for the Leuven dataset was 1h48min (SD ± 70 min) yielding 293 epochs of 20 min. For the propofol dataset, mean recording time was 1h32min (SD ± 42 min) yielding 53 epochs of 20 min. Mean recording time for the Utrecht data was 05h25min (SD ± 3 h13min) including 342 epochs of 20 min.

Due to the differences in the sampling frequency for both datasets, two different analyses were done with the data. In the first analysis the Leuven and Propofol dataset were filtered with a mean average filter and then downsampled to a sampling frequency of 0.333 Hz, the analysis was performed in these data. In the second analysis the signals from the Leuven and propofol dataset were downsampled to a common sampling frequency of 0.0167 Hz (periodicity 60s) in order to ensure the best compatibility between both medical centers. Furthermore, the influence of the sampling frequency on the scores, using the Leuven and Propofol dataset, was studied.

Correlation (COR) and coherence (COH) values were calculated in each 20-minutes epochs. The average of COH over the frequency band 0.0042-0.00837Hz (periodicity in the range 120-240s) for the 60s data, and over the frequency band 0.0033-0.04Hz for the 3s data (range 25-300s) [197], was used as score for the considered signal epoch [224, 30, 119, 140]. Since the concordance between the signals might vary as a function of time, a sliding window approach was used. To calculate the amplitude of the COH, the auto-power and cross-power spectra densities were estimated using the Welch averaged periodogram method. In this method, each 20 minute epoch was subdivided in 5 segments of duration 10 minutes with a overlap of 7.5 minutes.

The concordance scores computed from TOI versus MABP (method 1) and ΔHbD versus MABP (method 2) can be considered as two measurements from the same underlying process. Similarly, the concordance scores computed from rScO_2 versus MABP (method 1) and ΔHbT versus MABP (method 2), using the recordings from Utrecht, can be considered as two measurements of the same process. Two different analyses were performed with the scores: on patient level (with one mean value per patient) and epoch level (with one score value for each 20min epoch).

- On the patient level, the scores were averaged for neonates of whom multiple 20min epochs were available, in order to obtain one mean score value per baby. The paired t-test and Wilcoxon signed rank test were applied to investigate the difference in the mean COR and mean COH score between 1) TOI/MABP and ΔHbD /MABP and 2) rScO_2 /MABP and ΔHbT /MABP.
- On the epoch level, generalized linear mixed models were used to take into account all the scores over each 20min epoch (multiple measurements) per baby.

The influence of the variations in MABP on cerebral autoregulation assessment was studied using the concordance scores corresponding to epochs with high variations in MABP separately ($\text{MABP} > 10\text{mmHg}$). Bland Altman plots were constructed to visualize the agreement between the two methods. All reported p-values were two-tailed and we considered as statistically significant a nominal p-value < 0.05 . The statistical analysis was performed using the SAS System, version 9.1, SAS Institute Inc., Cary, NC, USA.

5.3 Results

5.3.1 Analysis on the patient level

Table 5.1 shows the differences in mean concordance scores computed from ΔHbD (ΔHbT) versus MABP (method 1) compared to TOI (rScO_2) versus MABP (method 2). All data were sampled at 60 sec. Using the NIRO 300 recordings from the Propofol dataset, the mean COR and COH, computed from ΔHbD versus MABP compared to TOI versus MABP were not statistically significantly different (p-values 0.22 and 0.45 respectively). For the Leuven dataset, the mean COR scores, computed from ΔHbD versus MABP compared to TOI versus MABP were not statistically significantly different (p-value 0.40).

On the other hand, the mean COH, computed from ΔHbD versus MABP compared to TOI versus MABP was borderline significantly different (p-values 0.04), with a difference of 5.5%. However, these differences remain clinically unimportant and fall within the normal variation of the parameters. This implies that both methods can be used interchangeably.

Using the INVOS4100 data recordings from Utrecht, the mean COR and COH scores, computed from ΔHbT versus MABP compared to rScO₂ versus MABP, were statistically significantly different (all p-values < 0.01), with differences 9.3% and 5.8% respectively. The larger differences can be explained by the fact that ΔHbT less reflects CBF compared to ΔHbD [216]. Moreover, there are large difficulties in measuring ΔHbT using the INVOS4100.

5.3.2 Analysis on the epoch level

Table 5.2 shows the p-values indicating the statistical significance of the differences in concordance scores computed from ΔHbD (resp., ΔHbT) versus MABP (method 1) compared to TOI (resp., rScO₂) versus MABP (method 2). Here, the concordance scores are compared for each 20 min epoch. For each infant multiple measurements are available. Generalized linear mixed models were used to assess the differences between both methods.

In the Propofol dataset sampled at 60 seconds, the differences in COR and COH scores, computed from ΔHbD versus MABP compared to TOI versus MABP were statistically not significant (with p-values 0.21 and 0.38). Similar results hold for the Leuven dataset sampled at 60 seconds: the corresponding differences were all statistically not significant (with p-values 0.95 and 0.08). Using the INVOS4100 data recordings from Utrecht, the differences in COR and COH scores, computed from ΔHbT versus MABP compared to rScO₂ versus MABP were statistically significant (with p-values < 0.01 in both cases), with differences of 9.7% and 7.5% respectively.

5.3.3 Analysis for epochs with high variations in MABP

Table 5.3 shows the p-values indicating the statistical significance of the differences in concordance scores computed from ΔHbD (resp., ΔHbT) versus MABP (method 1) compared to TOI (resp., rScO₂) versus MABP (method 2). Only 20min epochs with high variations in MABP (> 10 mmHg) were retained for the analysis. In the propofol dataset sampled at 60 s, the COR and COH scores, computed from ΔHbD versus MABP compared to TOI versus MABP were statistically not significantly different (with p-values 0.96 and 0.76

Propofol	$\Delta\text{HbD}/\text{MABP}$ vs TOI/MABP		
	Mean (\pm std)	Mean (\pm std)	p-value
	Median (Min-Max)	Median (Min-Max)	
COR	45.6 \pm 21.0 43.1 (14.9 - 82.2)	39.1 \pm 17.2 35.7 (12.6 - 69.4)	0.22
COH	47.2 \pm 17.4 45.8 (16.0 - 80.9)	44.2 \pm 12.1 46.3 (21.1 - 57.3)	0.45
Leuven	$\Delta\text{HbD}/\text{MABP}$ vs TOI/MABP		
	Mean (\pm std)	Mean (\pm std)	p-value
	Median (Min-Max)	Median (Min-Max)	
COR	42.2 \pm 10.2 40.1 (29.1 - 67.1)	39.7 \pm 10.4 38.2 (19.3 - 59.9)	0.40
COH	44.2 \pm 11.3 42.1 (23.7 - 64.5)	38.7 \pm 8.5 39.8 (18.9 - 58.6)	0.04
Utrecht	$\Delta\text{HbT}/\text{MABP}$ vs $\text{rScO}_2/\text{MABP}$		
	Mean (\pm std)	Mean (\pm std)	p-value
	Median (Min-Max)	Median (Min-Max)	
COR	32.4 \pm 5.0 33.8 (22.6 - 42.4)	41.7 \pm 7.6 40.0 (31.5 - 65.6)	<0.01
COH	33.0 \pm 7.9 31.3 (18.0 - 48.0)	38.8 \pm 7.0 36.6 (27.8 - 55.0)	0.01

Table 5.1: Significance of differences in concordance scores computed from ΔHbD (resp., ΔHbT) versus MABP (method 1) compared to TOI (resp., rScO_2) versus MABP (method 2). All data were sampled at 60 sec and scores given in percentage.

respectively). Similar results were obtained for the Leuven dataset sampled at 60 s, where these differences were also shown to be statistically no significant (with p-values 0.57 and 0.68 respectively). Using the INVOS4100 data recordings from Utrecht, the differences in COR and COH scores, computed from ΔHbT versus MABP compared to rScO_2 versus MABP were no longer statistically significant (with p-values 0.09 and 0.21 respectively).

Propofol 60 seconds data (n=53, 14 subjects)	$\Delta\text{HbD}/\text{MABP}$ vs TOI/MABP		
	Mean (\pm std)	Mean (\pm std)	p-value
	Median (Min-Max)	Median (Min-Max)	
COR	46.5 \pm 29.8 44.6 (0.1 - 99.8)	39.8 \pm 27.6 34.2 (0.8 - 88.3)	0.21
COH	48.0 \pm 22.4 47.9 (8.3 - 95.4)	44.7 \pm 20.2 43.5 (4.1 - 91.0)	0.38
Leuven 60 seconds data (n=284, 20 subjects)	$\Delta\text{HbD}/\text{MABP}$ vs TOI/MABP		
	Mean (\pm std)	Mean (\pm std)	p-value
	Median (Min-Max)	Median (Min-Max)	
COR	43.1 \pm 24.1 40.5 (0.8 - 94.7)	43.2 \pm 23.2 43.3 (0.2 - 94.7)	0.95
COH	42.8 \pm 24.5 39.9 (2.2 - 96.8)	39.3 \pm 22.1 38.2 (0.9 - 93.9)	0.08
Utrecht 60 seconds data (n=342, 20 subjects)	$\Delta\text{HbT}/\text{MABP}$ vs rScO ₂ /MABP		
	Mean (\pm std)	Mean (\pm std)	p-value
	Median (Min-Max)	Median (Min-Max)	
COR	31.9 \pm 21.0 28.6 (0.1 - 82.3)	41.6 \pm 25.0 41.9 (0.04 - 95.8)	<0.01
COH	31.3 \pm 19.3 29.8 (0.5 - 87.1)	38.8 \pm 23.3 35.9 (0.6 - 97.8)	<0.01

Table 5.2: Significance of the differences in concordance scores computed from ΔHbD (resp., ΔHbT) versus MABP (method 1) compared to TOI (resp., rScO₂) versus MABP (method 2) for all scores in the patients, the scores are given in percentage. The number of considered 20min epochs is denoted by n.

5.3.4 Patient data sampled at 3 sec

In addition, to study the influence of the sampling frequency on the scores, the differences in mean concordance scores (COR and COH) computed from ΔHbD versus MABP (method 1) compared to TOI versus MABP (method 2) in the propofol and the Leuven datasets were analyzed on a patient level, as well as on epoch level. Although p-values were lower, similar conclusions hold as for the 60 second data. Wherever differences were statistically significant, they always remained lower than 5.6%.

Propofol 60 seconds data (n=14, 8 subjects)	$\Delta\text{HbD}/\text{MABP}$ vs TOI/MABP		
	Mean (\pm std)	Mean (\pm std)	p-value
	Median (Min-Max)	Median (Min-Max)	
COR	55.2 \pm 28.4 55.0 (12.7 - 99.8)	54.7 \pm 26.3 69.5 (9.3 - 83.4)	0.96
COH	44.0 \pm 23.9 42.3 (8.3 - 95.4)	41.7 \pm 23.5 39.4 (13.0 - 91.0)	0.76
Leuven 60 seconds data (n=46, 15 subjects)	$\Delta\text{HbD}/\text{MABP}$ vs TOI/MABP		
	Mean (\pm std)	Mean (\pm std)	p-value
	Median (Min-Max)	Median (Min-Max)	
COR	47.1 \pm 26.7 50.2 (1.3 - 92.7)	44.2 \pm 25.5 46.8 (3.7 - 93.1)	0.57
COH	46.1 \pm 27.8 45.0 (4.0 - 96.8)	43.8 \pm 25.3 44.0 (3.3 - 91.3)	0.68
Utrecht 60 seconds data (n=62, 15 subjects)	$\Delta\text{HbT}/\text{MABP}$ vs $\text{rScO}_2/\text{MABP}$		
	Mean (\pm std)	Mean (\pm std)	p-value
	Median (Min-Max)	Median (Min-Max)	
COR	35.4 \pm 22.9 35.2 (0.1 - 74.7)	43.1 \pm 27.0 42.0 (0.04 - 92.5)	<0.09
COH	35.3 \pm 20.7 33.8 (0.8 - 82.6)	40.3 \pm 25.9 37.7 (1.1 - 97.8)	<0.21

Table 5.3: Significance of the differences in concordance scores computed from ΔHbD (resp., ΔHbT) versus MABP (method 1) compared to TOI (resp., rScO_2) versus MABP (method 2) for 20min epochs with variations in MABP $>$ 10mmHg. Scores are given in percentage. The number of considered 20min epochs is denoted by n.

5.4 Discussion

Impaired cerebral autoregulation is considered a risk factor for brain injury in the sick premature infant [76, 216, 234, 197]. However, previous studies using intermittent static measurements [217] showed that CBF is independent from MABP over a wide pressure range in premature babies. When there is a lack of autoregulation, oxygen delivery is a function of CBF and cerebral arterial oxygen content. Hence, it would be of clinical interest to have a continuous measure of autoregulation. Therefore, NIRS was used by Tsuji et al. [216].

Tsuji et al [215] and Soul et al [198] validated ΔHbD as a good measure of CBF. Moreover, as total ΔHb (ΔHbT) reflects changes in cerebral blood volume (ΔCBV) [236] in patients with lack of autoregulative properties, as the ones included in this study, it is possible that ΔHbT reflects CBF. The main problem of these measurements is that they are very sensitive to movements and thus only applicable in research settings. More recently, spatially resolved spectroscopy introduced new parameters like TOI and rScO₂, reflecting ΔHb oxygen saturation predominantly of the venous compartment [109]. These parameters are less sensitive to movements and provide absolute values.

As shown in Tables 5.1, 5.2, and 5.3 no important differences exist in using TOI instead of ΔHbD and using rScO₂ instead of ΔHbT for the measurement of autoregulation. The NIRS-derived parameter ΔHbT has been validated as a measure of blood volume, so it does not represent changes in blood flow. Because data were obtained in stable infants, changes in CBF and CBV could be expected to be equivalent, as confirmed in our study. Significant differences, if any, in mean COR and mean COH scores between both methods are less than 7% when sampling the data at 60 s, which is still within the normal variation induced for the NIRS parameters [219]. Using rScO₂ instead of ΔHbT as measure for autoregulation, larger differences (up to 9.7%) were noticed. This can be produced for the difficulties in measuring ΔHbT using the INVOS4100 (this value is not user-accessible and was highly sensitive to artifacts) or because ΔHbT less reflects CBF compared with ΔHbD [215]; however, there is no evidence to prove these assumptions. These differences can still be considered as normal, therefore, clinically unimportant when used, e.g. for detection of impaired autoregulation. However, all these differences become insignificant when only the larger variations in MABP (>10 mm Hg) are taken into account for the calculation of the COH and COR scores, as presented in Table 5.3. Small changes in MABP yield low values in their power spectral density. Because our COH/COR score calculations are using spontaneous MABP changes, a lot of which are small, these might affect their reliability as confirmed by Hahn et al [82]. Therefore, these epochs of higher MABP variations enable a more reliable detection of (im)paired autoregulation. They better assess the autoregulative properties of the brain and are clinically more important. Even though there are no important statistical differences between the methods, large discrepancies in the COR and COH values on an infant-to-infant basis exist. Hence, the agreement is not very high either. These discrepancies, as mentioned before, can be attributed to the normal variations of the NIRS parameters and to the fact that model assumptions are only approximately valid in practice. The NIRS parameters only indirectly measure CBF and their coupling with MABP approximately reflects autoregulation assuming SaO₂ constant, which is only approximately valid. More importantly, what really matters here is the lower sensitivity of TOI and rScO₂ to movement artifacts compared with ΔHbD

and ΔHbT . Therefore, they represent a more robust variable to assess the autoregulation status of the infants.

Hence, this enables the direct clinical use of signal processing methods for the automated and continuous calculation of the coupling between $\Delta\text{HbD}/\text{TOI}$ and $\Delta\text{HbT}/\text{rScO}_2$ versus MABP, using NIRS, mostly by means of COR and COH. However, these scores are not a precise measurement of autoregulation but rather a reflection of the autoregulation status of the baby. It is important to recognize here the potential limitations of the use of COR and the COH analysis to investigate moment-to-moment autoregulation mechanisms, because these approaches assume a linear and stationary relationship between the measured NIRS signals and MABP, which can produce misleading results in a system with nonlinear and nonstationary properties. Future research should be oriented to evaluate these effects. Finally, the scores should be related to clinical outcome of the infants. The scores of our propofol dataset are shown to be related to clinical intervention because they change concordant to the administration of propofol [220].

5.5 Conclusion

None or little difference was found between scores computed from ΔHbD versus MABP compared to TOI versus MABP using NIRO300 recordings from Leuven, and between scores computed from ΔHbT versus MABP compared to rScO_2 versus MABP using INVOS4100 recordings from Utrecht. Using three different datasets, recorded in two different centers with two different devices and sampled at two different rates 3s and 60 s, a nice similarity has been shown in scores by replacing the measured NIRS signal ΔHbD by TOI when using a NIRO300 instrument, and by replacing ΔHbT by rScO_2 when using an INVOS4100 instrument. Hence, TOI and rScO_2 can be used for the calculation of cerebral autoregulation in neonates. It is however important to stress that this is only applicable for the relation between MABP and TOI or ΔHbD . This does not suggest that ΔHbD and TOI are the same, but yet that they can be interchanged for studies in autoregulation. Moreover, it was demonstrate that as the frequency range is restricted to lower frequencies (smaller than 0.008Hz) the correspondences between the scores calculated based on ΔHbD and TOI, or ΔHbT and rScO_2 , increase. These correspondences further increase when restricting the COH/COR score calculations to those epochs with large enough variations in MABP (> 10 mmHg). The importance of these findings is that now a reliable monitor to measure cerebral autoregulation non-invasively and continuously in preterm infants is available.

Chapter 6

Standardization of Traditional Methodologies for Cerebral Autoregulation Assessment

This chapter presents a study of the influence of the parameter setup on the scores provided by correlation, coherence and transfer function analysis in cerebral autoregulation (CA) assessment. Coherence and transfer function analysis, are based on the computation of the power spectrum densities. Traditionally, the power spectrum is computed using the Welch method. This method requires the definition of several parameters. Recently, it has been shown that an arbitrary selection of these parameters produces a high variability in the scores computed for CA assessment. Therefore, due to the fact that different centers use different parameters setup in their analysis, comparative analysis are difficult. In this chapter this problem is addressed by providing a methodological study of the influence of those parameters on the scores computed for CA assessment. As result appropriate values for these parameters are proposed. It is expected that this study helps in the standardization of the methods used in CA assessment. This chapter is based on paper 5 in my publication list.

6.1 Introduction

Correlation and transfer function analysis have been used in clinical studies in order to assess cerebral autoregulation. Correlation quantifies the strength of

the relation between MABP and CBF and has been used in patients after head injury [43]. Transfer function analysis, on the other hand, was first used by Giller for cerebral autoregulation assessment [66]. Giller showed that patients with impaired autoregulation presented higher coherence coefficients. Coherence, as well as transfer function gain and phase, is a frequency based method. Transfer function analysis is based on the system identification framework where the system, in this case the mechanisms involved in cerebral autoregulation, is treated as a black box and the frequency response is calculated based on measurements of the input and the output: MABP and CBF respectively [19]. Coherence and transfer function have also been used with NIRS signals in order to assess cerebral autoregulation [197, 234]. The core of transfer function analysis, and frequency based techniques, is the estimation of the power spectral and cross-spectral densities of the input and the output. This estimation is normally done using the Welch method [232]. This method takes advantage of the stationarity of a signal in order to reduce the influence of the noise, the bias and the variance in the spectrum estimation. However, if the signal presents non-stationarities the estimation is biased. In addition, extra parameters are needed in order to estimate the power spectra; an arbitrary choice of these parameters can produce misleading results. In the literature there is a lack of studies that investigate the influence of the selection of those parameters when used for cerebral autoregulation assessment. In addition, there is no consensus on which parameters to use, it is common to find different choices in different studies. Therefore, the main goal of this study is to investigate the influence of the change in these parameters on the final scores used for autoregulation assessment. Additionally, a secondary goal is to identify which method is more robust against changes on these parameters, as well as to identify the values to be selected when using correlation, coherence or transfer function for cerebral autoregulation assessment.

6.2 Data

For this study the Leuven dataset was used. The signals were filtered using a low-pass and a high-pass filter with cut-off frequencies of 0.15Hz and 0.003Hz respectively. The data were afterward downsampled to a sampling frequency $F_s = 0.3\text{Hz}$. As the information we are interested in is located in frequencies lower than 0.1Hz, this cut-off frequency does not affect the frequency range we are interested in. Artifacts such as movements and changes in baseline were detected and removed by the preprocessing explained before in chapter 4. Hence, a continuous recording was divided in smaller segments free of artifacts, only segments with length longer than 40 minutes were kept for further analysis. Remaining artifacts which could not be detected in the previous step were

deleted manually. Figure 6.1 shows the data from one measurement segment for one patient. The scores from correlation, coherence and gain are also shown. The coherence and gain values were averaged in three different frequency bands: 0.003Hz-0.02Hz very low frequency (VLF), 0.02Hz-0.05Hz low frequency (LF) and 0.05Hz-0.1Hz high frequency (HF).

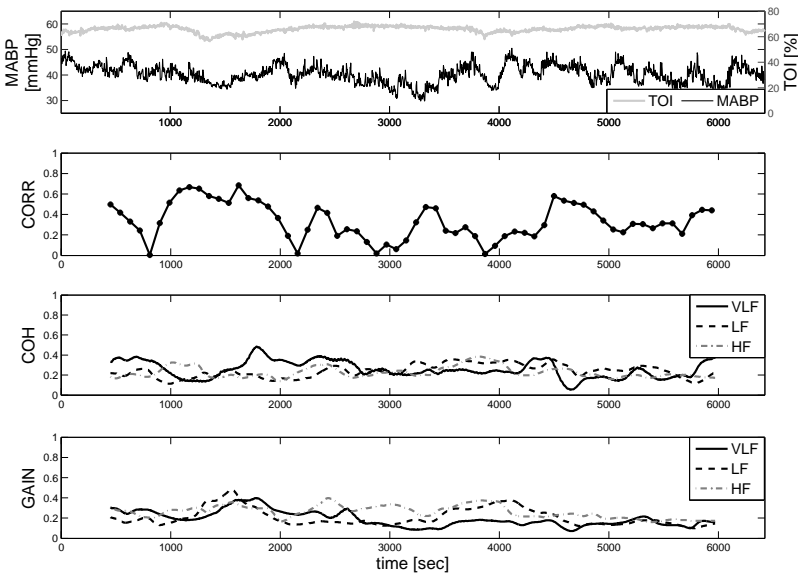


Figure 6.1: Correlation, coherence and gain values for measurements from one patient. In the upper figure the raw data: MABP and TOI. In the second figure the correlation values; the signal was divided in overlapping epochs of 15 minutes long and with a 90% overlapping. The third figure presents the coherence values averaged in three different frequency bands VLF (0.003Hz-0.02Hz), LF (0.02Hz-0.05Hz) and HF (0.05Hz-0.1Hz), the signal was divided in epochs of 15 minutes long, a sub-window length of 5 minutes was used in the Welch method with an overlapping percentage of 90%. The last figure shows the gain values for the same parameter setup as for the coherence.

6.3 Methods

Cerebral autoregulation was assessed using four different methods; namely, correlation, coherence, modified coherence and transfer function. The influence of the epoch length, overlapping percentage and sub-window length on the final scores, produced by each method, was evaluated. From here on, the term epoch refers to the segment on which the scores are calculated, the term sub-window refers to the segment used in the Welch method. The overlapping percentage refers to different parameters in the correlation and the frequency based methods, it will be further explained when needed.

6.3.1 Methodology for correlation

To assess cerebral autoregulation using correlation (COR) the data is divided in epochs, of which the length is user-defined. The calculated COR is then assigned to each epoch and the procedure is repeated until the complete signal is analyzed. Normally, there is no overlapping between consecutive epochs; however, by including an overlapping a more detailed view of the evolution in the common dynamics of the two signals is obtained. Furthermore, in order to assess cerebral autoregulation in neonates, some extra parameters (e.g. mean, standard deviation, among others) are derived from the time series of calculated COR values. There is a delay between MABP and TOI of approximately 10 seconds in neonates [81]. We have performed the analysis taking this delay into account.

In this study we are interested on studying the influence of the epoch length and the overlapping percentage, for consecutive epochs, on the resulting COR scores. In order to analyze this influence the following setup was used:

1. The signals were segmented in consecutive overlapping epochs of length T_i , where T_i varies from 10-30 minutes.
2. Overlapping percentages (O_j) between consecutive epochs ranging from 10%-90% were used.
3. The COR scores were calculated for each epoch of length T_i and Overlapping O_i .
4. The mean value of the resulting COR scores, for each T_i and O_i , was assigned to each patient.
5. A sensitivity analysis was used to quantify the impact of T_i and O_i on the scores calculated in the previous step.

6.3.2 Methodology for coherence

Coherence (COH) is based on the calculation of cross- and auto-power spectrum. In order to estimate the cross-spectral and auto-spectral power densities the Welch method is used [232]. For two signals x and y , this method segments the signals in consecutive overlapping sub-windows (x_{L_i, O_j} , y_{L_i, O_j}) of length L_i , and overlapping percentage O_j . The power spectrum for each segment is computed and the average among all the segments is used as the power spectrum of the signal. When x and y are stationary signals, this procedure reduces the bias and the variance in the estimation of the power spectrum, as the differences in the power spectrum for different sub-windows are only attributed to noise which is reduced through averaging. Lower values of L_i and/or higher values for O_j produce more sub-windows which improves the estimation of the power spectrum. For stationary signals, an O_j higher than 50% does not reduce significantly the bias and variance in the power spectrum estimation. In addition, the lowest value of L_i is given by the lowest frequency component of interest in the analysis.

In real life applications the signals x and y are recorded for several hours and are highly affected by non-stationarities. In order to reduce the influence of these non-stationarities in the power spectrum estimation, the most intuitive action is to reduce the length of the x and y ; therefore, the signals are segmented in overlapping epochs of length T_i . By using maximum overlapping between consecutive epochs a good resolution in time for the evolution of the common dynamics between the signals can be obtained. The relation between the non-stationarities and the length of the sub-windows and their overlapping percentage (L_i, O_j) used in the Welch method has not been analyzed for cerebral autoregulation assessment. Studies of cerebral autoregulation using NIRS signals are focused to the low frequency range 0.003Hz – 0.1Hz. Therefore, in order to assess frequency components of 0.003Hz, theoretically, a sub-window of 5 minutes length is needed, which impose a limit for L_i .

In this study the influence of the epoch length, T_i , and the sub-window overlapping percentage, O_j , on the resulting COH scores will be investigated. In order to analyze these influences the following setup was used:

1. The signals were segmented in consecutive overlapping epochs of length T_i , where T_i varies from 10-30 minutes. Maximum overlapping between consecutive epochs was used.
2. The sub-window length was fixed to $L_i = 5$ minutes.
3. Overlapping percentages, O_j , between consecutive sub-windows ranging from 10%-90% were used.

4. The COH scores were calculated as a function of the each epoch of length T_i and the sub-window overlapping O_j .
5. The mean value of the resulting COH scores along the epochs, for each T_i and O_j , was assigned to each patient. This results in a vector of COH values, in the frequency domain, per patient.
6. A sensitivity analysis was used to quantify the impact of T_i and O_j on the COH scores.

A similar setup was used for all frequency based methods.

Modified Coherence

As spontaneous measurements of MABP may lack enough variation needed to provide meaningful estimates of the coherence values [199], Hahn et al [82] developed a modified version of the coherence where each frequency component of the coherence is weighted by the percentage of the MABP power presented at that frequency component. This modified coherence vector (MoCOH) corrects for the segments with small variations in MABP. In order to study the influence of the epoch length T_i and the sub-window overlapping percentage O_j , for consecutive sub-windows, the same setup as in COH was used.

6.3.3 Methodology for Transfer Function

As for the coherence, the cross-spectral and auto-spectral densities are estimated using the Welch method; therefore, the same restrictions of stationarity are required. The transfer function can be analyzed by its magnitude and phase. The magnitude or gain of the transfer function represents the strength of the relationship between the signals at each frequency component. The phase of the transfer function represents the phase delay at each frequency component between the signals. The influence of the epoch length T_i and the sub-window overlapping percentage O_j , for consecutive sub-windows, on the transfer function values was studied using the same setup as in COH.

6.4 Sensitivity Analysis

Two different analysis were performed to evaluate the sensitivity of each method to changes in the parameters. In both cases a sensitivity analysis approach

was followed. On one hand, a global analysis using a modified version of the elementary effects technique was used. The results given by this technique will indicate which method, overall, is most robust to changes in the parameters. On the other hand, a variance based method was used to evaluate the influence of each parameter separately. More detailed information about these methods can be found in [183].

6.4.1 Elementary effects

The elementary effects (EE) method is a way to characterize the influence of a variable in a model. The method works as follows: Suppose a model Y depends of a set of variables $X_i = \{X_1, X_2, \dots, X_k\}$, the elementary effect of the variable i for $i = \{1, \dots, k\}$ in the model Y is defined as:

$$EE_i = \frac{Y(X_1, \dots, X_i + \Delta, \dots, X_k) - Y(X_1, X_2, \dots, X_k)}{\Delta} \quad (6.1)$$

where Δ represents the step change in the discrete variable X_i and $Y(X_1, X_2, \dots, X_k)$ represents a reference from the model output and should be fixed when calculating each EE_i . The EE of the variable i can now be characterized as the mean value of EE_i and its standard deviation. High values of EE_i indicate that the variable i has a high impact in the model Y . However, normalization should be used when comparing different models, as the EE values are not normalized among different models. Therefore the following modification was included:

1. For each method (model) used to assess cerebral autoregulation, an array consisting of the scores calculated for each combination of parameters was created. Let this array be $Y(N, F, T, O)$ where N represents the number of patients, F the frequency components (for frequency based methods), T the epoch length and O the overlapping percentage. The parameters vary as explained before.
2. For a fixed N and F the EE analysis was performed, using as reference the median of the model. This produces an array $EE_Y(N, F, EET, EEO)$.
3. With N and F fixed, a ratio between the energy of EE_Y and the energy of Y was calculated, $R(N, F)$. This ratio can be interpreted as the percentage of energy in Y due to its variations. The lower this value the less variability in the output of Y , which indicates that Y is more robust to variations in the model parameters.

$$R(N, F) = \frac{EE_Y^T EE_Y}{Y^T Y} \quad (6.2)$$

4. In order to check the influence of the parameters in different frequency components the mean value along the patients dimension of $R(N, F)$ was taken as a sensitivity measure for the model Y , it will be called normalized sensitivity index (NSI). The standard deviation of $R(N, F)$ can also be used as a sensitivity measure, however it only indicates the variability of the variations of Y along the patients and not the overall variation due to the change in the parameters.

$$NSI = \frac{1}{N} \sum_N R(N, F) \quad (6.3)$$

6.4.2 Variance based approach

The goal of variance based methods is to identify which variables in a model Y are responsible for most of the variations in the model output. These variables will then be the most relevant ones for Y . The sensitivity measure using the variance based method is computed as follows:

$$S_i = \frac{Var(Y|X_i)}{Var(Y)} \quad (6.4)$$

where $Var(Y|X_i)$ is the variance of the model Y with X_i constant and $Var(Y)$ is the variance of the model output. The lower the value S_i , the higher the influence of the variable X_i in the model output Y . Indeed, low values of S_i indicate that most of the variability in the model is due to the variable X_i . The following analysis was performed in our study:

1. As in the previous case, for each method (model) used to assess cerebral autoregulation, an array consisting of the scores calculated for each combination of parameters was created, Let this array be $Y(N, F, T, O)$ where N represents the number of patients, F the frequency components (for frequency based methods), T the epoch length and O the overlapping percentage. The parameters vary as explained before.
2. For a fixed N and F the sensitivity measure S_O was calculated for varying overlapping percentages.

3. For a fixed N and F the sensitivity measure S_T was calculated for varying epoch length.
4. Mean values among the population and the frequency were taken to analyze the effects of the epoch length and overlapping percentages in the output of the methods.

6.4.3 Test for stationarity

A process is called stationary if its mean and standard deviation does not change with time. Due to the changing nature of the physiological signals they represent non-stationary processes. In order to probe if the signals included in this study were non-stationary and to find the maximum length of a window were its behavior might be represented by a stationary process, or as a trend stationary process, we performed the KPSS test for stationarity. A detailed description of the test can be found in [111].

In this analysis the following setup was used:

1. The signals were segmented in non-overlapping epochs of length varying from 1 minute up to 30 minutes.
2. For each epoch the KPSS test was performed separately in the MABP and the TOI signals.
3. For each epoch length, the percentage of epochs indicating a non-stationary process was noted.

6.5 Results

6.5.1 Test for Stationarity

Figure 6.2 shows the results for KPSS test for stationarity applied for the MABP and TOI signals. From the results it can be seen that when the epoch length is increased more segments in the dataset present non-stationarities. It can also be seen that the MABP presents more non-stationary segments than the TOI. This is expected, since the variations in TOI are slower and less abrupt than the variations in MABP. Therefore, it can be said that TOI is “more” stationary than MABP for a given epoch length.

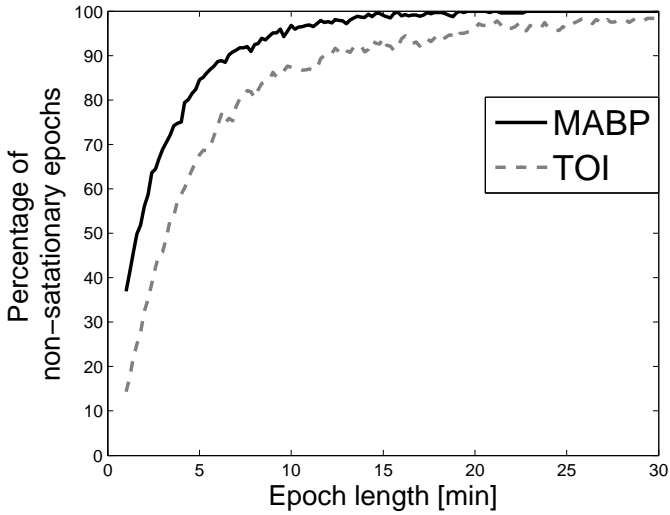


Figure 6.2: Percentage of non-stationary epochs presented in the dataset vs the epoch length.

6.5.2 Elementary Effects Analysis

In the figures 6.3 and 6.4 the results from the elementary effects analysis are shown. In figure 6.3, the influence of the change in the parameters, represented by the NSI, is plotted against each frequency component. The figure shows a lower influence of the methods in the low frequency range, which may be caused by the stronger power density of the signal in that region. Among all the frequency based methods, the gain presents the lowest sensitivity index, while the COH and the MoCOH present the highest indices. In particular it can be seen that for the “high” frequencies, above 0.04Hz, COH, MoCOH and the phase present high variations. This behavior can be expected as these scores are more sensitive to high frequency noise than the gain. The performance of correlation is not shown in figure 6.3 as it does not depend on frequency.

Figure 6.4 presents a scatter plot of the mean value of the scores among the patients, which was presented in figure 6.3, and its standard deviation. For the frequency based methods each point in the scatter plot corresponds to a frequency component. The closer to the origin (0,0), the more robust the method to the changes in the parameters. The figure shows that the correlation outperforms all the methods. In some way this is expected, since it is the simplest method where the influence of the parameters should be lower. For

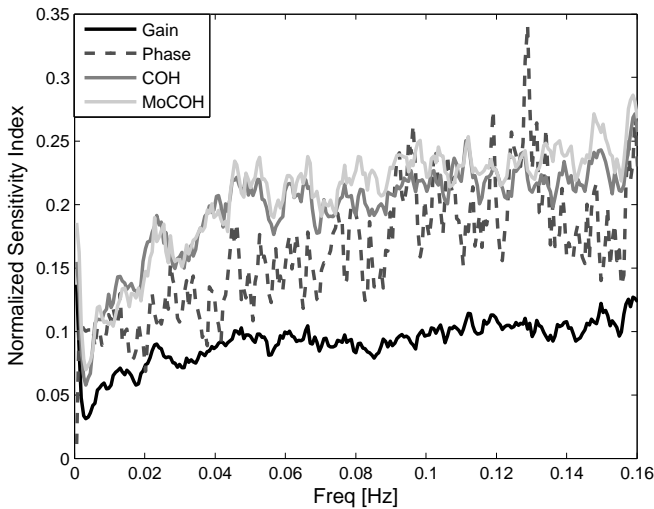


Figure 6.3: Mean value of the normalized sensitivity index among the patients vs frequency.

the frequency based methods, the gain presents the best results. Results from the phase are not shown as they possess a high variability and will not allow a good display of the performance of the other methods. As in figure 6.3, it can be seen that the performance of the COH and MoCOH is similar.

6.5.3 Variance Based Analysis

In figures 6.5 and 6.6 the results from the variance based analysis are shown. In figure 6.5 the analysis of the influence of the epoch length in the methods is depicted. For correlation it is observed that the shorter the length of the epoch the lower the influence in the variation of the scores. Longer epochs induce a higher variability in the scores. This is due to the non-stationary effects because longer windows are more likely to be affected by non-stationarities than shorter windows. On the other hand, the frequency based methods, namely COH, MoCOH and gain present a similar behavior. In general, they also present a high variability for short time epochs, epoch length < 14 minutes. This is due to the restricted amount of sub-windows that are available for that epoch in the calculation of the averaged power spectrum. When using the Welch method for the estimation of the power spectrum, the epoch under analysis should be divided in sub-windows. As the amount of these sub-windows increases the

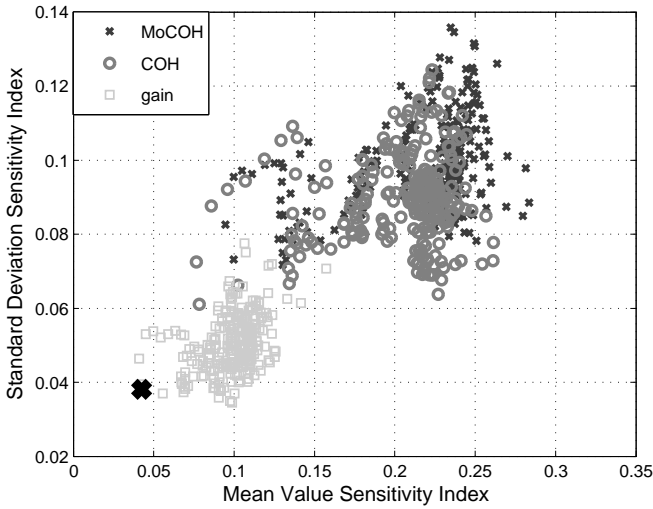


Figure 6.4: Mean value of the sensitivity index versus its standard deviation.

variance in the estimation of the power spectrum decreases. It is observed that this is achieved with windows of length longer than 14 minutes. However, epochs of length higher than 22 minutes introduce a higher variability in the method output. This might be due to the inclusion of more non-stationarities segments in the window under analysis, as in the CORR method. The phase presents a similar behavior as that of the other frequency based methods in the region of epoch lengths 14-22 minutes. For shorter windows the influence of the epoch length is lower.

In figure 6.6 the results for the analysis of the overlapping percentage, for consecutive sub-windows, are shown. As the percentage of overlapping increases, the COR, COH, MoCOH and gain methods present a higher sensitivity index, which represents a lower variability in their model output due to that overlapping percentage. This is due to the fact that more sub-windows are included in the averaging of the scores per patient. According to the Welch method for stationary signals, it is known that more than 50% of overlapping, in the sub-windows, does not reduce significantly the variance and the bias in the estimation of the power spectrum. According to figure 6.6, this percentage, for our data, is 60%. This is an indication that mild non-stationarities are affecting the estimation of the power spectrum. When the overlapping percentage is increased, more sub-windows are included in the epoch under analysis; by including more sub-windows, when averaging, the effect of non-stationarities

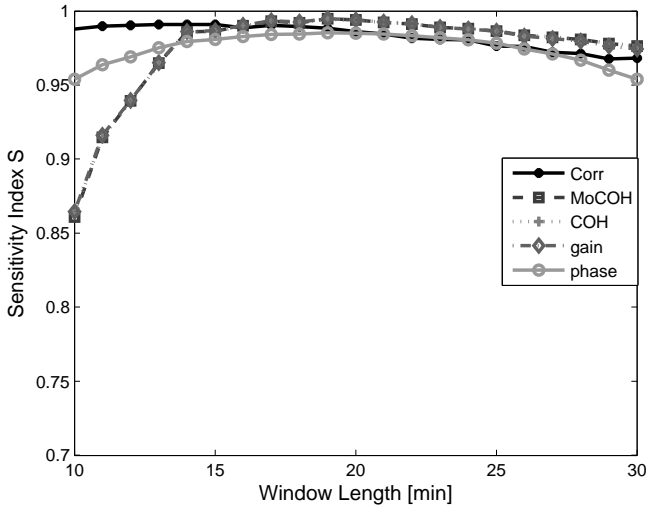


Figure 6.5: Influence of the window length on the performance of the methods for cerebral autoregulation assessment.

is reduced. The phase presents a strange behavior as the influence of the overlapping percentage in its output seems to decrease up to 50% of overlapping and to increase afterward. However, as shown in the previous figures, the phase is seemingly not a reliable measure when the parameters are not chosen carefully. It is also important to note that the frequency based methods seem to stabilize faster than the CORR with increasing overlapping percentage.

6.6 Discussion

Variations in the CORR, COH, MoCOH and transfer function scores, depicted in figure 6.1, indicate the presence of a non-stationarity behavior in the relationship between MABP and TOI. This is confirmed in the results shown in figure 6.2. These non-stationarities are more evident when the length of the epochs is increased. To our knowledge, there are no limitations for using CORR in presence of non-stationarities. However, COH and transfer function analysis were developed for the analysis of linear and time-invariant systems. This is mainly due to the convergence in the power spectrum estimation of the time-series involved in the analysis. In presence of non-stationarities the power

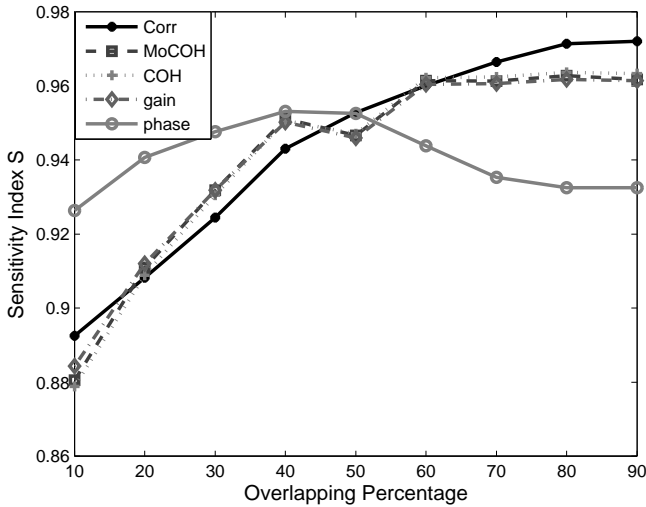


Figure 6.6: Influence of the overlapping percentage on the performance of the methods for cerebral autoregulation assessment.

spectrum estimation might not converge, in such cases it is not possible to use methods based on Fourier analysis to study the relation between variables.

Correlation is by far the simplest way to compute the relation between two signals. However, one of the most important drawbacks is that delayed dynamics generate smaller COR coefficients, producing misleading results. Even though the delay between MABP and TOI is approximately 10 seconds in neonates [81], this delay is patient dependent and should be calculated for each patient in order to produce information related to physiology. Studies involving correlation for autoregulation assessment generally divide the signals in non-overlapping segments, where COR is calculated for each segment and scores are derived from the generated COR time series. To some extent this approach reduces the influence of non-stationarities in the derived scores, as they are averaged out. However, we found that the selection of the window length and the overlapping percentage for consecutive epochs have a great impact on the CORR scores. Longer windows introduce non-stationary effects, while low overlapping percentages will introduce high variability in the patients score. Based on our results, on one hand, the length of the epochs, for CORR, COH, MoCOH and transfer function methods should be selected between 14-22 minutes, these epoch lengths guarantee convergence of the power spectrum estimation and reduce the amount of non-stationarities in the analyzed segment. On the

other hand the overlapping percentage between consecutive sub-windows should be higher than 60% in the frequency based methods, this minimizes the effect of non-stationarities due to an increase in the number of sub-windows that will be used in the power spectrum estimation. The overlapping percentage between consecutive epochs in the COR method should be higher than 80%. In this way, not only the variability of the method output is reduced but, when using correlation, the temporal resolution in cerebral autoregulation assessment is also improved.

COH, as COR, is a measure of the strength of the linear relation between two variables. However, its measurement is done in the frequency domain. Although COH is not affected by delays between the signals as COR, it is highly affected by non-stationarities and non-linearities. When using COH for cerebral autoregulation assessment several parameters should be tuned. First, as in COR, the signals should be segmented in epochs. Second, each epoch should be divided in sub-windows, the length and the overlapping percentage of consecutive sub-windows as well as the length of the epochs should be defined. Normally, longer epochs produce lower COH values, which may indicate the presence of more non-stationary segments in the epoch under analysis. Short epochs produce noisier COH values due to the smaller number of sub-windows. The length of the sub-window is linked to the lowest frequency expected in the signal. Theoretically, the length of the sub-window should be at least the inverse of the lowest frequency expected in the signal. In practice, the estimation is improved as more oscillations are included; however, as was mentioned before, longer windows are more likely to include more non-stationary segments. Cerebral autoregulation studies, using NIRS signals, have focused on frequencies higher than 0.003Hz which represents oscillations of 300s (5 minutes) and lower than 0.1Hz which represents oscillations of (10s) [159, 67]. In this study we fixed the length of the sub-window to 5 minutes, for simplicity reasons. The selection of the overlapping percentage, for consecutive sub-windows, is not as straight forward as for the sub-window length. In the case of stationary signals an overlapping higher than 50% does not reduce significantly the variance and bias in the power spectrum density estimation and guarantees its convergence [232]. This is due to the fact that consecutive sub-windows represent the same process and the differences are attributed only to noise, therefore, when averaging the power spectral density of sub-windows the noise is greatly reduced. However, if non-stationarities are present the impact of the overlapping on the coherence values becomes important. In this study, we found that an overlapping higher than 60% does not reduce the variability in the power spectrum estimation; this points out the presence of mild non-stationarities in the signal, as the gain scores converge only when this overlapping percentage was reached. If strong non-stationarities were present in the epoch under analysis, the scores would not have converged, or convergence will be reached for higher overlapping percentages.

The effect of the change in the overlapping percentage and window length in the MoCOH and the gain were similar to those for COH. This is expected as all these methods are based on the power spectrum density estimation.

When used for cerebral autoregulation assessment we found that the gain and the CORR are the most robust methods. However COR presents some limitations that are overcome by the gain score, mainly related to delayed dynamics. We also found that the change of the parameters affect less the low frequency components compared to the high frequency components. This can be due to the fact that the power of the signals is located in the low frequency ranges and that the high frequencies are affected by noise. Gommer et al. [72] found that the transfer function gain and phase were robust to changes in the preprocessing when used to quantify cerebral autoregulation. They calculated the transfer function gain and phase, using the Welch method for the estimation of the power spectrum, with 2 different sub-window length 51.2s and 409.6s and an overlapping of 50% for consecutive sub-windows, the length of the epoch under analysis was 15 minutes. They found that the gain and phase values were hardly affected by the selection of these parameters and the pre-processing method used in the data. In contrast with [72] in this study was analyzed the influence of the overlapping percentage between consecutive sub-windows and the length of the epochs on the transfer function, coherence and modified coherence parameters. Gain is the most robust method for quantifying cerebral autoregulation, but the results provided by this study do not favor the phase score. In addition, Hanh et al [81] validated the use of frequency analysis methods to assess cerebral autoregulation. They found that the gain in combination with coherence presented the best performance, although it still lacks of precision for clinical use.

6.7 Conclusion

Assessment of cerebral autoregulation is a complex problem that has been addressed in different ways. Due to the lack of significant results, that relate cerebral autoregulation assessment with clinical outcome, its use in clinical practice has been limited. However, these results may be due to the wrong selection of methods or a wrong setup used in its assessment. In this study is shown that transfer function gain and COR are the most robust methods to changes in the setup of the parameters, when compared to transfer function phase, COH and MoCOH. However, the COR has problems when delays are present in the signals under analysis. Moreover, the transfer function can assess the causal relationship between MABP and CBF. When frequency based methods are used, this study concludes that epoch lengths between 14-22

minutes and overlapping percentages, for consecutive sub-windows, higher than 60% improve the estimation of the power spectrum and reduce the influence of non-stationarities. We also propose the gain as the most robust method for cerebral autoregulation studies.

Chapter 7

Clinical Case Studies

In this chapter the clinical studies performed during my doctoral research are presented. Section 7.1 presents a study of the performance of the methods for cerebral autoregulation assessment for the prediction of clinical outcome in neonates. Section 7.2 describes a study where the myogenic and metabolic mechanism for CA are assessed. In section 7.3 a study of the evaluation of the methods for cerebral hemodynamics assessment in a population of infants undergoing ECMO procedure, using CCA, is introduced. In section 7.4 the use of oblique subspace projection for cerebral hemodynamics monitoring is introduced. Section 7.5 presents results from the use of wavelet based transfer function WBTF and nonlinear regression (KPCR) in the study of the relation between some systemic variables and CBF/TOI measurements. Section 7.6 presents the results for a study where cerebral autoregulation is assessed in infants from mothers that underwent treatment for hypertension using Labetalol. Section 7.7 presents the results from a study where the hemodynamical variables in the muscle of children with Duchenne muscle dystrophy was evaluated. Finally, in section 7.8 the use of subspace projections in the detection of sleep apnea episodes is illustrated. The content in this chapter is based on papers 1, 3, 4, 7, 13, 15 and 16 from my publication list.

7.1 Cerebral autoregulation assessment I

7.1.1 Introduction

The main goal of this study is to investigate whether coherence and transfer function derived scores for autoregulation can predict short term outcome in premature infants.

CA can be assessed by analyzing the relation between MABP and CBF, which can be measured continuously. The similarity in the dynamics of both signals has been quantified so far by means of correlation, (partial) coherence and transfer function analysis [216, 76], among other methods. Intervals with a correlation, (partial) coherence coefficient > 0.5 are considered to present impaired autoregulation. In order to include all this information in a single value, two scores have been used: the Pressure Passive Index (PPI) [197], defined as the percentage of 10-min epochs with impaired autoregulation, and the Critical Percentage of Recording Time (CPRT), which represents the percentage of the total measuring time during which impaired cerebral autoregulation is detected [194]. MABP can be measured continuously by classical clinical monitors. CBF however is difficult to measure continuously. By means of Near-Infrared Spectroscopy (NIRS), rScO₂, ΔHbD and TOI reflects changes in CBF in case of constant SaO₂ [198, 234, 206].

7.1.2 Data

For this study the Leuven and the Utrecht dataset were used. Assessment of CA was done via analysis of the MABP/HbD and MABP/TOI for the Leuven dataset, and MABP/rScO₂ for the Utrecht dataset. Coherence and transfer function were used to measure the linked dynamics between MABP and CBF. After preprocessing, the signals were divided into segments of 20 minutes with the maximum overlap (step size: one sample). For each segment, the transfer function gain and phase coefficients were calculated. The average of the coefficients in the frequency ranges 0.003Hz - 0.02Hz (very low frequency range: VLF), 0.02Hz - 0.05Hz (low frequency range: LF) and 0.05Hz - 0.1Hz (high frequency range: HF) were calculated for further analysis [234].

With respect to clinical outcomes, infants were classified as abnormal whenever bleedings, PVL (Periventricular Leukomalacia) and/or IVH (IntraVentricular Hemorrhage) occurred, else they were classified as normal. To assess whether the concordance scores were predictive for outcome (normal or abnormal), the non-parametric Kruskal-Wallis test was applied. The statistical analysis was

performed using the statistics toolbox from MATLAB. All reported p-values were two-tailed and a nominal p-value < 0.05 was considered as statistically significant.

7.1.3 Results

Figures 7.1 and 7.2 show the results for the different scores in different frequency bands. The TF gain and TF phase, and COH are represented in the x-axis by the numbers 1, 2 and 3 respectively. The scores for the normal population present a **N** after the number of the respective score, whilst the scores for the abnormal population are indicated with an **A**. COH values vary between 0-1, phase values are given in rad/sec, gain values are given in [%/mmHg] for the analysis of MABP-TOI and MABP-rScO₂ or [μ mol/L.mmHg] for the analysis of MABP- Δ HbD.

In the Leuven dataset 45% (9/20) of the infants had a bad outcome. The box plots in figure 7.1 show that no significant differences can be seen between the scores. However, some trends are observed in the gain values. First of all in the VLF and LF the scores for MABP/ Δ HbD present a trend towards being higher for the normal than for the abnormal population. For MABP/TOI the scores present a trend towards being higher in the normal population in the VLF; however, the scores for the LF and HF present a trend towards being higher for the abnormal population. Higher scores in the abnormal population are expected, since they indicate a stronger coupling in the dynamic between the signals, which is likely to occur when autoregulation is impaired.

In the Utrecht dataset 34% (13/38) of the infants had a bad outcome. The scores for this population do not provide much evidence of a relation between scores for autoregulation and clinical outcome. A small trend can be observed in the HF, where the gain values tend to be higher in the abnormal population when compared with the normal infants. The p-values for the statistical test are shown in table 7.1. From the table it can be seen that only the gain in the VLF between MABP/ Δ HbD and in the HF between MABP/TOI produced significant differences between the populations. However, in the former case the gain values were higher in the normal population. In the analysis between MABP/TOI, in the HF, the gain values were higher in the population with abnormal outcome.

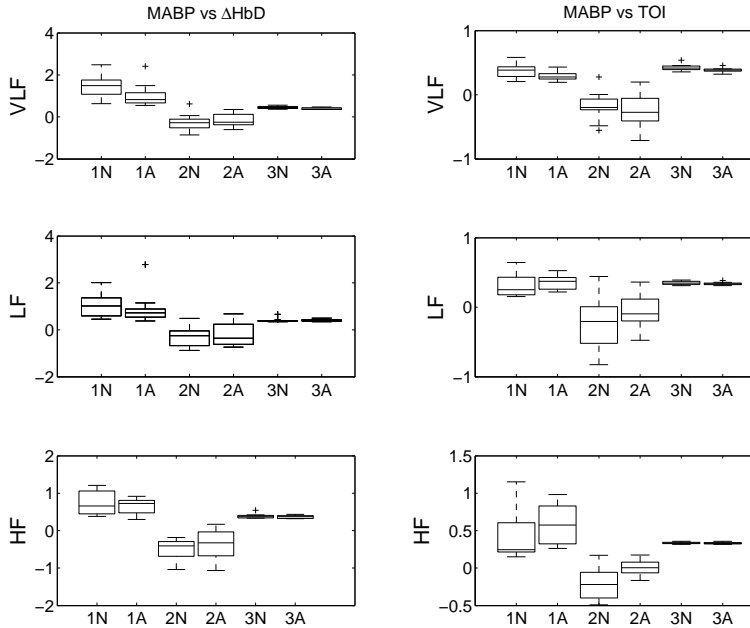


Figure 7.1: Boxplot indicating the differences in the score values between the normal (N) and abnormal (A) populations for the Leuven dataset. The transfer function gain (1), transfer function phase (2) and coherence values (3) are shown from left to right in each plot. From top to bottom the rows represent the average scores in three different frequency bands, VLF, LF and HF. The left column indicates the scores obtained for the analysis of MABP/ Δ HbD, the right column represent the scores obtained from the analysis of MABP/TOI.

7.1.4 Discussion

Impaired cerebral autoregulation is considered a risk factor for brain injury in the sick, premature infant [216] [197] [234] and has been associated with mortality in this population. Continuous measurements of MABP and CBF are thus of interest to assess cerebral autoregulation due to its importance in neonatal monitoring.

Autoregulation assessment can be done by means of coherence and transfer function analysis. Normally, high COH and gain scores or low phase values

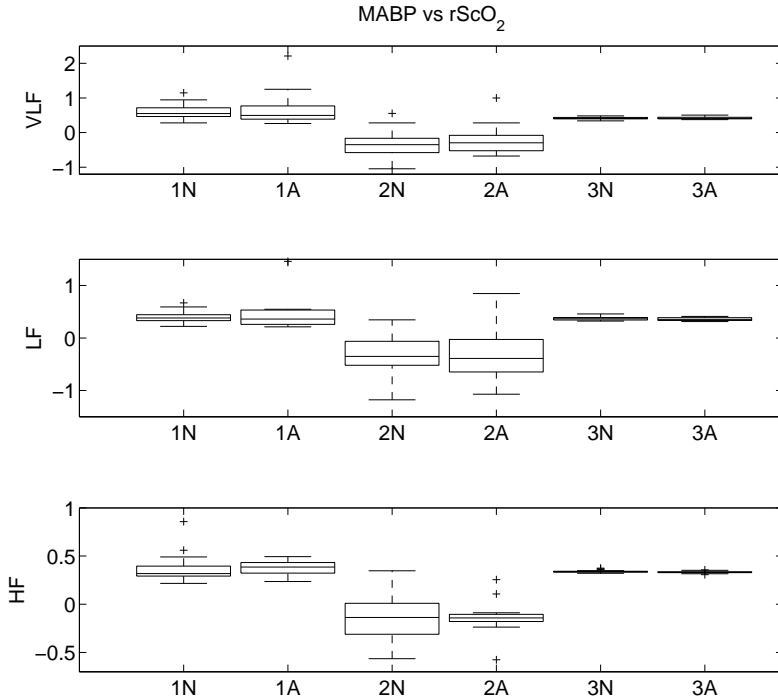


Figure 7.2: Boxplot indicating the differences in the score values between the normal (N) and abnormal (A) populations for the Utrecht dataset. The transfer function gain (1), transfer function phase (2) and coherence values (3) are shown from left to right in each plot. From top to bottom the rows represent the average scores in three different frequency bands, VLF, LF and HF. The scores were obtained by analyzing the relation between MABP/rScO₂ .

indicate a strong link between the dynamics of the MABP and the CBF signals, which may be caused by a failure in the autoregulative mechanism in the infant. However, in this study no strong evidence has been found between this scores and clinical outcome, which is in agreement with the results provided by other studies [81].

From the results provided in this study, the gain score seems to be the most reliable one to be used in clinical practice, since it was the only one who presented significant differences between the subjects. However, the size of the population

	Leuven		Utrecht
	MABP/ Δ HbD	MABP/TOI	MABP/rScO ₂
Gain VLF	0.0167	0.1194	0.617
Gain LF	0.3051	0.2706	0.8175
Gain HF	0.5184	0.034	0.1277
Phase VLF	0.9093	0.1599	0.5083
Phase LF	0.4704	0.5184	0.8175
Phase HF	0.2390	0.0874	0.7005
COH VLF	0.1194	0.3423	0.5692
COH LF	0.7903	0.4250	0.3324
COH HF	0.2100	0.3423	0.1356

Table 7.1: p-values obtained using the Kruskal-Wallis test between the scores.

is small and strong conclusion cannot be drawn from this study. However, other studies have also favored the gain score for cerebral autoregulation assessment [81].

7.1.5 Conclusions

No strong evidence was found between the scores for CA assessment and short term clinical outcome of the neonates. However, trends were observed, especially in the gain values. This study favors the gain score, even though it lacks precision. CA is a complex process that requires extra information given by other parameters. CO₂ reactivity is an important variable that affects the status of CA. This study indicates that the actual methods for CA assessment might benefit from the use of more complex methodologies that involved more physiological measurements.

7.2 Cerebral autoregulation assessment II

7.2.1 Introduction

Cerebral autoregulation is a complex process that refers to the maintenance of a constant cerebral blood flow (CBF) over a broad range of arterial blood pressures. This process avoids damage in the brain due to hemorrhagic brain injury and ischemia. Several mechanisms are involved in this process. So far,

evidence of the myogenic, metabolic and neurogenic ones has been described in the literature [164]. Cerebral autoregulation can be assessed by analyzing the relation between mean arterial blood pressure (MABP) and CBF, which can be measured continuously. The similarity in the dynamics of both signals has been quantified so far by means of correlation, (partial) coherence [216, 234, 193], among other methods. However, the role of other variables in cerebral autoregulation such as: partial pressure of carbon dioxide ($p\text{CO}_2$) and partial pressure of oxygen ($p\text{O}_2$) have not been well explored in clinical studies.

The main goal of this study is to examine how well the myogenic and the metabolic mechanisms involved in cerebral autoregulation can be assessed by mean of transfer function analysis and near-infrared spectroscopy (NIRS) signals. Moreover, it was studied how these derived measures are related to the long-term and short-term clinical outcome in premature infants.

7.2.2 Methodology

For this study the Zurich dataset was used. Assessment of the myogenic mechanism in cerebral autoregulation was done via analysis of the MABP/HbD transfer function; the metabolic mechanism was assessed by analysis of the $p\text{CO}_2$ /HbD transfer function. After preprocessing, the signals were divided into segments of 20 minutes with the maximum overlap (step size: one sample). For each segment, the transfer function gain and phase coefficients were calculated. The average of the coefficients in the frequency ranges 0.003Hz - 0.02Hz (very low frequency range: VLF), 0.02Hz - 0.05Hz (low frequency range: LF) and 0.05Hz - 0.1Hz (high frequency range: HF) were calculated [234] for further analysis. Moreover, in order to study the influence of different frequencies in autoregulation assessment, the values of the gain and the phase in all frequencies were also analyzed.

With respect to clinical outcomes, infants were classified as abnormal for short-term or long-term according to their clinical scores. For short-term outcomes, infants were classified as abnormal whenever bleeding, periventricular leukomalacia (PVL), intra-ventricular hemorrhage (IVH) or death occurred; otherwise they were classified as normal. For long-term clinical outcomes classification the Bayley scores (Mental and Physicomotor Development Index: MDI and PDI, respectively) were used. Infants were classified as normal if MDI and PDI > 85, otherwise they were classified as abnormal. In addition, in order to study the relation between birth weight (BW) and autoregulation state, the scores of infants with very low birth weight ($\text{BW} < 1200\text{g}$) were group-wise compared to those with a $\text{BW} > 1200\text{g}$. To assess whether the concordance scores were predictive for outcome (normal or abnormal) the non-parametric

Kruskal-Wallis test was applied, due to the lack of normality in the data distributions. The statistical analysis was performed using the statistics toolbox from MATLAB. All reported p -values were two-tailed and a nominal $p < 0.05$ was considered as statistically significant.

7.2.3 Results

Table 7.2 presents the median, minimum and maximum values of the gain and phase scores, calculated in the VLF, LF and HF frequency ranges for the normal and abnormal population according to the short-term and long-term classification criteria. In the short-term outcome analysis there were 23 infants classified as normal and 19 infants classified as abnormal, while in the long-term analysis 8 infants were classified as normal and 34 infants as abnormal. Statistically significant differences between the groups were found only in the gain score for the HF range, with a median value of 0.43 and 0.20 for the normal and abnormal classes ($p = 0.02$). All other scores did not differ significantly between the normal and abnormal subgroups.

Figure 7.4 shows the high-pass and low-pass filter characteristic behavior for the gain median values. However, for the myogenic mechanism (MABP-HbD) it seems that the high-pass filter behavior is only present in the normal population. The metabolic ($p\text{CO}_2$ -HbD) sub-system presents a low-pass filter behavior in both classes. The area under the curves was compared for the normal and the abnormal population. The areas for the median gain values for the myogenic mechanism were 0.096 and 0.043 ($\mu\text{mol.Hz/mmHg.L}$) for the normal and abnormal population respectively; for the metabolic mechanism the areas were 1.67 and 1.23 ($\mu\text{mol.Hz/mmHg.L}$). Those areas were statistically different between normal and abnormal populations, with ($p = 0.022$ and $p = 0.042$ for the myogenic and metabolic mechanism respectively).

Figure 7.3 presents the p -values from the Kruskal-Wallis test performed for the gain values of the metabolic subsystem ($p\text{CO}_2$ -HbD) in frequency domain for the BW analysis. In this analysis 15 infants were classified as abnormal with $\text{BW} < 1200g$ and 27 infants classified as normal with $\text{BW} > 1200g$. The differences between the median values in the normal and abnormal subgroups are statistically more significant in the VLF frequencies.

7.2.4 Discussion

Cerebral autoregulation is a property of the brain and is regulated by three different mechanisms, namely: the myogenic, metabolic and the neurogenic. On

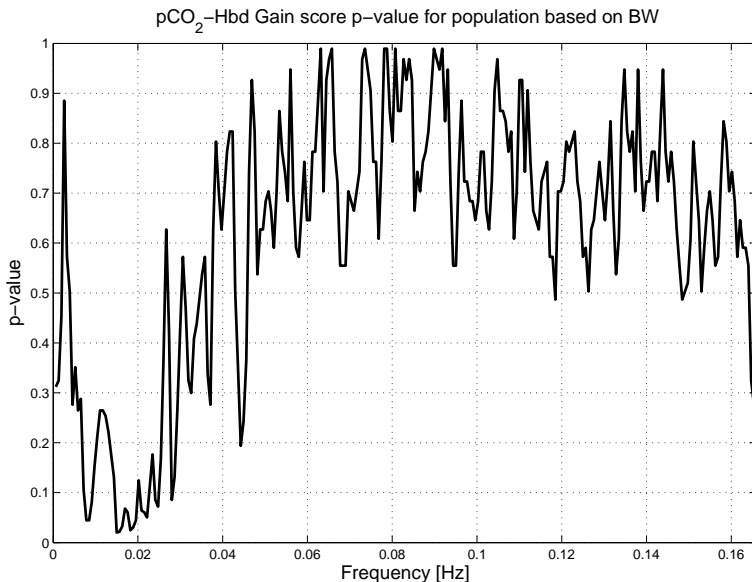


Figure 7.3: p-values from the Kruskal-Wallis test performed for each gain value (pCO₂-HbD) in frequency domain.

the one hand, the myogenic mechanism is in charge of minimizing the impact of the variations in MABP on the CBF. This mechanism is hypothesized to behave as a high-pass filter, where the slow oscillations in MABP are damped but the fast oscillations are reflected in the CBF [164]. This hypothesis appears to be correct according to the results provided in Figure 7.4. However, this high-pass characteristic was only found outside the normal frequency ranges where autoregulation is normally explored, and it is absent in the abnormal population. If only the VLF, LF and HF ranges are analyzed the system behavior reflects a low-pass filter characteristic. This can be due to the disturbances introduced by the pCO₂ in the MABP and CBF in the VLF. On the other hand, the metabolic mechanism is hypothesized to behave as a low-pass filter [164]. In this system the slow variations in pCO₂ are reflected in the CBF while the fast variations are neglected. This is consistent with the results presented in Figure 7.4. This behavior can be attributed to the time constant involved in the metabolic mechanism to adjust the muscular tone around the vascular wall. Thus fast changes in pCO₂ are too slow to produce big changes in CBF.

Outcome	Range	Scores	Normal	Abnormal	p-value
Short Term	VLF	Gain			
		MABP-HbD	0.79(0.37:2.04)	0.55(0.34:2.43)	0.07
		pCO ₂ -MABP	15.30(7.03:66.52)	14.61(6.21:28.05)	0.55
		Phase			
		MABP-HbD	-0.15(-1.08:0.45)	-0.06 (-0.68:0.77)	0.71
		pCO ₂ -MABP	0.01(-0.40:0.30)	-0.06(-0.54:0.32)	0.45
	LF	Gain			
		MABP-HbD	0.48(0.19:4.45)	0.39(0.15:5.23)	0.07
		pCO ₂ -MABP	17.03(9.00:43.13)	13.72(4.94:41.43)	0.24
		Phase			
		MABP-HbD	-0.08(-1.0:0.32)	-0.07(-0.58:0.67)	0.71
		pCO ₂ -MABP	0.02(-0.20:0.28)	-0.02(-0.23:0.20)	0.31
HF	Gain				
	MABP-HbD	0.43(0.11:10.02)	0.20(0.09:14.74)	0.02	
	pCO ₂ -MABP	9.28(3.02:42.48)	6.72(2.08:45.12)	0.14	
	Phase				
	MABP-HbD	0.005 (-0.42:1.39)	-0.005(-0.27:0.26)	0.81	
	pCO ₂ -MABP	-0.01(-0.15:0.14)	-0.01(-0.17:0.16)	0.79	
Long Term	VLF	Gain			
		MABP-HbD	0.80(0.43:1.78)	0.66(0.34:2.43)	0.22
		pCO ₂ -MABP	14.57(8.75:66.52)	15.44(6.21:56.54)	0.79
		Phase			
		MABP-HbD	-0.21(-1.08:0.29)	-0.09(-0.76:0.77)	0.40
		pCO ₂ -MABP	-0.01(-0.54:0.23)	-0.03(-0.43:0.32)	0.70
	LF	Gain			
		MABP-HbD	0.45(0.32:1.63)	0.39(0.15:5.23)	0.35
		pCO ₂ -MABP	16.65(11.78:23.23)	14.02(4.94:43.13)	0.50
		Phase			
		MABP-HbD	-0.07(-0.67:0.32)	-0.18(-1.00:0.67)	0.77
		pCO ₂ -MABP	-0.03(-0.23:0.20)	0.014(-0.20:0.28)	0.46
HF	Gain				
	MABP-HbD	0.45(0.21:4.00)	0.23(0.09:14.74)	0.23	
	pCO ₂ -MABP	9.62(6.35:12.08)	7.95(2.08:45.12)	0.54	
	Phase				
MABP-HbD	0.17(-0.42:1.39)	-0.03(-0.32:0.26)	0.09		
pCO ₂ -MABP	-0.04(-0.09:0.14)	-0.013(-0.17:0.16)	0.92		

Table 7.2: Comparison between normal and abnormal population scores for short-term and long-term outcomes using the gain and the phase. For the short term 23 infants presented a normal outcome, and 19 presented an abnormal outcome. For the long term outcome, 8 infants presented a normal outcome and 34 presented an abnormal outcome. Values are presented as median(min:max).

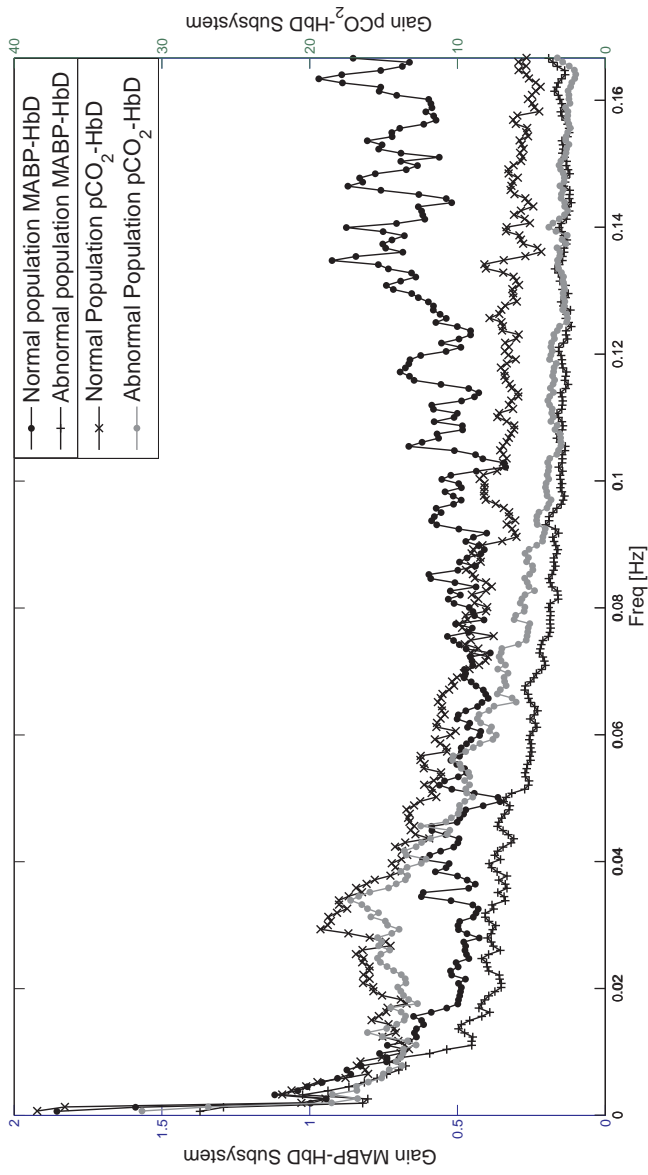


Figure 7.4: Median values of the gain frequency response for the MABP/HbD and the pCO₂/HbD sub-systems.

The gain and phase values in the myogenic and the metabolic sub-systems have been used to classify between normal and abnormal infants, based on different criteria. Only infants with abnormal short-term outcomes presented statistically different gain scores for the myogenic mechanism. All the other gain and phase scores shown in Table 7.2 did not present statistically significant differences between the normal and abnormal populations. Moreover, the scores in normal population tend to be higher than the ones from the abnormal population, contrary to what is expected. Indeed, according to the literature, higher gain values indicate a stronger coupling between HbD and MABP, which indicates impaired cerebral autoregulation and increases the probability of developing an abnormal outcome. Nevertheless, important trends could be observed. As shown in Table 7.2, all median values of the gain score tend to be higher in the normal than the abnormal population. Moreover, Figure 7.4 shows that the difference in median values for the normal and abnormal population becomes more pronounced at higher frequencies. The results from this study indicate the importance of the frequency range selected for cerebral autoregulation assessment as shown in figure 7.3. Moreover, the frequency response shown in Figure 7.4 suggests that the metabolic mechanism can be acting as a modulator of the myogenic mechanism action in the VLF.

7.3 ECMO study I

7.3.1 Introduction

Extracorporeal membrane oxygenation (ECMO) is a life support system that provides support for the heart and/or the lungs in patients with intractable cardio-respiratory failure. In veno-arterial (VA) ECMO patients are cannulated from the major neck vessels, the right common carotid artery (RCCA) and internal jugular vein (IJV). Blood drains from the patient and gets oxygenated externally by the ECMO circuit and returns back to the patient. VA ECMO bypasses both the heart and lungs and provides cardiac and respiratory support. Veno-venous (VV) ECMO bypasses only the lungs and in this case the patient has only one double lumen cannula inserted in the IJV. VV ECMO does not provide cardiac support. Neonates supported on ECMO often suffer from periods of hemodynamic instability, hypoxia and/or hypercapnia. In addition, the ECMO procedure itself may cause physiological changes due to ligation of the major neck vessels, heparinization, hemodilution and reduced arterial pulsatility, which can cause alterations in cerebral blood flow and potentially disrupt autoregulation [123]. Consequently, ECMO patients have increased risk for brain injury with reported abnormal neuroimaging ranging from 28% to 52%

depending in the imaging technique used [32]. Liem et al. [123] reported that MABP, SaO₂, pO₂ and pCO₂ were some of the variables that better explained changes in ΔHbT . Ejike et al. [56] reported no significant correlation between changes in ECMO flow and rScO₂ and a negative correlation between rScO₂ and pCO₂. Papademetriou et al. described oscillations in brain and peripheral haemodynamics during changes in ECMO flow, as measured with NIRS, and its use as a marker of cerebral autoregulation [161, 160].

Several studies have described changes in the cerebral hemodynamics before, during and after ECMO procedure. Liem et al [123] reported that mean arterial blood pressure (MABP), arterial oxygen saturation (SaO₂) and partial pressures of oxygen and CO₂ measured transcutaneously were some of the variables that better explained changes in total haemoglobin (ΔHbT) measured by NIRS. Ejike et al [56] reported that the regional cerebral oxygenation presented a negative correlation with arterial partial pressure of CO₂ (pCO₂) and no significant correlation with changes in ECMO flow. Papademetriou et al [161] used dual-channel NIRS system during ECMO flow changes and reported the presence of low frequency oscillations (<0.1 Hz) in peripheral oxyhemoglobin (ΔHbO_2), which are not present in cerebral ΔHbO_2 , demonstrating differences between cerebral and peripheral hemodynamic in this patient group.

Several studies have investigated the relationship between spontaneous changes in MABP and cerebral NIRS signals as assessment of brain autoregulation [234, 26, 35]. Brady et al [26] investigated correlation between NIRS and MABP in pediatric patients undergoing cardiac surgery with cardiopulmonary bypass for correction of congenital heart defects. They found an association between hypotension during cardiopulmonary bypass and impairment of autoregulation. The relation between MABP and ΔHbD and TOI by means of correlation, coherence and partial coherence analysis, and its use in clinical outcome prediction has been previously studied [35]; although higher values were found in the population with adverse clinical outcome, indicating stronger relation between MABP and $\Delta\text{HbD}/\text{TOI}$, no strong evidence was established. However, ECMO is a complex procedure and the study of the interrelation of hemodynamic variables, only, with MABP may not be sufficient.

In this study canonical correlation analysis (CCA) is used to investigate the differences between the interrelations in cerebral and peripheral NIRS measurements with the systemic variables in ECMO patients. In this analysis the systemic variables were defined as the independent dataset, while the cerebral and peripheral NIRS measurements were defined as dependent variables.

7.3.2 Methods

For this study the ECMO dataset was used. The interrelations between the set of peripheral and cerebral NIRS changes with the systemic variables were studied using two different approaches. The first approach used the complete measurement period and the ECMO flow when available as a parameter in the analysis. In the second approach, the signals were segmented in epochs of constant ECMO flow and the methods were applied separately to each epoch. In addition, in order to normalize the results to be comparable among the patients, we estimated the ratio between the percentage of variance in the peripheral NIRS explained by the systemic variables and the percentage of variance of the cerebral NIRS explained by the systemic variables. We call this index the peripheral to cerebral hemodynamics ratio (PCHR) and its calculation is indicated in equation (7.1). PCHR can be used to quantify the differences in the interrelations between both, cerebral and peripheral, circulation mechanisms versus systemic variations. PCHR values lower than 1 indicates that variations in the systemic variables are more likely to be reflected in the brain than in the muscle.

$$\text{PCHR} = \frac{\sigma_C^2}{\sigma_P^2} \quad (7.1)$$

where σ_C^2 and σ_P^2 represents the total explained variance of the cerebral and peripheral hemodynamics due to variations in the systemic variables. In addition biplots were used in order to display the overall relationship between the variables.

7.3.3 Results

Table 7.3 shows PCHR for different ECMO flows and for the full measurement period. Results for the full measured period show that only patient 4 presented a $\text{PCHR} > 1$, indicating that the variations in the systemic variables were more likely to be reflected in the brain NIRS measurements rather than the peripheral in that patient; in the other patients the peripheral NIRS changes are more likely to be affected by variations in the systemic variables. In addition, patient 3, in contrast with the other patients, was the only one who presented, at every ECMO flow rate, consistently $\text{PCHR} < 1$ and as it happened was the only patient in our group that the clinicians were confident to reduce the flow down to 70% from baseline.

	ECMO Flow Percentage							Full Period
	100%	90%	80%	70%	80%	90%	100%	
Patient 1	0.56	0.76	1.19	–	–	1.59	1.00	0.85
Patient 2	0.68	1.55	1.61	–	–	0.55	–	0.82
Patient 3	0.91	0.95	0.49	0.89	0.91	0.47	0.38	0.91
Patient 4	0.66	1.68	0.73	–	–	0.71	1.00	1.21
Patient 5	0.75	1.42	–	–	–	–	1.33	0.82

Table 7.3: Ratio between the percentage of the variance in the cerebral hemodynamic and the peripheral hemodynamic explained by variations in the systemic variables (PCHR), for different ECMO flow percentages and the full measurements period. Spaces marked with – indicate that there was not possible to perform the analysis due to the lack of measurements

Table 7.4 shows which systemic variables contributed more to the changes in cerebral/peripheral NIRS variables, when analyzing the completed measurement period. HR and skin temperature were the systemic variables that affected the most the cerebral and/or peripheral hemodynamical variables in the patients. MABP, CVP, Skin Temperature, SaO₂ and ECMO affected the NIRS variables in a lower extent.

	Patient 1	Patient 2	Patient 3	Patient 4	Patient 5
HR	B	B/L	L	B/L	B/L
MABP	B/L	B	L	X	B
CVP	B	B	L	B/L	X
CoreT	X	B	B/L	–	X
SkinT	L	B/L	B/L	B/L	B/L
SaO ₂	X	L	B/L	–	B/L
RR	X	B/L	–	X	X
EtCO ₂	X	–	B	X	X
Flow	–	B/L	B/L	B/L	–

Table 7.4: Ratio between the percentage of the variance in the cerebral hemodynamics and the peripheral hemodynamics explained by variations in the systemic variables (PCHR), for different ECMO flow percentages and the full measurements period. Spaces marked with – indicate that it was not possible to perform the analysis due to the lack of measurements.

7.3.4 Discussion

PCHR <1 , but close to 1, were observed in 4 out of 5 patients when analyzing the full measurement period. Earlier studies on neonates supported on ECMO indicate that autoregulation may be disrupted [123]; which can be the cause of PCHR values close to 1 as the brain hemodynamic and oxygenation changes will respond passively to systemic variations. In addition, when reducing ECMO flows is expected that the peripheral circulation would be more affected by systemic changes than the brain circulation. At baseline level (100% ECMO flow) all patients reported a PCHR <1 , when reducing the flow to 90% 3 out of 5 patients reported PCHR >1 , indicating that systemic changes were more reflected in the cerebral circulation than in the peripheral circulation; while patient 5 could not accommodate extra reductions in the flow and was returned to baseline level. At 80% flow 2 out of 4 patients presented PCHR >1 ; furthermore, in this stage, 3 of the patients could not accommodate more reductions in the flow and were returned to baseline level. Only patient 3 was able to accommodate a reduction to 70% in the ECMO flow and was the only patient who presented consistently PCHR <1 . When returning ECMO flow to baseline level, 3 out of 4 patients presented PCHR >1 . These results suggest that at low ECMO flows cerebral circulation is more vulnerable to changes in systemic variables.

In the population studied HR and skin temperature were the variables that affected the most the cerebral and peripheral NIRS signals. Out of 5 patients MABP was correlated with cerebral and peripheral hemodynamical variables in 3 and 2 patients respectively. Out of 4 patients SaO₂ was correlated with cerebral and peripheral hemodynamical variables in 3 and 2 patients respectively. Out of 4 patients EtCO₂ was correlated with the cerebral hemodynamical variables in one patient. Furthermore, ECMO flow presented a strong correlation with cerebral and peripheral NIRS variables in all the patients with flow measurements. The lack of homogeneity in relation to the systemic variables that affect the cerebral or peripheral circulation in our study suggests differences in the clinical condition of each patient; however, due to the small patient numbers is difficult to deduct any clinical hypothesis. Interestingly enough and in contrast with these results, Tisdall et al [212] in healthy adults found that changes in SaO₂ and EtCO₂ highly contribute to changes in the cerebral NIRS TOI signal. In addition, CCA pointed out that variation in the skin temperature highly affect the cerebral and peripheral NIRS changes; conversely, Harper et al [85] reported that a change in core temperature can produce changes in blood flow due to changes in blood viscosity and metabolic rate, among other reasons.

Several factors should be taken into account before interpreting the results provided by CCA. Among the limitations, the length of the signal under analysis and the presence of noise, non-linearities and nonstationarity can

be cited. In order to overcome some of these problems, and compare the results between patients, normalization such as the PCHR ratio should be used; otherwise, the results should be interpreted carefully. Cerebral and peripheral haemodynamic and oxygenation changes are caused by multiple factors; several systemic variables should be analyzed in order to obtain a general idea of the underlying mechanism affecting them. CCA is a useful tool to investigate this problem as it helps to assess and quantify the interrelation between both sets of variables, simultaneously.

7.4 ECMO study II

7.4.1 Introduction

Studies about the coupling between systemic and hemodynamical variables have been performed by means of regression models [56, 212]. Although these approaches seem to provide good results they can be highly affected by the presence of multicollinear variables and nonstationarities. In the previous section the interactions of these variables by means of CCA was studied. Although CCA provides a strong theoretical framework to study the coupling between multivariable datasets, the results are difficult to analyze due to its abundance which reduce its clinical value. Subspace projections methods, on the other hand, address straightforwardly this problem producing results that are not only easy to interpret mathematically but also clinically. The main goal of subspace projection techniques in signal processing is to mitigate the influence of noise in a signal of interest. Thus, orthogonal subspace projection (OrSP) and oblique Subspace Projection (OSP) aim to reduce orthogonal and oblique noise, respectively; where the noise can be due to measurement noise or contamination by other signal dynamics.

The main goal of this study is to investigate how OrSP and OSP can be used to decouple the dynamics of the systemic variables (SV) from the cerebral-peripheral hemodynamical variables (CHV, PHV). In addition the decoupled signals will be used to quantify the strength of the coupling between SV and the hemodynamical variables (HV).

7.4.2 Methods

In this study measurements from a patient, 3 days old, from the ECMO dataset are used to illustrate how the algorithms works. The systemic and NIRS measurements from the patient are shown in figure 4.3.

Decoupling algorithm

The problem was addressed in two different ways. On one hand, the projection of the cerebral and peripheral hemodynamical variables (CHV, PHV) in the subspace spanned by the systemic variables (SV) decomposes CHV and PHV in a part that is linearly related to SV and a part that is orthogonal to it. The orthogonal part can be interpreted as the part of the HV that is related to measurement noise, not measured variables and nonlinear coupling with SV. On the other hand, the CHV and PHV can be projected onto each one of the SV by calculating the corresponding oblique projection matrices. The wavelet transform of the SV was used as a basis to define their signal subspace. In this study a 5th level discrete wavelet decomposition, with Daubechies 4 as mother wavelet, was considered. Moreover, in order to account for possible coupling delays, the wavelet decomposition of SV and its delayed versions were included in the regressors matrix. In this study a delay of three samples was used. In addition, the ratios between the power of the projected and original signals, were computed as a measure of the coupling between the variables.

By using OrSP, the projection of the CHV/PHV will represent the part of the signal that is linearly related to the SV. The ratio between the power of the projected CHV and the PHV is proposed as a monitoring variable to assess the status of the mechanisms that regulates cerebral haemodynamics. Furthermore, by using OSP the same ratio between the power of the projected CHV and PHV onto each SV, separately, can be used to monitor the influence of each SV on the cerebral haemodynamics.

7.4.3 Results

In figure 7.5, the decomposition of the cerebral and peripheral TOI in the components corresponding to each SV is shown. The peripheral TOI is more affected than the cerebral TOI by variations in SV; this might be due to intrinsic mechanisms that regulate cerebral hemodynamics. The ratio PC/PP was 0.62 for ΔHbO_2 , 0.058 for ΔHHb and 0.045 for TOI. In table 7.5 the ratios between the powers of the projected CHV/PHV in the SV are displayed. These ratios reveal the SV that affect at most the HV. This table shows that variations in SaO_2 possess the highest impact in the variations of CHV and PHV. However, its influence is more pronounced in the peripheral hemodynamics. In addition EtCO_2 appears to have a higher impact in the cerebral than in the peripheral hemodynamics.

Algorithm 5 Decoupling algorithm

input: Systemic Variables: $SV(m \times n)$, and Haemodynamic Variables: $CHV(m \times d)$ and $PHV(m \times d)$.

output: Projected CHV/PHV : $CHV_P((m - 3) \times d \times n)$ and $PHV_P((m - 3) \times d \times n)$, ratios for: the projected CHV/PHV onto SV , P and for the projections onto each SV , $Pow(d \times n)$.

begin

$SV \leftarrow SV - \hat{S}V$

$aux \leftarrow DWT(SV)$

$base \leftarrow$ block Hankel matrix of aux , using a delay of 3 samples.

$CHV_aux \leftarrow$ projection of CHV onto $C(base)$.

$PHV_aux \leftarrow$ projection of PHV onto $C(base)$.

$P \leftarrow$ ratio between power CHV_aux/PHV_aux ;

for $i=1:n$

 Compute oblique projector for the i^{th} SV .

for $k=1:d$

$CHV_P(:, k, i) \leftarrow$ CHV onto the i^{th} SV

$PHV_P(:, k, i) \leftarrow$ Projection of PHV onto the i^{th} SV

$Pow(k, i) \leftarrow$ ratio between the power of $CHV_P(:, k, i)$ and $PHV_P(:, k, i)$

end for

end for

end

7.4.4 Discussion

OrSP and OSP were able to decompose the CHV/PHV in a series of components related to each SV . This approach is useful as it serves as a basis for the quantification of the coupling between the hemodynamical and the systemic variables. The strength of the coupling can be measured by computing the ratios between the power of the components in the decomposed and the original signal for each SV . By including wavelets as a basis for the subspace of the systemic variables the non-stationary effects are taken into account and the influence of the noise is reduced; however, further studies are needed in order to validate these results and evaluate their clinical impact. In addition, the effect of nonlinear coupling should be further studied. In summary, in this study we have presented a way to decouple the influence of SV in CHV and PHV . This information may yield high clinical impact since it tells to the clinician which variable has the highest impact in the cerebral hemodynamics. Based on this information the clinician can prepare an adequate treatment.

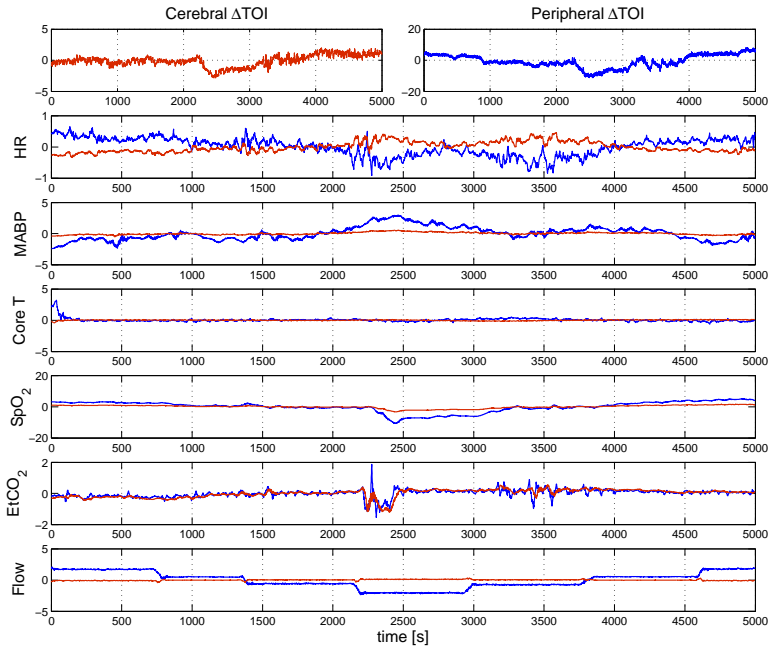


Figure 7.5: Decomposition of the Cerebral and Peripheral TOI in the components related to each one of the systemic variables under analysis. In red the decomposition for the cerebral TOI is shown, while blue represents the decomposition for peripheral TOI.

7.5 Lamb Study

7.5.1 Introduction

The main goal of this study is to investigate the use of the wavelet based transfer function (WBTF) and the nonlinear method presented in a previous chapter in the study of cerebral hemodynamics. This dataset is adequate to test this methodologies, since the lambs were subject to controlled changes in MABP, which represents a challenge that activates several physiological mechanisms that try to maintain the cerebral hemodynamical homeostasis. Furthermore, since measurements of CBF and TOI are available this will allow to compare if they produce similar results.

	HbO ₂	HHb	TOI
Cerebral Hemodynamics			
HR	5.43	0.41	1.72
MABP	2.07	4.76	2.41
Core T	4.24	4.25	0.32
SaO ₂	26.63	48.70	71.61
EtCO ₂	17.89	1.39	4.63
Flow	8.83	4.44	0.46
Peripheral Hemodynamics			
HR	2.23	5.03	0.49
MABP	15.13	7.55	7.28
Core T	1.68	0.79	0.56
SaO ₂	38.20	68.09	70.57
EtCO ₂	4.02	9.31	0.37
Flow	5.57	1.43	9.63

Table 7.5: Percentage of power in the corresponding Peripheral or Cerebral Hemodynamical variable due to the systemic variables. Values are expressed in %

7.5.2 Data and Methods

In this study the Lamb dataset will be used. First, the use of WBTF will be presented. For this purpose the 4th derivative of the complex Gaussian wavelet was used as mother wavelet. The analysis was performed in the frequency range 0.003 - 0.1Hz, therefore scales from 5-160 were used in the study. Furthermore, the mean profile in frequency for the gain and the phase of the transfer function were obtained for the relation between MABP/CBF and MABP/TOI. Furthermore, the time profiles for the gain were also obtained.

Second, for the analysis of the nonlinear methods, the EtCO₂ and MABP were used as regressor for the TOI and the CBF, independently. The regression was tuned using a KPCR model, separately for each target function. The segment used in this study has a duration of 23 minutes, with $f_s = 1\text{Hz}$. Therefore, the data contains a total of 1380 samples. To accelerate the training a subset consisting of 345 equidistant points from the original dataset was used for training. Once the model was tuned the output for the complete set was estimated. Furthermore, the nonlinear contribution from MABP and EtCO₂

was estimated. Finally, a test set covering the range of the original signals was artificially generated in order to produce a surface where the influence of MABP and the EtCO₂ on the TOI and the CBF is displayed.

7.5.3 Results

Wavelet Based Transfer Function

Figures 7.6 and 7.7 show the results from the gain values of the WBTF between MABP/CBF and MABP/TOI respectively. The figures clearly indicate that the system is nonstationary, meaning that variations in the CA mechanism, in the frequency domain, are observed along the measured time. In addition, huge peaks are seen in the low frequency components, these peaks are related to the slow frequency challenges in MABP. These peaks might be related to metabolic activity that is modulating the action of the CA and it is result of a compensatory physiological effort to restore CBF [157, 144, 114]. The figures also show a varying pattern where the response to changes in MABP on the CBF and TOI behave like a low-pass filter or like a high-pass filter. Normally high gain values in the low frequencies are observed during periods of slow changes in MABP.

The mean average profile of the gain in the frequency domain for the relations MABP/CBF and MABP/TOI are shown in figure 7.8. In the literature it has been mentioned that the response of the CA mechanism to a challenge in MABP behaves like a high-pass filter [243, 164]. It can be seen that this is true for the relation between MABP/CBF, except for some gain values in the VLF range, that might be related to metabolic activity. However, for the relation between MABP/TOI, this relation does not hold. In fact, the transfer function behaves more like a band pass filter, where the slow and the high oscillations in MABP do not reflect a change in cerebral oxygenation. In addition, taken into account the results provided by Wong et al., the relation between TOI and CBF is coherent for frequencies below 0.1Hz [235], it can be seen that when the TOI approaches this frequency its frequency response diverge from the one of the CBF.

The mean average profile of the gain in the time domain is shown in figure 7.9. This profile clearly shows that the gain values fluctuate along the time domain. Large variations are due to the influence of the low frequency components observed previously. When comparing the profiles from the MABP/CBF and MABP/TOI they do not differ much, however, as mentioned before, TOI values seem to be more sensitive to changes in MABP.

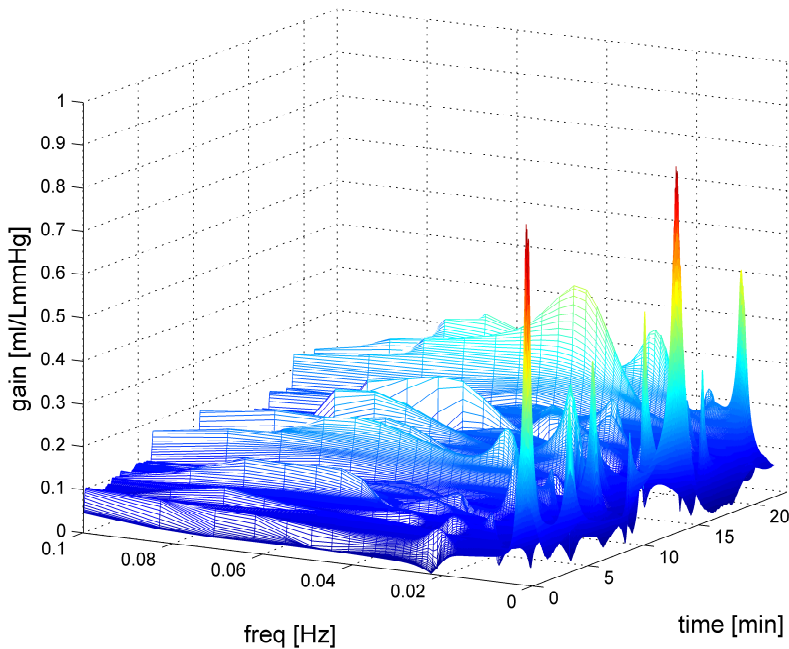


Figure 7.6: Gain values obtained from the WBTF between MABP and CBF.

KPCR and subspace projections

Figures 7.10 and 7.11 show the results from the KPCR regression model and the decomposition algorithm for the relation between $\{\text{MABP}, \text{EtCO}_2\}$ with TOI and $\{\text{MABP}, \text{EtCO}_2\}$ with CBF. First, it can be seen that when a scatter plot using the raw measurements the relation lacks of structure due to the influence of noise. The nature of the noise that hides the relation between the regressors and the target function might be from the environment or physiological. By performing the decomposition proposed in this chapter, the influence of other variables is eliminated and the relation between each regressor and the target function is found. From the scatter plot between MABP/TOI it is interesting that a kind of autoregulation plateau is observed from the estimated model. On the other hand, the relation between EtCO_2/TOI is opposed to what is expected. Normally hypocapnia should produce vasoconstriction, however, in the obtained model there is a moderate increase in oxygenation levels. However, the changes in EtCO_2 for this dataset were not large, for this reason, this regressor might lack of power to be corrected represented in this regression

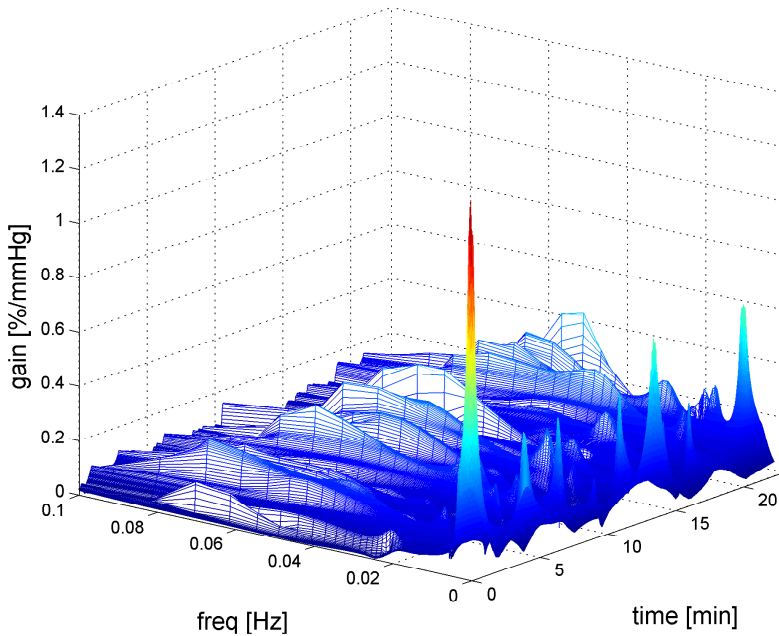


Figure 7.7: Gain values obtained from the WBTF between MABP and TOI.

setting. Finally, the figure also shows that the regression model can adequately describe most of the dynamics of TOI, using MABP and EtCO_2 , the residuals might be due to other physiological variables that have not been measured and instrumentation noise.

On the other hand, results from MABP/CBF are quite similar to the ones obtained for TOI. However, the regression model was able to fit better the changes in CBF, this may suggest that TOI is affected by fluctuations of other variables not measured in this experiment.

Finally, the generated surfaces for the relation between the regressors and TOI/CBF are shown in figures 7.12 and 7.13. These figures are interesting to explore the coupled relation between MABP, EtCO_2 and TOI/CBF. When comparing them with the cerebral autoregulation curve, presented in chapter 1 figure 1.1, it can be seen that cerebral autoregulation is a far more complex process. The curve presented in figure 1.1 only reflects the average action of the autoregulation mechanisms, and does not take into account the influence of other physiological variables. To the best of our knowledge this has only been

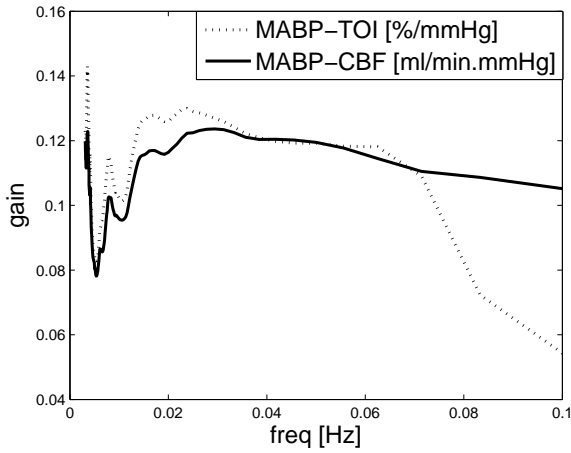


Figure 7.8: Mean value for the gain along the frequency axis. The solid line represents the relation between MABP/CBF, while the relation between MABP/TOI is seen as a dashed line.

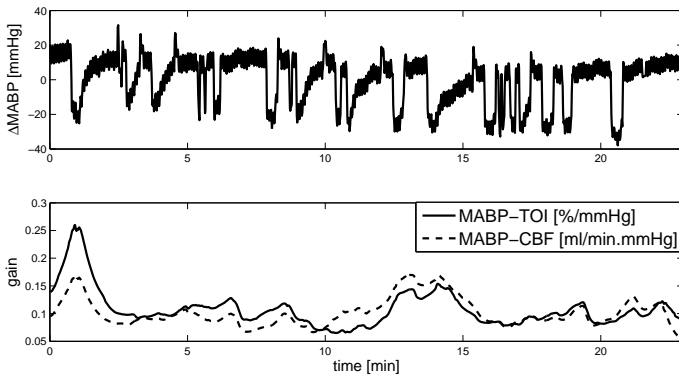


Figure 7.9: Mean value for the gain along the time axis. The solid line represents the relation between MABP/TOI, while the relation between MABP/CBF is seen as a dashed line.

shown in a recent paper where they use principal dynamic modes to describe this relation, together with a nonlinear Volterra model [133]. How this methodology compares to the one we proposed is yet to be investigated.

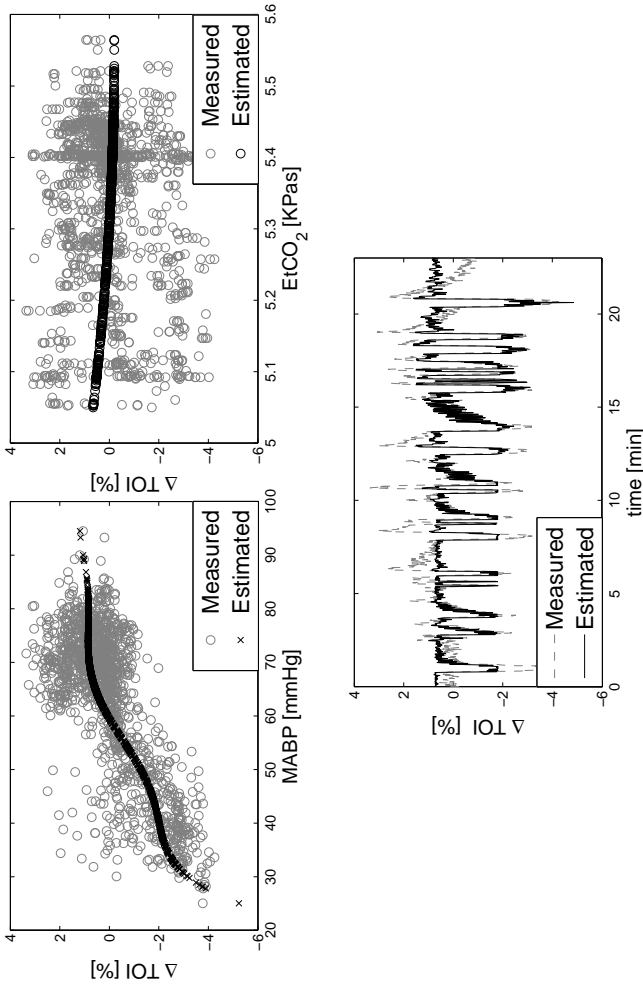


Figure 7.10: Results from the KPCR regression model. The upper figure shows the scatter plots between the MABP/ ΔTOI and $EtCO_2$ / ΔTOI , for the original data, in gray circles, and the projections obtained using the methodology proposed in this thesis, in black crosses. The lower plot shows the original recordings of ΔTOI , in a gray dashed line, and the estimated output of the KPCR model, in the solid black line.

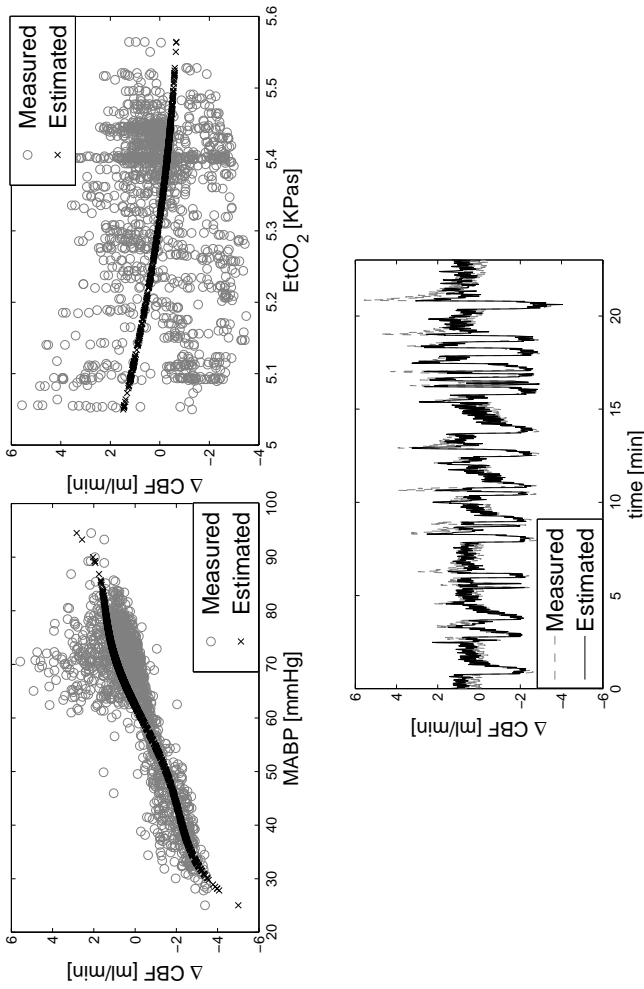


Figure 7.11: Results from the KPCR regression model. The upper figure shows the scatter plots between the MABP/ Δ CBF and EtCO₂/ Δ CBF, for the original data, in gray circles, and the projections obtained using the methodology proposed in this thesis, in black crosses. The lower plot shows the original recordings of Δ TOI, in a gray dashed line, and the estimated output of the KPCR model, in the solid black line.

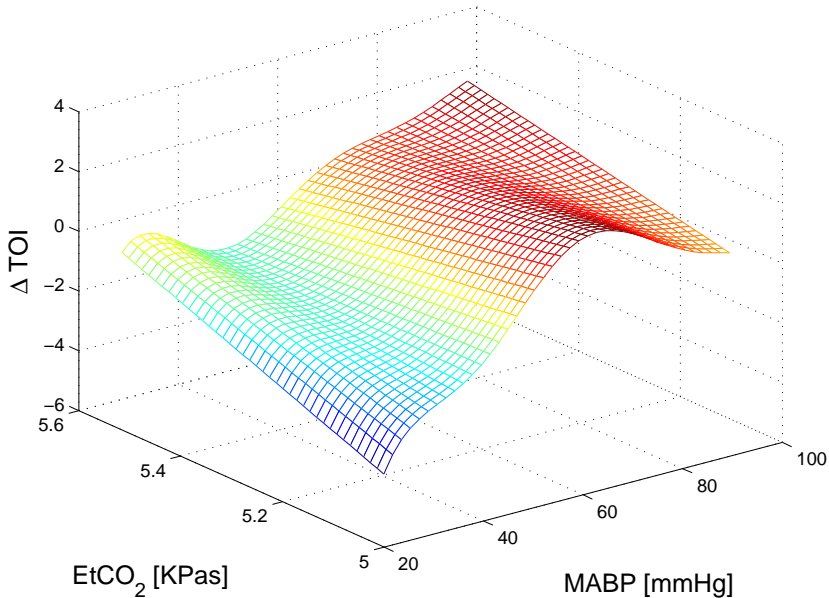


Figure 7.12: Surface representing the nonlinear relation between MABP and EtCO₂ on the cerebral TOI.

7.5.4 Discussion

This study has shown that WBTF and KPCR are able to identify some key aspects of CBF regulation. On one hand, WBTF is able to identify the changes in the system. Low frequency components were observed in the gain spectrum. We hypothesized they are due to the influence of other physiological variables. On the other hand, WBTF is able to identify the high pass characteristics of the CA mechanism, when analyzing the relation between MABP/CBF,. However, the gain for MABP/TOI presents a band-pass mechanism, to the best of my knowledge this has not been reported in the literature, which makes it an interested topic for future research. Finally, the time profile of the gain seems to be a promising parameter to identify the variability of the CA mechanism. Further research is needed in order to define whether this profile is useful for clinical applications. Possible research directions should investigate the extraction of features from the time profile that can be linked to clinical outcome, and the adaptation of this method for bedside monitoring.

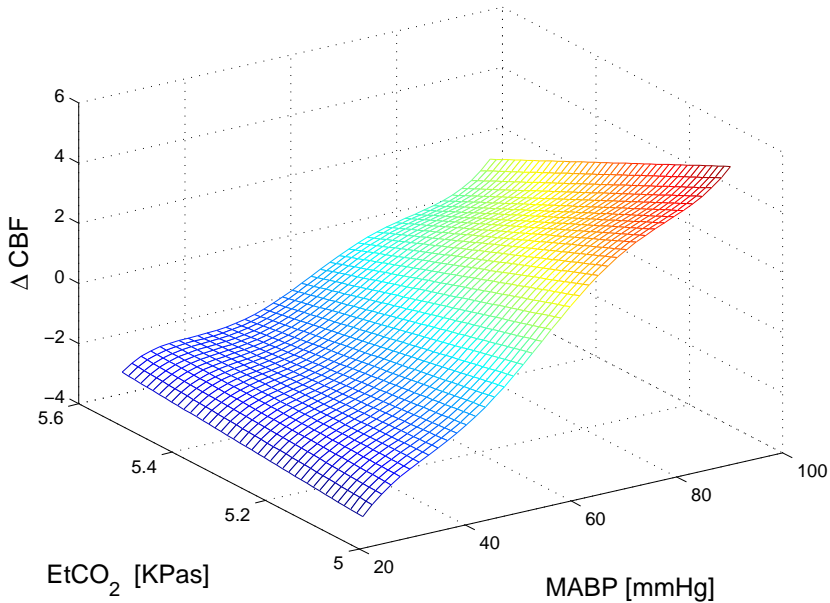


Figure 7.13: Surface representing the nonlinear relation between MABP and EtCO₂ on the CBF.

On the other hand, KPCR also shows interesting results. The decomposition algorithm proposed in this thesis retrieves a curve similar to the autoregulation plateau for the relation between MABP and CBF/TOI. However, the relation between EtCO₂ and CBF/TOI indicated an opposite relation than expected. But, it was between the range of variation of the variable. We speculate that this is due to the lack of variations in this regressor. Therefore, it lacks of enough variations in order to produce robust results. This decomposition scheme is of high clinical impact, since it provides a mathematical tool that the clinicians can use to identify the impact of the treatment of one specific variable on another one. In the framework of cerebral hemodynamics monitoring, i.e it can help the clinicians to identify if treatment for hypertension improves the oxygenation in the brain.

7.6 Labetalol study

7.6.1 Introduction

Hypertension is the most common medical disorder encountered during pregnancy and is estimated to occur in about 6-8% of pregnancies [142]. Hypertensive disorders of pregnancy (HDP) should be treated in order to prevent maternal complications and improve fetal maturity by permitting prolongation of pregnancy and minimizing fetal exposure to possible adverse effects of antihypertensive treatment. There are several advantages and disadvantages of HDP treatment [142]. In pregnancy longer than 34 weeks, induction of labour in the occurrence of hypertension and pre-eclampsia is generally considered the best treatment to improve maternal and neonatal outcome. However, there is considerable morbidity in late preterms explained by the mode of delivery and gestational age [113]. Labetalol is a selective $\alpha-1$ (peripheral vasodilation) and non-selective β receptor antagonist (preventing reflex tachycardia and maintaining cardiac output), which is often used in HDP treatment. Due to its lipophilic properties it easily passes the placental barrier, which is in essence a lipid membrane. Hypotension, bradycardia and hypoglycaemia are possible neonatal side effects, but may also occur in (preterm) infants regardless of labetalol exposure. Labetalol's half-life in adults is approximately 6 hours but accumulation occurs. However, half-life after maternal use in a preterm baby with clinical signs of β -blockage was 24 hours [84]. Conflicting evidence exists for specific neonatal side effects described after use of labetalol for maternal hypertension. Nevertheless oral and intravenous labetalol is used as a first or second-line treatment in HDP due to its highly effective antihypertensive properties and because it has a better profile than hydralazine and other β -blockers [131, 130]. Scarce information on neonatal cerebral hemodynamics in gestational hypertension and pre-eclampsia is available. However, not much is known about the true influence of maternal use of labetalol on the neonatal hemodynamical parameters (bradycardia, hypotension) in the brain, mainly since cerebral fetal circulation is subject to changes due to brain-sparing in severe pre-eclampsia.

The main goal of this study is to investigate labetalol-induced effects on neonatal cerebral autoregulation mechanisms during the first three days of life.

7.6.2 Methods

For this study the Labetalol dataset was used. The signals were preprocessed as indicated in the algorithm 4. The resulting signals were filtered with

a mean average filter and then downsampled to 1Hz in order to obtain a common sampling frequency. Cerebral autoregulation was assessed by means of correlation, coherence and transfer function analysis between MABP and $r\text{ScO}_2$. The correlation, coherence and transfer function scores were calculated using a time-sliding window of length 15 minutes and overlapping time of 1 minute. Coherence and transfer function analysis were performed using the Welch method for the calculation of the respective cross-power and auto-power spectral densities. This method involves a further segmentation of the signals into 5-minute epochs with an overlapping of 4.5 minutes. The average of the coefficients in the frequency ranges 0.003Hz-0.02Hz (very low frequency range: VLF), 0.02Hz- 0.05Hz (low frequency range: LF) and 0.05Hz-0.1Hz (high frequency range: HF) were calculated [234] for further analysis.

To assess whether the scores and pulse pressure values were different between the populations the non-parametric Kruskal-Wallis test was used, due to the lack of normality in the data distributions. The statistical analysis was performed using the statistics toolbox from MATLAB. All reported p-values were two-tailed and a nominal p-value < 0.05 was considered as statistically significant.

7.6.3 Results

When comparing the correlation, coherence and gain values for the three different populations, taking the complete measurements for the first three days of life per group, no statistically significant differences between the scores were found. However, when the analysis was performed in a day-by-day basis, the HDP+Lab presented higher values of gain during the first day of life, in the VLF and LF bands, when compared with the gain values for the Control and the HDP-Lab group ($p < 0.05$). In addition, the gain values during the first day of life, in the VLF and LF bands, for the HDP+Lab population were higher than the values in the second and third day ($p < 0.05$). This behavior indicates a progression towards normality. Figure 7.14 shows the gain for a representative subject from the HBP+Lab group. Correlation, coherence and phase were still not statistically significant. Pulse pressure values were lower for the HDP+Lab group when compared with the other groups. In addition, for the three populations the pulse pressure values were lower during the first day of life and presented an increased profile in the second and third day. Figure 7.15 shows the median values of pulse pressure for the three different populations and its evolution during the first three days of life. In Table 7.6 the median values of pulse pressure and its range of variation (minimum \pm maximum values) are indicated.

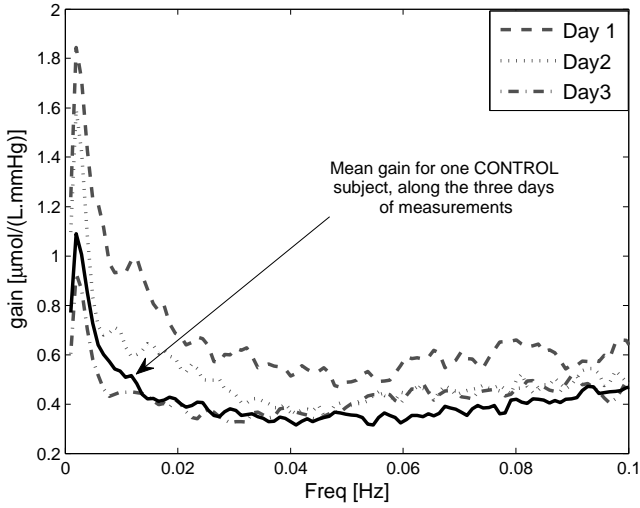


Figure 7.14: Gain values for a representative subject from the HDP+Lab group. Gain values during the first, the second, and third day are shown together with the values from a control subject for comparison.

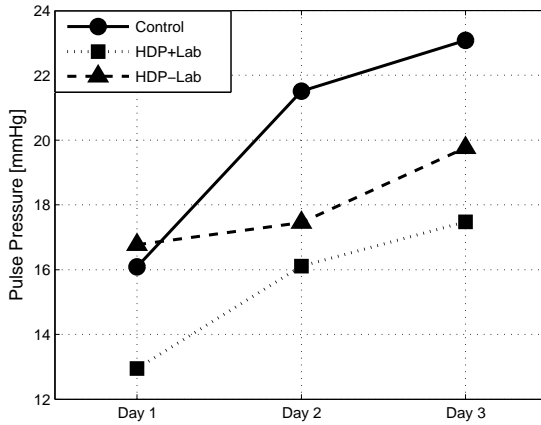


Figure 7.15: Median values of pulse pressure for the three different groups, Control, HDP+Lab and HDP-Lab, during the first three days of life.

	Day 1	Day 2	Day 3
Control	16.08 (5.97-27.54)	21.50 (10.25-28.47)	23.07 (15.73-32.64)
HDP+Lab	12.94 (9.32-20.17)	16.10 (8.24-25.11)	17.47 (7.67-27.11)
HDP-Lab	16.76 (9.05-23.18)	17.45 (9.87-27.34)	19.76 (10.04-27.87)

Table 7.6: Pulse pressure values for the different populations during the first three days of life (all values are given in mmHg).

7.6.4 Discussion

In this study we found that the maternal use of labetalol induces high values of the transfer function gain between MABP and rScO₂. These high values are concomitants with low values of pulse pressure. In [101] low values of pulse pressure indicate the presence of vasodilation due to the use of drugs for hypertension treatment. However, labetalol is a non-selective β antagonist; its action also reduces cardiac contractility which is reflected as a reduction in pulse pressure. When comparing pulse pressure values from the HDP+Lab and HDP-Lab group a stronger reduction is observed in the HDP+Lab group, this may be caused by a combination of vasodilation and reduction in cardiac contractility. We hypothesized that vasodilation was present in this group due to the concomitant reduction in pulse pressure and increase in transfer function gain values. Vasodilation reduces the effect of the myogenic mechanism responsible for cerebral autoregulation, which increases the transfer function gain. This vasodilation may be produced by the accumulation of labetalol due to its maternal use [175]. Interestingly, a trend towards normality can be seen in the gain and pulse pressure values. The gain values return to normality by the end of the third day, while the pulse pressure values were still lower than normal by then. This may be due to a decrease in labetalol. This vasodilatory effect might also be caused by brain-sparing. In [187] higher mean values in cerebral blood flow velocity were reported in children with evidence of brain-sparing. However, no differences were found in the amount of neonates that presented brainsparing between the HDP+Lab and HDP-Lab groups.

Correlation, Coherence and transfer function phase did not present differences between the studied populations. This may be due to the fact that impaired cerebral autoregulation is reflected not only by a coupled dynamics between MABP and cerebral blood flow, but also by the strength of this relation. This strength is assessed by the gain of the transfer function but not by the correlation and coherence scores. Moreover, in a recent study carried out in our group [37], we found that, among the aforementioned methods, transfer function analysis is the most robust method for cerebral autoregulation assessment. This result

is in agreement with the results provided by [81].

7.6.5 Conclusion

In conclusion, there is evidence indicating that labetalol induces changes in the cerebral autoregulation mechanism of the neonates possibly due to its accumulation. This accumulation of labetalol might produce vasodilation, which leads to high values of gain, impairing the myogenic mechanism of cerebral autoregulation. Further studies are necessary to evaluate whether this phenomenon also has an effect on the later neurological outcome of the patients.

7.7 Duchenne Muscular Dystrophy Study

7.7.1 Introduction

Duchenne muscular dystrophy (DMD) is an X-linked recessive muscle disease affecting 1 in 3500 newborn boys worldwide. Besides progressive weakness of the skeletal muscles leading to loss of ambulation by the age of 12 years, DMD patients develop cardiac and respiratory complications that lead to early morbidity and mortality [58]. DMD is caused by mutations in the DMD gene which encodes for dystrophin, a subsarcolemmal protein critical for muscle membrane integrity. One pathway to explain the pathogenesis of DMD involves enhanced sympathetic vasoconstriction by a downregulation of the neuronal nitric oxide synthase (NOS) in DMD, resulting in functional muscle ischemia determined by a mismatch between the metabolic demand and blood flow supply in exercising muscles [184].

Further advancement in both pathogenic understanding as in non-invasive disease-monitoring capabilities using a combination of near-infrared-spectroscopy (NIRS) and surface-EMG (sEMG) may contribute to the development and assessment of novel therapeutic approaches for DMD. So far, NIRS has been utilized in DMD-subjects to assess significant changes in tissue oxygenation induced by defective reflex sympathetic activation in exercising muscles [184]. Changes in the reoxygenation phase due to contraction-induced alterations in oxidative metabolism have not yet been investigated. The main goal of this study is to investigate in young children the potential use of concomitant measurements of sEMG and NIRS to assess differences in the oxidative metabolism before, during and after the contraction of the biceps brachii of DMD patients versus age-matched healthy controls.

7.7.2 Methods

In this study the Duchenne dataset will be used. sEMG and NIRS signals were measured while executing the protocol shown in figure 4.4. Figure 7.16 shows the differences between a recording from a control and a DMD subject. Measurements with sEMG provide more information about differences in electrical activity between controls and DMD. Additionally, sEMG is used for an exact cut-off point for the start and the end of the contraction and the relaxation phase. Two features were extracted from the EMG recordings: mean power frequency (MPF) and the Shannon entropy. The MPF represents the frequency at which most of the power of the EMG signal is produced and decreases linearly during muscle fatigue due to a reduction in the firing pattern of the muscle fibers [62, 207]. MPF changes with time, therefore for its calculation, the EMG signal is divided in overlapping segments, for each segment the MPF value is computed. The calculation of the MPF for each segment is done using the following formula:

$$MPF(i) = \frac{\sum_{k=1}^{NFFT/2} f_k \mathbf{X}_i(k)}{\sum_{k=1}^{NFFT/2} \mathbf{X}_i(k)} \quad (7.2)$$

where $\mathbf{X}_i(k)$ represents the k^{th} component component of the power spectrum density of a segment i obtained from the EMG signal, $NFFT$ is the number of points used in the computation of the Fourier transform and f_k is the k^{th} component of the frequency vector. Three features were extracted from the MPF time series:

- The MPF value at the beginning of contraction. This parameter was called MPF_1
- The MPF value at the end of contraction. This parameter was called MPF_2
- The slope of the MPF decay. This feature was called $MPF\ slope$.

On the other hand, the Shannon entropy is a measurement that reflects the signal variation [95]. entropy is computed as follows:

$$h = - \sum_i p(x_i) \log_a p(x_i) \quad (7.3)$$

where $p(x_i)$ represents the probability density of the variable x , and a represents the base of the logarithm. Depending on the selection of the base, the units for the entropy change.

Since atrophy in DMD leads to a reduced number of active motor units this reduces the complexity of the EMG signal. In this study it is hypothesized that the entropy values are lower in the DMD population when compared with control.

During exercise TOI in the muscle describes a characteristic behavior, which relates to the activity [62, 207]. In figure 4.5 the response of the TOI to a contraction is depicted. At the beginning of the contraction, consistent with the fast deoxygenation, the TOI-curve describes a fast linear decay, followed by a stabilization phase. The final stabilization value of the TOI is given by the relation between demand and consumption of oxygen, which is related to the strength of the contraction. At the end of the contraction, TOI exhibits a steep increase towards baseline levels. In this study the TOI profile has been characterized using the following parameters:

- During the linear decay phase at the beginning of the contraction, the slope and the time until a stable TOI is reached were measured. These parameters are called *TOI slope* and *Time to Linear Decay (TLD)*.
- The reduction in TOI was calculated as the difference between the TOI before contraction and its stabilization value after contraction. This parameter is called ΔTOI .

These parameters are displayed in Figure 7.17.

Meanwhile, HHb and HbO₂ exhibit also a characteristic behavior during activity. However, the dynamics of these signals present patterns that were not present in the TOI. Therefore, in order to characterize their behavior extra parameters were needed. The response of HbO₂, HbT and HHb to a contraction is shown in figure 4.5. Figure 7.18 shows the dynamical response of the HbO₂ together with the parameters that describe its dynamics. During contraction HbO₂ exhibits a linear decay until a stable level is reached. This level is sustained until the end of the contraction and represents the level when the oxygen demand and the consumption are in equilibrium with the oxygen supply. At the beginning of the recuperation phase, the HbO₂ increases fastly and exceeds the baseline level. After a maximum is reached the HbO₂ values converge to the baseline levels. The HbO₂ dynamics were characterized using the following parameters:

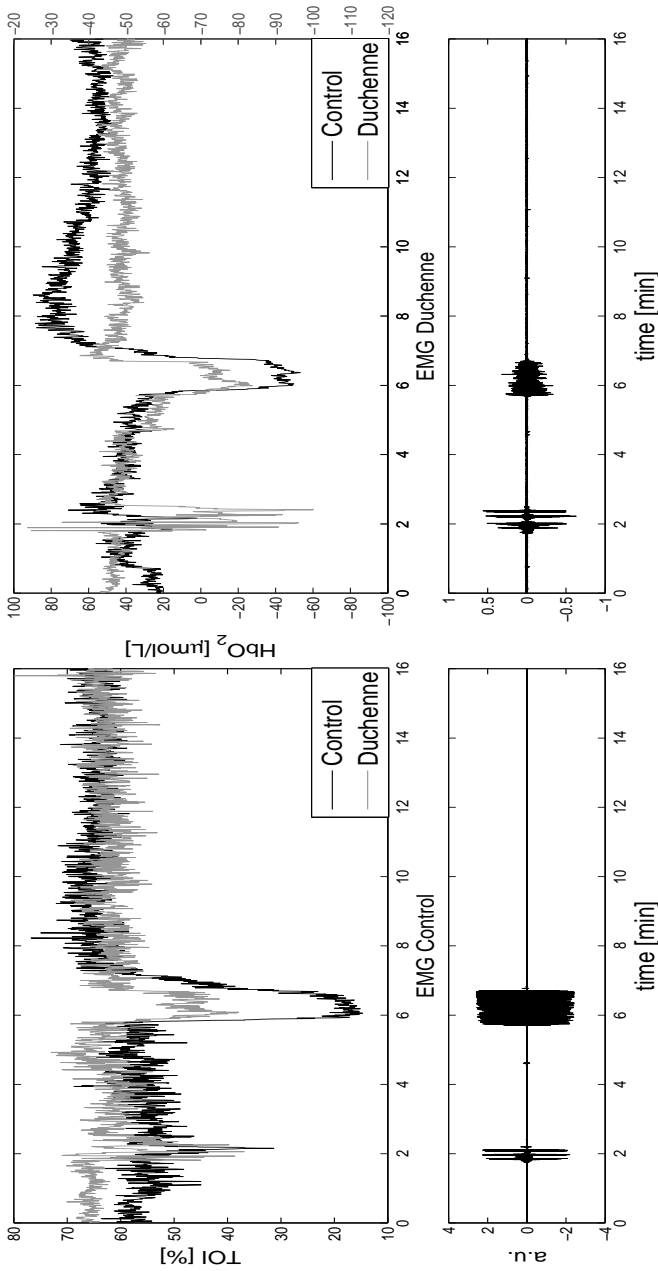


Figure 7.16: Differences in the muscular hemodynamics between a control and a DMD subject. The upper-left figure shows the differences in TOI induced by the contraction. In the upper-right figure, the changes in ΔHbO_2 are presented. In the lower figures the sEMG recordings from the control (lower-left) and the DMD (lower-right) subjects are shown.

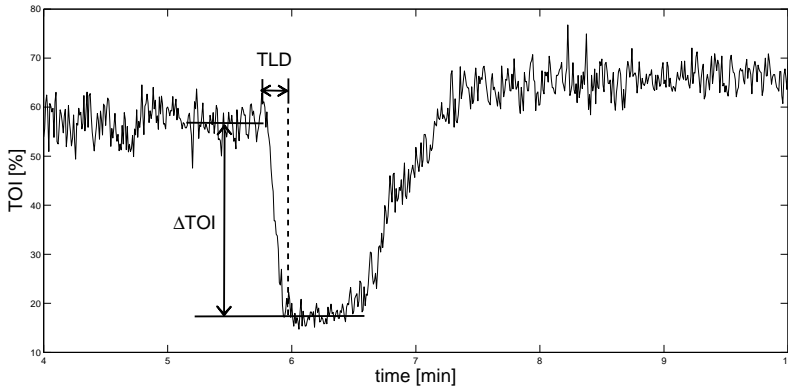


Figure 7.17: Illustration of the parameters used to characterized the dynamics of TOI.

- During the linear decay phase at the beginning of the contraction, the slope of the decay was measured. This parameter is called *HbO₂ slope 1*.
- The reduction in HbO₂ was calculated as the difference between its baseline level, before contraction, and its stabilization value after contraction. This parameter is called $\Delta_1 HbO_2$.
- After release of the contraction the slope of the increase in HbO₂ is measured. This parameter is called *HbO₂ slope 2*.
- The time when the HbO₂ reaches its maximum value was measured. This value is called *Time to OverShoot (TOS)*.
- The difference between the maximum after contraction and the baseline level was measured. This parameter is called $\Delta_2 HbO_2$.
- The maximum value after contraction was called *OverShoot (OS)*. It was calculated as follows:

$$OS = \frac{\Delta_2 HbO_2}{\Delta_1 HbO_2} \times 100\%. \quad (7.4)$$

- The time when HbO₂ return to the baseline level after the release of the contraction was measured. This values was called *Time OverShoot Ends (TOSE)*.

HHb and HbT related features were calculated in a similar way as the ones for HbO₂. Comparisons were made using a Mann-Whitney U test. Correlations between parameters were analyzed by using a Pearson correlation coefficient, $p < 0.05$ was considered statistically significant.

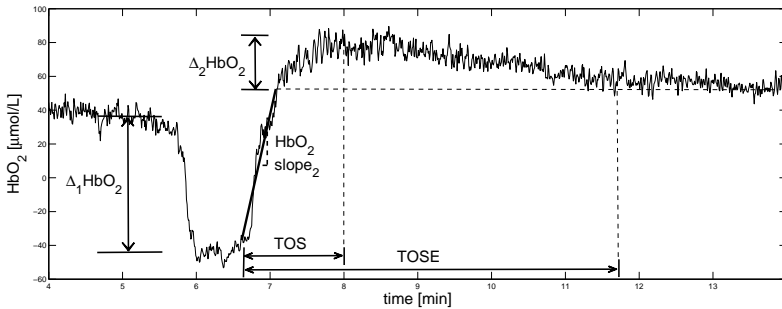


Figure 7.18: Illustration of the parameters used to characterized the dynamics of HbO₂.

7.7.3 Results

In total, 8 DMD patients and 11 age-matched healthy controls were included. A demographic description of the patients is shown in table 7.7 Except for the maximal voluntary isometric contraction (MVIC) and height, demographics at baseline were not different between both groups. Significant differences in height between DMD and controls were observed in earlier studies due to the use of deflazacort [93]. Deflazacort is a drug used to improve the strength in children with DMD.

	DMD (n=8)	Control (n=11)	p-value
Age (yrs)	11.5 (9-12)	10(9-12)	0.067
Weight (Kg)	35.9 (24.3-54.0)	39.5 (31.7-58.2)	0.283
Height (m)	1.29 (1.16-1.60)	1.47 (1.37-1.52)	0.013
BMI (Kg/m ²)	20.41 (18.05-29.4)	19.78 (15.78-27.68)	0.322
Skin Fold (mm)	9.5 (6-18)	6.2 (3.0-12.0)	0.068

Table 7.7: Demographic description of the DMD and control populations. Data presented as median (min-max).

Results from the EMG and NIRS derived measurements are shown in table 7.8, values are shown as median (min-max). The EMG signal showed no significant difference in MPF between both groups. The entropy, as mentioned before as a potential surrogate parameter for the functional loss of muscle fibers, was not statistically significant between both groups, but higher entropy values were found in the control population. In addition entropy values were positively correlated with ΔTOI ($r^2 = 0.550, p = 0.007$), TOS ($r^2 = 0.455, p = 0.029$) and TOSE ($r^2 = 0.512, p = 0.013$).

Before the contraction, there was no significant difference in oxygenation between both groups. During the contractions, all individuals deoxygenated in varying extents, with values ranging from 2.50% to 41.67%. DMD patients were observed to deoxygenate significantly less and slower than controls (ΔTOI $p = 0.032$, TOI slope $p = 0.048$) but without significant difference in TLD .

After the contraction, reoxygenation was observed in both groups. In all individuals except two an overshoot in the HbO_2 signal was observed. One individual had no overshoot ($\text{OS} = 0.0\%$) and another individual did not reach baseline oxygenation level at that time ($\text{OS} = -2.19\%$). It was observed that DMD subjects presented significantly shorter TOS ($p = 0.026$) and TOSE ($p = 0.003$).

Lastly, the HbT -signals showed no significant differences for all parameters between both groups. However, a trend is observed for the parameter HbT TOSE ($p = 0.069$). Concerning the HbT TOS , it can be seen that in controls there is a mild correlation between ΔTOI and HbT TOS ($r^2 = 0.417; p = 0.203$), but in DMD a positive correlation between ΔTOI and HbT TOS is observed ($r^2 = 0.772; p = 0.025$).

Additionally in the DMD group it was observed that the 6 minutes walk test (6MWT), an interesting measure for disease progression, was positively correlated with ΔTOI ($r^2 = 0.692, p = 0.040$), TOS ($r^2 = 0.781, p = 0.019$) and the TOSE ($r^2 = 0.77, p = 0.021$). The linear regression between the TOS vs 6MWT is shown in figure 7.19. Regression results for the ΔTOI and the TOSE are similar.

7.7.4 Discussion

This study has shown that by using EMG and NIRS measurements it is feasible to produce quantitative assessment for disease progression in children with DMD. Additionally, differences were observed on the dynamics of NIRS during contraction-induced deoxygenation and reoxygenation between DMD and controls. In DMD, the progression of the disease is monitored via indirect

	DMD (n=8)	Control (n=11)	p-value
EMG			
MPF ₁ (Hz)	56.46 (45.45;68.31)	57.32 (46.86;62.63)	0.804
MPF ₂ (Hz)	42.21 (36.23;59.80)	46.02 (31.27;59.09)	0.563
MPF slope (Hz/s)	-0.18 (-0.31 ; -0.02)	-0.11 (-0.32 ; -0.07)	0.508
Entropy (bits)	3.67 (2.63 ; 4.01)	3.94 (3.35;4.87)	0.137
TOI			
ΔTOI (%)	11.62 (2.50;27.17)	34.69 (6.09;41.67)	0.032*
TOI slope (%/s)	-0.87 (-3.13 ; -0.18)	-2.37 (-5.02 ; -0.44)	0.048*
TLD (s)	11.25 (8.70;18.70)	13.20 (7.95;27.40)	0.772
HHb			
Δ ₁ HHb (μmol/L)	11.60 (-3.50 ; 65.15)	53.71 (15.15;119.50)	0.010*
Δ ₂ HHb (μmol/L)	-13.51 (-86.02 ; 1.35)	-54.53 (-130.30 ; -11.77)	0.021*
HHb slope 1 (μmol/L/s)	1.61 (0.49;6.70)	4.67 (0.57;19.18)	0.039*
HHb slope 2 (μmol/L/s)	-0.44 (-1.41 ; -0.05)	-0.50 (-1.95 ; -0.08)	0.804
HbO₂			
Δ ₁ HbO ₂ (μmol/L)	-17.36 (-57.90 ; -3.99)	-45.61 (-120.20 ; -13.93)	0.021*
Δ ₂ HbO ₂ (μmol/L)	25.35 (3.58;119.20)	44.45 (7.78;175.30)	0.117
HbO ₂ slope 1 (μmol/L/s)	-3.07 (-9.41 ; -0.40)	-3.31 (-8.90 ; -1.33)	0.409
HbO ₂ slope 2 (μmol/L/s)	2.44 (0.67;10.07)	3.70 (-1.40;18.30)	0.869
HbO ₂ OS (s)	59.96 (0.00;108.50)	51.36 (-2.19;99.90)	0.741
HbO ₂ TOS (s)	19.20 (10.80;65.60)	64.30 (12.70;170.00)	0.026*
HbO ₂ TOSE (s)	68.15 (42.10;212.60)	285.30 (73.60;440.30)	0.003*
HbT			
Δ ₁ HbT (μmol/L)	-12.74 (-30.50;13.42)	2.49 (-90.20;26.60)	0.457
Δ ₂ HbT (μmol/L)	18.87 (-6.12;56.28)	9.74 (-25.10;104.50)	0.620
HbT slope 2 (μmol/L/s)	6.54 (2.67;19.30)	11.06 (2.03;90.07)	0.283
HbT OS (s)	86.22 (0.00;212.60)	118.50 (42.30;899.00)	0.283
HbT TOS (s)	16.45 (2.00;41.00)	32.30 (8.20;65.30)	0.364
HbT TOSE (s)	118.85 (15.00;281.70)	204.40 (136.10;304.60)	0.069

Table 7.8: Measured features from the EMG and NIRS signals. the values are given as median (min;max). The * indicates the features that were significantly different between the DMD and the control populations ($p < 0.5$).

measurements. The 6MWT is the most frequently used clinical tool validated for monitoring progression [137]. However, it is highly influenced by behavioral problems and neuromuscular problems e.g. falling. Additionally, 6MWT cannot be measured in patients that have already lost ambulence and are wheelchair-

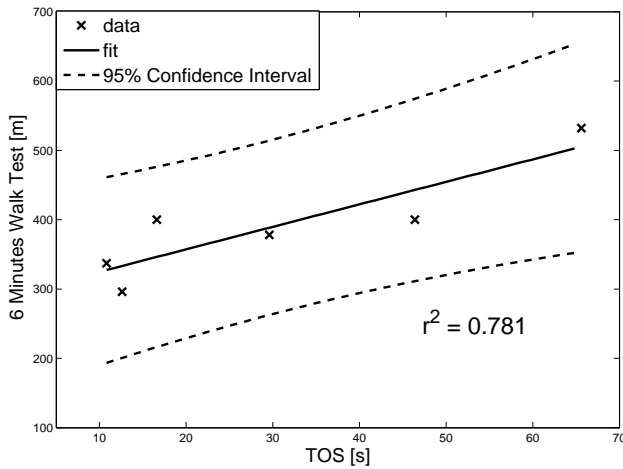


Figure 7.19: Linear regression between the TOS and the 6MWT. Functional assessment was not possible in 2 patients, due to a lower limb fracture and loss of ambulation.

bound. A noninvasive objective method for assessing disease progression is not yet readily available. However, it becomes more important since recently more clinical trials with gene correction therapy are being performed with promising results observing, due to therapy, an increase in 6MWT [128, 70]. In this study appropriated surrogate parameters for assessing muscle state and disease progression have been proposed. During contraction a decrease in tissue oxygenation (ΔTOI) relative to rest is provoked. This parameter was observed to be significantly higher in the control group. Additionally, it was found that the ΔTOI was positively correlated with the 6MWT, indicating that it has the potential to be used as a surrogate parameter for clinical progression in DMD.

In the reoxygenation phase a different profile in dynamical parameters was observed between DMD and controls. An overshoot of the HbO_2 occurred shortly after contraction due to increased oxygen delivery. In DMD, this overshoot occurred earlier. HbO_2 also returned earlier to baseline levels, reflected in a significantly smaller TOS and TOSE. Interestingly, it was observed that these parameters were also positively correlating with the 6MWT. The underlying explanation of this different dynamical profile could be attributed to (patho-) physiological differences. An overshoot of HbO_2 reflects an increase in oxygen delivery at the beginning of the relaxation, and is due to 2 phenomena. First, an increase in blood flow caused by the release of the intramuscular pressure

on arterioles and venules along the muscles fascicular lines. Second, an abrupt stop of high oxygen consumption from contracting skeletal muscle except for any accumulated oxygen debt [132, 129]. The faster reoxygenation in DMD might be the result from either a faster increase in blood volume or a smaller oxygen debt. At the beginning of the relaxation, the release of intramuscular pressure, correlated with the amount of force (MVIC) and the ΔTOI , should be lower in the DMD group, which results in smaller changes in blood volumes. This phenomenon was not observed in this study since the increase in blood volume, reflected as the slope-value of the total amount of hemoglobin and the ΔHbT TOS, was not significantly different between the groups. Possibly, this effect of the change in blood volume is too small to be detected in this limited trial and will be significant in a larger trial. Alternatively, it can be hypothesized, considering functional muscle ischemia in DMD mentioned earlier as an alternative pathophysiological mechanism, that this effect of intramuscular pressure is attenuated in controls due to a significant autoregulatory hyperemia during the prolonged exercise, resulting in non-significant changes in blood volumes.

This defective autoregulatory effect in DMD which causes a functional muscle ischemia, is depicted in the literature as the NO-hypothesis. Due to the loss of neuronal NOS, which is located subsarcolemmal in the dystrophin-glycoprotein complex, loss of autoregulatory vasodilation occurs during contraction. The absence of dystrophin leading to deficiency of neuronal NOS has been proven in mouse models as well as in humans. Recent studies showed that neural NOS has an important role in the autoregulation of the blood flow during the contraction. Sander et al [184] showed using NIR spectrometry that this protective mechanism is absent in DMD.

Since the faster increase in blood volume seems less plausible for explaining the dynamical differences between both groups, alternatively a smaller accumulated oxygen debt in DMD can be considered. It cannot be excluded that although exercise intensity was relatively equal, less absolute force was asked in the DMD-group, resulting in a smaller oxygen debt. Further studies with absolute equal force will be necessary to clarify in what extent the smaller accumulated oxygen debt contributes to the dynamical differences or if other pathophysiological processes are interfering. At the end of the relaxation phase, when the HbO_2 returns to baseline level, the parameter HbT TOSE was observed to be significantly different, indicating that there seems to be a sustained relative vasodilation in controls compared to DMD. It can be hypothesized that a higher oxygen debt in controls could result in alternative biochemical pathways attributing to this sustained relative vasodilation. More studies are needed to investigate and clarify this phenomenon.

The measurements of this study were performed with NIRS-technology, which has several advantages over more conventional hemodynamical techniques as it is a relatively cheap and portable device. It has no risk to patients and can be routinely used safely in children. It provides continuous monitoring of muscle oxygen availability in resting phase as well as during contractions, in particular within the microcirculation which is most accessible to metabolic products released during contractions, e.g. NO, and may have a relation to the DMD underlying pathophysiology [210].

However, NIRS has also some limitations to be taken into account. First, it is assumed that hemoglobin (Hb) is the only absorbing chromophore. The muscle however also contains myoglobin (Mb), which has absorption spectra similar to the one of Hb. The contribution of myoglobin to the NIRS-signal is still controversial; some studies postulate that only 20% of the signal is explained by absorption of Mb. In the literature little is known on the Hb/Mb ratio. Most studies report hemoglobin to contribute most to the signal alteration [62, 207, 83, 64]. Secondly, the effect of the heterogeneity of the muscle tissue on the NIRS-signal is still unknown. In DMD patients the muscle is progressively replaced by fat and fibrous tissue, which contains a lower oxygen metabolism. In this study the initial values of the TOI are not significantly different between both groups, therefore it is hypothesized that this effect is minimal. NIRS parameters may also be confounded by tissue properties including the subcutaneous fat layer since the latter has a lower metabolism and different optical characteristics [14]. In children, the subcutaneous fat layer is small and in our population the skinfold measure was not statistically different between the groups. Therefore, we can assume that the differences in TOI and HBT reflect the metabolic and hemodynamical alterations in the muscle itself.

In addition EMG was used to monitor the myoelectrical signal. As expected, the controls showed a larger difference in EMG activity. The entropy of the EMG measurements, as mentioned before as a parameter for the functional loss of muscle fibers is theoretically interesting. In this study, however, the entropy did not present statistically significant differences between the control and the DMD populations. This could be due to the attachment of the EMG electrodes; indeed, in some small subjects the biceps was not big enough to attach the EMG electrodes and the NIRS optode, appropriately together, at 1 cm of the midline. Therefore, the electrodes could have been positioned too far away from the active motor units leading to an underestimation of the variations in the signal. However, entropy seems to be positively correlated with the Δ TOI and the MVIC. Therefore, larger trials in future studies are needed to clarify this relationship.

Because this study recruited a small group, these results should be interpreted carefully. However, despite these limitations it can be concluded that these

preliminary EMG - NIRS measurements showed some important findings. First, non-invasive continuous monitoring of skeletal muscle oxygenation by NIRS, combined with EMG, can be used to study the response of a sustained contraction in controls and DMD and it is feasible in young children. Second, there are indications that the EMG and NIRS reveal information about the assessment of muscle state and disease progression, as in this study significant differences in contraction-induced deoxygenation and reoxygenation patterns were observed between healthy controls and DMD children. Interestingly, it was observed that ΔTOI , HbO_2 TOS and HbO_2 TOSE correlated with the subject functional performances on a 6 minute walking test. This shows the great potential of this novel combined EMG-NIRS technology as an objective DMD-monitoring instrument in the clinic as well as in future therapeutic studies.

7.8 Sleep Apnea Study

7.8.1 Introduction

In the framework of cardiopulmonary coupling, the goal is to quantify the influence of the respiration on the heart rate (HR) in order to use this information as a monitoring parameter. In general, this relationship is altered during episodes of breathing disorders. In [211], the authors describe that elevated coupling in the low frequency range (LF) between HR and respiration was observed during obstructive apnea episodes, when compared with normal breathing patterns; while elevated coupling in the high frequency range (HF) was observed during normal breathing patterns. In this section the use of subspace projection in biomedical signal analysis will be illustrated in the assessment of cardiopulmonary coupling during apnea.

7.8.2 Data and Methods

ECG and breathing recordings from the Physionet Sleep Apnea Database were used [165, 71]. From this dataset 8 recordings contain concomitant measurements of respiration and ECG; they were selected for further processing. In each one of these measurements breathing was recording using thoracic, abdominal and nasal sensors. The methodology was applied independently for each breathing sensor in order to study their influence on the results provided by subspace projections. Each recording includes a set of annotations, one for each minute of recording, which indicates the presence or absence of apnea episodes. The 8 recordings yield a total of 1328 minutes from which 489 contain apnea episodes

and 839 are normal segments. From the selected segments the tachogram was derived from the ECG and was resampled, together with the respiratory signal, at 5Hz. In order to quantify the cardiopulmonary coupling, the tachogram was decomposed, using orthogonal subspace projections, in 2 signals: one dependent of respiration and one independent from it. The cardiopulmonary coupling was quantified as the ratio between the squared norm of the projected and original tachogram. This ratio can be understood as the percentage of energy in the heart rate related to respiration. A 5th level DWT of the respiration was used as basis for the calculation of the projection matrices, the mother wavelet selected was the Daubechies 4 wavelet function. The use of the wavelet transform as basis allows the quantification in different frequency bands of the coupling between respiration and HR, expressed here by means of the approximation coefficients in the frequency 0-0.078Hz and the detail coefficients in the frequency band 0.78-2.5 Hz.

7.8.3 Results

Strong coupling in the low frequency band was found between the HR and the respiration during apnea episodes, while normal segments exhibit strong coupling in the high frequency band. Projecting the heart rate in the subspace defined by the approximation coefficients, the ratio between the projected HR in this respiratory subspace and its total power was significantly higher for segments with apnea than for normal segments, 41.7% vs 7.1% ($p < 0.001$ using the Kruskal-Wallis test). When the detail coefficients were used as basis a stronger influence of respiration in the normal segments was observed, 19.6% vs 3.4% ($p < 0.001$). Table 7.9 presents a detailed description of the results. In Figure 7.20 results from the subspace projections are shown. The Figure presents the respiration and the HR for a normal and an apnoeic segment. Furthermore, the decomposition of the HR in the projections onto the low and high frequencies of the respiration is depicted.

	Apnoeic	Normal	p-value
Approx. Coeff. [0-0.078Hz] <i>median (min-max)</i>	41.7% (0.1% - 83.4%)	7.1% (0% - 62.6%)	< 0.001
Det. Coeff. [0.078-2.5Hz] <i>median (min-max)</i>	3.4% (0% - 41.8%)	19.6% (0.2% - 65.1%)	< 0.001

Table 7.9: Percentage of power of the HR on the low and high frequency subspaces of the respiratory signal for the apnoeic and normal segments.

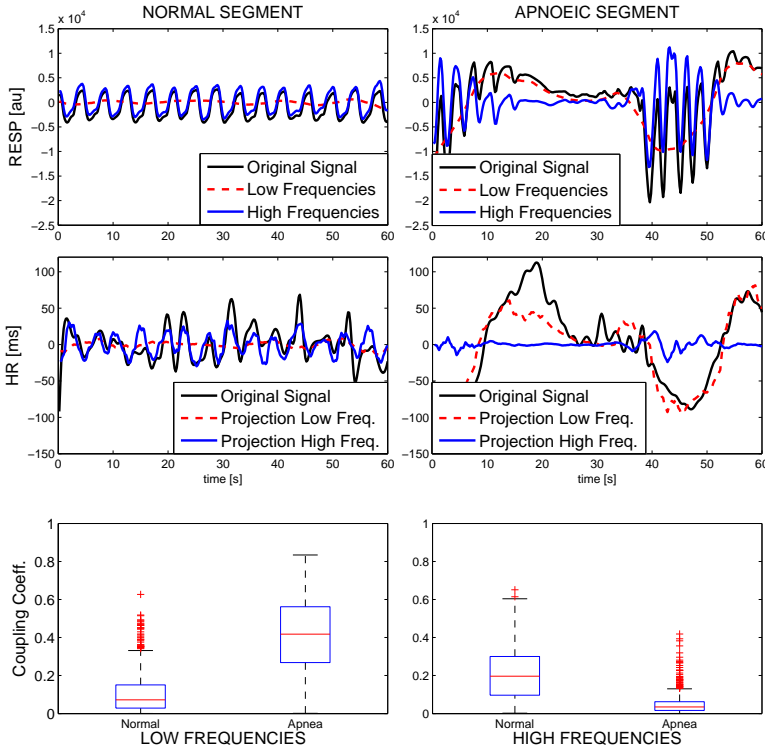


Figure 7.20: Results provided by the orthogonal projections of the HR onto the respiration subspaces in the study of sleep apnea. The first row presents the raw respiratory signal taken from the nasal sensor in black, the approximation coefficients in red and the sum of the detail coefficients in blue. The second row presents the HR signal in black, its projection onto the subspace spanned by the approximation coefficients in red, and its projection onto the subspace spanned by the detail coefficients in blue. The third row presents the box plot of the ratio between the power of the projected HR and the total HR power in the normal and apnoeic segments for the approximation (left) and detail coefficients (right). During apnoeic segments the coupling between respiration and HR is moved to lower frequencies.

7.8.4 Discussion

Using subspace projections a higher power in the coupling between HR and respiration for the low frequencies was found in apnoeic segments when compared

to normal segments, whilst normal segments exhibit a stronger coupling in the high frequencies. These results suggest that the cardio-respiratory coupling is moved from high frequencies to low frequencies during apnea episodes. These results are in agreement with the results published in [71]. By using the coupling coefficients in the low frequencies in a linear classifier for apnea detection the ROC curves shown in Figure 7.21, one per each respiratory sensor, are obtained. Even though all the sensors presented a good performance, the nasal sensor provided the highest discriminative power with an area under the ROC curve (AUC = 0.90). This is expected as the nasal sensor represents the gold standard for respiratory measurements. This results suggest that subspace projections could be of interest in the extraction of features for sleep apnea detection.

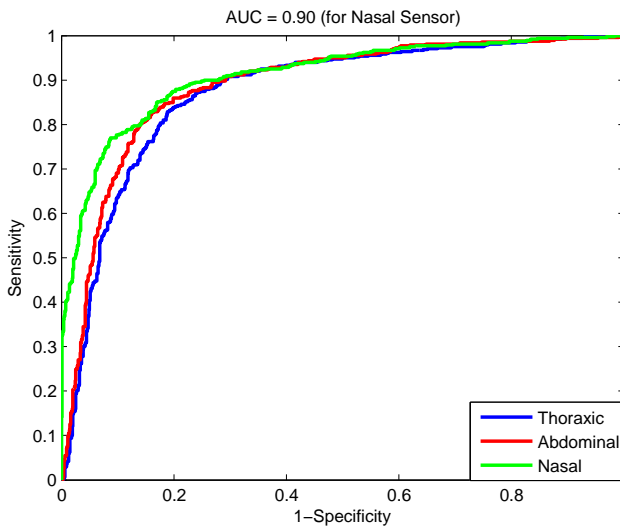


Figure 7.21: ROC curve for a linear classifier using the ratio between the power of the projected HR onto the approximation coefficients of the respiratory signal and the total power of the HR. The ratio was computed independently for the respiratory data measured from a thoracic, abdominal and nasal sensor. The AUC for the thoracic and abdominal sensor were 0.87 and 0.88, respectively.

Chapter 8

Summary and Future Work

In this chapter a summary of the main findings in this thesis dissertation will be given, as well as suggestions for future research directions.

8.1 Summary

In this thesis several problems related to the monitoring of cerebral hemodynamics using NIRS have been addressed. First of all I will mention the main findings in the mathematical methodologies employed. Afterwards the main results in the clinical case studies will be summarized.

Concerning linear methodologies, a novel framework based on the definition of orthogonal and oblique subspace projectors was proposed. This method expands the basis for the signal subspace by decomposing the regressor variables using a discrete wavelet transform. Furthermore, the newly formed regressor matrix is expanded using a block Hankelization procedure. By decomposing each regressor using a discrete wavelet transform the degrees of freedom in the model are increased, as well as the dimensionality of the subspace defined by the regressor matrix. In this thesis, this methodology was tested successfully in several clinical applications, namely in the ECMO and sleep apnea studies. In addition, the methodology was adapted for online monitoring, where the differences between subspaces defined by consecutive projectors were reduced. In this context, the methodology was used to preprocess NIRS signal. This algorithm allows to decouple the dynamics of SaO_2 from the NIRS measurements, which is desired for monitoring of cerebral hemodynamics, as indicated at several places in the

manuscript.

Concerning nonlinear methodologies two methods were explored. The first contribution is related to the use of a robust LS-SVM regression model for the interpolation of segments contaminated by artifacts. In this context an extra weight vector was introduced in the cost function defined in the robust LS-SVM problem. This slight modification favours the fitting at the borders. This is important for online monitoring applications, since the discontinuities between consecutive preprocessed segments are reduced. The second contribution is related to the development of a decomposition algorithm that is able to retrieve the nonlinear relation between a specific regressor and the target function. This decomposition facilitates the interpretation of nonlinear models, since it is able to retrieve the direct, or combined, influence of some variables in the regression model. This methodology was based on the definition of projection matrices in a reproducing kernel Hilbert space (RKHS). This concept can facilitate the introduction of other methods such as subspace system identification in the RKHS. Some of those models already exist in the literature, but this methodology approaches the problem from a different point of view providing a geometrical interpretation of the problem. In addition, an interesting relation between the kernel tuning parameter and the trace of the projection matrix in the RKHS was investigated. It was shown that small σ values are related to high dimensional subspaces, which induces over-fitting. Larger σ values, on the other hand, produce dimensionally smaller subspaces, which are related to underfitting. In addition, the dimensionality of the subspace represented by the KPCR model, was used to define a reduced set of variables that is able to reproduce similar results, providing a framework for the development of a sparse KPCR.

In addition, in this thesis we have validated the use of TOI and rScO₂ for CA assessment. Traditionally, ΔHbD and ΔHbT have been used for CA assessment. However, these methodologies are prone to movement artifacts. TOI and rScO₂ represent a more robust technology that produces more stable measurements. Moreover, in order to standardize the methodologies used in clinical practice for CA assessment, a set of parameters for the use of transfer function, coherence and correlation methods has been proposed. These parameters were selected by the evaluation of their impact on the scores they produce. This is an important topic that lately have caught the attention of research in the field, which highlights the importance of this study.

Concerning clinical case studies, several results have been reported in this manuscript. First, canonical correlation analysis (CCA) was introduced in the analysis of cerebral hemodynamics. This methodology was tested in patients undergoing ECMO, and scores indicating the relation between systemic and hemodynamical variables were presented. In this study, the relation between

systemic and peripheral hemodynamical variables was proposed as a reference to evaluate the status of the cerebral hemodynamics regulation. Nowadays, there is no gold standard for the evaluation of cerebral hemodynamics regulation. However, it is known that changes in systemic variables are attenuated in the cerebral hemodynamics by the mechanisms that protect the brain, these mechanisms are absent in the peripheral circulation. Therefore, it is expected that changes in systemic variables are more reflected in the peripheral than in the cerebral hemodynamics. By defining the relation between the systemic variables and the peripheral hemodynamics as a reference, an appropriate patient dependent framework for the monitoring of cerebral hemodynamics is obtained. However, when using CCA, only the relation between the variables, but not the strength of this relation, is evaluated. By incorporating subspace projections in this framework, the strength of this relation is measured. Both methodologies present an interesting framework for the monitoring of cerebral hemodynamics. However, the clinical impact of these methods is yet to be validated.

Wavelet based transfer function (WBTF) has been proposed for the use in cerebral hemodynamics monitoring. WBTF is an appropriate methodology for the study of nonstationary interactions between two signals. In this dissertation, interesting preliminary results for the use of WBTF in biomedical signal processing have been presented.

In addition, the subspace projections obtained from a KPCR model were tested in a real dataset. In the application used, the data was obtained from an anesthetized lamb. Variations in MABP were induced in order to produce hypotension and induce “impaired” cerebral autoregulation. As result it was shown that KPCR was able to fit adequately the data. Furthermore, by using the projections onto the regressor variables, the model was able to retrieve the autoregulative curve. This curve describes a nonlinear relation between MABP and CBF, which was hidden when observing the raw measurements. These results indicate the high potential that this methodology possess for clinical applications. Additionally, since this methodology was developed independently from the clinical applications, it can be applied to different fields.

Concerning the studies performed in the labetalol dataset, we found that the maternal use of labetalol alters the CA mechanism in the newborns during the first days of life. This alteration might be related to a vasodilatory effect similarly to the one caused by hypocapnia. Even though the effect of labetalol on the neonates disappears by the third day after birth, its relation with clinical outcome in the patients is unknown.

In this thesis we also proposed the use of NIRS for the monitoring of disease progression in DMD patients. In this framework, we found a different

hemodynamical pattern of re-oxygenation after a sustained contraction in DMD patients when compared to control subjects. Interestingly enough, this behavior correlates with the standard test that assesses the status of the disease. The main advantage of the proposed parameters is that the test can be performed in patients that are unable to walk. This fact makes NIRS attractive for the monitoring of therapeutic response in these population.

In a final clinical case study, the effect of an apnoeic event in the coupling between the heart rate and the respiration was investigated. This study showed that this relation is moved from “high” to “low” frequencies during an apnea episode. Based on this information, a score that indicates the strength of the coupling between HR and respiration in the “low” and “high” frequencies, was proposed as a feature for the detection of apnoeic episodes.

In summary, in this thesis several methodologies have been developed to address the problems that cerebral hemodynamics monitoring has to face. First of all, preprocessing algorithms for NIRS signals have been developed. Second, multivariate signal processing techniques have been introduced in the field of cerebral hemodynamics monitoring. Based on the results provided by those methodologies, scores that indicate the status of the cerebral hemodynamics mechanisms were proposed. In addition, a methodological framework that facilitates the clinical interpretation of a nonlinear multivariate model has been introduced. Finally, the methods developed in this thesis were tested in a series of clinical studies.

8.2 Discussion

Cerebral hemodynamics is a complex process that involves the interaction of several mechanisms and physiological variations. Therefore, the development of methodologies for its appropriate monitoring should take into account the multivariable, nonlinear and nonstationary nature of these mechanisms. However, by taking into account all these characteristics the complexity of the monitoring algorithms is increased.

On one hand, traditional techniques such as correlation, coherence and transfer function require a low computational cost; which make them easy to implement at the patient bedside. In addition, due to its simplicity the scores produced are easy to interpret. Moreover, since these methodologies have been studied in several fields, they represent a robust framework for a monitoring system. However, these methods assume several conditions that might be violated in clinical practice. First of all, they assume that the system under study is univariate. Therefore, the influence of variables that are not taken into account

can influence the results, leading to misinterpretation of the results. Second, these methodologies assume a linear relationship between the signals under study. In the context of cerebral hemodynamics monitoring, one can argue that due to the fact that the variations in the signals under analysis are small, the linearity condition is met. But, in the presence of strong nonlinearities these conditions does not hold. In addition, some of these methods explore only the presence of a linear relationship between the variables and not its strength. In the context of monitoring cerebral hemodynamics, not only the presence of a coupling between systemic variations and hemodynamical variables is needed, but also the strength of this coupling. Therefore, methodologies like correlation and coherence are not suited for this task, since they only evaluate the presence of a linear relation between the variables under study. Transfer function gain, on the other hand, does retrieve information related to the strength of this coupling, which makes it, in comparison with correlation and coherence, a more suitable method for cerebral hemodynamics monitoring. But, even though all these methodologies are simple, fast and robust, they lack clinical interpretability, and can produce misleading results.

On the other hand, more complicated methodologies such as canonical correlation analysis (CCA), and subspace projections(O(r)SP) represent a more suitable framework for the monitoring of cerebral hemodynamics. These methodologies can manage multivariate data, which allows to evaluate the influence of several systemic variables on the cerebral circulation at the same time. CCA on one hand, can be seen as a multivariate extension of correlation analysis, while O(r)SP might be more closely related to transfer function analysis. As in the previous case, O(r)SP represents a more robust methodology for the monitoring of cerebral hemodynamics than CCA. This is due to the fact that CCA, as correlation, can only evaluate the presence of a linear relationship between the variables studied, while O(r)SP is able to indicate the strength of this coupling. In addition O(r)SP, as proposed in this thesis, can retrieve the individual contribution of each measured systemic variable on the cerebral hemodynamics. This is of clinical importance since it represents a tool that can be used in order to evaluate the efficacy of treatment. As an example, O(r)SP can be used in order to evaluate if the treatment for hypotension improves the cerebral oxygenation in the neonates. However, these methodologies also present some drawbacks. On one hand, they are more complicated and require more computational power for their calculation. However, this latter problem does not pose any difficulty, since in clinical practice it is tolerable to generate scores for cerebral hemodynamics status every coupled of minutes. These methodologies can be implemented at the patient bedside with the help of adequate hardware. On the other hand, as mentioned before, these methodologies evaluate the presence of linear relationships between the data. Therefore, in presence of strong nonlinearities these methods can produce misleading results.

In contrast with the aforementioned methodologies, kernel principal component regression (KPCR) takes into account the multivariate and nonlinear nature of the mechanisms involved in cerebral hemodynamics regulation. One of the major drawbacks of nonlinear methodologies is the lack of clinical interpretability. This issue has been addressed in this thesis by the inclusion of subspace projection techniques, which allow to obtain the nonlinear, or linear, contribution of each systemic variable on the cerebral hemodynamics. However, this method is a lot more complex and requires of a higher computational cost. The main bottleneck of this method lies in the tuning of the kernel bandwidth. By addressing this issue a faster implementation of the KPCR model can be obtained.

In summary, sophisticated nonlinear methodologies for the monitoring of cerebral hemodynamics, such as KPCR, provide of information that is relevant in clinical practice, but they require a high computational cost. More simple techniques that take into account only linear relationships between the variables, such as CCA and O(r)SP, can be a good alternative for the nonlinear methods when there are limitations in computational power and time. Finally, it is recommended to use simple methodologies, such as correlation, coherence and transfer function, with care, since they may produce misleading results.

8.3 Future Work

Several issues are yet to be addressed in the methodologies and the clinical case studies presented in this dissertation. First of all, the subspace projection method proposed in this thesis, which extends the regressor matrix by decomposing the regressors using DWT, can be further improved by introducing this extension in a subspace system identification framework. Furthermore, confidence intervals for the regression and the projection can be defined in order to complete a theoretical frame for this problem formulation.

Second, concerning nonlinear methodologies there are also several aspects to be addressed. First of all, it is interesting to explore the relation between the dimensionality of the subspace where the data lie in the RKHS and the kernel parameter σ . By finding a suitable relationship it can lead to models where the tuning might be avoided. Advantages can be taken from the similarity of this problem to the model selection in the KPCA formulation, where the tuning is based on the structure of the input data without taking into account a target vector. Furthermore, the relation between σ and the dimensionality of the subspace in the RKHS can be further exploited in order to define the best model, providing a limit for the number of desired components. In other words, let's assume that the user is interested in generating a KPCR model using only

N datapoints. If the relation between σ and the model projection matrix in the RKHS is known, the best σ for such a model can be found. Furthermore, in this dissertation the KPCR model was studied using only a RBF kernel. The influence of the kernel function in the proposed methodology is yet to be evaluated. The selection of the RBF kernel in this thesis was somehow arbitrary, even though the RBF kernel is one of the most popular kernels due to its generalization capabilities, and the ability to reproduce other kernel functions.

Another important issue to investigate in the proposed KPCR methodology is the influence of noise in the decomposition algorithm. In the toy examples presented, a moderate noise level was used. The examples showed that some residuals were obtained when projecting the data onto the subspace defined by regressor variables that were not directly involved in the model. Therefore, we hypothesized that by increasing the noise level, the magnitude of these residuals will increase. In addition, regressor variables with lower variations might not adequately be described by the model. To what extent this can be tolerated in clinical applications, is yet to be studied. Furthermore, the KPCR model, as presented in this work, can only identify static relationships between the regressor variables and the target function. In order to be able to identify dynamical nonlinear relationships a redefinition of the regressor matrix is needed. Such a modification can be related to the extension of the regressor matrix by the use of a DWT decomposition. In some preliminary results that were not presented in this thesis, it was observed that by including such modification in a LS-SVM regression model, the estimated output is smoothed. This indicates a reduction in the influence of the noise in the regressors.

Concerning the monitoring of cerebral hemodynamics, first of all, the preprocessing algorithms need to be improved by automating the detection of artifacts. The methodology presented in this study is semi-automatic, it relies on the manual selection of segments contaminated with artifacts. Since there are several algorithms in the literature that already address this issue, what needs to be investigated is how to adapt the methods presented in this thesis to comply with their requirements. In addition, studies for CA and cerebral hemodynamics need to be validated in larger populations; however, a gold standard is yet to be defined. In addition, the scores for cerebral hemodynamics monitoring, proposed in this manuscript, need to be validated in clinical studies with a larger population.

Additionally, in the labetalol study it is important to investigate the relation between the findings presented in this thesis and the clinical outcome in the neonates. Concerning the Duchenne study, future research should be oriented to increasing the size of the population in order to have a stronger validation for the scores proposed in this thesis. Moreover, the relation between the sEMG variations and the HbO_2 dynamics needs to be explored.

Finally, this thesis has proposed several methodologies for monitoring cerebral hemodynamics. These methodologies are ready to be used in clinical trials in order to evaluate their clinical impact. As an example, the methodologies developed in this thesis will be used in the analysis of signals obtained from patients included in the European HIP Trial FP7-HEALTH/ 2007-2013 (n° 260777), which is a clinical trial that aims at defining correct treatment for hypotension in prematurely born infants. Since measurements of brain oxygenation will be available in the population included in the trial, the algorithms developed in this thesis represent a methodological framework for the evaluation of the cerebral hemodynamics regulation in these infants.

Bibliography

- [1] R. Aaslid, K.F. Lindegaard, W. Sorteberg, and H. Nornes. Cerebral autoregulation dynamics in humans. *Stroke*, 20(1):45–52, 1989. pages 7, 8
- [2] Philip N Ainslie and James Duffin. Integration of cerebrovascular co2 reactivity and chemoreflex control of breathing: mechanisms of regulation, measurement, and interpretation. *American Journal of Physiology-Regulatory, Integrative and Comparative Physiology*, 296(5):R1473–R1495, 2009. pages 2, 8
- [3] Pippa G Al-Rawi, Peter Smielewski, and Peter J Kirkpatrick. Evaluation of a near-infrared spectrometer (niro 300) for the detection of intracranial oxygenation changes in the adult head. *Stroke*, 32(11):2492–2500, 2001. pages 13
- [4] Mark I Alpert and Robert A Peterson. On the interpretation of canonical analysis. *Journal of Marketing Research*, pages 187–192, 1972. pages 55
- [5] Denis I Altman, William J Powers, Jeffrey M Perlman, Peter Herscovitch, Sara L Volpe, and Josepemberh J Volpe. Cerebral blood flow requirement for brain viability in newborn infants is lower than in adults. *Annals of neurology*, 24(2):218–226, 1988. pages 4
- [6] Rolph E Anderson, Joseph F Hair, RL Tatham, and WC Black. *Multivariate data analysis*. Pearson, 2006. pages 55
- [7] S Antoniuk, RV Da Silva, et al. [periventricular and intraventricular hemorrhage in the premature infants]. *Revista de neurologia*, 31(3):238, 2000. pages 4
- [8] V Apgar. A proposal for a new method of evaluation of the newborn. *Classic Papers in Critical Care*, 32:449, 1952. pages 97
- [9] Dawna Armstrong and Margaret G Norman. Periventricular leucomalacia in neonates complications and sequelae. *Archives of disease in childhood*, 49(5):367–375, 1974. pages 4

- [10] Simon R Arridge, M Cope, and DT Delpy. The theoretical basis for the determination of optical pathlengths in tissue: temporal and frequency analysis. *Physics in medicine and biology*, 37(7):1531, 1992. pages 11
- [11] Praveen Ballabh. Intraventricular hemorrhage in premature infants: mechanism of disease. *Pediatric research*, 67(1):1–8, 2010. pages 4
- [12] Betty Q Banker and Jeanne-Claudie Larroche. Periventricular leukomalacia of infancy form of neonatal anoxic encephalopathy. *Archives of Neurology*, 7(5):386–410, 1962. pages 4
- [13] Charles P Barfield, Victor YH Yu, Oji Noma, Johji Kukita, Leo J Cussen, Ann Oates, and Adrian M Walker. Cerebral blood volume measured using near-infrared spectroscopy and radiolabels in the immature lamb brain. *Pediatric research*, 46(1):50–56, 1999. pages 18
- [14] MCP Beekvelt, MS Borghuis, BGM Engelen, RA Wevers, and WNJM. Colier. Adipose tissue thickness affects in vivo quantitative near-ir spectroscopy in human skeletal muscle. *Clinical Science*, 101:21–28, 2001. pages 104, 180
- [15] August Beer. Bestimmung der absorption des rothen lichts in farbigen flüssigkeiten. *Ann. Phys. Chem*, 86(2):78–90, 1852. pages 11
- [16] Richard T Behrens and Louis L Scharf. Signal processing applications of oblique projection operators. *Signal Processing, IEEE Transactions on*, 42(6):1413–1424, 1994. pages 61
- [17] Frank Bel, Margot Bor, Theo Stijnen, Jan Baan, and Jan H Ruys. Aetiological role of cerebral blood-flow alterations in development and extension of peri-intraventricular haemorrhage. *Developmental Medicine & Child Neurology*, 29(5):601–614, 1987. pages 4
- [18] David A Benaron, C Dean Kurth, James M Steven, Maria Delivoria-Papadopoulos, and Britton Chance. Transcranial optical path length in infants by near-infrared phase-shift spectroscopy. *Journal of Clinical Monitoring and Computing*, 11(2):109–117, 1995. pages 96
- [19] Julius S Bendat and Allan G Piersol. *Random data: analysis and measurement procedures*, volume 729. Wiley, 1986. pages 120
- [20] Paul Benni, Bo Chen, Francine Dykes, Scott Wagoner, Micheal Heard, April Tanner, Teresa Young, Khodayar Rais-Bahrami, Oswaldo Rivera, and Billie Short. Validation of the cas neonatal nirs system by monitoring vv-ecmo patients. *Oxygen Transport to Tissue XXVI*, pages 195–201, 2005. pages 18

- [21] Frederic Bevilacqua, Andrew J Berger, Albert E Cerussi, Dorota Jakubowski, and Bruce J Tromberg. Broadband absorption spectroscopy in turbid media by combined frequency-domain and steady-state methods. *Applied optics*, 39(34):6498–6507, 2000. pages 16
- [22] RF Bonner, R Nossal, S Havlin, and GH Weiss. Model for photon migration in turbid biological media. *JOSA A*, 4(3):423–432, 1987. pages 11
- [23] E. Bor-Seng-Shu, W.S. Kita, E.G. Figueiredo, W.S. Paiva, E.T. Fonoff, M.J. Teixeira, and R.B. Panerai. Cerebral hemodynamics: concepts of clinical importance. *Arquivos de Neuro-Psiquiatria*, 70(5):352–356, 2012. pages 3
- [24] G.B. Boylan, K. Young, R.B. Panerai, J.M. Rennie, and D.H. Evans. Dynamic cerebral autoregulation in sick newborn infants. *Pediatric research*, 48(1):12–17, 2000. pages 5
- [25] Ken M Brady, Jennifer K Lee, Kathleen K Kibler, Piotr Smielewski, Marek Czosnyka, R Blaine Easley, Raymond C Koehler, and Donald H Shaffner. Continuous time-domain analysis of cerebrovascular autoregulation using near-infrared spectroscopy. *Stroke*, 38(10):2818–2825, 2007. pages 66
- [26] Ken M Brady, Jennifer O Mytar, Jennifer K Lee, Duke E Cameron, Luca A Vricella, W Reid Thompson, Charles W Hogue, and R Blaine Easley. Monitoring cerebral blood flow pressure autoregulation in pediatric patients during cardiac surgery. *Stroke*, 41(9):1957–1962, 2010. pages 149
- [27] Milena Bray, Ilaria Stucchi, Monica Fumagalli, Lorenza Pugni, Luca Ramenghi, Massimo Agosti, and Fabio Mosca. Blood withdrawal and infusion via umbilical catheters: effect on cerebral perfusion and influence of ibuprofen. *Neonatology*, 84(3):187–193, 2003. pages 4
- [28] Jane E Brazy and Darrell V Lewis. Changes in cerebral blood volume and cytochrome aa₃ during hypertensive peaks in preterm infants. *The Journal of pediatrics*, 108(6):983–987, 1986. pages 10, 17
- [29] Derek W Brown, Paul A Picot, Jafar Gharavi Naeini, Roger Springett, David T Delpy, and Ting-Yim Lee. Quantitative near infrared spectroscopy measurement of cerebral hemodynamics in newborn piglets. *Pediatric research*, 51(5):564–570, 2002. pages 18
- [30] NC Brun, A Moen, K Borch, OD Saugstad, and G Greisen. Near-infrared monitoring of cerebral tissue oxygen saturation and blood volume in newborn piglets. *American Journal of Physiology-Heart and Circulatory Physiology*, 273(2):H682–H686, 1997. pages 18, 110

- [31] HU Bucher, AD Edwards, AE Lipp, and G Duc. Comparison between near infrared spectroscopy and ^{133}Xe clearance for estimation of cerebral blood flow in critically ill preterm infants. *Pediatric research*, 33(1):56–60, 1993. pages 18
- [32] Dorothy Bulas and Penny Glass. Neonatal ecmo: neuroimaging and neurodevelopmental outcome. *Seminars in perinatology*, 29(1):58–65, 2005. pages 149
- [33] C Sidney Burrus, Ramesh A Gopinath, and Haitao Guo. *Introduction to wavelets and wavelet transforms: a primer*, volume 23. Prentice hall Upper Saddle River NJ, 1998. pages 39
- [34] A Caicedo, D De Smet, G Naulaers, L Ameye, J Vanderhaegen, P Lemmers, F van Bel, and S Van Huffel. Cerebral tissue oxygenation and regional oxygen saturation can be used to study cerebral autoregulation in prematurely born infants. *Pediatric research*, 69(6):548–553, 2011. pages 8
- [35] A Caicedo, D De Smet, J Vanderhaegen, G Naulaers, M Wolf, P Lemmers, F Van Bel, L Ameye, and S Van Huffel. Impaired cerebral autoregulation using near-infrared spectroscopy and its relation to clinical outcomes in premature infants. *Adv. Exp. Med. Biol*, 701:233–239, 2011. pages 149
- [36] A Caicedo, G Naulaers, M Wolf, P Lemmers, F Bel, L Ameye, and S Huffel. Assessment of the myogenic and metabolic mechanism influence in cerebral autoregulation using near-infrared spectroscopy. *Advances in Experimental Medicine and Biology*, pages 37–44, 2012. pages 8
- [37] A Caicedo, I Tachtsidis, MD Papademetriou, and Sabine Van Huffel. Decoupling the influence of systemic variables in the peripheral and cerebral haemodynamics during ecmo procedure by means of oblique and orthogonal subspace projections. In *Engineering in Medicine and Biology Society (EMBC), 2012 Annual International Conference of the IEEE*, pages 6153–6156. IEEE, 2012. pages 169
- [38] PP Chow, JG Horgan, and KJ Taylor. Neonatal periventricular leukomalacia: real-time sonographic diagnosis with ct correlation. *American journal of roentgenology*, 145(1):155–160, 1985. pages 4
- [39] M Cope and DT Delpy. System for long-term measurement of cerebral blood and tissue oxygenation on newborn infants by near infra-red transillumination. *Medical and biological engineering and computing*, 26(3):289–294, 1988. pages 11

- [40] Heather Coughtrey, Janet M Rennie, and David H Evans. Variability in cerebral blood flow velocity: observations over one minute in preterm babies. *Early human development*, 47(1):63–70, 1997. pages 4
- [41] Nello Cristianini and John Shawe-Taylor. *An introduction to support vector machines and other kernel-based learning methods*. Cambridge university press, 2000. pages 72
- [42] Rinaldo Cubeddu, Antonio Pifferi, Paola Taroni, Alessandro Torricelli, and Gianluca Valentini. Compact tissue oximeter based on dual-wavelength multichannel time-resolved reflectance. *Applied optics*, 38(16):3670–3680, 1999. pages 16
- [43] Marek Czosnyka, Piotr Smielewski, Peter Kirkpatrick, David K Menon, and John D Pickard. Monitoring of cerebral autoregulation in head-injured patients. *Stroke*, 27(10):1829–1834, 1996. pages 120
- [44] Ingrid Daubechies et al. *Ten lectures on wavelets*, volume 61. SIAM, 1992. pages 39
- [45] Piers EF Daubeney, Sally N Pilkington, Ellen Janke, Gareth A Charlton, David C Smith, and Steven A Webber. Cerebral oxygenation measured by near-infrared spectroscopy: comparison with jugular bulb oximetry. *The Annals of thoracic surgery*, 61(3):930–934, 1996. pages 110
- [46] Hal Daumé III. From zero to reproducing kernel hilbert spaces in twelve pages or less, 2004. pages 79
- [47] Katrien De Cock, Guillaume Mercere, Bart De Moor, et al. Recursive subspace identification for in flight modal analysis of airplanes. In *International Conference on Noise and Vibration Engineering, ISMA 2006*, 2006. pages 65
- [48] DT Delpy, M Cope, Pi Van der Zee, S Arridge, Susan Wray, and J Wyatt. Estimation of optical pathlength through tissue from direct time of flight measurement. *Physics in medicine and biology*, 33(12):1433, 1988. pages 11, 16, 17
- [49] Jacques DeReuck, Amrik S Chattha, and Edward P Richardson Jr. Pathogenesis and evolution of periventricular leukomalacia in infancy. *Archives of neurology*, 27(3):229, 1972. pages 4
- [50] R.R. Diehl, D. Linden, D. Lücke, and P. Berlit. Phase relationship between cerebral blood flow velocity and blood pressure a clinical test of autoregulation. *Stroke*, 26(10):1801–1804, 1995. pages 38

- [51] Vera Dietz, Martin Wolf, Matthias Keel, Kv Siebenthal, Oskar Baenziger, and H-U Bucher. *2*. pages 2, 20, 29
- [52] D DiSalvo et al. The correlation between placental pathology and intraventricular hemorrhage in the preterm infant. the developmental epidemiology network investigators. *Pediatric research*, 43(1):15, 1998. pages 4
- [53] Alexander Dullenkopf, Anna Kolarova, Gabriele Schulz, Bernhard Frey, Oskar Baenziger, and Markus Weiss. Reproducibility of cerebral oxygenation measurement in neonates and infants in the clinical setting using the niro 300 oximeter*. *Pediatric Critical Care Medicine*, 6(3):344–347, 2005. pages 19
- [54] Arlene Duncan, Judith H Meek, Matthew Clemence, CE Elwell, L Tyszczyk, M Cope, and D Delpy. Optical pathlength measurements on adult head, calf and forearm and the head of the newborn infant using phase resolved optical spectroscopy. *Physics in medicine and biology*, 40(2):295, 1995. pages 11
- [55] AD Edwards, C. Richardson, M. Cope, JS Wyatt, DT Delpy, and EOR Reynolds. Cotside measurement of cerebral blood flow in ill newborn infants by near infrared spectroscopy. *The Lancet*, 332(8614):770–771, 1988. pages 18
- [56] Janeth C Ejike, Kenneth A Schenkman, Kristy Seidel, Chandra Ramamoorthy, and Joan S Roberts. Cerebral oxygenation in neonatal and pediatric patients during veno-arterial extracorporeal life support. *Pediatric Critical Care Medicine*, 7(2):154–158, 2006. pages 149, 153
- [57] Clare Elwell. *A practical users guide to near infrared spectroscopy*. Hamamatsu Photonics KK, 1995. pages 11, 15, 18
- [58] Alan EH Emery. *Duchenne muscular dystrophy*. Oxford University Press OxfordNova York, 2002. pages 170
- [59] P Fallon, IG Roberts, FJ Kirkham, AD Edwards, A Lloyd-Thomas, and MJ Elliott. Cerebral blood volume response to changes in carbon dioxide tension before and during cardiopulmonary bypass in children, investigated by near infrared spectroscopy. *European journal of cardio-thoracic surgery*, 8(3):130–134, 1994. pages 20
- [60] Sergio Fantini, Maria-Angela Franceschini, John S Maier, Scott A Walker, Beniamino B Barbieri, and Enrico Gratton. Frequency-domain multichannel optical detector for noninvasive tissue spectroscopy and oximetry. *Optical Engineering*, 34(1):32–42, 1995. pages 16

- [61] Sergio Fantini, Dennis Hueber, Maria Angela Franceschini, Enrico Gratton, Warren Rosenfeld, Phillip G Stubblefield, Dev Maulik, and Miljan R Stankovic. Non-invasive optical monitoring of the newborn piglet brain using continuous-wave and frequency-domain spectroscopy. *Physics in medicine and biology*, 44(6):1543, 1999. pages 13, 16
- [62] Francesco Felici, Valentina Quaresima, Luigi Fattorini, Paola Sbriccoli, Gian Carlo Filligoi, Marco Ferrari, et al. Biceps brachii myoelectric and oxygenation changes during static and sinusoidal isometric exercises. *Journal of electromyography and kinesiology: official journal of the International Society of Electrophysiological Kinesiology*, 19(2):e1, 2009. pages 171, 172, 180
- [63] Marco Ferrari, Leonardo Mottola, and Valentina Quaresima. Principles, techniques, and limitations of near infrared spectroscopy. *Canadian Journal of Applied Physiology*, 29(4):463–487, 2004. pages 11
- [64] Marco Ferrari, Makii Muthalib, Valentina Quaresima, Marco Ferrari, Makii Muthalib, and Valentina Quaresima. The use of near-infrared spectroscopy in understanding skeletal muscle physiology: recent developments. *Philosophical Transactions of the Royal Society A: Mathematical, Physical and Engineering Sciences*, 369(1955):4577–4590, 2011. pages 180
- [65] Joshua B Fishkin, Peter TC So, Albert E Cerussi, Sergio Fantini, Maria Angela Franceschini, and Enrico Gratton. Frequency-domain method for measuring spectral properties in multiple-scattering media: methemoglobin absorption spectrum in a tissuelike phantom. *Applied optics*, 34(7):1143–1155, 1995. pages 16
- [66] Cole A Giller et al. The frequency-dependent behavior of cerebral autoregulation. *Neurosurgery*, 27(3):362, 1990. pages 120
- [67] Cole A Giller and Martin Mueller. Linearity and non-linearity in cerebral hemodynamics. *Medical engineering & physics*, 25(8):633–646, 2003. pages 29, 133
- [68] Christine A Gleason, Charles Hamm, and MD Jones. Effect of acute hypoxemia on brain blood flow and oxygen metabolism in immature fetal sheep. *American Journal of Physiology-Heart and Circulatory Physiology*, 258(4):H1064–H1069, 1990. pages 5
- [69] Jan Goddard-Finegold, Penelope T Louis, Diana L Rodriguez, Yadin David, Charles F Contant, and Peter Rolfe. Correlation of near infrared spectroscopy cerebral blood flow estimations and microsphere

- quantitations in newborn piglets. *Neonatology*, 74(5):376–384, 1998. pages 18
- [70] Nathalie M Goemans, Mar Tulinius, Johanna T van den Akker, Brigitte E Burm, Peter F Ekhart, Niki Heuvelmans, Tjadine Holling, Anneke A Janson, Gerard J Platenburg, Jessica A Sipkens, et al. Systemic administration of pro051 in duchenne’s muscular dystrophy. *New England Journal of Medicine*, 364(16):1513–1522, 2011. pages 178
- [71] Ary L Goldberger, Luis AN Amaral, Leon Glass, Jeffrey M Hausdorff, Plamen Ch Ivanov, Roger G Mark, Joseph E Mietus, George B Moody, Chung-Kang Peng, and H Eugene Stanley. Physiobank, physiotoolkit, and physionet: Components of a new research resource for complex physiologic signals. *Circulation*, 101(23):e215–e220, 2000. pages 181, 184
- [72] Erik D Gommer, Eri Shijaku, Werner H Mess, and Jos PH Reulen. Dynamic cerebral autoregulation: different signal processing methods without influence on results and reproducibility. *Medical and Biological Engineering and Computing*, 48(12):1243–1250, 2010. pages 134
- [73] Enrico Gratton, Sergio Fantini, Maria Angela Franceschini, Gabriele Gratton, and Monica Fabiani. Measurements of scattering and absorption changes in muscle and brain. *Philosophical Transactions of the Royal Society B: Biological Sciences*, 352(1354):727, 1997. pages 16
- [74] Gorm Greisen. Cerebral blood flow in preterm infants during the first week of life. *Acta Paediatrica*, 75(1):43–51, 1986. pages 5
- [75] Gorm Greisen. Cerebral blood flow and energy metabolism in the newborn. *Clinics in perinatology*, 24(3):531–546, 1997. pages 20
- [76] Gorm Greisen. Autoregulation of cerebral blood flow in newborn babies. *Early human development*, 81(5):423–428, 2005. pages 2, 7, 115, 138
- [77] Gorm Greisen. To autoregulate or not to autoregulate that is no longer the question. *Seminars in Pediatric Neurology*, 16(4):207–215, 2009. pages 38
- [78] Gorm Greisen and Werner Trojaborg. Cerebral blood flow, paco₂ changes, and visual evoked potentials in mechanically ventilated, preterm infants. *Acta Paediatrica*, 76(3):394–400, 1987. pages 5
- [79] Aslak Grinsted, JC Moore, S Jevrejeva, et al. Application of the cross wavelet transform and wavelet coherence to geophysical time series. *Nonlinear processes in geophysics*, 11(5/6):561–566, 2004. pages 43

- [80] Robert L Grubb, Marcus E Raichle, John O Eichling, and Michel M Ter-Pogossian. The effects of changes in paco₂ cerebral blood volume, blood flow, and vascular mean transit time. *Stroke*, 5(5):630–639, 1974. pages 18
- [81] Gitte H Hahn, Christian Heiring, Ole Pryds, and Gorm Greisen. Applicability of near-infrared spectroscopy to measure cerebral autoregulation noninvasively in neonates: a validation study in piglets. *Pediatric research*, 70(2):166–170, 2011. pages 8, 31, 38, 66, 122, 132, 134, 141, 142, 170
- [82] Gitte Holst Hahn, Karl Bang Christensen, Terence S Leung, and Gorm Greisen. Precision of coherence analysis to detect cerebral autoregulation by near-infrared spectroscopy in preterm infants. *Journal of biomedical optics*, 15(3):037002–037002, 2010. pages 38, 116, 124
- [83] Takafumi Hamaoka, Kevin K McCully, Valentina Quaresima, Katsuyuki Yamamoto, and Britton Chance. Near-infrared spectroscopy/imaging for monitoring muscle oxygenation and oxidative metabolism in healthy and diseased humans. *Journal of biomedical optics*, 12(6):062105–062105, 1999. pages 180
- [84] A Haraldsson and W Geven. Half-life of maternal labetalol in a premature infant. *Pharmacy World & Science*, 11(6):229–231, 1989. pages 166
- [85] A. Murray Harper and Sheila Jennett, editors. *Cerebral Blood Flow and Metabolism*. Physiological Society Study Guides. Manchester University Press, 1990. pages 2, 152
- [86] Hauke R Heekeren, Rudiger Wenzel, Hellmuth Obrig, Jan Ruben, J-P Ndayisaba, Qingming Luo, A Dale, Shoko Nioka, Matthias Kohl-Bareis, Ulrich Dirnagl, et al. Toward noninvasive optical human brain mapping: improvements of the spectral, temporal, and spatial resolution of near-infrared spectroscopy. In *BiOS'97, Part of Photonics West*, pages 847–857. International Society for Optics and Photonics, 1997. pages 13
- [87] Hermie J Hermens, Bart Freriks, Roberto Merletti, Dick Stegeman, Joleen Blok, Günter Rau, Cathy Disselhorst-Klug, and Göran Hägg. *European recommendations for surface electromyography*. Roessingh Research and Development The Netherlands, 1999. pages 102
- [88] Kris Hermus, Patrick Wambacq, and Hugo Vanhamme. A review of signal subspace speech enhancement and its application to noise robust speech recognition. *EURASIP Journal on Advances in Signal Processing*, 2007(1):045821, 2006. pages 62

- [89] Siroid Herold, Mtlica Brozovic, J Gibbs, AA Lammertsma, KL Leenders, D Carr, JS Fleming, and T Jones. Measurement of regional cerebral blood flow, blood volume and oxygen metabolism in patients with sickle cell disease using positron emission tomography. *Stroke*, 17(4):692–698, 1986. pages 6
- [90] L. Hoegaerts, JAK Suykens, J. Vandewalle, and B. De Moor. Subset based least squares subspace regression in rkhs. *Neurocomputing*, 63:293–323, 2005. pages 82
- [91] Yoko Hoshi. Functional near-infrared optical imaging: Utility and limitations in human brain mapping. *Psychophysiology*, 40(4):511–520, 2003. pages 13
- [92] Harold Hotelling. Relations between two sets of variates. *Biometrika*, 28(3/4):321–377, 1936. pages 54
- [93] Sylvie Houde, Michèle Filiatrault, Anne Fournier, Julie Dubé, Sylvie D’Arcy, Denis Bérubé, Yves Brousseau, Guy Lapierre, and Michel Vanasse. Deflazacort use in duchenne muscular dystrophy: an 8-year follow-up. *Pediatric neurology*, 38(3):200–206, 2008. pages 175
- [94] Jessica P Houston, Alan B Thompson, Michael Gurfinkel, and Eva M Sevic-Muraca. Sensitivity and depth penetration of continuous wave versus frequency-domain photon migration near-infrared fluorescence contrast-enhanced imaging. *Photochemistry and photobiology*, 77(4):420–430, 2003. pages 13
- [95] Shunsuke Ihara. *Information theory for continuous systems*, volume 2. World Scientific Publishing Company Incorporated, 1993. pages 171
- [96] Akira Ishimaru. Diffusion of a pulse in densely distributed scatterers. *JOSA*, 68(8):1045–1050, 1978. pages 14
- [97] Franz F Jöbsis et al. Noninvasive, infrared monitoring of cerebral and myocardial oxygen sufficiency and circulatory parameters. *Science (New York, NY)*, 198(4323):1264, 1977. pages 9, 17
- [98] Ian Jolliffe. *Principal component analysis*. Wiley Online Library, 2005. pages 76
- [99] M Douglas Jones Jr, Richard J Traystman, Michael A Simmons, and RA Molteni. Effects of changes in arterial o2 content on cerebral blood flow in the lamb. *American Journal of Physiology-Heart and Circulatory Physiology*, 240(2):H209–H215, 1981. pages 5, 6

- [100] Claude Julien. The enigma of mayer waves: facts and models. *Cardiovascular research*, 70(1):12–21, 2006. pages 38
- [101] EA Karpanou, GP Vyssoulis, CI Stefanadis, and DV Cokkinos. Differential pulse pressure response to various antihypertensive drug families. *Journal of human hypertension*, 20(10):765–771, 2006. pages 169
- [102] K. Kashihara, T. Kawada, M. Sugimachi, and K. Sunagawa. Wavelet-based system identification of short-term dynamic characteristics of arterial baroreflex. *Annals of biomedical engineering*, 37(1):112–128, 2009. pages 43
- [103] John D Kenny, Joseph A Garcia-Prats, James L Hilliard, Anthony JS Corbet, and Arnold J Rudolph. Hypercarbia at birth: A possible role in the pathogenesis of Intraventricular hemorrhage. *Pediatrics*, 62(4):465–467, 1978. pages 4
- [104] Seymour S Kety and Carl F Schmidt. The effects of altered arterial tensions of carbon dioxide and oxygen on cerebral blood flow and cerebral oxygen consumption of normal young men. *Journal of Clinical Investigation*, 27(4):484, 1948. pages 6
- [105] Seymour S Kety and Carl F Schmidt. The nitrous oxide method for the quantitative determination of cerebral blood flow in man: theory, procedure and normal values. *Journal of Clinical Investigation*, 27(4):476, 1948. pages 17
- [106] Seunghwan Kim and Jae Hoon Lee. Near-infrared light propagation in an. *ETRI Journal*, 27(4), 2005. pages 11
- [107] Raymond C Koehler, M Douglas Jones Jr, and Richard J Traystman. Cerebral circulatory response to carbon monoxide and hypoxic hypoxia in the lamb. *American Journal of Physiology-Heart and Circulatory Physiology*, 243(1):H27–H32, 1982. pages 5
- [108] Wolfgang M Kuebler, Axel Skell, Oliver Habler, Martin Kleen, Gerhard EH Kuhnle, Martin Welte, Konrad Messmer, and Alwin E Goetz. Noninvasive measurement of regional cerebral blood flow by near-infrared spectroscopy and indocyanine green. *Journal of Cerebral Blood Flow & Metabolism*, 18(4):445–456, 1998. pages 18
- [109] C Dean Kurth and Brian Uher. Cerebral hemoglobin and optical pathlength influence near-infrared spectroscopy measurement of cerebral oxygen saturation. *Anesthesia & Analgesia*, 84(6):1297–1305, 1997. pages 116

- [110] Takashi Kusaka, Yoshio Hisamatsu, Kou Kawada, Kensuke Okubo, Hitoshi Okada, Masanori Namba, Tadashi Imai, Kenichi Isobe, and Susumu Itoh. Measurement of cerebral optical pathlength as a function of oxygenation using near-infrared time-resolved spectroscopy in a piglet model of hypoxia. *Optical review*, 10(5):466–469, 2003. pages 11
- [111] Denis Kwiatkowski, Peter CB Phillips, Peter Schmidt, and Yongcheol Shin. Testing the null hypothesis of stationarity against the alternative of a unit root: How sure are we that economic time series have a unit root? *Journal of econometrics*, 54(1):159–178, 1992. pages 127
- [112] Jean-Henri Lambert. *JH Lambert, et al. Photometria, sive de Mensura et gradibus luminis, colorum et umbrae.* sumptibus viduae E. Klett, 1760. pages 11
- [113] Josje Langenveld, Anita CJ Ravelli, Anton H van Kaam, David P van der Ham, Maria G van Pampus, Martina Porath, Ben Willem Mol, and Wessel Ganzevoort. Neonatal outcome of pregnancies complicated by hypertensive disorders between 34 and 37 weeks of gestation: a 7 year retrospective analysis of a national registry. *American journal of obstetrics and gynecology*, 205(6):540–e1, 2011. pages 166
- [114] NA Lassen. Brain extracellular ph: the main factor controlling cerebral blood flow. *Scandinavian Journal of Clinical & Laboratory Investigation*, 22(4):247–251, 1968. pages 2, 158
- [115] Ju Young Lee, Han Suk Kim, Euiseok Jung, Eun Sun Kim, Gyu Hong Shim, Hyun Joo Lee, Jin A Lee, Chang Won Choi, Ee-Kyung Kim, Beyong Il Kim, et al. Risk factors for periventricular-intraventricular hemorrhage in premature infants. *Journal of Korean medical science*, 25(3):418–424, 2010. pages 4
- [116] Richard W Leech and Ellsworth C Alvord Jr. Morphologic variations in periventricular leukomalacia. *The American journal of pathology*, 74(3):591, 1974. pages 4
- [117] Petra MA Lemmers, Mona C Toet, and Frank van Bel. Impact of patent ductus arteriosus and subsequent therapy with indomethacin on cerebral oxygenation in preterm infants. *Pediatrics*, 121(1):142–147, 2008. pages 19
- [118] Petra MA Lemmers and Frank van Bel. Left-to-right differences of regional cerebral oxygen saturation and oxygen extraction in preterm infants during the first days of life. *Pediatric Research*, 65(2):226–230, 2009. pages 19

- [119] J Leuridan and B Rost. Multiple input estimation of frequency response functions: diagnostic techniques for the excitation. In *American Society of Mechanical Engineers, Design and Production Engineering Technical Conference, Dearborn, MI*, volume 85-DET, page 107, 1985. pages 33, 110
- [120] Jia Li, Gencheng Zhang, Helen Holtby, Bruno Bissonnette, Golden Wang, Andrew N Redington, and Glen S Van Arsdell. Carbon dioxide complex gas in a complex circulation: Its effects on systemic hemodynamics and oxygen transport, cerebral, and splanchnic circulation in neonates after the norwood procedure. *The Journal of Thoracic and Cardiovascular Surgery*, 136(5):1207–1214, 2008. pages 20
- [121] Adam Liebert, Heidrun Wabnitz, Jens Steinbrink, Hellmuth Obrig, Michael Möller, Rainer Macdonald, Arno Villringer, and Herbert Rinneberg. Time-resolved multidistance near-infrared spectroscopy of the adult head: intracerebral and extracerebral absorption changes from moments of distribution of times of flight of photons. *Applied optics*, 43(15):3037–3047, 2004. pages 16
- [122] K.D. Liem and G. Greisen. Monitoring of cerebral haemodynamics in newborn infants. *Early human development*, 86(3):155–158, 2010. pages 2, 18, 19, 20
- [123] KD Liem, JCW Hopman, B Oeseburg, AFJ De Haan, C Festen, and LAA Kollée. Cerebral oxygenation and hemodynamics during induction of extracorporeal membrane oxygenation as investigated by near infrared spectrophotometry. *Pediatrics*, 95(4):555–561, 1995. pages 148, 149, 152
- [124] Benyong Liu. Kernel discrimination via oblique projection. In *Image Analysis and Signal Processing (IASP), 2011 International Conference on*, pages 707–711. IEEE, 2011. pages 80
- [125] Hanyu Liu and Zhenya He. A sliding-exponential window rls adaptive filtering algorithm: properties and applications. *Signal processing*, 45(3):357–368, 1995. pages 65
- [126] Lennart Ljung. *System identification*. Wiley Online Library, 1999. pages 34, 35, 36
- [127] Ildiko E. Frank and Jerome H Friedman. A statistical view of some chemometrics regression tools. *Technometrics*, 35(2):109–135, 1993. pages 77
- [128] Qi-Long Lu, Toshifumi Yokota, Shin'ichi Takeda, Luis Garcia, Francesco Muntoni, and Terence Partridge. The status of exon skipping as a therapeutic approach to duchenne muscular dystrophy. *Molecular Therapy*, 19(1):9–15, 2010. pages 178

- [129] David R Lynch, Gwen Lech, Jennifer M Farmer, Laura J Balcer, William Bank, Britton Chance, and Robert B Wilson. Near infrared muscle spectroscopy in patients with friedreich's ataxia. *Muscle & nerve*, 25(5):664–673, 2002. pages 179
- [130] LA Magee, E Elran, SB Bull, A Logan, and G Koren. Risks and benefits of beta-receptor blockers for pregnancy hypertension: overview of the randomized trials. *European journal of obstetrics, gynecology, and reproductive biology*, 88(1):15–26, 2000. pages 166
- [131] Laura A Magee, Chris Cham, Elizabeth J Waterman, Arne Ohlsson, and Peter Von Dadelszen. Hydralazine for treatment of severe hypertension in pregnancy: meta-analysis. *Bmj*, 327(7421):955, 2003. pages 166
- [132] Maria A Maguire, Timothy W Weaver, Bruce M Damon, et al. Delayed blood reoxygenation following maximum voluntary contraction. *Medicine and science in sports and exercise*, 39(2):257, 2007. pages 179
- [133] VZ Marmarelis, DC Shin, and R. Zhang. Linear and nonlinear modeling of cerebral flow autoregulation using principal dynamic modes. *The Open Biomedical Engineering Journal*, 6:42, 2012. pages 6, 8, 9, 161
- [134] SJ Matcher, K Nahid, M Cope, and DT Delpy. Absolute so< sub>2</sub> measurements in layered media. In *Biomedical Optical Spectroscopy and Diagnostics*. Optical Society of America, 1996. pages 13
- [135] Steven J Matcher, P Kirkpatrick, K Nahid, Mark Cope, and David T Delpy. Absolute quantification methods in tissue near infrared spectroscopy. In *Proc Spie*, volume 2389, pages 486–495, 1995. pages 13, 17
- [136] Kevin K McCully, Takafumi Hamaoka, et al. Near-infrared spectroscopy: what can it tell us about oxygen saturation in skeletal muscle. *Exerc Sport Sci Rev*, 28(3):123–7, 2000. pages 10
- [137] Craig M McDonald, Erik K Henricson, Jay J Han, R Ted Abresch, Alina Nicorici, Gary L Elfring, Leone Atkinson, Allen Reha, Samit Hirawat, and Langdon L Miller. The 6-minute walk test as a new outcome measure in duchenne muscular dystrophy. *Muscle & nerve*, 41(4):500–510, 2010. pages 104, 177
- [138] Sebastian Mika, Bernhard Schölkopf, Alex Smola, Klaus-Robert Müller, Matthias Scholz, and Gunnar Rätsch. Kernel pca and de-noising in feature spaces. *Advances in neural information processing systems*, 11(1):536–542, 1999. pages 78

- [139] M Moran, J Miletin, K Pichova, and EM Dempsey. Cerebral tissue oxygenation index and superior vena cava blood flow in the very low birth weight infant. *Acta Paediatrica*, 98(1):43–46, 2009. pages 18
- [140] Geert Morren, Gunnar Naulaers, Philippe Lemmerling, Sabine Van Huffel, Paul Casaer, and Hugo Devlieger. Quantitation of the concordance between cerebral intravascular oxygenation and mean arterial blood pressure for the detection of impaired autoregulation. *Adv Exp Med Biol*, 510:403–408, 2003. pages 110
- [141] FA Mosca, M Colnaghi, M Lattanzio, M Bray, S Pugliese, and M Fumagalli. Closed versus open endotracheal suctioning in preterm infants: effects on cerebral oxygenation and blood volume. *Neonatology*, 72(1):9–14, 1997. pages 20
- [142] Marvin Moser, Catherine M Brown, Carl H Rose, and Vesna D Garovic. Hypertension in pregnancy: is it time for a new approach to treatment? *Journal of Hypertension*, 30(6):1092, 2012. pages 166
- [143] Reinier A Mullaart, Jeroen CW Hopman, Jan J Rotteveel, Otto Daniëls, Gerard Stoeltinga, and Anton FJ De Haan. Cerebral blood flow fluctuation in neonatal respiratory distress and periventricular haemorrhage. *Early human development*, 37(3):179–185, 1994. pages 4
- [144] J.M. Murkin, J.K. Farrar, W.A. Tweed, F.N. McKenzie, and G. Guiraudon. Cerebral autoregulation and flow/metabolism coupling during cardiopulmonary bypass the influence of paco₂. *Anesthesia & Analgesia*, 66(9):825–832, 1987. pages 2, 8, 158
- [145] Lassen NA. Cerebral blood flow and oxygen consumption in man. *Physiological Reviews*, 39:183–238, 1959. pages 7
- [146] Nicole Nagdyman, Peter Ewert, Björn Peters, Oliver Miera, Thilo Fleck, and Felix Berger. Comparison of different near-infrared spectroscopic cerebral oxygenation indices with central venous and jugular venous oxygenation saturation in children. *Pediatric Anesthesia*, 18(2):160–166, 2008. pages 15
- [147] Nicole Nagdyman, Thilo Fleck, Sven Barth, Hashim Abdul-Khaliq, Brigitte Stiller, Peter Ewert, Michael Huebler, Hermann Kuppe, and PeterE Lange. Relation of cerebral tissue oxygenation index to central venous oxygen saturation in children. *Intensive care medicine*, 30(3):468–471, 2004. pages 18
- [148] Nicole Nagdyman, Thilo Fleck, Stephan Schubert, Peter Ewert, Björn Peters, Peter E Lange, and Hashim Abdul-Khaliq. Comparison between

- cerebral tissue oxygenation index measured by near-infrared spectroscopy and venous jugular bulb saturation in children. *Intensive care medicine*, 31(6):846–850, 2005. pages 110
- [149] Gunnar Naulaers. *Non-invasive measurements of the neonatal cerebral and splanchnic circulation by near-infrared spectroscopy*. PhD thesis, KU Leuven, 2003. pages 2, 11, 15, 19
- [150] Gunnar Naulaers, Bart Meyns, Marc Miserez, Veerle Leunens, Sabine Van Huffel, Paul Casaer, Michael Weindling, and Hugo Devlieger. Use of tissue oxygenation index and fractional tissue oxygen extraction as non-invasive parameters for cerebral oxygenation. *Neonatology*, 92(2):120–126, 2007. pages 18, 19
- [151] Gunnar Naulaers, Geert Morren, Sabine Van Huffel, Paul Casaer, and Hugo Devlieger. Cerebral tissue oxygenation index in very premature infants. *Archives of Disease in Childhood-Fetal and Neonatal Edition*, 87(3):F189–F192, 2002. pages 19
- [152] Eiji Okada and David T Delpy. Near-infrared light propagation in an adult head model. i. modeling of low-level scattering in the cerebrospinal fluid layer. *Applied optics*, 42(16):2906–2914, 2003. pages 11
- [153] Eiji Okada and David T Delpy. Near-infrared light propagation in an adult head model. ii. effect of superficial tissue thickness on the sensitivity of the near-infrared spectroscopy signal. *Applied optics*, 42(16):2915–2922, 2003. pages 11
- [154] Alan V Oppenheim, Ronald W Schafer, John R Buck, et al. *Discrete-time signal processing*, volume 2. Prentice hall Englewood Cliffs, NJ., 1989. pages 41
- [155] Peter Van Overschee, BLD Moor, David A Hensher, John M Rose, William H Greene, Kenneth Train, W Greene, E Krause, J Gere, and R Hibbeler. *Subspace Identification for the Linear Systems: Theory–Implementation*. Boston: Kluwer Academic Publishers, 1996. pages 62
- [156] H. Owen-Reece, M. Smith, CE Elwell, JC Goldstone, et al. Near infrared spectroscopy. *British journal of anaesthesia*, 82:418–426, 1999. pages 1, 9, 10
- [157] RB Panerai, ST Deverson, P. Mahony, P. Hayes, and DH Evans. Effect of co₂ on dynamic cerebral autoregulation measurement. *Physiological measurement*, 20(3):265, 1999. pages 2, 8, 158

- [158] R.B. Panerai, D.M. Simpson, S.T. Deverson, P. Mahony, P. Hayes, and D.H. Evans. Multivariate dynamic analysis of cerebral blood flow regulation in humans. *Biomedical Engineering, IEEE Transactions on*, 47(3):419–423, 2000. pages 8, 9
- [159] R.B. Panerai, R.P. White, H.S. Markus, and D.H. Evans. Grading of cerebral dynamic autoregulation from spontaneous fluctuations in arterial blood pressure. *Stroke*, 29(11):2341–2346, 1998. pages 29, 133
- [160] Maria D Papademetriou, Ilias Tachtsidis, Murad Banaji, Martin J Elliott, Aparna Hoskote, and Clare E Elwell. Optical topography to measure variations in regional cerebral oxygenation in an infant supported on veno-arterial extra-corporeal membrane oxygenation. *Oxygen Transport to Tissue XXXIII*, pages 71–76, 2012. pages 149
- [161] Maria D Papademetriou, Ilias Tachtsidis, Terence S Leung, Martin J Elliott, Aparna Hoskote, and Clare E Elwell. Cerebral and peripheral tissue oxygenation in children supported on ecmo for cardio-respiratory failure. *Oxygen Transport to Tissue XXXI*, pages 447–453, 2010. pages 149
- [162] Lu-Ann Papile, Abraham M Rudolph, and Michael A Heymann. Autoregulation of cerebral blood flow in the preterm fetal lamb. *Pediatric research*, 19(2):159–161, 1985. pages 5
- [163] Michael S Patterson, Britton Chance, Brian C Wilson, et al. Time resolved reflectance and transmittance for the non-invasive measurement of tissue optical properties. *Appl. Opt*, 28(12):2331–2336, 1989. pages 13, 14
- [164] Tingying Peng, Alexander B Rowley, Philip N Ainslie, Marc J Poulin, and Stephen J Payne. Multivariate system identification for cerebral autoregulation. *Annals of Biomedical Engineering*, 36(2):308–320, 2008. pages 9, 143, 145, 158
- [165] T Penzel, GB Moody, RG Mark, AL Goldberger, and JH Peter. The apnea-ecg database. In *Computers in Cardiology 2000*, pages 255–258. IEEE, 2000. pages 181
- [166] Jeffrey M Perlman, Steven Goodman, Katherine L Kreusser, and Joseph J Volpe. Reduction in intraventricular hemorrhage by elimination of fluctuating cerebral blood-flow velocity in preterm infants with respiratory distress syndrome. *New England Journal of Medicine*, 312(21):1353–1357, 1985. pages 4
- [167] Jeffrey M Perlman, Joseph B McMenamin, and Joseph J Volpe. Fluctuating cerebral blood-flow velocity in respiratory-distress syndrome. *New England Journal of Medicine*, 309(4):204–209, 1983. pages 4

- [168] Anna Petrova and Rajeev Mehta. Near-infrared spectroscopy in the detection of regional tissue oxygenation during hypoxic events in preterm infants undergoing critical care. *Pediatric Critical Care Medicine*, 7(5):449–454, 2006. pages 19
- [169] Anna Petrova and Rajeev Mehta. Regional tissue oxygenation in association with duration of hypoxaemia and haemodynamic variability in preterm neonates. *Archives of Disease in Childhood-Fetal and Neonatal Edition*, 95(3):F213–F219, 2010. pages 19
- [170] Tuan H Pham, Frederic Bevilacqua, Thorsten Spott, Jan S Dam, Bruce J Tromberg, and Stefan Andersson-Engels. Quantifying the absorption and reduced scattering coefficients of tissuelike turbid media over a broad spectral range with noncontact fourier-transform hyperspectral imaging. *Applied optics*, 39(34):6487–6497, 2000. pages 16
- [171] Tuan H Pham, Olivier Coquoz, Joshua B Fishkin, Eric Anderson, and Bruce J Tromberg. Broad bandwidth frequency domain instrument for quantitative tissue optical spectroscopy. *Review of Scientific Instruments*, 71(6):2500–2513, 2000. pages 16
- [172] O Pryds and AD Edwards. Cerebral blood flow in the newborn infant. *Archives of Disease in Childhood-Fetal and Neonatal Edition*, 74(1):F63–F69, 1996. pages 5
- [173] O Pryds, G Greisen, H Lou, B Friis-Hansen, et al. Vasoparalysis associated with brain damage in asphyxiated term infants. *The Journal of pediatrics*, 117(1 Pt 1):119, 1990. pages 20
- [174] Ole Pryds. Control of cerebral circulation in the high-risk neonate. *Annals of neurology*, 30(3):321–329, 1991. pages 5
- [175] Sushmita Purkayastha, Ashwini Saxena, Wendy L Eubank, Besim Hoxha, and Peter B Raven. α 1-adrenergic receptor control of the cerebral vasculature in humans at rest and during exercise. *Experimental Physiology*, 98(2):451–461, 2013. pages 169
- [176] Rangaraj Rangayyan. *Biomedical Signal Analysis: A case study approach*. John Wiley & Sons, 2002. pages 105
- [177] Jarl Risberg, Daniel Ancrì, and David H Ingvar. Correlation between cerebral blood volume and cerebral blood flow in the cat. *Experimental Brain Research*, 8(4):321–326, 1969. pages 18
- [178] I Roberts, P Fallon, FJ Kirkham, A Lloyd-Thomas, C Cooper, R Maynard, M Elliot, AD Edwards, et al. Estimation of cerebral blood flow with near

- infrared spectroscopy and indocyanine green. *Lancet*, 342(8884):1425, 1993. pages 18
- [179] Roman Rosipal, Andrzej Cichocki, Leonard J Trejo, Paisley Univ.(United Kingdom). Dept. of Computing, and Information Systems;. *Kernel principal component regression with em approach to nonlinear principal components extraction*. University of Paisley, 2000. pages 77, 82
- [180] Roman Rosipal and Leonard J Trejo. Kernel partial least squares regression in reproducing kernel hilbert space. *The Journal of Machine Learning Research*, 2:97–123, 2002. pages 82
- [181] Peter J Rousseeuw and Annick M Leroy. *Robust Regression and Outlier Detection*. Wiley, 2003. pages 73
- [182] AB Rowley, SJ Payne, I Tachtsidis, MJ Ebden, JP Whiteley, DJ Gavaghan, L Tarassenko, M Smith, CE Elwell, and DT Delpy. Synchronization between arterial blood pressure and cerebral oxyhaemoglobin concentration investigated by wavelet cross-correlation. *Physiological measurement*, 28(2):161, 2007. pages 42, 43
- [183] Andrea Saltelli, Marco Ratto, Terry Andres, Francesca Campolongo, Jessica Cariboni, Debora Gatelli, Michaela Saisana, and Stefano Tarantola. *Global sensitivity analysis: the primer*. Wiley-Interscience, 2008. pages 125
- [184] Mikael Sander, Bahman Chavoshan, Shannon A Harris, Susan T Iannaccone, James T Stull, Gail D Thomas, and Ronald G Victor. Functional muscle ischemia in neuronal nitric oxide synthase-deficient skeletal muscle of children with duchenne muscular dystrophy. *Proceedings of the National Academy of Sciences*, 97(25):13818–13823, 2000. pages 170, 179
- [185] Ola Didrik Saugstad. Oxidative stress in the newborn—a 30-year perspective. *Neonatology*, 88(3):228–236, 2005. pages 19
- [186] Craig Saunders, Alexander Gammerman, and Volodya Vovk. Ridge regression learning algorithm in dual variables. In *(ICML-1998) Proceedings of the 15th International Conference on Machine Learning*, pages 515–521. Morgan Kaufmann, 1998. pages 82
- [187] Sicco A Scherjon, Hans Oosting, Joke H Kok, and HA Zondervan. Effect of fetal brainsparing on the early neonatal cerebral circulation. *Archives of Disease in Childhood-Fetal and Neonatal Edition*, 71(1):F11–F15, 1994. pages 169

- [188] Bernhard Schölkopf, Alexander Smola, and Klaus-Robert Müller. Nonlinear component analysis as a kernel eigenvalue problem. *Neural computation*, 10(5):1299–1319, 1998. pages 78
- [189] Naoki Shimizu, Fay Gilder, Bruno Bissonnette, John Coles, Desmond Bohn, and Katsuyuki Miyasaka. Brain tissue oxygenation index measured by near infrared spatially resolved spectroscopy agreed with jugular bulb oxygen saturation in normal pediatric brain: a pilot study. *Child's Nervous System*, 21(3):181–184, 2005. pages 18
- [190] Robert M Shuman and Leonard J Selednik. Periventricular leukomalacia: a one-year autopsy study. *Archives of neurology*, 37(4):231, 1980. pages 4
- [191] L Skov, O Pryds, and G Greisen. Estimating cerebral blood flow in newborn infants: comparison of near infrared spectroscopy and ^{133}Xe clearance. *Pediatric research*, 30(6):570–573, 1991. pages 18, 19
- [192] L Skov, J Ryding, O Pryds, and G Greisen. Changes in cerebral oxygenation and cerebral blood volume during endotracheal suctioning in ventilated neonates. *Acta Paediatrica*, 81(5):389–393, 1992. pages 20
- [193] D Smet, J Jacobs, Lieveke Ameye, Joke Vanderhaegen, Gunnar Naulaers, P Lemmers, F Bel, M Wolf, and S Huffel. The partial coherence method for assessment of impaired cerebral autoregulation using near-infrared spectroscopy: potential and limitations. *Oxygen Transport to Tissue XXXI*, pages 219–224, 2010. pages 30, 33, 143
- [194] Dominique De Smet, Joke Vanderhaegen, Gunnar Naulaers, and Sabine Van Huffel. New measurements for assessment of impaired cerebral autoregulation using near-infrared spectroscopy. *Oxygen transport to tissue xxx*, pages 273–278, 2009. pages 138
- [195] Line C Sorensen and Gorm Greisen. Precision of measurement of cerebral tissue oxygenation index using near-infrared spectroscopy in preterm neonates. *Journal of biomedical optics*, 11(5):054005–054005, 2006. pages 19
- [196] Line C Sorensen, Terence S Leung, and Gorm Greisen. Comparison of cerebral oxygen saturation in premature infants by near-infrared spatially resolved spectroscopy: observations on probe-dependent bias. *Journal of biomedical optics*, 13(6):064013–064013, 2008. pages 19
- [197] Janet S Soul, Peter E Hammer, Miles Tsuji, J Philip Saul, Haim Bassan, Catherine Limperopoulos, Donald N Disalvo, Marianne Moore, Patricia Akins, Steven Ringer, et al. Fluctuating pressure-passivity is common in the cerebral circulation of sick premature infants. *Pediatric research*, 61(4):467–473, 2007. pages 5, 20, 29, 110, 115, 120, 138, 140

- [198] Janet S Soul, George A Taylor, David Wypij, Adré J Duplessis, and Joseph J Volpe. Noninvasive detection of changes in cerebral blood flow by near-infrared spectroscopy in a piglet model of hydrocephalus. *Pediatric research*, 48(4):445–449, 2000. pages 116, 138
- [199] Luzius A Steiner, David Pfister, Stephan P Strebel, Danila Radolovich, Peter Smielewski, and Marek Czosnyka. Near-infrared spectroscopy can monitor dynamic cerebral autoregulation in adults. *Neurocritical care*, 10(1):122–128, 2009. pages 124
- [200] Ralf Steinmeier, Christian Bauhuf, Ulrich Hübner, Robby P Hofmann, and Rudolf Fahlbusch. Continuous cerebral autoregulation monitoring by cross-correlation analysis: Evaluation in healthy volunteers. *Critical care medicine*, 30(9):1969–1975, 2002. pages 31
- [201] Johan AK Suykens, Joseph De Brabanter, Lukas Lukas, and Joos Vandewalle. Weighted least squares support vector machines: robustness and sparse approximation. *Neurocomputing*, 48(1):85–105, 2002. pages 72
- [202] Johan AK Suykens, Tony Van Gestel, Jos De Brabanter, Bart De Moor, and Joos Vandewalle. *Least squares support vector machines*. World Scientific Publishing Company Incorporated, 2003. pages 72
- [203] Susumu Suzuki, Sumio Takasaki, Takeo Ozaki, and Yukio Kobayashi. A tissue oxygenation monitor using nir spatially resolved spectroscopy. In *Proceedings of SPIE, the International Society for Optical Engineering*, volume 3597, pages 582–592. Society of Photo-Optical Instrumentation Engineers, 1999. pages 13, 15, 17
- [204] W Szymonowicz, AM Walker, VYH Yu, ML Stewart, J Cannata, and L Cussen. Regional cerebral blood flow after hemorrhagic hypotension in the preterm, near-term, and newborn lamb. *Pediatric research*, 28(4):361–366, 1990. pages 5
- [205] Ilias Tachtsidis. *Experimental measurements of cerebral haemodynamics and oxygenation and comparisons with a computational model: a near-infrared spectroscopy investigation*. PhD thesis, University College London, London, UK, 2005. pages 11, 15
- [206] Ilias Tachtsidis, Martin Tisdall, David T Delpy, Martin Smith, and Clare E Elwell. Measurement of cerebral tissue oxygenation in young healthy volunteers during acetazolamide provocation: a transcranial doppler and near-infrared spectroscopy investigation. *Oxygen Transport to Tissue XXIX*, pages 389–396, 2008. pages 138

- [207] Joachim Taelman, Joke Vanderhaegen, Mieke Robijns, Gunnar Naulaers, Arthur Spaepen, and Sabine Van Huffel. Estimation of muscle fatigue using surface electromyography and near-infrared spectroscopy. *Adv Exp Med Biol*, 701:353–9, 2011. pages 171, 172, 180
- [208] Mamoru Tamura, Yoko Hoshi, and Fumihiko Okada. Localized near-infrared spectroscopy and functional optical imaging of brain activity. *Philosophical Transactions of the Royal Society B: Biological Sciences*, 352(1354):737, 1997. pages 13
- [209] Cajo JF Ter Braak. Interpreting canonical correlation analysis through biplots of structure correlations and weights. *Psychometrika*, 55(3):519–531, 1990. pages 58
- [210] Gail D Thomas, Jim Hansen, and Ronald G Victor. Atp-sensitive potassium channels mediate contraction-induced attenuation of sympathetic vasoconstriction in rat skeletal muscle. *Journal of Clinical Investigation*, 99(11):2602, 1997. pages 180
- [211] Robert Joseph Thomas, Joseph E Mietus, Chung-Kang Peng, Geoffrey Gilmartin, Robert W Daly, Ary L Goldberger, and Daniel J Gottlieb. Differentiating obstructive from central and complex sleep apnea using an automated electrocardiogram-based method. *Sleep*, 30(12):1756, 2007. pages 181
- [212] Martin M Tisdall, Christopher Taylor, Ilias Tachtsidis, Terence S Leung, Clare E Elwell, and Martin Smith. The effect on cerebral tissue oxygenation index of changes in the concentrations of inspired oxygen and end-tidal carbon dioxide in healthy adult volunteers. *Anesthesia & Analgesia*, 109(3):906–913, 2009. pages 152, 153
- [213] Christopher Torrence and Gilbert P Compo. A practical guide to wavelet analysis. *Bulletin of the American Meteorological society*, 79(1):61–78, 1998. pages 40, 42, 43, 47
- [214] A Torricelli, A Pifferi, L Spinelli, P Taroni, V Quaresima, M Ferrari, and R Cubeddu. Multi-channel time-resolved tissue oximeter for functional imaging of the brain. In *Instrumentation and Measurement Technology Conference, 2004. IMTC 04. Proceedings of the 21st IEEE*, volume 3, pages 1980–1983. IEEE, 2004. pages 16
- [215] Miles Tsuji, Adre Duplessis, George Taylor, Robert Crocker, and Joseph J Volpe. Near infrared spectroscopy detects cerebral ischemia during hypotension in piglets. *Pediatric research*, 44(4):591–595, 1998. pages 4, 109, 116

- [216] Miles Tsuji, J Philip Saul, Adre du Plessis, Eric Eichenwald, Jamil Sobh, Robert Crocker, and Joseph J Volpe. Cerebral intravascular oxygenation correlates with mean arterial pressure in critically ill premature infants. *Pediatrics*, 106(4):625–632, 2000. pages 4, 109, 112, 115, 138, 140, 143
- [217] Lidia Tyszczyk, Judith Meek, Clare Elwell, and JS Wyatt. Cerebral blood flow is independent of mean arterial blood pressure in preterm infants undergoing intensive care. *Pediatrics*, 102(2):337–341, 1998. pages 115
- [218] Mark A Underwood, Jay M Milstein, and Michael P Sherman. Near-infrared spectroscopy as a screening tool for patent ductus arteriosus in extremely low birth weight infants. *Neonatology*, 91(2):134–139, 2007. pages 19
- [219] Frank van Bel, Petra Lemmers, and G. Naulaers. Monitoring neonatal regional cerebral oxygen saturation in clinical practice: value and pitfalls. *Neonatology*, 4:237–244, 2008. pages 8, 19, 20, 66, 110, 116
- [220] Joke Vanderhaegen, Gunnar Naulaers, Sabine Van Huffel, Christine Vanhole, and Karel Allegaert. Cerebral and systemic hemodynamic effects of intravenous bolus administration of propofol in neonates. *Neonatology*, 98(1):57–63, 2010. pages 117
- [221] Joseph J Volpe. Neurobiology of periventricular leukomalacia in the premature infant. *Pediatric research*, 50(5):553–562, 2001. pages 5
- [222] Joseph J Volpe. Intraventricular hemorrhage in the premature infant current concepts. part ii. *Annals of neurology*, 25(2):109–116, 2004. pages 4
- [223] Joseph J Volpe. *Neurology of the Newborn*. Saunders, 2008. pages 4, 5
- [224] Kurt von Siebenthal, Jan Beran, Martin Wolf, Matthias Keel, Vera Dietz, Seema Kundu, and Hans Ulrich Bucher. Cyclical fluctuations in blood pressure, heart rate and cerebral blood volume in preterm infants. *Brain and Development*, 21(8):529–534, 1999. pages 110
- [225] J.A. Wahr, K.K. Tremper, S. Samra, and D.T. Delpy. Near-infrared spectroscopy: theory and applications. *Journal of cardiothoracic and vascular anesthesia*, 10(3):406–418, 1996. pages 9, 10
- [226] David F Walnut. *An introduction to wavelet analysis*. Birkhäuser Boston, 2001. pages 39
- [227] SP Wardle, R Garr, CW Yoxall, and AM Weindling. A pilot randomised controlled trial of peripheral fractional oxygen extraction to guide blood

- transfusions in preterm infants. *Archives of Disease in Childhood-Fetal and Neonatal Edition*, 86(1):F22–F27, 2002. pages 19
- [228] Stephen P Wardle and A Michael Weindling. Peripheral fractional oxygen extraction and other measures of tissue oxygenation to guide blood transfusions in preterm infants. In *Seminars in perinatology*, volume 25, pages 60–64. Elsevier, 2001. pages 19
- [229] Stephen P Wardle, C William Yoxall, and A Michael Weindling. Determinants of cerebral fractional oxygen extraction using near infrared spectroscopy in preterm neonates. *Journal of Cerebral Blood Flow & Metabolism*, 20(2):272–279, 2000. pages 6, 19, 20
- [230] H Marc Watzman, C Dean Kurth, Lisa M Montenegro, Jonathan Rome, James M Steven, and Susan C Nicolson. Arterial and venous contributions to near-infrared cerebral oximetry. *Anesthesiology*, 93(4):947, 2000. pages 18
- [231] Markus Weiss, Alexander Dullenkopf, Anna Kolarova, Gabriele Schulz, Bernhard Frey, and Oskar Baenziger. Near-infrared spectroscopic cerebral oxygenation reading in neonates and infants is associated with central venous oxygen saturation. *Pediatric Anesthesia*, 15(2):102–109, 2005. pages 18
- [232] Peter Welch. The use of fast fourier transform for the estimation of power spectra: a method based on time averaging over short, modified periodograms. *Audio and Electroacoustics, IEEE Transactions on*, 15(2):70–73, 1967. pages 32, 36, 120, 123, 133
- [233] M. Wolf, M. Ferrari, and V. Quaresima. Progress of near-infrared spectroscopy and topography for brain and muscle clinical applications. *Journal of biomedical optics*, 12(6):062104–062104, 2007. pages 1, 9, 15, 16
- [234] Flora Y Wong, Terence S Leung, Topun Austin, Malcolm Wilkinson, Judith H Meek, John S Wyatt, and Adrian M Walker. Impaired autoregulation in preterm infants identified by using spatially resolved spectroscopy. *Pediatrics*, 121(3):e604–e611, 2008. pages 8, 29, 115, 120, 138, 140, 143, 149, 167
- [235] Flora Y Wong, Makoto Nakamura, Theodora Alexiou, Vojta Brodecky, and Adrian M Walker. Tissue oxygenation index measured using spatially resolved spectroscopy correlates with changes in cerebral blood flow in newborn lambs. *Intensive care medicine*, 35(8):1464–1470, 2009. pages 66, 105, 158

- [236] JS Wyatt, M Cope, DT Delpy, CE Richardson, AD Edwards, S Wray, and EO Reynolds. Quantitation of cerebral blood volume in human infants by near-infrared spectroscopy. *Journal of Applied Physiology*, 68(3):1086–1091, 1990. pages 18, 116
- [237] JS Wyatt, M Cope, DT Delpy, P Van der Zee, S Arridge, AD Edwards, and EOR Reynolds. Measurement of optical path length for cerebral near-infrared spectroscopy in newborn infants. *Developmental neuroscience*, 12(2):140–144, 1990. pages 11, 96
- [238] JS Wyatt, AD Edwards, M Cope, DT Delpy, DC McCormick, A Potter, and EOR Reynolds. Response of cerebral blood volume to changes in arterial carbon dioxide tension in preterm and term infants. *Pediatric research*, 29(6):553–557, 1991. pages 20
- [239] Haruo Yanai, Kei Takeuchi, and Yoshio Takane. *Projection matrices, generalized inverse matrices, and singular value decomposition*. Springer, 2011. pages 61
- [240] SeongHun Yoon, Mario Zuccarello, and Robert M Rapoport. pco₂ and ph regulation of cerebral blood flow. *Frontiers in Physiology*, 3:365, 2012. pages 2
- [241] DP Younkin, M Reivich, JL Jaggi, WD Obrist, and M Delivoria-Papadopoulos. The effect of hematocrit and systolic blood pressure on cerebral blood flow in newborn infants. *Journal of Cerebral Blood Flow & Metabolism*, 7(3):295–299, 1987. pages 5
- [242] Charles W Yoxall and A Michael Weindling. Measurement of cerebral oxygen consumption in the human neonate using near infrared spectroscopy: cerebral oxygen consumption increases with advancing gestational age. *Pediatric research*, 44(3):283–290, 1998. pages 19
- [243] R. Zhang, J.H. Zuckerman, C.A. Giller, and B.D. Levine. Transfer function analysis of dynamic cerebral autoregulation in humans. *American Journal of Physiology-Heart and Circulatory Physiology*, 274(1):H233–H241, 1998. pages 7, 158
- [244] R. Zhang, J.H. Zuckerman, K. Iwasaki, T.E. Wilson, C.G. Crandall, and B.D. Levine. Autonomic neural control of dynamic cerebral autoregulation in humans. *Circulation*, 106(14):1814–1820, 2002. pages 8
- [245] Yi Zheng, Zhili Zhang, Qian Liu, Chuanhua Cao, and Hui Gong. Design and evaluation of a portable continuous-wave nir topography instrument. In *Fourth International Conference on Photonics and Imaging in Biology and Medicine*, pages 60470X–60470X. International Society for Optics and Photonics, 2006. pages 13

Curriculum vitae

Alexander Caicedo Dorado was born in Bogota-Cundinamarca, Colombia on June 21, 1984. In December 2004 he received the degree of electrical engineer from the University of Ibague, in Ibague Colombia.

During 2005 he worked as teaching assistant at the University of Ibague, Colombia. In May 2005 he started his Master studies on Control Engineering. From May 2006 to February 2007, he traveled to Ghent, in Belgium, in the framework of the LaBioProC network for the development of his master thesis at the Ghent University. In December 2007 he received his degree of MSc. on Control engineering from the University of Ibague joint with the LabioProC Network. During May 2007 to January 2009 he worked at the University of Ibague in Colombia as teaching assistant.

In February 2009, he joined the BioMed research group at the Department of Electrical Engineering (ESAT-SCD) of the KU Leuven. He started as a predoctoral student. From July 2009 he is a PhD student under the supervision of Prof. Dr. Ir. Sabine Van Huffel and Prof. Dr. Gunnar Naulaers. From April to June 2011, he did an internship at the University college London in UK. His research work during his PhD was focused on signal processing for cerebral hemodynamics monitoring.

List of publications

Papers in international journals

1. **Caicedo A**, De Smet D, Vanderhaegen J, Naulaers G, Wolf M, Lemmers P, van Bel F, Ameye L, and Van Huffel S. Impaired cerebral autoregulation using near-infrared spectroscopy and its relation to clinical outcomes in premature infants. *Adv. Exp. Med. Biol.* 2011, 701: 233-239.
2. **Caicedo A**, De Smet D, Naulaers G, Ameye L, Vanderhaegen J, Lemmers P, van Bel F, Van Huffel S. Cerebral tissue oxygenation and regional oxygen saturation can be used to study cerebral autoregulation in prematurely born infants. *Pediatr Res.* 2011, 69(6): 548-553
3. **Caicedo A**, Naulaers G, Wolf M, Lemmers P, van Bel F, Ameye L, Van Huffel S. Assessment of the Myogenic and Metabolic Mechanism Influence in Cerebral Autoregulation Using Near-Infrared Spectroscopy. *Adv. Exp. Med. Biol.* 2012, 737: 37-44
4. **Caicedo A**, Papademetriou MD, Elwell CE, Hoskote A, Elliott MJ, Van Huffel S, Tachtsidis I. Canonical correlation analysis in the study of cerebral and peripheral haemodynamics interrelations with systemic variables in neonates supported on ECMO. *Adv Exp Med Biol.* 2013, 765: 23-29.
5. **Caicedo A**, Naulaers G, Lemmers P, van Bel F, Wolf M, Van Huffel S. Detection of cerebral autoregulation by near-infrared spectroscopy in neonates: performance analysis of measurement methods. *J Biomed Opt.* 2012, 17(11): 117003
6. Widjaja D., Varon C., **Caicedo A**, Suykens J.A.K., Van Huffel S. Application of Kernel Principal Component Analysis for Single Lead

ECG-Derived Respiration. *IEEE Trans Biomed Eng* 2012, 59(4): 1169-1176. (*Finalist of the IEEE-EMBS Benelux Chapter award, January 2013*).

7. **Caicedo A**, Thewissen L, Naulaers G, Lemmers P, van Bel F, Van Huffel S. Effect of Maternal use of Labetalol on the Cerebral Autoregulation in Premature Infants. *Adv Exp Med Biol.* 2013, Vol 789, chapter 15. to appear

Internal reports

8. **Caicedo A**, Varon C., Suykens J., Van Huffel S. Projection Matrices in Reproducing Kernel Hilbert Spaces for Kernel Principal Component Regression¹H Magnetic Resonance Spectroscopy signals. *Internal Report 13-51*. ESAT-SCD, KU Leuven, April 2013.

Papers submitted in international journals

9. Aisha S.S. van den Abeelen M, Simpson D, Lotte J Y Wang, Rong Zhang, Takashi Tarumi, Caroline A Rickards, Stephen P, Georgios D.M, Kyriaki K, Marmarelis V, Shin D, Tzeng YC, Ainslie PN, Gommer E, Muller M, **Caicedo A**, Smielewski P, Yelicich B, Puppo C, Liu X, Czosnyka M, Wang N, Novak V, Panerai RB, Claassen J Multi-centre study: Between-centre variability in transfer function analysis, a widely used method for linear quantification of the dynamic pressure-flow relation: the CARNet study. *Journal of Medical Engineering and Physics.* February 2013, submitted.
10. Widjaja D., **Caicedo A**, Vlemincx E., Van Diest I., Van Huffel S. Separation of respiratory influences from the tachogram: a methodological evaluation. *Journal of Medical & Biological Engineering & Computing.* April 2013, submitted.

Chapters in books with peer review

11. Naulaers G., **Caicedo A**, Van Huffel S., Use of Near-Infrared Spectroscopy In the Neonatal Intensive Care Unit *Neonatal Monitoring Technologies: Design for Integrated Solutions*, (Chen W., Oetomo SB., and Feijs L., eds.), IGI Global (Hershey, Pennsylvania US), 2011, pp. 56-83.

Books - as editor

12. Van Huffel S., Naulaers G., **Caicedo A**, Bruley D.F., Harrison D.K. Editors, Oxygen Transport to Tissue XXXV, Springer, New York, Book Series: Adv. Exp. Med. Biol. 2013. Vol 789 *to appear*

Papers in proceedings of international conferences

13. **Caicedo A**, Naulaers G, Wolf M, Lemmers P, Van Bel F, Ameye L, Van Huffel S. Cerebral autoregulation assessment in premature infants: Clinical relevance. Proceedings of the Biosignal 2010 conference (Advanced technologies in intensive care and sleep medicine), Berlin, Germany, July 14-16, 2010, 4 pages.
14. **Caicedo A**, Van Huffel S. Weighted LS-SVM for function estimation applied to artifact removal in biosignal processing. Proceedings of the 32th annual international conference of the IEEE Engineering in Medicine and Biology Society (EMBC 2010), Buenos Aires, Argentina, 2010, paper 1578: 988 - 991.
15. **Caicedo A**, Tachtsidis I, Papademetriou MD, Van Huffel S. Decoupling the influence of systemic variables in the peripheral and cerebral haemodynamics during ECMO procedure by means of oblique and orthogonal subspace projections. Proceedings of the 34th annual international conference of the IEEE Engineering in Medicine and Biology Society, (EMBC 2012), San Diego, USA, 2012, pp: 6153 - 6156.
16. **Caicedo A**, Naulaers G., Van Huffel S. Preprocessing by means of Subspace Projections for Continuous Cerebral Autoregulation Assessment Using NIRS. Proceedings of the 35th annual international conference of the IEEE Engineering in Medicine and Biology Society, (EMBC 2013), Osaka, Japan, July 3-7, 2013. *To appear*
17. Widjaja D., Varon C., **Caicedo A**, Van Huffel S. An improved ECG-Derived Respiration Method using Kernel Principal Component Analysis. Proceedings of the 38th Annual Computing in Cardiology (CinC2011), Hangzhou, China, Sep. 2011, pp. 45-48.

Abstracts in proceedings of (inter)national conferences

18. **Caicedo A**, De Smet D, Vanderhaegen J, Naulaers G, Wolf M, Lemmers P, van Bel F, Ameye L, Van Huffel S. Assessment of cerebral autoregulation using Near-Infrared Spectroscopy and its relation to short and long term clinical outcomes in premature infants. "IAP VI/4 DYSCO Dynamical systems control and optimization study day" 27th November 2009. Leuven, Belgium.
19. **Caicedo A**, De Smet D, Vanderhaegen J, Naulaers G, Wolf M, Lemmers P, van Bel F, Ameye L, Van Huffel S. Impaired cerebral autoregulation and its relation to clinical outcomes in premature infants. Proceedings 8th Belgian day on Biomedical Engineering, M. Nyssen (Ed.), Dec. 4, 2009, Published by Koninklijke Vlaamse Academie van België voor Wetenschappen en Kunsten, pp.51.
20. **Caicedo A**, De Smet D, Vanderhaegen J, Naulaers G, Wolf M, Lemmers P, van Bel F, Ameye L, Van Huffel S. Assessment of cerebral autoregulation using Near-Infrared Spectroscopy and its relation to short and long term clinical outcomes in premature infants. Abstracts 2nd Workshop on "Optical Imaging of Brain Function", funded by the WE-Heraeus Foundation, December 7-10, 2009, Bad Honnef, Germany.
21. **Caicedo A**, Naulaers G, Wolf M, Lemmers P, van Bel F, Ameye L, Van Huffel S. Assessing Cerebral Autoregulation for Neonatal Monitoring. Proceedings 9th Belgian day on Biomedical Engineering, M. Nyssen (Ed.), Nov. 26th, 2010, Published by Koninklijke Vlaamse Academie van België voor Wetenschappen en Kunsten, pp.92.
22. **Caicedo A**, Naulaers G, Wolf M, Ameye L, Van Huffel S. Assessment of Metabolic and Myogenic Activity in Cerebral Autoregulation for Neonatal Monitoring. Presented at the 6th International Conference on Brain monitoring and Neuroprotection in the Newborn, February 10-12 2011.
23. **Caicedo A**, Thewissen L, Naulaers G, Lemmers P, van Bel F, Van Huffel S. Influence of Maternal use of Labetolol in Pulse Pressure and Cerebral Autoregulation. Proceedings 10th Belgian day on Biomedical Engineering, M. Nyssen (Ed.), Dec. 2nd, 2011, Published by Koninklijke Vlaamse Academie van België voor Wetenschappen en Kunsten, pp.88.
24. **Caicedo A**, Thewissen L, Naulaers G, Lemmers P, Van Huffel S, van Bel F. Effects of Maternal Use of Labetalol on the Autoregulation Mechanisms in Newborns. Presented at the 2012 annual meeting of the Pediatric Academic Societies. Boston, USA. April 28th - May 1st, 2012.

25. **Caicedo A**, Varon C and Van Huffel S. Cardiopulmonary Coupling in Sleep Apnea Assessed by Means of Orthogonal Subspace Projection. Presented at 5th international conference MEDSIP 2012: Advances in medical signal and information processing. Liverpool England, July 2012.
26. **Caicedo A**, Thewissen L, Naulaers G, Lemmers P, van Bel F, Van Huffel S. Influence of Maternal use of Labetolol in Pulse Pressure and Cerebral Autoregulation. Presented at the 2nd international CarNET Conference. Radboud University Nijmegen Medical Centre Nijmegen, The Netherlands. September, 2012.
27. **Caicedo A**, Thewissen L, Naulaers G, Lemmers P, van Bel F, Van Huffel S. Effects of Maternal use of Labetalol on the Autoregulation Mechanisms in newborns: a Comparison Study between 4 Different Populations. Presented at the 7th International Conference on brain Monitoring and Neuroprotection in the Newborn. Tampa, Florida, USA. September 13-15, 2012.
28. **Caicedo A**, Varon C, Van Huffel S. Orthogonal subspace projections in sleep apnea detection. Proceedings 9th Belgian day on Biomedical Engineering, M. Nyssen (Ed.), Dec, 7th, 2012, Published by Koninklijke Vlaamse Academie van België voor Wetenschappen en Kunsten.

FACULTY OF ENGINEERING
DEPARTMENT OF ELECTRICAL ENGINEERING (ESAT)
SCD-SISTA
Kasteelpark Arenberg 10 box 2446
B-3001 Leuven
acaicedo@esat.kuleuven.be

